DYNAMICS OF PREMIXED FLAMES IN NON-AXISYMMETRIC DISTURBANCE FIELDS

A Dissertation
Presented to
The Academic Faculty

by

Vishal S. Acharya

In Partial Fulfillment
of the Requirements for the Degree
Doctor of Philosophy in the
School of Aerospace Engineering

Georgia Institute of Technology
December 2013

DYNAMICS OF PREMIXED FLAMES IN NON-AXISYMMETRIC DISTURBANCE FIELDS

Approved by:

Dr. Tim Lieuwen
Advisor, Professor
School of Aerospace Engineering
Georgia Institute of Technology

Dr. Vigor Yang
William R.T.Oakes Professor and Chair
School of Aerospace Engineering
Georgia Institute of Technology

Dr. Suresh Menon
Professor
School of Aerospace Engineering
Georgia Institute of Technology

Dr. Jeff Jagoda
Professor, Associate Chair for Graduate studies and Research
School of Aerospace Engineering
Georgia Institute of Technology

Dr. Fei Han
Manager, Combustion Dynamics & Diagnostics Lab, Aero Thermal & Mechanical Systems
GE Global Research Center
Niskayuna, NY, USA

Date Approved: June 13, 2013

To my parents, my wife and my well-wishers

ACKNOWLEDGEMENTS

"If I have seen further than others, it is by standing upon the shoulders of giants."

– Isaac Newton

This journey towards my Ph.D. degree has truly been more rewarding and important than its destination and there are so many to whom I am grateful for sharing in this journey.

This thesis is first and foremost dedicated to my advisor Prof. Tim Lieuwen. His patience, guidance, motivation and encouragement have spearheaded the possibility of this research work. His impact on my research outlook, ethics and professional values has matured me from a mere graduate student to the skilled and confident research professional that I am today. I am grateful to him for teaching me the importance of patience, tolerance and most importantly, persistent hard work. He truly pushed to test the limits of my technical thinking and application. Apart from his guidance, I thank him and his family for the many weekends that he hosted our research group out at his cabin for some well needed break from work. It has been a truly memorable and rewarding 6 years at the combustion lab as part of a different kind of family.

I would also like to make important mention of Prof. Satyanarayana R. Chakravarthy and Prof. R. I. Sujith from my undergraduate days at IIT Madras, who set the tone for my research interest and curiosity. I am exteremely humbled by their adoption of me into their research groups while I was merely an undergraduate student interested in applied mathematics problems. They exposed me to the intertwining concepts of Fluid Mechanics, Acoustics and Combustion that later culminated to an interest in combustion instability. Without their guidance and steadfast motivation, I

would not have taken to research and career move towards doing my PhD. I would also like to thank other members of the Rarifield Gas Dynamics Lab, which is where I worked from 4 years from 2003 to 2007. These include OJ Sreenivasan, Guru, Priya, Varun, Rahul, Lipika, Trinath and C Balaji.

The Ben Zinn Combustion Lab which came to be my second home after I came to Georgia Tech has always been filled with people who in one way or another have made my research and personal life a very memorable one. I have to begin by first considering the members of Room 112 where I spent 5 years of my PhD life. I like to thank Venkat 'Nelson' Narra for gracious giving me his desk to work on when I first got here and giving me my first advice on working with Tim. I also like to add that he offered me a room in his apartment when I first came and I am grateful to him for making it very easy. I like to thank Preetham and Santosh Hemchandra, who I used to secretively call "The Two Towers", not because they were tall, but they were the seniormost in Tim's theoretical research sub-group. Their communications with me which started 6 months before I came to the lab have been very helpful in getting me started with my research. Their advice at multiple steps of the work was very helpful in aligning me with a different school of thought at the research lab. I am very grateful to both of them for mentoring me and getting me on my feet when I first came to Georgia Tech. Next, I would like to mention Dong-Hyuk Shin or Tom as we all called him and Shreekrishna, both of whom shared the room with me for many years to come. As a collective, we accomplished in solving many of the mathematical problems that the entire research group and sometimes even the lab would face. I am immensely grateful to Tom for the numerous occasions in which we debugged code or checked mathematical derivations

and solutions. Shreekrishna gets a very special mention from me, first since we have known each other for 11 years now, having had the same undergraduate advisor as well, and second since I got a lot of advice on decision-making at the lab and under Tim during my time there. He has been a beacon of support and guidance for me all these years and continues to be so, while I work with him at GE as part of the USA Program. I will be forever indebted to him for the help, advice and direction that he has given me and continues to give me. I would like to mention Alberto Amato who has been a very important personality in the group for me. His fondness for a certain youtube channel, random rantings (and swearings) in Italian and the many times that he would just fall for anytime I say (even if it was hard to believe) has been a constant source of amusement and relaxation during otherwise busy work schedules at the lab. I am also grateful for the many times that he provided valuable input to my research work and the numerous occasions that we made plans to go and catch the latest movies. I would also like to mention Nick Magina, Jordan Blimbaum and Luke Humpries, who were the newest additions to the group after me, for the interesting times we have had as members of Room 112. Moving to the larger combustion lab family, I would like to first thank Bobby Noble for orienting me with the dos and don'ts of the combustion lab when I first came here and for his very good sense of humor that he graciously shared often giving me comic relief in an otherwise busy day. I am also immensely grateful to him for advice he has given me regarding various administrative related questions pertaining to my stay at the lab and as a student. I would like to thank David Scarborough for bearing with me (and the rest of us in Room 112) for the noise we would make in our discussions as neighbors. By no means are any of the other Lieuwen group members, any less

important, and I would like to thank (in no order) Jackie O'Connor (who introduced me to the still-mysterious dynamics of swirling flows), Jack Crawford, Prabhakar Venkateswaran, Andrew Marshall, Ben Emerson (with whom I could do some experimental work and validate my models), Chris Foley, Mike Malanoski & Mike Aguilar (for being patient with me on numerous occasions when I requested for experimental data) and Ianko Chterev. I would also like to make a mention of our lab interns Ben Giardina, Mouna Romani, Tayfun Akin, Qiao Zhang, Yanqin Li and Tao Sun.

I would like to thank the members of the extended combustion lab, Prof. Ben Zinn (who told me that I was one of the best Quals performers he has seen! ☺), Prof. Jerry Seitzman (whose combustion class was the best ever in my life), Brad Ochs, Ben Wilde, Santosh Shanbhogue, Yash Kochar, Karthik Periagaram, Yogish & Sai (who took me in as a room-mate for 2 years), Arun Radhakrishnan (who got me my mobile phone number when I first got here), Chilu, KC, Nori and Nishant.

I am grateful to Prof. Jeff Jagoda who as the Associate Chair for Graduate Studies and Research at the School of Aerospace Engineering provided very important and valuable guidance at the start of my PhD when I first came to Georgia Tech. The many interactions with him regarding selection of courses and the administrative procedures involved with CPT and other activities were very helpful and eased my mind in all of these occasions.

I am grateful to Dr. Fei Han who accepted me as a R&D Intern under his program at GE Global Research in Niskayuna, NY, where I had my first real world experience in performing research in an industry environment. It truly made me understand the

differences between academic research objectives and the research objectives of a large company like GE. I am very appreciative of Preetham who along with Fei was very key in helping me get going with work at GE and also provided much needed support when work was slow. I would also like to mention Dheeraj Kapilavai, Yonduck Sung, Kenji Miki who shared in my triumphs and woes during my internship period. I would also like to thank Shiva Srinivasan and the entire USA Program team at GE Energy and Penn State for their many valuable feedbacks over the numerous and endless telecons that we have had over the past 5 years. This includes team members Shreekrishna, Domenic Santavicca and Nick Bunce. Over the years, they have given me direction for my research as well as its applicability in real-world combustion systems such as those offered by GE.

I have felt quite blessed with the flurry of friends that I have had over my time here at Georgia Tech. In no particular order, I would like to thank Manisha, Anand, Karthik, Kiruthika, Preksha, Ashwini, Shaloo, Priyanka, Nishanth, Prashanth and Rohit. In their own unique ways, they have all been a source of support and company.

Last but never the least; I would like to talk about family. They have been the single most driving force for anything in my life. I would like to thank my parents who have been very supportive and encouraging of my many decisions in life, including my decision to pursue a PhD away from home. I like to thank my maternal grandparents who took charge to get me focused in my studies and paved the way for my interest in mathematics and physics that eventually helped me enter the prestigious IIT system in India. I will forever be indebted to them for this. Towards the last few years of my PhD, I was blessed to have a new support system: my wife. Preethi is someone who brings tears to my eyes, even as I try to write this and nothing I say or write here can do justice to

what she means to me and what she has helped me through when I was trying to get my PhD done. She has been my single beacon of support and motivation that has helped me get things done. Her understanding of me, which is unparalleled has been very important for me to have a clear mind when I had to get work done. I am immensely indebted to her for the rest of my life, for driving me to be the person I am and in the process, helping me to be the professional that I now am.

Finally, I would like to thank Prof. Vigor Yang, Prof. Suresh Menon, Prof. Jeff Jagoda and Dr. Fei Han for agreeing to be committee members at my defense at a time that kept their lives very busy with travel, and offering constructive criticism of the work that has gone into this thesis.

TABLE OF CONTENTS

LIST OF FIGURES

LIST OF SYMBOLS AND ABBREVIATIONS

English Upper-case

A	Spatially integrated ("global") flame area.
$\hat{B}_{i,m}$	Amplitude of helical mode m for velocity component in the *i*-coordinate direction.
CH^*	Chemilumenescence.
D	Bluff-body (or) nozzle diameter.
$\hat{F}_M$	Scalar monopole sound source strength.
$\hat{F}_{D,i}$	Vector component in the *i*-coordinate direction of the dipole sound source strength.
$\hat{F}_{Q,ij}$	Tensor component (i, j) of the quadrupole sound source strength.
F_L	Flame Transfer Function for Longitudinal Acoustic mode.
F_T	Flame Transfer Function for Transverse Acoustic mode.
F_{TL}	Transfer function between induced Longitudinal and source Transverse fluctuations.
$F_{L\omega}$	Transfer function between induced vortical disturbances due to, and longitudinal fluctuations.
$F_{T\omega}$	Transfer function between induced vortical disturbances due to, and transverse fluctuations.
F_ω	Flame Transfer Function due to induced vortical fluctuations.
G	Level set function.

${}_cH_{i,m}; {}_sH_{i,m}$	Asymmetry coefficients for the mean flow.
L	Flame edge position used in Chapter 6.
L_{11}	Integral length scale for turbulence.
L_f	Characteristic flame length scale (flame height).
M	Mach number.
P	Total sound power.
Q	Global unsteady heat release rate.
R	Non-dimensional center-body radius.
$R_{\max}$	Maximum radial location corresponding to flame height L_f.
S	Characteristic swirl number.
St	Strouhal number based on ratio of characteristic axial time-scale and acoustic time-scale.
St_2	Strouhal number based on ratio of characteristic flame wrinkle transport time-scale and acoustic time-scale.
St_Ω	Strouhal number based on ratio of characteristic axial time-scale and swirling time-scale.
$St_{\Omega,2}$	Strouhal number based on ratio of characteristic flame wrinkle transport time-scale and swirling time-scale.
St_c	Strouhal number based on ratio of flow disturbance convection time-scale and acoustic time-scale.
U_0	Characteristic mean velocity scale.
U_c	Phase speed of the velocity disturbance.

$U_{c,f}$	Phase speed of flame position fluctuation projected in axial direction.
$U_{c,v}$	Phase velocity of vortical velocity fluctuation projected in axial direction.
V	Volume of integration for Rayleigh criterion.

English Lower-case

c	Speed of sound
$\vec{e}_i$	Normal vector along the *i*-coordinate direction.
f_0	Forcing frequency.
$f(s), g(s)$	Characteristic functions, defined in Eq.(3.36).
h_R	Heat of reaction.
k_c	Non-dimensional phase speed of disturbance, $=U_c/U_0$.
m	Helical mode number for flow disturbance.
n	Azimuthal mode number for mean flow.
p	Pressure.
q	Unsteady heat release rate per unit volume.
s	Characteristic coordinate.
s_L	Laminar flame speed.
s_T	Turbulent flame speed.
s_f	Displacement speed (or) front speed.
$\vec{u}$	Velocity vector.

u, v	Axial and transverse velocity components (Chapter 6).
u_f	Flame front velocity in front-fixed reference frame.
u'_{ref}	Reference velocity disturbance for use with Flame Transfer Function.
u'_{rms}	Root Mean Square Turbulent velocity.

Greek Upper-case

Ω	Characteristic azimuthal frequency (or) angular rate of swirl.

Greek Lower-case

α	Growth rate of flow disturbance amplitude.
δ_f	Flame thickness
ε	Non-dimensional disturbance amplitude of velocity fluctuations.
η	Non-axisymmetry parameter for mean flow and mean flame shape.
λ_a	Acoustic wavelength.
λ_c	Convective wavelength.
ν	Kinematic viscosity.
ξ	Flame location used by the model.
ρ	Density.
σ	Swirl parameter (or), Ratio of azimuthal frequency and acoustic forcing frequency.
φ	Phase of flame wrinkling.

χ	Ratio of characteristic flame length-scale and acoustic length-scale (wavelength), $= L_f / \lambda_a$.
ψ	Half angle of the stationary flame.
ω	Angular acoustic frequency.

Common subscripts

$( )_{r,\theta,z,x}$	Radial, azimuthal, axial and transverse x-direction component, respectively.
$( )_{t,n}$	Tangential and normal components to the mean flame surface, respectively.
$( )_a$	Acoustic contribution.
$( )_v$	Vortical contribution.

Scripted Fonts

$\mathscr{V}$	Volumetric flow rate through the flame surface.
$\mathscr{W}$	Amplitude of flame wrinkling

Operators

$\overline{( )}$	Mean component.
$\langle \rangle$	Ensemble average.
$( )'$	Fluctuating component.
$\widehat{( )}$	Frequency domain representation of corresponding time domain quantity.

$\lvert(\ )\rvert$	Magnitude of complex quantity.
$\angle(\ )$	Phase of complex quantity.

Abbreviations

AI	Absolute Instability
CI	Convective Instability
FTF	Flame Transfer Function
IP	In-Phase forcing condition
$K-H$	Kelvin-Helmholtz instability
NO_x	Nitric Oxides
OP	Out-of-Phase forcing condition
PVC	Precessing Vortex Core
VBB	Vortex Breakdown Bubble

SUMMARY

With strict environmental regulations, gas turbine emissions have been heavily constrained. This requires operating conditions wherein thermo-acoustic flame instabilities are prevalent. During this process the combustor acoustics and combustion heat release fluctuations are coupled and can cause severe structural damage to engine components, reduced operability, and inefficiency that eventually increase emissions. In order to develop an engine without these problems, there needs to be a better understanding of the physics behind the coupling mechanisms of this instability. Among the several coupling mechanisms, the "velocity coupling" process is the main focus of this thesis.

The majority of literature has treated axisymmetric disturbance fields which are typical of longitudinal acoustic forcing and axisymmetric excitation of ring vortices. Two important non-axisymmetric disturbances are: (1) transverse acoustics, in the case of circumferential modes of a multi-nozzle annular combustor and (2) helical flow disturbances, seen in the case of swirling flow hydrodynamic instabilities. These disturbances have a spatial dependence of the form $\hat{u}_i' \propto \exp(im\theta)$ where m is (1) the asymmetric mode in the case of transverse acoustic forcing, and (2) the helical mode number in the case of helical flow disturbances. With significantly less analytical treatment of this non-axisymmetric problem, a general framework is developed for three-dimensional swirl-stabilized flame response to non-axisymmetric disturbances. The dynamics are tracked using a level-set based *G*-equation applicable to infinitely thin flame sheets. For specific assumptions in a linear framework, general solution

characteristics are obtained. The results are presented separately for axisymmetric and non-axisymmetric mean flames.

The unsteady heat release process leads to an unsteady volume generation at the flame front due to the expansion of gases. This unsteady volume generation leads to sound generation by the flame as a distributed monopole source. A sound generation model is developed where ambient pressure fluctuations are generated by this distributed fluctuating heat release source on the flame surface. The flame response framework is used to provide this local heat release source input. This study has been specifically performed for the helical flow disturbance cases to illustrate the effects different modes have on the generated sound. Results show that the effects on global heat release and sound generation are significantly different.

Finally, the prediction from the analytical models is compared with experimental data. First, a two-dimensional bluff-body stabilized flame experiment is used to obtain measurements of both the flow and flame position in time. This enables a local flame response comparison since the data are spatially resolved along the flame. Next, a three-dimensional swirl-stabilized lifted flame experiment is considered. The measured flow data is used as input to the *G*-equation model and the global flame response is predicted. This is then compared with the corresponding value obtained using global *CH** chemilumenescence measurements.

CHAPTER 1

INTRODUCTION

1.1 History and Motivation

Since the dawn of civilization, the ability to provide energy in its various forms has been the primary driver of progress. Specifically, the use of flames to provide heat during extreme cold and for cooking by primitive man, to the use of fossil fuels for transportation and power in the modern age, energy has been the primary source of development for a civilization. However, during the modern age, the demand for energy has increased exponentially, both with new technologies as well the increase in human population. For this reason, hydrocarbons such as natural gas have been used as a source of energy primarily due to their ready availability. However, their use leads to the production of pollutant emissions such as Nitrous oxides (NO_x) and Carbon monoxide (CO).

Non-premixed combustion systems, adopt a separate fuel and oxidizer stream that mix in the combustion chamber. The combustion occurs at stoichiometry (no amount of fuel or oxidizer remains at the end of the combustion process). This unfortunately corresponds to an unacceptable level of emissions. Due to health concerns, environmental regulations require very strict adherence to the permissible level of pollutants generated by a combustion device and its approval for commercial use. Since lean premixed operation allows for lower levels of NO_x and CO, combustor operation away from the stoichiometric condition was required. This has led to a shift from a non-premixed combustion operation to a premixed combustion mode. In the premixed mode of operation, the fuel and oxidizer are premixed ahead of the combustion zone. With a fuel-

lean premixed mixture, the emissions levels could be reduced to that accepted by environmental standards.

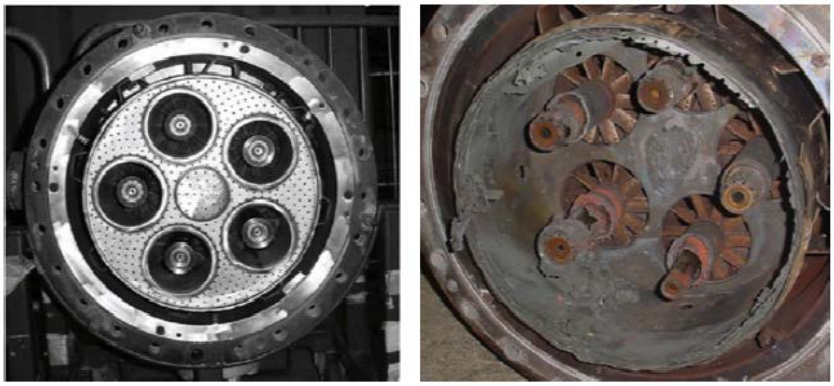

(a) **(b)**

Figure 1 : Combustor components from a burner assembly showing (a) New assembly, and (b) Destroyed assembly. Images reproduced from Ref. [1].

Although, this shift helped reduce emissions considerably, it was not without other problems. Significant of this was the problem of combustion instability. During combustion instability, self-excited oscillations occur in the combustor volume where the natural acoustic modes of this volume couple with the heat release from the combustion process. This was first suggested by Lord Raleigh [2]. In this coupling process, the heat release oscillations can positively feedback to the pressure oscillations, thereby leading to an unbounded growth in amplitude. Apart from gas turbines [9, 10], this has been observed in combustion systems of rockets [3-8]. The high amplitudes can cause structural damage, and also negate the emissions reduction advantage. Some of the damage caused by this phenomenon is shown in Figure 1. This oscillatory combustion process can also lead to unsteady thermal stresses that degrade the life-span of components such as liners and casings and eventually lead to reduced combustor operability. The compounded losses from all of these can easily run into millions of

dollars and hence it warrants a study into the underlying mechanisms of such a process and how it can be controlled.

1.2 Combustion Instability

In 1896, Lord Rayleigh published "The Theory of Sound" [2], which presented the general features of "vibrations maintained by heat" (as they were referred to in the 1800s). He recognized the crucial phase relationship between the communication of heat and the vibration in a resonator. The classical demonstration consisted of a hydrogen flame burning inside an open tube. Pressure variations in the tube cause the flow of gas, and therefore the heat release, volume expansion, and backpressure on the nozzle to vary during the "vibration". If the product of the fluctuating parts of the backpressure (p') and heat release rate (q'), integrated over a cycle of the vibration, is positive, in the absence of damping the vibration will be maintained. In other words, if the fluctuating heat release is more in phase than out of phase with the vibration in the resonator, conditions are right for feeding energy into the vibration. This was referred to as the "Rayleigh criterion" (shown in Eq.(1.1)) and the observed flame behavior was referred to as a "singing flame". This is the earliest observance of the modern combustion instability process.

$$\oint_V \int_t p'(\vec{x},t)q'(\vec{x},t)dtdV \geq 0 \tag{1.1}$$

Note that the superscript "prime" denotes fluctuations about the mean quantity. As simple as this equation may seem, the pressure fluctuations and heat release fluctuations are tightly coupled. Their interactions are governed by several processes related to the dynamical flow behavior, chemical reactions and the geometry of the combustion

volume. For a given point in the combustor, the heat release process adds energy locally to the acoustic field when the magnitude of the phase between the pressure and heat release oscillations is less than 90 degrees. In situations where the flame region is small relative to an acoustic wavelength, the spatially integrated heat release fluctuations, $Q'(t)$, is of particular interest for combustion noise and thermoacoustic instability problems. This is given by:

$$Q'(t) = \oint_V q'(\vec{x},t)dV \tag{1.2}$$

For this "acoustically compact" case, it is this single quantity, $Q'(t)$, which controls the noise generation by flames and/or the thermoacoustic stability of a ducted system, regardless of the spatial details, $q'(\vec{x},t)$. For this reason, apart from the local response, $q'(\vec{x},t)$, the global response, $Q'(t)$, will also be of focus in this thesis. The instantaneous global heat release rate is given by:

$$Q(t) = \int_{flame} \rho_u s_L h_R dA \tag{1.3}$$

This equation shows that the unburnt density (ρ_u), the flame speed (s_L), the heat of reaction (h_R) and the flame surface area (A) affect the heat release rate. Some of the mechanisms that affect these quantities are: acoustic velocity fluctuations [11, 12], convected/vortical fluctuations [13-17], and equivalence ratio fluctuations [18-22] to name a few. They manifest as broadband fluctuations over a continuum of length and time scales, as well as very narrowband oscillations [9, 23]. In particular, the lightly damped acoustic modes manifest as temporally narrowband oscillations. These upstream disturbances perturb the flame leading to fluctuations in the heat release rate. Since this oscillating heat release from the flame is a monopole acoustic source [24], it generates

sound. This generated sound (acoustic oscillations) could then amplify in accordance with the aforementioned Rayleigh criterion (Eq.(1.1)). This completes the feedback loop in the mechanism, as shown in Figure 2. Among these mechanisms, this thesis focusses on the response due to velocity oscillations, which shall be the focus of the next section.

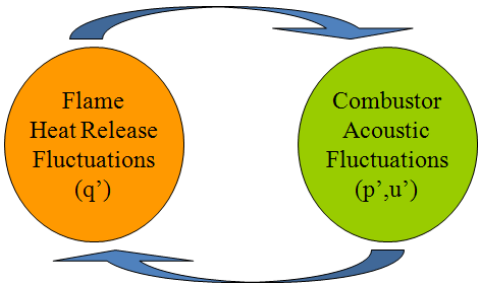

Figure 2 : Combustion instability feedback loop between disturbance sources and heat release oscillations.

1.3 Velocity Response Mechanism

The response of a premixed flames to velocity oscillations consists of that due to the direct acoustic disturbances [11, 12] and the induced convected vortical disturbances [13-17, 25]. When the equivalence ratio and unburnt density are constant, the only quantities affecting the heat release rate are the flame speed and the flame surface area (Eq.(1.3)).

For low frequencies, the flame speed remains constant and hence only the surface area fluctuations lead to heat release rate fluctuations. However, the oscillating stretch along the flame, due to both hydrodynamic straining and curvature, grows in importance with frequency, causing oscillations in flame speed. These also lead to perturbations in the heat release rate oscillations. The frequency ranges in which these routes become important have been shown by Preetham *et al.* [26] and Wang *et al.* [27]. The response to velocity perturbations has been analyzed by researchers using both experimental and theoretical techniques.

1.3.1 Experiments

First, consider an overview of important experiments in the literature. Bloxsidge *et al.* [28] experimentally investigated the response of confined flames to weak harmonic

sound waves experimentally and showed that the unsteady combustion process was driven by velocity fluctuations at an axisymmetric center body that acted as a flame holder with the flame stabilized in the wake. They discussed the thermoacoustics of the duct using an empirical relationship between the heat release obtained and the specified velocity perturbations (also referred to as the transfer function, discussed later). Durox *et al.* [29] studied a flame that was excited by acoustics waves produced by a loudspeaker placed upstream of the flame and observed the distortions of the flame front that convected downstream with the mean flow. Bourehla and Baillot [30] systematically characterized the variety of flame holding behavior and flame shapes for a laminar Bunsen flame excited by low frequency high amplitude velocity perturbations. Significant experimental work has also been performed by groups from France in this regard [12, 23, 29-33]. Since the focus of this thesis is a theoretical and numerical analysis, next we summarize the important contributions made by researchers in this regard.

1.3.2 Modeling

The theoretical analysis of thin premixed flames has been performed using the *G*-equation. This equation is a level-set equation that governs the dynamics of surface motion in an ambient velocity field. The use of the *G*-equation for treating premixed flames was first proposed by Markstein [34] and later adapted to turbulent premixed flames by Williams [35, 36] as well as Matalon and Matkowsky [37]. Boyer and Quinard [38] studied the dynamics of an anchored premixed flame and concluded that the temporal evolution of the flame front was due to interference of wrinkles convecting along the flame shoulder and wrinkles induced due to the flow. Fleifil *et al.* [11] studied the response of a premixed flame to velocity disturbances and calculated the transfer function, which revealed that the heat release is related to the inducing velocity disturbances by a time-lag law. Dowling [39] provided the theoretical basis for the empirical observations of Bloxsidge *et al.* [28]. Candel and co-workers [12, 23, 29, 40-

43] have used the *G*-equation to develop models with varying fidelities. Most of these works have used simplified assumptions of the flame. Preetham and co-workers [26, 44] have advanced the modeling efforts by accounting for non-compactness of flame geometry, unsteady flame curvature, hydrodynamic strain effects and gas expansion across the flame. Specifically, the results from the gas-expansion study [44] showed that redefining an effective Strouhal number would enable the use of results from the constant density cases.

Existing flame response studies have primarily focused on the flame response to axisymmetric disturbances, such as ring vortices excited by the flow forcing. However, there are two important instances where the forcing is non-axisymmetric, a feature, which excites an additional degree of freedom into the problem. First, during transverse instabilities, the flame may be subjected to transverse acoustic oscillations, which induce an intrinsically non-axisymmetric forcing on the flame. In addition, helical modes may be excited during both axial and transverse acoustic instabilities due to the nature of hydrodynamics in the flow.

1.4 Thesis Research Focus and Layout

This thesis focusses on the velocity coupled mechanism of the combustion instability process. While prior work by various researchers have focused on axisymmetric flames responding to axisymmetric disturbances, the primary focus of this research work is to understand the response of three-dimensional premixed flames to non-axisymmetric disturbances. In particular, swirling flows are considered with two important sources of non-axisymmetric disturbance fields being transverse acoustic waves and helical flow disturbances. This first chapter in the thesis has summarized: (i) the importance and complications of the combustion instability phenomena, (ii) the velocity coupled

mechanism and (iii) the need for theoretical models to better understand the physics of the phenomena.

In Chapter 2, the physics of the dynamical flow features are presented. First, we consider swirling flows in general and their hydrodynamic content. Second, the physics of the disturbance fields are described in detail, namely that due to (i) transverse acoustic instabilities and (ii) helical flow disturbances.

In Chapter 3, the theoretical formulation based on the *G*-equation is presented. It begins by considering the premixed flame regime in which the model and its assumptions are valid. Next, the importance of linear and non-linear analysis is presented. Since the *G*-equation is non-linear and not analytically tractable directly, a linear approach is used. This linear analysis illustrates the features of the flame perturbation solution both in terms of local flame response and the global heat release fluctuations. Finally, these heat release fluctuations lead to sound emissions and a linear acoustic analysis of the sound generated is presented. These are then simplified for an axisymmetric mean flame. The analysis is then further expanded to consider weakly non-axisymmetric mean flames as well. A numerical solver is described that solves the non-linear partial differential equation governing the flame position dynamics. This solver can capture non-linearity effects due to high amplitude disturbances as well as the effects of strong asymmetries in the mean flow and mean flame shape. Finally, a triple decomposition of the disturbance field into acoustic, vortical and entropy contributions is presented. This is then used to illustrate the analytical form of the acoustic and vortical disturbances used in the example problems.

In Chapter 4, example calculations are presented for the flame response to transverse acoustic disturbances. First, the linear analytical framework for small amplitude disturbances is used. It presents both local flame response features as well as global flame response characteristics. It also illustrates the comparison of global flame response between that due to transverse disturbances and longitudinal disturbances. The relative importance of the transverse instability mode with respect to the longitudinal instability mode is then understood.

In Chapter 5, example calculations are presented for the flame response to helical flow disturbances, The linear analytical model is used to illustrate the difference in local and global flame response to different helical modes and hence the important flow field modes affecting flame response. These solutions are then used to explicitly calculate the far-field sound generation. Finally, an example illustration of the effect of weakly non-axisymmetric flames is presented by adding a small asymmetry to the mean flow in the above example flow-field. The resulting changes in global flame response due to helical modes are described. Finally, the numerical solver is used to illustrate the effects of strong asymmetry in the mean flame/flow.

In Chapter 6, the linear model is used in conjunction with experimental. For this, a two-dimensional bluff-body stabilized flame in a high Reynolds number flow is considered. Due to the two-dimensional nature of the flame and flow, flow and flame data are available that are resolved both spatially and temporally. Using these, local flame response predictions are made and compared with measurements.

In Chapter 7, the linear model is used in conjunction with data from a swirling lifted flame. In this case, due to the three-dimensional nature of the flow and flame, local

measurements are not possible. However, global flame response measurements are made using line of sight integrated *CH** chemiluminescence. Particle Image Velocimetry (PIV) is used for flow measurements in an axial plane (plane along the flow direction) and a few discrete transverse planes (perpendicular to the flow). These are used to obtain the helical mode nature of the flow-field which is input to the model. The model is then used to predict the global flame response from the model and then compare with that measured from the experiment.

The final chapter of this thesis presents recommendations and suggestions for future work.

CHAPTER 2

FLOW FIELD PHYSICS

This chapter describes the key flow features of swirling flows and the disturbance flow field for the non-axisymmetric disturbances namely: (i) transverse acoustic disturbances and (ii) helical flow disturbances.

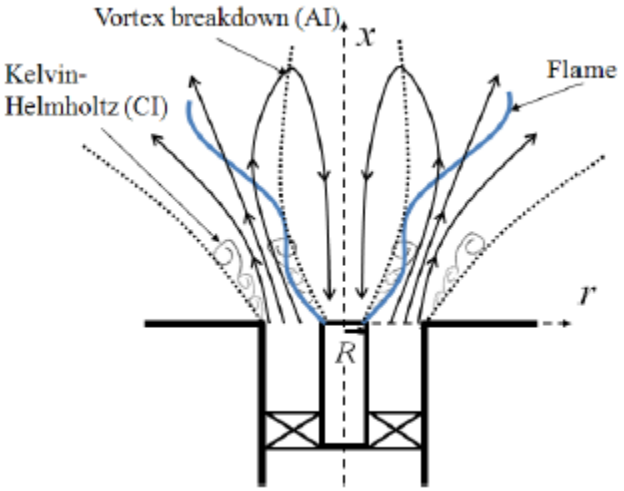

Figure 3 : Flow structure of an annular swirling jet showing the Kelvin-Helmholtz instability in the shear layers as well as the Vortex Breakdown region. CI: Convective Instability, AI: Absolute Instability. Reproduced from Ref. [45].

2.1 Swirling Flows

Consider an annular swirling reacting flow as pictured in Figure 3. The flame is stabilized on the center-body. Two important hydrodynamic features are: (1) the two shear layers (three-dimensional) that begin at the inner and outer edges of the annular nozzle exit, and (2) the central recirculation zone above the center-body. The shear layers are subject to the Kelvin-Helmholtz (K-H) instability in both the axial and azimuthal direction, leading to the vortical roll up of the fluid in the separating boundary layer into tightly concentrated regions of vorticity [45-49]. The convectively unstable nature of

these shear layers makes them particularly sensitive to acoustic forcing [45, 46, 50-52]. This leads to the vortex shedding frequency locking on to the acoustic frequency [45, 46, 53-59]. The flame wrinkling and heat release response of center-body stabilized flames to flow forcing is dominated by these flow structures disturbing the flame.

The vortex breakdown phenomenon is common to high swirl number cases that are typical of gas turbine flows. When radial and axial vorticity is converted to azimuthal vorticity, an absolute instability is created leading to this vortex breakdown. However, at high swirl numbers, the breakdown is a vortex breakdown bubble. The main feature of the bubble is its ability to channel flow around it and hence leading to an annular jet like flow. For reacting flow, the gas expansion due to heat release causes an axial flow acceleration that then decreases the swirl number and increases axial velocity gradients and shear. In the case of the absolutely unstable vortex breakdown bubble, the effect of acoustics is dependent on the shape and strength of the bubble. An attached bubble lacks the vertical degree of freedom, as compared to the lifted bubble. This leads to a significant effect of the upstream stagnation point moving. The effect of acoustics on the stagnation bubble and the resultant effect on unsteady combustion have been documented [60, 61].

Swirling flows also exhibit narrowband oscillations due to the precession of the vortex core, referred to as the PVC [60]. Depending upon the frequency of excitation, the oscillations of the PVC can be diminished or amplified [62]. Specifically, if the acoustic frequency and the narrowband oscillations match, it leads to amplification [63]. Others have seen a system response at the difference of the PVC frequency and forcing frequency [64, 65]. Very high amplitudes of acoustic excitation can lead to changes in

time-average flow behavior and hence the hydrodynamics as well. In this situation, the entire system locks-in on the acoustic frequency. These swirl flow instabilities play a significant role in determining the flame response.

Swirling flow dynamics control flow recirculation, flame stabilization, flame shape, dynamic stability limits, as well as a number of other critical combustion parameters. Because of the profound influences of the swirling flow field upon the flame shape, such as flame angle, swirl has important influences upon unsteady flame dynamics. For example, it is known that the Strouhal number, *St*, is an important parameter describing flame transfer functions. Changes in flame length because of modifications in swirl number exercise significant influences on the flame response to harmonic perturbations. This effect is implicit, however, in that swirl does not explicitly enter the dynamical equations for the flame dynamics, but rather through its influence upon parameters such as flame angle or flame length.

Swirl has explicit effects on the dynamics of the flame as well. For example, Palies *et al.* [66] studied longitudinally forced swirl flames and showed two distinct velocity coupled mechanisms which controlled the flame response. The first mechanism was the "direct excitation" of the flame by the flow disturbances, a mechanism common to non-swirling flows that has previously been treated in detail [12, 23, 67, 68]. This first mechanism has been very successfully analyzed using level set approaches, see Dowling *et al.* [69], Schuller *et al.* [43], and Preetham [44]. In addition, Palies *et al.* [66] and others [51, 70-73] have showed that an additional, "indirect" mechanism occurs that is unique to swirl flows and is of comparable influence on the flame response to that of the "direct" mechanism. Specifically, acoustic waves propagating through swirlers excite

axial vortical disturbances, leading to modulations in swirl number. It has been postulated that these swirl number modulations, in turn, lead to oscillations in flame angle, a parameter with a well-known influence upon flame dynamics.

This thesis considers an additional mechanism through which swirl explicitly influences flame dynamics in cases where the flame or excitation is non-axisymmetric. This is a "direct excitation" mechanism and is closely linked to the coupling of flame/flow non-axisymmetries and the propagation of flame wrinkles in the azimuthal direction. While a number of prior studies have noted the propagation of wrinkles by the time averaged flow, including the azimuthal component [74], there are no explicit calculations of these swirl effects on the flame dynamics. However, these swirl effects can introduce rather substantial qualitative impacts on the flame response. These are seen particularly in its local dynamics and in planar visualizations of the flame.

2.2 Transverse Acoustic Excitation Sources

The different possibilities for acoustic mode excitation in combustion chambers are shown in Figure 4. Longitudinal mode instabilities are along the main flow direction, radial modes are transverse in the radial direction and circumferential modes are transverse along the circumferential direction such as is typically seen in multi-nozzle annular combustor configurations.

A variety of combustion systems have been plagued by longitudinal mode instabilities [9, 46, 75-80] while transverse instabilities have been a key instability concern in rockets and afterburners for decades [8, 81-91]. More recently, transverse oscillations have grown problematic in low NO_x gas turbines, both in ground-based and aero-engine applications [80, 92-96]. Due to the differences in the length scales involved,

these transverse oscillations generally occur at lower frequencies (i.e., 100's of Hz) in annular combustion chambers [94, 97-101] and at higher frequencies (i.e., 1000's of Hz) in can combustion chambers [98, 102].

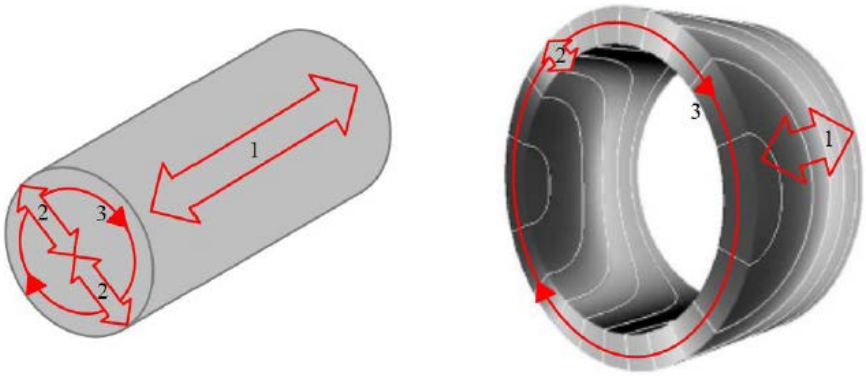

(a) **(b)**

Figure 4 : Acoustics modes for (a) can combustor, and, (b) annular combustor, showing (1) longitudinal mode, (2) radial mode, and, (3) circumferential/azimuthal mode. Reproduced from Ref. [45].

In the case of annular combustion chambers, the length scale of the acoustic mode is along the circumference and each nozzle is subjected to a different field depending on its location relative to this acoustic mode. In comparison, longitudinal mode oscillations are along the main flow direction and hence affect each nozzle equally. This effect is also compounded by the nature of the acoustic mode, which could either be a standing wave or a traveling wave. In the case of a standing wave, certain nozzles experience velocity nodes while certain others experience pressure nodes and these two contrasting acoustic forcing conditions lead to significant differences in the flame response as well. In the case of traveling wave instability, the mode shape spins around the circumference and the differences between nozzles is a function of the acoustic frequency and the flame temperature (acoustic speed).

The Rayleigh criterion mentioned in Eq.(1.1) showed the importance of the relationship between $p'(t)$ and $q'(t)$ for the growth or decay of an instability. If the absolute value of the phase between the pressure and heat release oscillations is less than $\pi/2$, then the instability will amplify and vice versa. The pressure fluctuations are dependent on the acoustic modes of the combustion chamber, its geometry and the properties of combustion (such as post flame temperature), and the heat release fluctuations are in turn a function of these pressure fluctuations and complicated flow phenomena. These flame-flow dynamics are described using a transfer function approach. Since the focus of this thesis is the velocity coupled mechanism, the form of the transfer function is to relate velocity disturbances to disturbances in the heat release:

$$\frac{\hat{Q}'}{\bar{Q}} = \widehat{FTF}\,\frac{\hat{u}'_{ref}}{\bar{u}} \tag{2.1}$$

Here, $\hat{Q}'$ is the heat release fluctuation in frequency space, $\hat{u}'_{ref}$ is a reference fluctuating velocity in frequency space that is dependent on the spatial nature of the velocity disturbance and $\widehat{FTF}$ is the Flame Transfer Function in frequency domain.

In the case of longitudinal mode oscillations, the acoustic disturbance directly affects the flame response, which is the "root wave" effect [12, 44]. This acoustic disturbance also excites vortical flow oscillations. Swirling flows possess hydrodynamic flow instabilities that are excited by the prevalent acoustic modes. These disturbance pathways are shown in Figure 5(a).

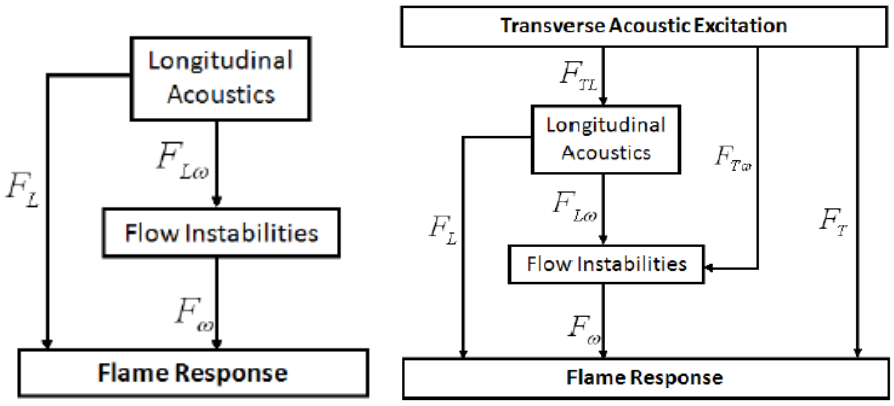

(a) **(b)**

Figure 5 : Velocity disturbance pathways that lead to flame response for (a) longitudinally forced flame, (b) transversely forced flame. The quantities indicated by *F* denote the transfer functions along those pathways. Reproduced from Ref. [45].

However, transverse velocity disturbances are different. In addition to the vortical flow excitation, the transverse acoustic modes also cause an oscillating pressure drop across the nozzle and this leads to longitudinal oscillations [103-105]. These longitudinal oscillations, when traversing the swirler, can then lead to swirl flow fluctuations or swirl number fluctuations [51, 66, 70-73]. Large Eddy Simulations of a full annular combustor configuration by Staffelbach *et al.* [93] have shown that the longitudinal oscillations are the significant contributor to flame response, even though their initial source was the transverse oscillations. These have also been reported experimentally by O'Connor [45]. These pathways are shown in Figure 5(b). The transverse acoustic disturbances excite longitudinal mass flow fluctuations in the nozzle, which then further excite vortical disturbances. These vortical disturbances may also play an important, though indirect role, in the flame response as indicated by $F_{L\omega}$ in Figure 5(b). Thus the initial transverse disturbance field leads to a complex three dimensional disturbance field at the flame that, in reality, is hard to separate [45].

Although not a focus of this thesis, consider the transfer function F_{TL} shown in Figure 5(b). This transfer function describes the resulting axial velocity fluctuation at the

nozzle, relative to the incident transverse velocity fluctuation. If the gain of this transfer function is significantly greater than unity, the flame response may be largely a result of the longitudinally driven pathways. Conversely, if the amplitude of the transfer function is significantly less than unity, the dominant acoustic velocity fluctuation would be in the transverse direction and would drive both the vorticity generation, through $F_{T,\omega}$, and the flame response. Hence, a separate transverse to longitudinal velocity transfer function for different transverse acoustic field symmetries is important. This has been done experimentally by O'Connor [45, 106] and computationally by Blimbaum *et al.* [105]. The behavior of this velocity transfer function may be different for a nozzle located at a pressure node versus a pressure anti-node, and different still if there is a traveling component to the transverse acoustic field. The nozzle impedance had a large effect on the transverse to axial coupling at a pressure anti-node and in the case of traveling-wave acoustic excitation. The results from Blimbaum *et al.* [105] showed that the spatially-averaged pressure to axial velocity relationship was quite close to the one-dimensional, translated impedance value at the end of the side branch (nozzle). The notable exception to this result was when the nozzle was located at a pressure node, where the axial velocity characteristics are independent of the nozzle impedance. The importance of this acoustic coupling implies that the flame transfer function, in the case of transverse forcing, will be neither decoupled from the hydrodynamic fluctuations nor the system acoustics.

This thesis focuses specifically on swirling premixed flames subjected to transverse flow oscillations. Transverse excitation in the presence of swirl introduces new degrees of freedom because of its intrinsically non-axisymmetric nature, a point that is explicitly illustrated in Chapter 4 using example calculations. Transverse excitation is fundamentally different from longitudinal excitation in several key ways. First, while longitudinal disturbances are generally axisymmetric, or at least approximately so, transverse disturbances excite the flame in an intrinsically non-axisymmetric manner, as

shown in Figure 6(a). This causes significant azimuthal variations in local disturbance field at the flame sheet.

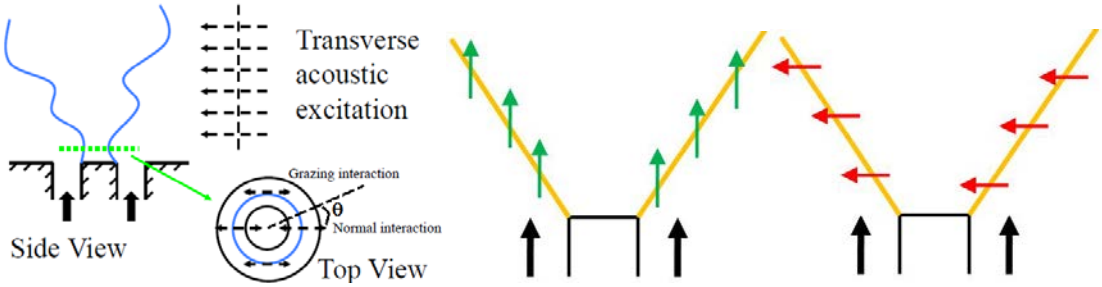

Figure 6 : (a) Flame interactions with transverse excitations; (b) Longitudinal forcing; (c) Transverse forcing.

Second, the volumetric flow rate through the flame, which is directly related to the spatially integrated low Strouhal number flame response, has the same sign at all azimuthal locations for longitudinal forcing, as shown in Figure 6(b), but of opposite sign in the case of transverse forcing, as shown in Figure 6(c). In Chapter 4, example calculations for both F_T and F_L are used to understand the relative importance of these transfer functions, but these shall assume disturbances of equal amplitudes for both cases ($F_{TL} \equiv 1$).

2.3 Helical Flow Disturbances

While acoustic waves often serve as the "clock" that controls the natural frequency of the self-excited system, it is generally the acoustically excited fluid mechanic instabilities that are the dominant source of flow oscillations.

Previous studies have detailed the dynamics of swirling flow instabilities in response to variations in longitudinal forcing for both non-reacting and reacting conditions. These studies have shown the development of helical instabilities in unforced

swirling flows, but most suggest that longitudinally forced flames are dominated by symmetric ring vortices [46, 64, 107]. Studies of transversely forced flames have shown that the nearfield flame wrinkling is dominated by ring or helical vortices, depending upon whether the flame is located at a pressure anti-node or node, respectively. These helical modes may be excited during both axial and transverse acoustic instabilities.

For example, Figure 7 shows a simulation by Huang and Yang [108], clearly indicating the helical flow disturbances in the combustor. Note that large swirl numbers lead to a significant breakdown of the helical flow features. Similarly, Figure 8 shows flame luminescence from O'Connor [45] indicating the presence of helical flow disturbances on a line of sight image of the flame.

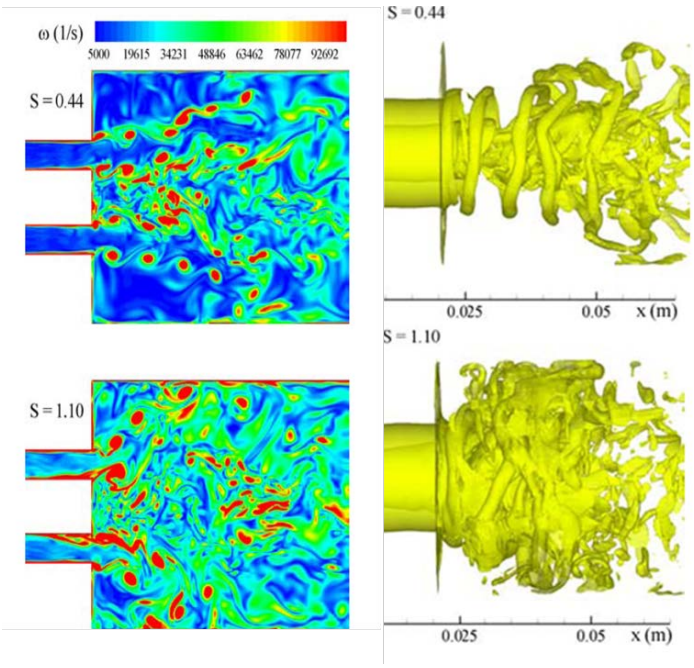

(a) **(b)**

Figure 7 : Snapshots from LES-level-set computations of (a) vorticity field magnitude and (b) iso-vorticity surfaces (75000 1/s) for a swirl number, S = 0.44, reproduced from Huang and Yang [108].

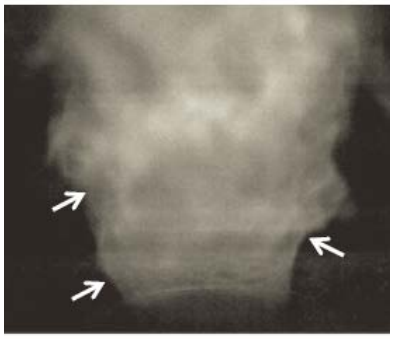

Figure 8 : Line of sight integrated flame luminosity for asymmetric forcing showing presence of helical flame disturbance, reproduced from O'Connor [45].

In order to fix some notation, consider the following azimuthal decomposition of the fluctuating flow field into helical modes as:

$$\hat{u}_i'(r,\theta,z,\omega) = \sum_{m=-\infty}^{\infty} \hat{B}_{i,m}(r,z,\omega) e^{im\theta}$$
$$\hat{B}_{i,m}(r,z,\omega) = \frac{1}{2\pi} \int_0^{2\pi} e^{-im\theta} \hat{u}_i'(r,\theta,z,\omega) d\theta \tag{2.2}$$

where $\hat{u}_i'$ is the Fourier transform of the fluctuating velocity field in the *i*-coordinate direction and $\hat{B}_{i,m}$ is the amplitude of its helical mode number *m*. Note that, $m = 0$ is the axisymmetric mode. The phase function of the disturbance at a fixed time is defined as $(kz + m\theta)$, where z is the axial flow direction and θ increases in the swirl direction. Hence, a positive mode (+*m*) has a line of constant phase with a sense of winding in the opposite direction to swirl. Conversely, a negative mode (-*m*) is co-rotating with the swirl. Hence, $m < 0$ and *m*>0 denote the co-swirling (counter-clockwise) and counter-swirling (clockwise) modes, respectively.

Helical modes are present in both swirling and non-swirling jets and wake flows. In non-swirling jets, the relative strengths of the axisymmetric, $m = 0$ mode and low order helical modes is a function of the separating boundary layer thickness very near the jet exit, while helical modes dominate downstream of the potential core [109-111].

Similarly, the dominant instability mode in non-swirling, axisymmetric wakes is the helical, $m = \pm 1$ modes [112, 113].

The presence of swirl further influences the hydrodynamic stability tendencies of the flow, and biases the strength of the positive and negative mode numbers. Depending upon the flow configuration and specific instability leading to the helical disturbances, they may either wind co- or counter-to the direction of swirl. For example, stability calculations were performed by Loiseleux *et al.* [114] for a Rankine vortex model with the following velocity profiles:

$$\begin{aligned} r < R: &\qquad \bar{U}_z(r) = U_0 + \Delta U, \quad \bar{U}_r(r) = 0, \quad \bar{U}_\theta(r) = \Omega r \\ r > R: &\qquad \bar{U}_z(r) = U_0, \quad \bar{U}_r(r) = 0, \quad \bar{U}_\theta(r) = \Omega R^2 / r \end{aligned} \tag{2.3}$$

They show that increasing swirl number decreases the temporal instability growth rate of the axisymmetric, *m*=0 mode. Impacts of swirl on helical modes are more complex, generally showing non-monotonic behavior. For example, the $m = -1$ is influenced differently by swirl in two ranges $0 \le S \le S_c$ and $S \ge S_c$, where $S = \Omega R / \Delta U$ is the swirl number and $S_c(m = -1) = 0.46$. In the range, $S \ge S_c$, increasing *S* decreases the temporal growth rate of all axial wave numbers, which, nonetheless, remain unstable for all *S*. For $S \le S_c$, increasing *S* has a stabilizing and destabilizing impact on low and high wave number disturbances, respectively.

Having considered some basic issues associated with hydrodynamic stability that explains why helical disturbances are present in swirl flows, we next consider the flame response problem. A number of observations of forced flames or flames during instabilities have noted the strong presence of helical disturbances along the flame [46]. In non-swirling flows, it is well known that important interference effects control the

axial flame wrinkling character, as vortices disturbing the flame, and the flame wrinkles excited by these convecting vortices, do not generally travel at the same speed. In swirling flows, the simultaneous presence of swirl and helical disturbances introduces important physics because of the simultaneous azimuthal and axial propagation of wrinkles by the flow [61]. As such, interference processes influence both the axial and azimuthal distribution of flame wrinkling and the distribution of the unsteady heat release. These flame wrinkle propagation processes cause the flame to respond differently to helical modes winding co- and counter- to the swirl direction.

Recent experimental work by Moeck *et al.* [64] studied the interaction of a helical flow mode with the heat release of a swirl-stabilized, premixed flame. Their results indicated that the helical mode excites azimuthally rotating heat release oscillations on the flame. They showed that these heat release oscillations cancel each other on opposite sides of the flame, an observation that is consistent with the analysis of axisymmetric flames presented later in this thesis. They also inferred that phase averaged images of the vertical cuts of the flame were different view angles of the same stationary structure. In addition, they presented a second order analysis of the *G*-equation to illustrate the sources of non-linear interactions between flame wrinkles excited by acoustic and vortical disturbances; e.g., the excitation of sum and difference frequencies in flame response. Additionally, experiments performed by Stohr *et al.* [65] characterized the phase-averaged, three-dimensional structure of the reaction zone, drawing similar conclusions as Moeck *et al.* [64]. Finally, recent experiments by Worth and Dawson [115] analyzed the global heat release dynamics due to self-excited circumferential instabilities in an annular combustor. Depending upon azimuthal location of the nozzle in the standing

wave, they showed that significantly different helical disturbances were excited in the flame, consistent with observations of O'Connor and Lieuwen [116]. They also showed that flames excited by helical disturbances, as opposed to axisymmetric structures, had much smaller amplitude of heat release oscillations, also consistent with the above observations.

In order to explicitly understand the behavior of helical modes in swirling flows, consider the experimental data from Malanoski *et al.* [117, 118]. In these experiments, PIV (Particle Image Velocimetry) measurements in different horizontal planes that are transverse to the axial flow are used to obtain the radial and azimuthal velocity field fluctuations. The helical mode decomposition was performed numerically on the measured data, using Eq.(2.2). They shed light on the mode strengths and their spatial evolution in reacting flows under both unforced and transverse acoustically forced conditions. These flow field results along with global chemiluminescence measurements are used in Chapter 7 for a model validation study. The experimental setup and diagnostics are detailed in Refs. [117, 118].

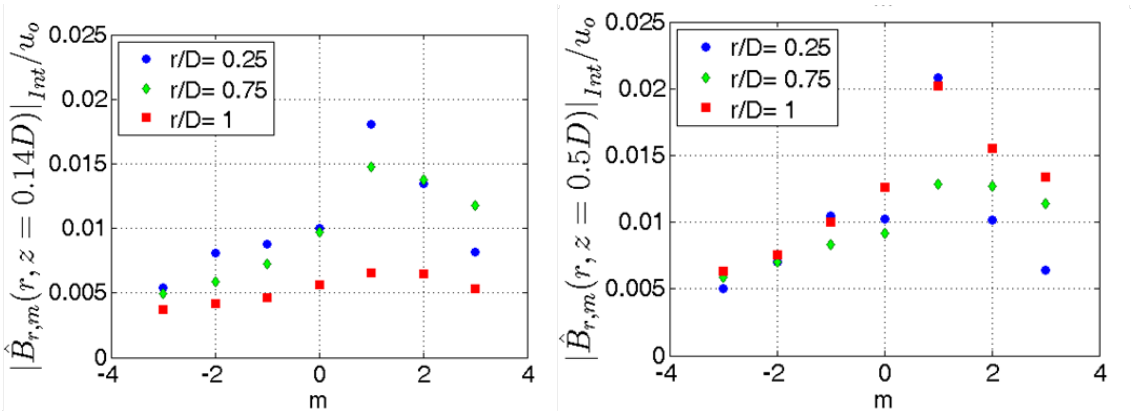

Figure 9 : RMS modal energy integrated from 0-1500 Hz for unforced radial velocity fluctuations as a function of mode number for 3 radii at two different axial planes (a) and (b). Plane (b) is downstream of (a). Data reproduced from Ref. [117].

First consider the case of an unforced flow by means of a power spectrum of each modal coefficient integrated over a frequency range ($f_1 < f < f_2$). This is indicated by:

$$\left|\hat{B}_{\mathbf{i},m}(r,z)\right|_{Int} = \sqrt{\frac{1}{fo}\int_{f_1}^{f_2} \hat{B}_{\mathbf{i},m} \bullet \hat{B}^{*}_{\mathbf{i},m} df} \tag{2.4}$$

where $\hat{B}_{\mathbf{i},m}$ has been defined in Eq.(2.2) and $f_0 = U_0 S/\pi D = 155\text{Hz}$. Note that πD and $S \bullet u_0$ denote the circumference of the nozzle exit and a characteristic azimuthal velocity, respectively. Thus St=1 represents a disturbance that propagates around the nozzle exit at the azimuthal reference velocity in one period and corresponds to 155 Hz. The RMS power spectra contribution from each mode is plotted in Figure 9 for 3 radial locations. It shows the dominance of the positive azimuthal modes, particularly the $m = +1$ helical mode. Data in Figure 10 show the radial distribution of the modal energy at the two axial planes, confirming the behavior of these modes for additional radial locations.

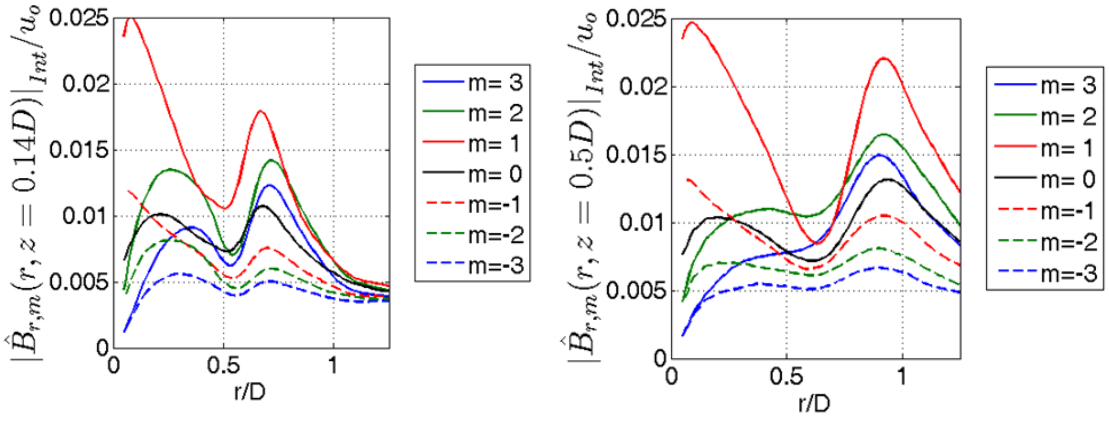

(a) **(b)**

Figure 10 : RMS modal energy integrated from 0-1500 Hz for unforced radial velocity fluctuations as a function of radial location for 7 mode numbers at two different axial planes (a) and (b). Plane (b) is downstream of (a). Data reproduced from Ref. [117].

As mentioned earlier in Section 2.2, the nozzle frequency is an important factor in determining the role of excited longitudinal disturbances when the original disturbance source is transverse acoustics [45, 105]. For example, consider the modal spectra for the (a) symmetric and (b) asymmetric forcing case shown in Figure 11. The $m = 0$ mode is the most excited mode during the symmetric forcing case as shown in Figure 11(a, top) where the peak is plotted at $f / f_{ext} = 1$*f/f*$_{ext}$=1. There are additional narrowband responses at the harmonic of the forcing frequency at $f / f_{ext} = 2$, as well as at $f / f_{ext} = 0.375$, or $St = 1.0$ for the $m = 0$ mode. The $m = \pm 1$ modes also exhibit narrowband responses at $f / f_{ext} = 1$ with amplitudes that are 5 and 3 times lower, respectively, than the magnitude for the $m = 0$ mode. These amplitudes are re-plotted only at the forcing frequency in Figure 11(a, bottom). At the upper axial plane, the response at $f / f_{ext} = 1$ is a factor of 2 less than the response at the lower plane. The tangential velocity helical mode spectra also has a narrowband response at $f / f_{ext} = 1$ and $f / f_{ext} = 2$, though the amplitudes are a factor of 2 less than the comparable magnitudes for the radial velocity. The dominant axisymmetric mode at the lower plane is consistent with results from experiments by O'Connor [45], indicative of the roll up of a vortex ring in the outer-shear layer. However, in that same study, they found that a helical mode quickly dominated the flow field farther downstream, while the $m = 0$ mode is still dominant at the downstream plane.

The out-of-phase forcing radial helical mode spectra still shows significant strength of the $m = 0$ mode, although the $m = \pm 1$ modes are of comparable strength as shown in the spectral plots in Figure 11(b, top) and the amplitude at 400 Hz in Figure

11(b, bottom). This result differs from O'Connor [45] which shows that the helical mode dominated the flow in the out-of-phase forcing case. This difference is due to differences in the acoustic sensitivity of the nozzles used in the two experiments.

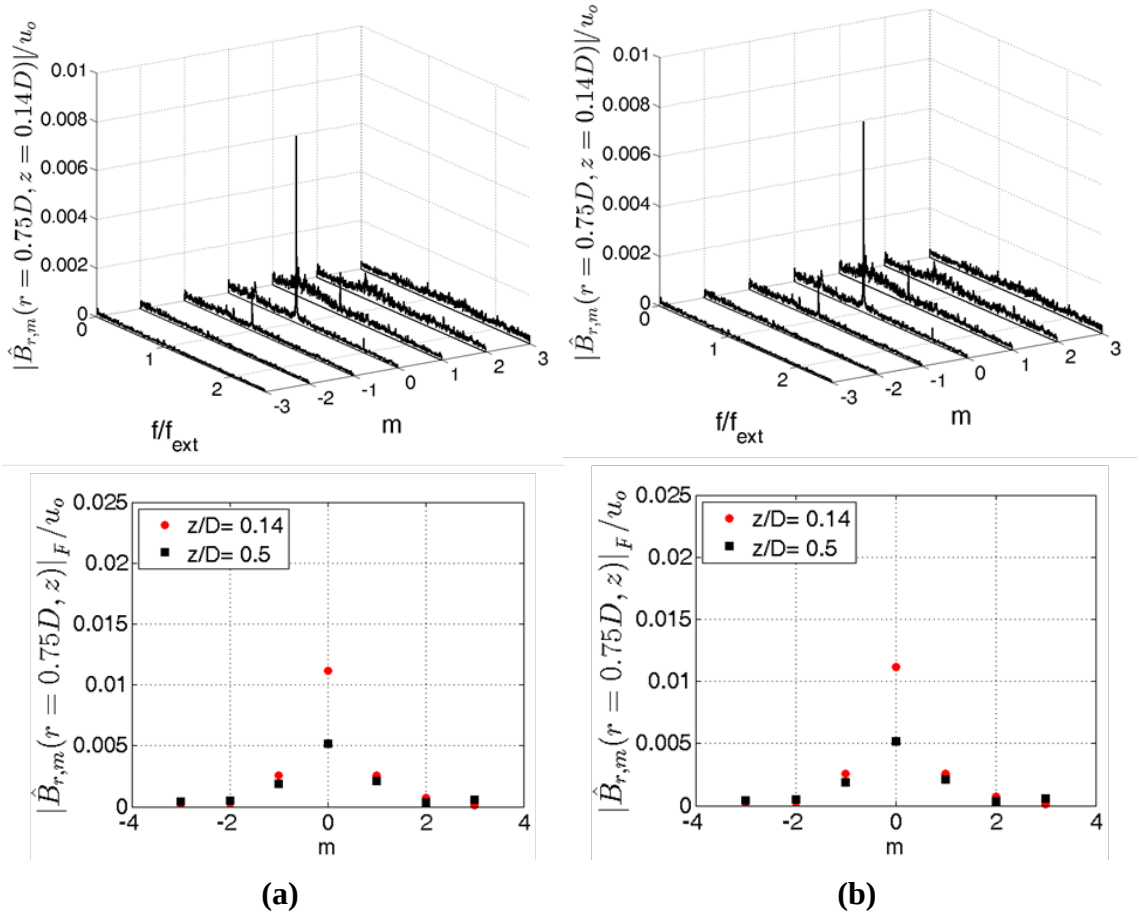

Figure 11 : (top) Ensemble averaged modal spectra for symmetric (in-phase) transverse acoustic excitation and (bottom) modal spectra amplitude at 400 Hz for each mode at two axial locations (*z/D*) for radial location *r/D*=0.75. (a) Symmetric/in-phase forcing and (b) Asymmetric/out-of-phase forcing. Data reproduced from Ref. [117].

Finally, consider the radial evolution of the different modes for different axial locations, as shown in Figure 12. The axisymmetric mode during symmetric forcing dominates across the burner radius, as indicated in the radial variation of the helical modes in Figure 12(a, b). The dominant response at $r = 0.75D$ is a direct result of the

convective instability of the shear layers becoming excited by the external acoustic forcing of the vortex ring.

The amplitude of the axisymmetric mode reduces to the magnitude of the $m = \pm 1$ during asymmetric forcing at the lower plane (a) and actually falls below the helical mode amplitudes at the downstream plane (b). This is shown in Figure 12(c, d). The axial evolution of the $m = 0$ mode described above is particularly significant for predicting the global unsteady heat release in Chapter 7. There these results are used as inputs to the unsteady flame response model described in Chapter 3, to predict the unsteady heat release from the flame and hence the global *FTF*. This predicted *FTF* is then compared with a measured *FTF* that is obtained from global chemiluminescence measurements.

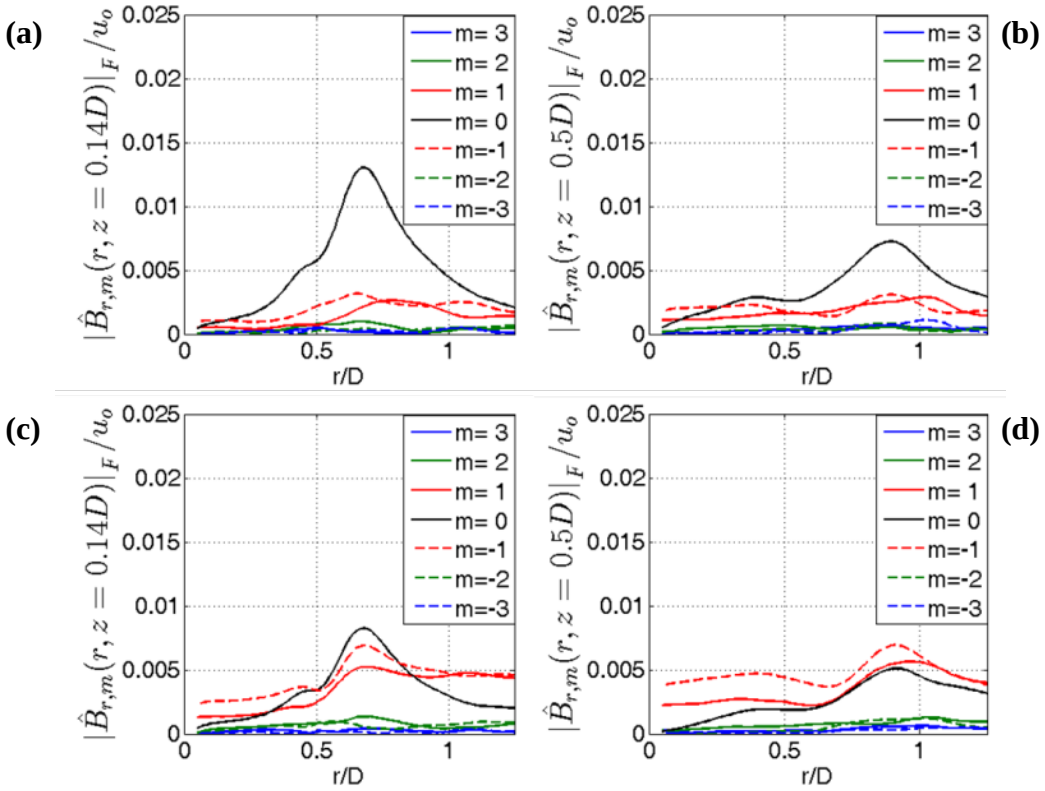

Figure 12 : Helical mode decomposition of radial velocity fluctuations for 400 Hz in-phase (a,b) and 400 Hz out-of-phase (c,d) acoustic excitation at two different axial planes (a) and (b). Plane (b) is downstream of (a). Data reproduced from Ref. [117].

Using the theoretical treatment of non-axisymmetric disturbance fields in Chapter 3, the thesis presents an analytical treatment for the response to helical flow disturbances. In particular, it focuses on flame wrinkling, spatially integrated heat release and sound emissions. It first focuses on results for a general three dimensional flame and then simplifies it for an axisymmetric flame. These general analyses are followed by explicit calculations in Chapter 5, for a solid body swirling flow showing the dependence of the induced fluctuations upon helical mode number, dimensionless swirl number, disturbance phase velocity, and dimensionless frequency. Furthermore, an analysis for non-axisymmetric flames is presented for both weak non-axisymmetries and strong non-axisymmetries.

CHAPTER 3

THEORETICAL FORMULATION

This chapter presents the modeling approaches used to study the dynamics of premixed flames to an imposed disturbance field, specifically velocity disturbances. The response of premixed flames to disturbances that are symmetric on either the two flame branches (for 2-D) or axisymmetric (for axisymmetric flames) has been extensively considered from a theoretical modeling perspective [11, 12, 29, 44]. In reality, no geometry or excitation field is perfectly axisymmetric. This inherent lack of symmetry does not introduce substantive changes to non-swirling flame dynamics, as we detail later. In a swirling flow, however, non-axisymmetric disturbances excite waves with an azimuthal dependence that propagates along a helical path. While numerous experimental studies of forced swirl flames have been published, they have primarily focused on the axial distribution of flame wrinkling [61, 76, 119-123] and have not discussed the azimuthal distribution.

First, the combustion regime diagram is presented to illustrate the region of validity for a level-set based thin flame analysis. Following this a comparison of linear and non-linear analysis is presented to illustrate the usefulness of a linear analysis. Next, the theory behind premixed flame front kinematics and the features of its governing equation are presented. Following this, a general solution procedure is shown along with its assumptions and limitations. This general solution is then used to compute the induced heat release fluctuations and finally, those induced heat release fluctuations are used to

evaluate the sound emissions. The analysis is presented in a general framework without any explicit functional forms for the model inputs.

3.1 Premixed Flame Combustion Regimes

Practical systems are comprised of complicated geometries that lead to the prevalence of turbulence in the flow and, hence, in the combustion process. Before discussing the flame front kinematics equation, the different regimes of combustion must be considered. This is done for premixed flames using the Borghi diagram [124] shown in Figure 13.

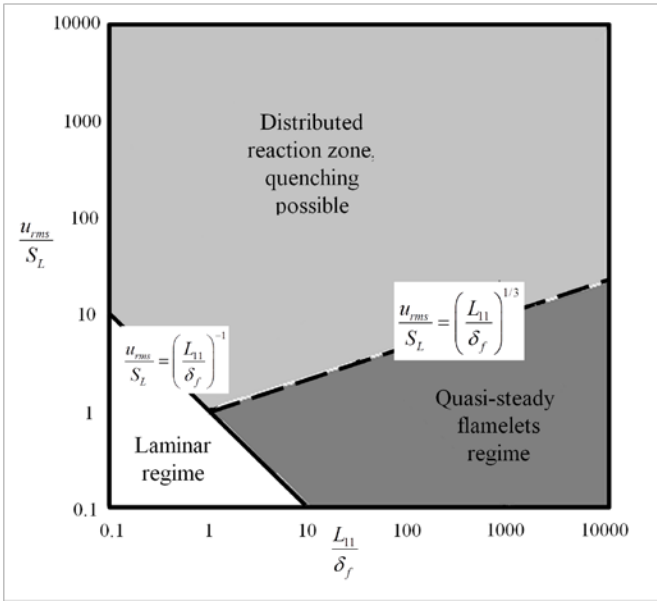

Figure 13 : Borghi diagram for different premixed combustion regimes depending on the values of u'_{rms}/s_L and L_{11}/δ_f . Reproduced from Ref. [124].

Here, the regimes are identified by the parameters u'_{rms}/s_L and L_{11}/δ_f . Here, u'_{rms} is the representative turbulence intensity, s_L is the laminar flame speed, L_{11} is the integral length scale and δ_f is the flame thickness. The first ratio denotes the competing effects of flame burning and flow turbulence and the second ratio denotes the relative thickness

of the flame combustion zone and the length scale of the combustor. Most practical systems operate in the quasi-steady flamelet regime [69] and thus the velocity coupled dynamics presented in this thesis is applied in this regime. In this regime, the combustion process is restricted to a very thin zone relative to other relevant length scales. Therefore, the flame is considered to be a front of essentially zero thickness, which separates reactants and products.

3.2 Linear and Non-Linear Flame Response

For small perturbations, the use of a linear analysis is sufficient. These analyses provide useful information such as frequency and growth rate of oscillations, as well as the operating conditions that could lead to a linearly unstable condition. When the perturbations are no longer small enough in the linear limit, non-linear processes can lead to a limit cycle. The amplitude of these limit cycle oscillations as well as the instability frequencies are equally important for operation.

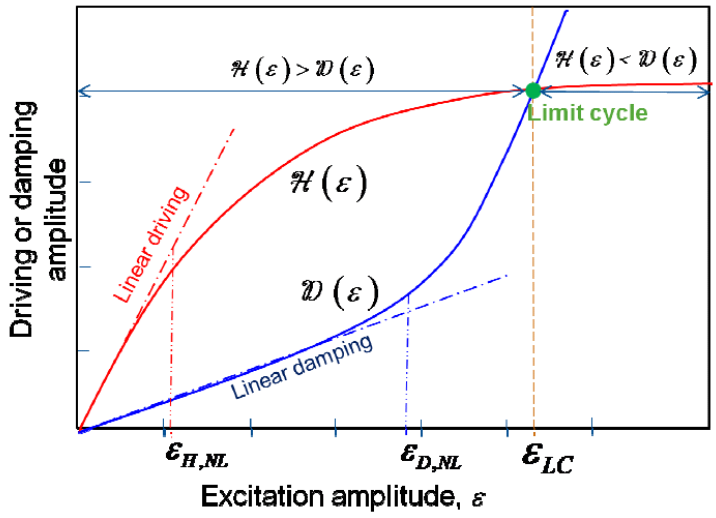

Figure 14 : Variation of Driving (red) and Damping (blue) as a function of excitation amplitude (ε). Reproduced from Ref. [124].

In order to predict limit cycle behavior, non-linear analysis is required. A typical example is shown in Figure 14. The balance between driving and damping processes at low oscillation amplitudes is generally controlled by linear processes. Hence, a linear analysis is sufficient to determine the growth rate of inherent disturbances in the combustor. But, as the amplitude of oscillation increases, nonlinear processes become increasingly important and they control the finite amplitude dynamics of the oscillations. Note, that at least one of the processes must be non-linear in order to reach limit cycle operation. Hence, a nonlinear analysis is always required to obtain and understand limit cycle behavior. The primary focus of this thesis is the linear response to velocity disturbances. In the next section, the dynamics of the flame front is presented using the level-set framework.

3.3 Flame Front Evolution

In this section, the mathematical nature of the equation governing the dynamics of moving fronts is discussed. Consider a field denoted by the variable $G(\vec{x},t)$ where the position vector in three dimensions is $\vec{x}$. A given iso-surface (iso-contour in two dimensions) of value G_0 can be denoted in general by:

$$G(\vec{x},t) = G_0 \tag{3.1}$$

Historically, this function is denoted as the level-set function, since it denotes the set of locations in space and time of a particular level. While mathematically an iso-contour denotes regions of the same property, this translates to the region of combustion or specifically, the locations of the premixed flame front. In a Lagrangian frame of reference that is fixed to the front, the differential representation of Eq.(3.1) is given by:

$$\left.\frac{DG(\vec{x},t)}{Dt}\right|_{G=G_0} = 0 \tag{3.2}$$

This states that the material derivative of the premixed flame front does not change as the front evolves. Translating this to an Eulerian frame of reference, the equation becomes:

$$\frac{\partial G}{\partial t} + \vec{u}_f \cdot \nabla G = 0 \tag{3.3}$$

Here $\vec{u}_f$ is the velocity of the premixed flame front. Note that while G is a field variable, the equation above does not denote a field equation, but rather governs the locations of the iso-contour given by $G = G_0$. In other words, it defines the implicit location of the premixed flame.

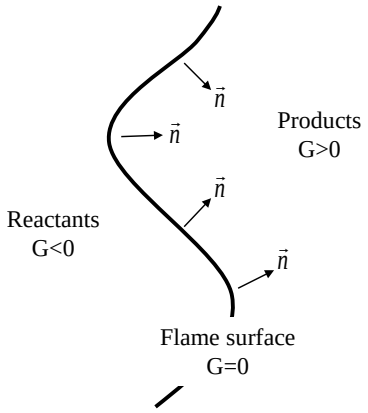

Figure 15 : Snapshot of the premixed flame front whose position is given by $G = 0$. Adapted from Ref. [124].

In case of premixed flames, the heat release from the combustion process is used to burn the reactant mass just upstream of the front. This leads to a normal propagating speed of the front or, the laminar flame speed, s_L. Hence, the velocity of the front $\vec{u}_f$ can be decomposed as: $\vec{u}_f = \vec{u} - s_L\vec{n}$. Here, $\vec{u}$ is the ambient flow velocity of the reactants just upstream of the flame front and $\vec{n}$ is the local normal vector, as shown in Figure 15.

Since, this is a normal vector to an iso-contour, it is given by: $\vec{n} = \nabla G / |\nabla G|$. Thus Eq.(3.3) can be further expanded to obtain:

$$\frac{\partial G}{\partial t} + \vec{u} \cdot \nabla G = s_L |\nabla G| \tag{3.4}$$

This equation in its presented form was first mentioned by Markstein [34] for use with dynamical flame propagation. It was later adapted more formally for use with turbulent flames by Williams [36]. Since then, several researchers [10, 11, 35, 37, 38, 44, 125-127] have used this so-called *G*-equation for premixed flame front dynamics in both analytical and numerical studies. The flame surface disturbances can also be affected by processes that control the local internal flame structure [128]. While we have considered the premixed flame to be a thin front, not accounting for the combustion process, these are still included in the laminar flame speed term. The reaction and diffusion processes that are internal to the thin flame structure are contained in this flame speed, s_L.

As mentioned earlier, this equation is valid only at points where $G = G_0$. However, for those points not on the flame surface, we may define $G < G_0$ for the reactants and $G > G_0$ for the products. This choice is also consistent with the direction of the normal vector as shown in Figure 15. Note that the value of G_0 is not important or of physical relevance, as seen from Eq.(3.4). This is a general scaling symmetry property of the equation [129]. However, no matter the choice of G_0 (which is conventionally chosen to be zero), the requirement for Eq.(3.4) is that the *G* field must be continuous and differentiable at the flame surface.

Since Eq.(3.4) represents an implicit location for the flame front it cannot be directly solved analytically. However, it can be solved explicitly by specifying a form for

the level-set function. For this, consider the center-body stabilized premixed flame shown in Figure 16, which is represented in the cylindrical coordinate system. The time averaged flame position is shown by the dashed curves, and the perturbed flame by the solid curves. For the flame front location denoted by $G(r,\theta,z,t)=0$, this is given by:

$$G(r,\theta,z,t)=z-\xi(r,\theta,t) \tag{3.5}$$

Here, $\xi(r,\theta,t)$ denotes the explicit position of the flame front in both space and time, measured vertically as shown in Figure 16. Note, however that this transformation to an explicit form limits the flame position to be a single-valued function.

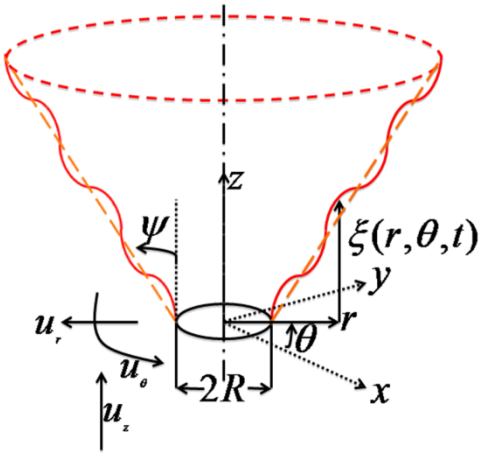

Figure 16 : Schematic of a center-body stabilized premixed flame.

Using a characteristic length scale, L_f (representative of the flame height), a characteristic velocity scale, U_0 (representative of the spatial axial flow field) and a characteristic time scale, L_f/U_0, and applying Eq.(3.5) to Eq.(3.4), leads to:

$$\frac{\partial\xi}{\partial t}+u_r\frac{\partial\xi}{\partial r}+\frac{u_\theta}{r}\frac{\partial\xi}{\partial\theta}+s_L\left[\left(\frac{\partial\xi}{\partial r}\right)^2+\frac{1}{r^2}\left(\frac{\partial\xi}{\partial\theta}\right)^2+1\right]^{1/2}=u_z \tag{3.6}$$

Assuming that the flame is stabilized on the center-body, it leads to the following boundary condition for ξ:

$$\xi(r=R,\theta,t)\big|_{flame-holder}=0 \tag{3.7}$$

The effects of flame base motion are not a focus in thesis, however a theoretical framework has been shown in Appendix A.

3.4 Linear Perturbation Analysis

In this section, a linear perturbation analysis of Eq.(3.6) is presented. The flame position and flow components can be decomposed into a steady mean (overbar) and a spatio-temporally varying disturbance (superscript prime), as:

$$\begin{aligned}\xi(r,\theta,t)&=\bar{\xi}(r,\theta)+\varepsilon\xi'(r,\theta,t)\\ u_i(r,\theta,t)&=\bar{U}_i(r,\theta)+\varepsilon u_i'(r,\theta,t)\end{aligned} \tag{3.8}$$

where *i* denotes the *r*, θ, or *z* coordinate. Note that while the velocity field is a function of all three spatial components, we are only interested in its value at the mean flame locations, $z=\bar{\xi}(r,\theta)$, for this linear analysis. The linear analysis is performed with respect to the small parameter ε. Substituting Eq.(3.8) into Eq.(3.6) results in terms of $O(1), O(\varepsilon)$ etc. Under the linear assumption, only the zeroth-order and first-order equations are taken into consideration. Following this standard linearization procedure [130], the evolution equations for the mean and linear perturbation in flame position may then be written as:

$$\bar{U}_r\frac{\partial\bar{\xi}}{\partial r}+\frac{\bar{U}_\theta}{r}\frac{\partial\bar{\xi}}{\partial\theta}=\bar{U}_z-s_L\left[\left(\frac{\partial\bar{\xi}}{\partial r}\right)^2+\left(\frac{1}{r}\frac{\partial\bar{\xi}}{\partial\theta}\right)^2+1\right]^{1/2} \tag{3.9}$$

$$\frac{\partial\xi'}{\partial t}+\vec{\bar{u}}_t\cdot\vec{\nabla}\xi'=\left(u_z'-u_r'\frac{\partial\bar{\xi}}{\partial r}-u_\theta'\frac{1}{r}\frac{\partial\bar{\xi}}{\partial\theta}\right) \tag{3.10}$$

where

$$\frac{\partial \overline{\xi}}{\partial r} = \cot \psi(r,\theta) \tag{3.11}$$

and the net tangential velocity vector along the flame surface, due to both the azimuthal and axial velocity components, is given by:

$$\vec{\bar{u}}_t = \vec{\bar{U}} - s_L \vec{n} \tag{3.12}$$

The Right Hand Side (RHS) forcing term in Eq.(3.10) can also be expressed as:

$$\left(u'_z - u'_r \frac{\partial \overline{\xi}}{\partial r} - u'_\theta \frac{1}{r} \frac{\partial \overline{\xi}}{\partial \theta} \right) = u'_n \left| \nabla G \right|_{G=0} \tag{3.13}$$

The above equations have been derived assuming that the laminar flame speed is constant in time and can vary spatially. This is a good assumption at low frequencies, however as shown by Preetham *et al.* [26] and Wang *et al.* [27], oscillatory curvature and/or hydrodynamic stretch can lead to modulation of the burning velocity, an effect that becomes important at high frequencies when the convective wavelength of the disturbance is of the same order of magnitude as the Markstein length. The time-averaged behavior governed by Eq.(3.9) states that the local normal component of the time-averaged velocity must match the local flame speed to obtain a steady flame. The linear perturbation equation shown in Eq.(3.10) is akin to wave transport phenomena. It indicates that perturbations in the flame position are generated by the local normal component of the flow disturbances (Eq.(3.13)) and that these are transported along the mean flame surface by the mean tangential velocity (Eq.(3.12)).

3.4.1 Local Flame Response

Since Eq.(3.10), follows that of wave transport phenomena, the method of characteristics [131-133] can be applied. In this method, the partial differential equation is transformed to an ordinary differential equation in characteristic space. The general

characteristic equations in characteristic space coordinates *s*, is expressed invariantly by the *Lagrange-Charpit* equations [132]:

$$\left.\begin{aligned} ds &= \frac{dr}{\left(\bar{U}_r - s_L \vec{n}\cdot\hat{e}_r\right)} \\ ds &= \frac{rd\theta}{\left(\bar{U}_\theta(r,\theta) - s_L \vec{n}\cdot\hat{e}_\theta\right)} \end{aligned}\right\} \Rightarrow \left.\begin{aligned} r &= r(r_p,\theta_p,s) \\ \theta &= \theta(r_p,\theta_p,s) \end{aligned}\right\} \Rightarrow s_p = s_p(r_p,\theta_p) \tag{3.14}$$

Here, $\vec{e}_r$ and $\vec{e}_\theta$ are the unit vectors in the radial and azimuthal directions, respectively. Note that r_p and θ_p are the spatial coordinates corresponding to a characteristic coordinate $s = s_p$. The motion of disturbances along the flame is then given by:

$$\frac{\left(\bar{U}_\theta - s_L \vec{n}\cdot\vec{e}_\theta\right)}{\left(\bar{U}_r - s_L \vec{n}\cdot\vec{e}_r\right)} d\ln r = d\theta \tag{3.15}$$

This equation shows the spiral flame surface wrinkle motion, whose specific trajectory depends on the local mean tangential velocity vector. The surface wrinkle motion is critically important in controlling the flame response.

The frequency domain representation of Eq.(3.10) is:

$$i2\pi St\hat{\xi}' + \left[\left(\bar{U}_r - s_L \vec{n}\cdot\vec{e}_r\right)\frac{\partial\hat{\xi}'}{\partial r} + \left(\bar{U}_\theta - s_L \vec{n}\cdot\vec{e}_\theta\right)\frac{1}{r}\frac{\partial\hat{\xi}'}{\partial\theta}\right] = \left(\hat{u}_z' - \hat{u}_r'\frac{\partial\bar{\xi}}{\partial r} - \hat{u}_\theta'\frac{1}{r}\frac{\partial\bar{\xi}}{\partial\theta}\right) \tag{3.16}$$

where the 'overhats' denote corresponding quantities in frequency domain. Here the non-dimensional frequency is denoted by the Strouhal number St which is defined as:

$$St = \frac{fL_f}{U_0} \tag{3.17}$$

It is the ratio of the characteristic flow time scale (L_f/U_0) and the acoustic time period, $1/f$.

In order to solve Eq.(3.16), the mean flow field, the laminar flame speed and fluctuating velocity field need to be specified at the flame. If we assume the density dump across the flame to be negligible, this assumption allows for prescribing a velocity field at the flame. In reality, the density jump across the flame alters the disturbance flow field, as discussed extensively in the literature [37, 134-137]. In general, flames have finite density jumps, although the weak density jump across flames is an important limit in its own right, as many practical applications utilizing highly compressed or vitiated flows have small density jumps. An important qualitative effect introduced by the density jump is to introduce the Darrieus-Landau flame instability, where the approach flow field is altered in such a way as to cause amplification of flame wrinkles [37]. The character of this hydrodynamic instability is altered by harmonic forcing as well. For example, low amplitude harmonic excitation leads to stabilization of the hydrodynamic instability, while large amplitude forcing introduces a new parametric instability, resulting in oscillation of flame sheet at the sub-harmonic of the forcing frequency [138].

A general non-axisymmetric disturbance field for the velocity components was presented in Eq.(2.2) and using this as the prescribed field at the flame, the solution to Eq.(3.16) in characteristic space is obtained as:

$$\hat{\xi}'(s_p)e^{i2\pi Sts_p(r_p,\theta_p)} = \sum_{m=-\infty}^{\infty} \int_{s=0}^{s=s_p(r_p,\theta_p)} \left\{ e^{im\theta(r_p,\theta_p,s)+i2\pi Sts} \left[\hat{B}_{z,m} - \frac{\partial \bar{\xi}}{\partial r}\hat{B}_{r,m} - \frac{1}{r}\frac{\partial \bar{\xi}}{\partial \theta}\hat{B}_{\theta,m} \right] \right\} ds$$

where (3.18)

$$\hat{B}_{i,m} = \hat{B}_{i,m}\left(r(r_p,\theta_p,s), \bar{\xi}\left(r(r_p,\theta_p,s), \theta(r_p,\theta_p,s)\right), St\right)$$

Here, $\hat{\xi}'(s_p) \equiv \hat{\xi}'(r_p,\theta_p)$. The flame response can be decomposed azimuthally as:

$$\hat{\xi}'(r,\theta,St) = \sum_{j=-\infty}^{\infty} e^{ij\theta}\hat{\xi}'_j(r,St) \tag{3.19}$$

This equation indicates the non-axisymmetric response of the flame to non-axisymmetries in the fluctuating flow field. In the next two sub-sections, the expressions for the induced heat release fluctuations and the sound generated are presented.

3.4.2 Induced Heat Release Fluctuations

The unsteady heat release per unit area of a premixed flame is given by $\rho s_L h_R$, where ρ is the fluid density, s_L is the laminar consumption speed and h_R is the heat of reaction. Thus, in a flame consuming homogeneous reactants and with a constant burning velocity, s_L, the heat release is directly proportional to the local surface area. This can also be seen from Eq.(1.3). Stretch sensitive flames that are wrinkled also introduce additional heat release fluctuations through flame speed oscillations [27, 125]. This effect becomes significant when the radius of wrinkling and/or scale of the velocity gradient is of the same order of magnitude as the Markstein length and is not considered further in this thesis. The differential surface area is given by:

$$dA = rd\theta dr\sqrt{1+\left(\frac{\partial \xi}{\partial r}\right)^2+\left(\frac{1}{r}\frac{\partial \xi}{\partial \theta}\right)^2} \tag{3.20}$$

The global flame surface area, directly proportional to global heat release for constant burning velocity flames, is given by,

$$A = \iint_{r,\theta} rd\theta dr\sqrt{1+\left(\frac{\partial \xi}{\partial r}\right)^2+\left(\frac{1}{r}\frac{\partial \xi}{\partial \theta}\right)^2} \tag{3.21}$$

Linearization of this equation yields the following decomposition for the global flame area:

$$\bar{A} = \iint_{r,\theta} r dr d\theta \sqrt{1 + \left(\bar{\xi}_r\right)^2 + \left(\bar{\xi}_\theta / r\right)^2}$$

$$\hat{A}' = \iint_{r,\theta} \left\{ r d\theta dr \frac{\left(\bar{\xi}_r \hat{\xi}_r' + \frac{1}{r^2} \bar{\xi}_\theta \hat{\xi}_\theta'\right)}{\sqrt{1 + \left(\bar{\xi}_r\right)^2 + \left(\bar{\xi}_\theta / r\right)^2}} \right\} \tag{3.22}$$

Where ξ_r and ξ_θ denote derivatives with respect to r and θ respectively. Thus, the fluctuations in local and global heat release can be calculated for a given problem by substituting the solutions for flame position in Eq.(3.18) into Eq.(3.22).

3.4.3 Sound Generation

In order to completely understand and control the behavior of oscillatory combustion, an understanding of the feedback from the unsteady heat release back to the acoustic pressure oscillations is required. The dynamical flow processes described in the previous sub-sections lead to an unsteady heat release from the flame surface. Specifically the unsteady expansion of gases at the flame front appears as an unsteady creation of volume locally and hence serves as a distributed monopole source [139]. Lieuwen *et al.* [140] used the *G*-equation to obtain heat release fluctuations from flow fluctuations and then used them as input to a wave equation model derived by Dowling (in Crighton *et al.* [141]). This wave equation describes noise production in a reacting flow that includes a variety of source terms associated with the direct flow noise itself, diffusive effects and direct and indirect combustion noise. The direct combustion noise was shown to be most dominant in most cases, leading to a linear wave equation of the form:

$$\frac{1}{c^2} \frac{\partial^2 p'}{\partial t^2} - \nabla^2 p' = -\frac{\partial}{\partial t} \left(\frac{(\gamma - 1)\tilde{q}'}{c^2} \right) \tag{3.23}$$

whose formal, frequency domain solution is:

$$\hat{p}'(\vec{x}_0,\omega)=\frac{-i\omega(\gamma-1)}{4\pi c^2}\oint_V\left[\hat{\tilde{q}}'(\vec{x}_s,\omega)\frac{\exp\left(ik\left|\vec{x}_s-\vec{x}_0\right|\right)}{\left|\vec{x}_s-\vec{x}_0\right|}\right]dV \tag{3.24}$$

Where $\hat{p}', c, \gamma$ and $\hat{\tilde{q}}'$ refers to the unsteady pressure, sound speed, ratio of specific heats, and unsteady rate of heat release per unit volume, respectively. Note that the unsteady heat release rate per unit volume is denoted by $\tilde{q}$ (as used in the acoustic wave equation shown in Eq.(3.23)) and the unsteady heat release rate per unit area is denoted by q (when used in evaluating the unsteady global heat release rate from the flame).

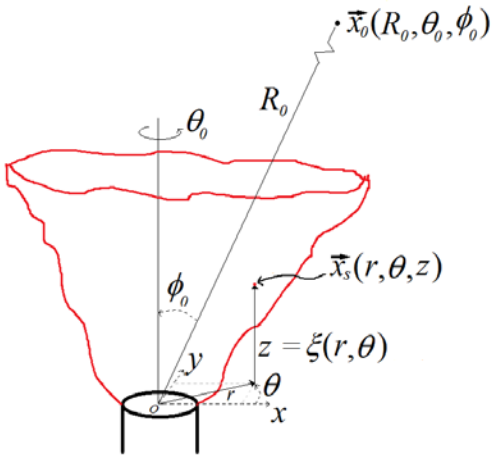

Figure 17 : Schematic showing source and observer coordinate systems for sound generation calculations. Note that the flame is described using cylindrical coordinates (r,θ,z) while the observer position is given in spherical coordinates (R_0,θ_0,ϕ_0).

The coordinate system that is used in the solution is illustrated in Figure 17, where the points $\vec{x}_s(r,\theta,z=\xi(r,\theta))$ describe the vector locations on the mean flame surface (in cylindrical polar coordinates with respect to origin *O*) and $\vec{x}_0(R_0,\theta_0,\phi_0)$ denotes the measurement point (in spherical coordinates with respect to origin *O*). For situations where the number of reactant and product moles differ, an additional source term is also

present, which is of much smaller magnitude for hydrocarbon-air flames [142] and is not considered in this thesis.

The heat release fluctuations are directly proportional to area fluctuations through the relationship:

$$\frac{\hat{\bar{q}}'}{\bar{\bar{q}}} = \frac{\hat{q}'}{\bar{q}} = \frac{d\hat{A}'}{d\bar{A}} \tag{3.25}$$

Note that this is true for a constant flame thickness, as is the case in this thesis. When substituted into Eq.(3.24), this yields:

$$\hat{p}'\left(\vec{x}_0,\omega\right) = \frac{-i\omega\left(\gamma-1\right)}{4\pi c^2}\bar{q}\oint_{\bar{A}}\left[\frac{\exp\left(ik\left|\vec{x}_s-\vec{x}_0\right|\right)}{\left|\vec{x}_s-\vec{x}_0\right|}\right]d\hat{A}' \tag{3.26}$$

For convenience of notation, we define the following:

$$\hat{p}'\left(\vec{x}_0,\omega\right) = \frac{i4\pi c^2}{\omega\left(\gamma-1\right)\bar{q}}\,\hat{p}'\left(\vec{x}_0,\omega\right) \tag{3.27}$$

For acoustically compact sources (i.e., for $kL_f \ll 1$, where L_f is the flame length and k is the acoustic wavenumber), it is useful to decompose the far-field sound as an expansion in powers of kL_f, where the terms then describe the lumped element source strength associated with the effective monopole, dipole, quadrupole, and so forth, source strengths. This multipole expansion method has been previously employed by Lieuwen and Zinn [143] for analyzing noise generated by unsteady combustion processes. Following Pierce [144], the pressure field from a compact flame can then be expressed as the following convergent series, referred to as a multi-pole expansion:

$$\hat{p}'\left(\vec{x}_0,\omega\right) = \hat{F}_M\frac{\exp(ikR_0)}{R_0} - \hat{F}_{D,i}\frac{\partial}{\partial x_i}\left(\frac{\exp\left(ikr_0\right)}{r_0}\right)\bigg|_{r_0=R_0} + \hat{F}_{Q,ij}\frac{\partial^2}{\partial x_i\partial x_j}\left(\frac{\exp\left(ikr_0\right)}{r_0}\right)\bigg|_{r_0=R_0} + \cdots \tag{3.28}$$

Note that this equation is presented using Einstein's tensor notation ($i, j \equiv x, y, z$), where $\hat{F}_M$, $\hat{F}_{D,i}$ and $\hat{F}_{Q,ij}$ denote the scalar monopole, vector dipole, and tensor quadrupole contributions, respectively. Each of these components are given by:

$$\begin{aligned}\hat{F}_M &= \oint_{\bar{A}} d\hat{A}' \\ \hat{F}_{D,i} &= \oint_{\bar{A}} x_{s,i}\left(r,\theta,z=\bar{\xi}(r,\theta)\right) d\hat{A}' \\ \hat{F}_{Q,ij} &= \frac{1}{2}\oint_{\bar{A}} \left(x_{s,i}x_{s,j}\right) d\hat{A}'\end{aligned} \tag{3.29}$$

where $\hat{F}_M \sim O(1)$, $\hat{F}_{D,i} \sim O(kL_f)$ and $\hat{F}_{Q,ij} \sim O(kL_f)^2$, and so forth. Note that the vector and tensor integrals can be calculated by using the Cartesian representation of $\vec{x}_s = r\cos\theta\vec{e}_x + r\sin\theta\vec{e}_y + \bar{\xi}(r,\theta)\vec{e}_z$. Note that the tensor $\hat{F}_{Q,ij}$ is symmetric, i.e. $\hat{F}_{Q,ij} = \hat{F}_{Q,ji}$. Thus, the monopole component is directly proportional to the flame surface area, the dipole contribution to the first moment of the surface area distribution, and so on. The transformation between the spherical coordinate system and the Cartesian system is useful in obtaining the derivatives, and is given by:

$$\frac{x}{r_0} = \sin\phi_0\cos\theta_0; \frac{y}{r_0} = \sin\phi_0\sin\theta_0; \frac{z}{r_0} = \cos\phi_0 \tag{3.30}$$

The components of the derivative vector shown in Eq.(3.28) which contribute to the dipole source term are:

$$\frac{\partial}{\partial x}\left(\frac{\exp(ikr_0)}{r_0}\right) = \frac{(ikr_0 - 1)\exp(ikr_0)}{r_0^2}\frac{x}{r_0} \tag{3.31}$$

The other derivatives are obtained by cyclically changing *x*, *y*, and *z*. The components of the derivative tensor that contributes to the quadrupole source term in Eq.(3.28) are:

$$\partial_{xx}\left[\frac{\exp(ikr_0)}{r_0}\right]=\frac{\partial^2}{\partial x^2}\left(\frac{\exp(ikr_0)}{r_0}\right)=\frac{(ikr_0-1)\exp(ikr_0)}{r_0^3}\left[1-\left\{3+\frac{(kr_0)^2}{(ikr_0-1)}\right\}\left(\frac{x}{r_0}\right)^2\right]$$
$$\partial_{xy}\left[\frac{\exp(ikr_0)}{r_0}\right]=\frac{\partial^2}{\partial x\partial y}\left(\frac{\exp(ikr_0)}{r_0}\right)=-\frac{(ikr_0-1)\exp(ikr_0)}{r_0^3}\left(\frac{x}{r_0}\right)\left(\frac{y}{r_0}\right)\left\{3+\frac{(kr_0)^2}{(ikr_0-1)}\right\} \quad (3.32)$$

Note that the other double-derivatives and cross-derivatives can be obtained by cyclically changing *x*, *y*, and *z*. These can then be transformed back to spherical coordinates using Eq.(3.30).

Finally, the total sound power radiated by the flame is given by:

$$\begin{aligned}P&=\int_{\phi_0=0}^{\pi}\left[\int_{\theta_0=0}^{2\pi}\left(\frac{1}{2\pi\rho c}\left|\hat{p}'(\vec{x}_0,\omega)\right|^2\right)R_0 d\theta_0\right]R_0\sin\phi_0 d\phi_0\\&=\left(\frac{\omega R_0(\gamma-1)\overline{q}}{4\pi c^2}\right)^2\int_{\phi_0=0}^{\pi}\left[\int_{\theta_0=0}^{2\pi}\left(\frac{1}{2\pi\rho c}\left|\hat{p}'(\vec{x}_0,\omega)\right|^2\right)d\theta_0\right]\sin\phi_0 d\phi_0\end{aligned} \quad (3.33)$$

The analysis so far has presented general expressions for the flame response, induced heat release fluctuations and sound generation. However, useful insights can be obtained by considering time-averaged flames that are axisymmetric.

3.5 Axisymmetric Mean Flames

3.5.1 Local Flame Response

While the above results are quite general, important simplifications can be made for axisymmetric flames. Single nozzle swirl flames often have shapes that are quite close to axisymmetric, and so this approximation is an important one. Assuming an axisymmetric flow field, Eqs.(3.9) and (3.16) take the form:

$$\overline{U}_r\cot\psi(r)=\overline{U}_z-s_L\left[\left(\cot\psi(r)\right)^2+1\right]^{1/2} \quad (3.34)$$

$$i2\pi St\hat{\xi}' + \left[\left(\bar{U}_r(r) + s_L\cos\psi(r)\right)\frac{\partial\hat{\xi}'}{\partial r} + \frac{\bar{U}_\theta(r)}{r}\frac{\partial\hat{\xi}'}{\partial\theta}\right] = \left(\hat{u}_z' - \hat{u}_r'\cot\psi(r)\right) \qquad (3.35)$$

This expression shows that fluctuations in the azimuthal velocity have no direct influence on the flame response. However, there is an indirect mechanism of influence by which azimuthal flow fluctuations can affect the flame response [50, 51, 66, 71, 72, 108] but this is not a focus in this thesis. Following Eq.(3.14), the *Lagrange-Charpit* equations for the characteristics are:

$$\begin{aligned} ds &= \frac{dr}{\bar{U}_r(r) + s_L\cos\psi(r)} \Rightarrow r = f(r_p, s) \\ ds &= \frac{f(r_p,s)d\theta}{\bar{U}_\theta(f(r_p,s), St_\Omega)} \Rightarrow d\theta = \frac{\bar{U}_\theta(f(r_p,s), St_\Omega)ds}{f(r_p,s)} \\ \Rightarrow \theta - \theta_p &= g(r_p, s, St_\Omega) - g(r_p, s_p, St_\Omega) \end{aligned} \qquad (3.36)$$

Here, St_Ω is the Strouhal number based on the axial and azimuthal time-scales of the flow. Note that the radial characteristic function f is independent of the azimuthal characteristic function g, while the converse is not true. This implies that the radial characteristic function is independent of swirl parameter St_Ω. The characteristic coordinate s_p is obtained from solving for $r=r_p$. Also, unlike the general case, θ_p can be separated from the function g. These observations are specific to axisymmetric flow fields. The final solution, obtained from Eq.(3.18), can now be written as:

$$\hat{\xi}'(s_p)e^{i2\pi St s_p(r_p)} = \sum_{m=-\infty}^{\infty} e^{im\left(\theta_p - g(r_p, St_\Omega)\right)} \int_{s=0}^{s=s_p(r_p)} \left\{ e^{img(r_p, St_\Omega, s) + i2\pi St s}\left[\hat{B}_{z,m} - \frac{\partial\bar{\xi}}{\partial r}\hat{B}_{r,m}\right]\right\} ds$$

where (3.37)

$$\hat{B}_{i,m} = \hat{B}_{i,m}\left(f(r_p,s), \bar{\xi}\left(f(r_p,s)\right), St\right)$$

An important observation from this result is that, for axisymmetric mean flows, helical modes in the flow, m, excite a corresponding helical motion in the flame, which is not

generally true as pointed out earlier. As such, using the helical mode decomposition of the flame in Eq.(3.19) we get:

$$\hat{\xi}'_{j=m}(r,St)e^{i2\pi Sts_p(r)} = e^{-img(r,St_\Omega)}\int_{s=0}^{s=s_p(r)}\left\{e^{img(r,St_\Omega,s)+i2\pi Sts}\left[\hat{B}_{z,m}-\frac{\partial\overline{\xi}}{\partial r}\hat{B}_{r,m}\right]\right\}ds \quad (3.38)$$

Note that the swirl parameter St_Ω always occurs along with the mode m, i.e. it always appears as $mg\left(r,St_\Omega,s\right)$. This, again, is true only for axisymmetric flow fields and has important implications for the impact of swirl on the sensitivity of the flame to different helical modes.

Rewrite the right side of Eq.(3.38) as:

$$\left.\begin{array}{l}\hat{B}_{z,m}\left(f(r,s),\overline{\xi}\left(f(r,s)\right),St\right)\\ -\dfrac{\partial\overline{\xi}}{\partial r}\hat{B}_{r,m}\left(f(r,s),\overline{\xi}\left(f(r,s)\right),St\right)\end{array}\right\} = \sin\left[\psi\left(f(r,s)\right)\right]\hat{B}_{n,m}\left(f(r,s),\overline{\xi}\left(f(r,s)\right),St\right) \quad (3.39)$$

where the subscript n refers to the normal component to the local time-averaged axisymmetric flame surface. Consider the general representation of this term, given by:

$$\sin\left[\psi\left(f(r,s)\right)\right]\hat{B}_{n,m}\left(f(r,s),\overline{\xi}\left(f(r,s)\right),St\right) = D\left(f(r,s)\right)\exp\left(-i2\pi\varphi\left(f(r,s),St_c\right)\right) \quad (3.40)$$

where $D\left(f\left(r,s\right)\right)$ is a real amplitude, $2\pi\varphi\left(f\left(r,s\right)\right)$ denotes the real spatial phase variation of the imposed flow fluctuation, and St_c is a Strouhal number based on the propagation speed of the imposed flow fluctuation. Substituting this in Eq.(3.38), we have:

$$\begin{array}{l}\hat{\xi}'_{j=m}(r,St)e^{i2\pi Sts_p(r)}\\ = e^{-img(r,St_\Omega)}\displaystyle\int_{s=0}^{s=s_p(r)}D\left(f\left(r,s\right),St\right)\exp\left\{img(r,St_\Omega,s)+i2\pi Sts-i2\pi\varphi\left(f\left(r,s\right),St_c\right)\right\}ds\end{array} \quad (3.41)$$

In general, the oscillatory function in the integrand leads to an integral that has finite bounds depending on $D\left(f\left(r,s\right)\right)$. When the "frequency" associated with this oscillatory term is zero, the integral does not oscillate and can potential grow monotonically with *s*, depending on the nature of $D\left(f\left(r,s\right)\right)$. This would lead to particularly large amplitudes of flame wrinkling. This "frequency" condition is given by:

$$m_0 g(r, St_\Omega, s) + 2\pi Sts - 2\pi\varphi\left(f\left(r,s\right), St_c\right) = 0 \tag{3.42}$$

As we will discuss in Chapter 5, the helical mode number $m = m_0$ that best satisfies this condition leads to the largest amplitudes of flame wrinkling.

3.5.2 Heat Release Fluctuations

The global flame surface area can be simplified from Eq.(3.22), which leads to:

$$\begin{aligned} \overline{A} &= 2\pi \int_r r dr \frac{1}{\sin\psi(r)} \\ \hat{A}' &= \sum_{m=-\infty}^{\infty} \int_{\theta=0}^{\theta=2\pi} e^{im\theta} d\theta \int_r r dr \cos\psi(r) \frac{\partial \hat{\xi}'_m(r, St)}{\partial r} \end{aligned} \tag{3.43}$$

We can derive a very significant result for a general, axisymmetric flame shape from this expression. For non-axisymmetric modes ($m \neq 0$), the integral over θ is zero, which implies that only the axisymmetric $m = 0$ mode contributes to the global flame area. This also implies that the global flame area is independent of the swirl parameter St_Ω, as can be seen from Eq.(3.38) for $m = 0$. The fluctuating flame area is then given by:

$$\hat{A}'_{m=0} = 2\pi \int_r \left\{ r\cos\psi(r) \frac{\partial}{\partial r} \left[e^{-i2\pi Sts_p(r)} \int_{s=0}^{s=s_p(r)} \left\{ e^{i2\pi Sts} \begin{bmatrix} \hat{B}_{z,0}\left(r, St, s\right) \\ -\frac{\partial \overline{\xi}}{\partial r} \hat{B}_{r,0}\left(r, St, s\right) \end{bmatrix} \right\} ds \right] \right\} dr \tag{3.44}$$

An important implication of these results is that helical modes, while introducing substantial wrinkling of the flame front, actually lead to no fluctuations in flame surface area in axisymmetric flows, a result that has also been experimentally verified by Moeck *et al.* [64]. Next, consider the far-field sound radiated by axisymmetric flames.

3.5.3 Sound Generation

The area fluctuation associated with the *m*-th mode response is given by:

$$d\hat{A}'_m = \underbrace{\frac{\bar{\xi}_r(r)}{\sqrt{1+\left(\bar{\xi}_r(r)\right)^2}}}_{\cos\psi(r)} \frac{\partial \hat{\xi}'_m(r,\omega)}{\partial r} e^{im\theta} r dr d\theta \tag{3.45}$$

Hence, Eq.(3.26) becomes:

$$\hat{p}'_m\left(\vec{x}_0,\omega\right) = \int_{\theta=0}^{2\pi} e^{im\theta} d\theta \int_r \left[\cos\psi(r) \frac{d\hat{\xi}'_m(r,\omega)}{dr} \frac{\exp\left(ik\left|\vec{x}_s - \vec{x}_0\right|\right)}{\left|\vec{x}_s - \vec{x}_0\right|} \right] r dr \tag{3.46}$$

This can be simplified further in the far-field (R_0 is very large compared to any spatial length quantity) to :

$$\hat{p}'_m\left(\vec{x}_0,\omega\right) = \frac{2\pi i^m e^{ikR_0 + im(\theta_0+\pi)}}{R_0} \int_r \left[J_m\left(kr\sin\phi_0\right) \cos\psi(r) \frac{d\hat{\xi}'_m(r,\omega)}{dr} e^{-ik\bar{\xi}(r)\cos\phi_0} \right] r dr \tag{3.47}$$

This equation clearly shows that directivity only exists in the ϕ_0 direction, and not the θ_0 direction, as would be anticipated for this axisymmetric geometry. Also of note is the fact that only the symmetric, $m = 0$ mode contributes to the sound radiation in the forward, $\phi_0 = 0$ direction.

Further insight into the far-field sound radiation characteristics can be obtained for low and high frequency limits or more precisely, for kL_f <<1 and >>1, respectively. The

kL_f <<1 compact flame limit is most readily analyzed using the multi-pole expansion of Eq.(3.28). We define the following integrals for ease of notation in subsequent equations:

$$I_{r,\alpha\beta,n} = \int_r r^{\alpha} \left(\overline{\xi}(r)\right)^{\beta} \cos\psi(r) \frac{\partial \hat{\xi}_n'}{\partial r} dr$$
$$I_{\theta,n} = \int_{\theta=0}^{2\pi} e^{in\theta} d\theta \tag{3.48}$$

Note that only $I_{\theta,n=0} = 2\pi$ is non-zero and that $I_{\theta,n\neq 0} = 0$. The scalar monopole source is given by:

$$\hat{F}_M = I_{\theta,m} I_{r,00,m} \tag{3.49}$$

The axisymmetric mode, $m = 0$, is the only mode that contributes to the monopole source strength. This implies that, to leading order in kL_f, the non-axisymmetric helical modes excite no far-field sound, or influence stability limits of ducted systems, from axisymmetric, compact flames. Hence, we have:

$$m = 0 : \hat{F}_M = 2\pi I_{r,00,m=0}$$
$$m \neq 0 : \hat{F}_M = 0 \tag{3.50}$$

and, thus the leading order contribution to the pressure field becomes:

$$m = 0 : \hat{p}_M'\left(\vec{x}_0, \omega\right) = 2\pi \frac{\exp\left(ikR_0\right)}{R_0} I_{r,00,m=0}$$
$$m \neq 0 : \hat{p}_M'\left(\vec{x}_0, \omega\right) = 0 \tag{3.51}$$

Where the subscript *M* refers to monopole. In reality, however, all flames have finite size which modifies this result. Thus, if the flame is non-compact, or the symmetric mode is weak, then helical modes still influence the sound generation by the flame, but the effect is of $O(kL_f)$ or higher. The dipole source vector is given by:

$$\hat{F}_{D,x} = \frac{1}{2}\left[I_{\theta,m+1} + I_{\theta,m-1}\right] I_{r,20,m}$$
$$\hat{F}_{D,y} = \frac{-i}{2}\left[I_{\theta,m+1} - I_{\theta,m-1}\right] I_{r,20,m} \tag{3.52}$$
$$\hat{F}_{D,z} = I_{\theta,m} I_{r,11,m}$$

Note, that only the axisymmetric and first helical modes, $|m| = 0,1$, contribute to the dipole source. The axisymmetric mode admits a vector component for the dipole in the *z*-direction only. The non-axisymmetric $|m| = 1$ lead to vector components in the *x* and *y* directions only. Equation (3.52) may be written as:

$$m = 0 : F_{D,z} = 2\pi I_{r,11,m=0}; F_{D,x} = F_{D,y} = 0$$
$$m = \pm 1 : \hat{F}_{D,x} = \pi I_{r,20,m=0}; \hat{F}_{D,y} = \pm i\hat{F}_{D,x}; F_{D,z} = 0 \tag{3.53}$$

The contribution to the pressure field is:

$$m = 0 : \hat{p}'_D\left(\vec{x}_0, \omega\right) = -\frac{2\pi\left(ikR_0 - 1\right)\exp(ikR_0) I_{r,11,m=0} \cos\phi_0}{R_0}$$
$$m = \pm 1 : \hat{p}'_D\left(\vec{x}_0, \omega\right) = -\frac{\pi\left(ikR_0 - 1\right)\exp(ikR_0 \pm i\theta_0) I_{r,20,m=0} \sin\phi_0}{R_0} \tag{3.54}$$

Note that the dipole contribution magnitudes have no directivity in θ_0 but only a directivity in ϕ_0. The θ_0 dependence occurs only in the phase of the pressure field for the $|m| = 1$ modes. Also, note that the directivities are different for the different modes. The axisymmetric $m = 0$ has a directivity that peaks at $\phi_0 = 0, \pi$ and radiates no contribution along $\phi_0 = \pi/2, 3\pi/2$. In contrast, the directivity is inverted for the for the non-axisymmetric $|m| = 1$ modes- i.e., it peaks in the direction orthogonal to the flow and emits no sound in the forward direction. .

The 6 components (for a symmetric tensor) of the quadrupole tensor are given by:

$$\hat{\underline{\underline{F}}}_{Q,xx} = \frac{I_{r,30,m}}{4}\left(I_{\theta,m} + \frac{1}{2}\left\{ I_{\theta,m+2} + I_{\theta,m-2} \right\} \right) \tag{3.55}$$

$$\hat{\underline{\underline{F}}}_{Q,xy} = \frac{I_{r,30,m}}{8i}\left(I_{\theta,m+2} - I_{\theta,m-2} \right) \tag{3.56}$$

$$\hat{\underline{\underline{F}}}_{Q,xz} = \frac{I_{r,21,m}}{4}\left(I_{\theta,m+1} + I_{\theta,m-1} \right) \tag{3.57}$$

$$\hat{\underline{\underline{F}}}_{Q,yy} = \frac{I_{r,30,m}}{4}\left(I_{\theta,m} - \frac{1}{2}\left\{ I_{\theta,m+2} + I_{\theta,m-2} \right\} \right) \tag{3.58}$$

$$\hat{\underline{\underline{F}}}_{Q,yz} = \frac{I_{r,21,m}}{4i}\left(I_{\theta,m+1} - I_{\theta,m-1} \right) \tag{3.59}$$

$$\hat{\underline{\underline{F}}}_{Q,zz} = \frac{I_{r,12,m} I_{\theta,m}}{2} \tag{3.60}$$

Here, the $m = 0$ mode contributes to the $\hat{F}_{Q,xx}, \hat{F}_{Q,yy}, \hat{F}_{Q,zz}$ components of the tensor only. The $|m| = 1$ modes contribute to the $\hat{F}_{Q,xz}, \hat{F}_{Q,yz}$ components only. The $|m| = 2$ mode contributes to the $\hat{\underline{\underline{F}}}_{Q,xx}, \hat{\underline{\underline{F}}}_{Q,yy}, \hat{\underline{\underline{F}}}_{Q,xy}$ components. Modes where |m|>2 do not contribute to the quadrupole moment. Thus, higher order helical modes become increasingly inefficient at causing sound radiation from compact flames, because of phase cancellation effects. Eqs.(3.55)-(3.60) can be further simplified depending on the mode numbers.

For $\hat{\underline{\underline{F}}}_{Q,xx}$ we have only $|m| = 0, 2$ contributing, leading to:

$$\begin{aligned} \hat{\underline{\underline{F}}}_{Q,xx,m=0} &= \frac{\pi I_{r,30,m=0}}{2} \\ \hat{\underline{\underline{F}}}_{Q,xx,m=\pm 2} &= \frac{\pi I_{r,30,m=\pm 2}}{4} \end{aligned} \tag{3.61}$$

For $\hat{\underline{\underline{F}}}_{Q,xy}$ we have only $|m| = 2$ contributing, leading to:

$$\hat{\underline{\underline{F}}}_{Q,xy,m=\pm 2} = \pm i\frac{\pi I_{r,30,m=\pm 2}}{4} \tag{3.62}$$

For $\hat{\underline{\underline{F}}}_{Q,xz}$ we have only $|m|=1$ contributing, leading to:

$$\hat{\underline{\underline{F}}}_{Q,xz,m=\pm 1} = \frac{\pi I_{r,21,m=\pm 1}}{2} \tag{3.63}$$

For $\hat{\underline{\underline{F}}}_{Q,yy}$ we have only $|m|=0,2$ contributing, leading to:

$$\begin{aligned}\hat{\underline{\underline{F}}}_{Q,yy,m=0} &= \frac{\pi I_{r,30,m=0}}{2} \\ \hat{\underline{\underline{F}}}_{Q,yy,m=\pm 2} &= -\frac{\pi I_{r,30,m=\pm 2}}{4}\end{aligned} \tag{3.64}$$

For $\hat{\underline{\underline{F}}}_{Q,yz}$ we have only $|m|=1$ contributing, leading to:

$$\hat{\underline{\underline{F}}}_{Q,yz,m=\pm 1} = \frac{\pm i\pi I_{r,21,m=\pm 1}}{2} \tag{3.65}$$

For $\hat{\underline{\underline{F}}}_{Q,zz}$ we have only $|m|=0$ contributing, leading to:

$$\hat{\underline{\underline{F}}}_{Q,zz,m=0} = \pi I_{r,12,m=0} \tag{3.66}$$

Using Eqs.(3.61)-(3.66) along with Eq.(3.32) and Eq.(3.28), we have:

$$\hat{p}'_{Q,m=0}\left(\vec{x}_0,\omega\right) = \frac{\pi\left(ikR_0-1\right)\exp\left(ikR_0\right)}{R_0^3}\left[\begin{array}{l}\dfrac{I_{r,30,m=0}}{2}\left(1-\left\{3+\dfrac{\left(kR_0\right)^2}{\left(ikR_0-1\right)}\right\}\sin^2\phi_0\right) \\ +I_{r,12,m=0}\left(1-\left\{3+\dfrac{\left(kR_0\right)^2}{\left(ikR_0-1\right)}\right\}\cos^2\phi_0\right)\end{array}\right] \tag{3.67}$$

$$\hat{p}'_{Q,m=\pm 1}\left(\vec{x}_0,\omega\right) = -\frac{\pi\left(ikR_0-1\right)\exp\left(ikR_0\pm i\theta_0\right)I_{r,21,m=\pm 1}\sin 2\phi_0}{R_0^3}\left\{3+\frac{\left(kR_0\right)^2}{\left(ikR_0-1\right)}\right\} \tag{3.68}$$

$$\hat{p}'_{Q,m=\pm 2}\left(\vec{x}_0,\omega\right) = -\frac{\pi\left(ikR_0-1\right)\exp\left(ikR_0\pm i2\theta_0\right)I_{r,30,m=\pm 2}\sin^2\phi_0}{4R_0^3}\left\{3+\frac{\left(kR_0\right)^2}{\left(ikR_0-1\right)}\right\} \tag{3.69}$$

Finally, the net contributions of each mode to the far-field sound, from just its monopole, dipole and quadrupole components are given by:

$$\hat{p}'_{m=0}\left(\vec{x}_0,\omega\right)=2\pi\frac{\exp\left(ikR_0\right)}{R_0}\left\{\begin{array}{l} I_{r,10,m=0}+\dfrac{\left(ikR_0-1\right)I_{r,11,m=0}\cos\phi_0}{R_0} \\ \dfrac{\left(ikR_0-1\right)}{2R_0^2}\left[\begin{array}{l}\dfrac{I_{r,30,m=0}}{2}\left(1-\left\{3+\dfrac{\left(kR_0\right)^2}{\left(ikR_0-1\right)}\right\}\sin^2\phi_0\right) \\ +I_{r,12,m=0}\left(1-\left\{3+\dfrac{\left(kR_0\right)^2}{\left(ikR_0-1\right)}\right\}\cos^2\phi_0\right)\end{array}\right]\end{array}\right\} \tag{3.70}$$

$$\hat{p}'_{m=\pm1}\left(\vec{x}_0,\omega\right)=-\frac{\pi\left(ikR_0-1\right)\exp(ikR_0\pm i\theta_0)}{R_0^2}\left\{\begin{array}{l} I_{r,20,m=0}\sin\phi_0 \\ -\dfrac{I_{r,21,m=\pm1}\sin 2\phi_0}{R_0}\left\{3+\dfrac{\left(kR_0\right)^2}{\left(ikR_0-1\right)}\right\}\end{array}\right\} \tag{3.71}$$

To summarize, the flame's monopole contribution comes from the $m=0$ mode only, the dipole contribution is influenced by the $|m|=0,1$ modes, while the quadrupole moment is influence by the $|m|=0,1,2$ modes. Higher order helical modes influence higher order multipoles, but not the monopole, dipole, or quadrupole components.

3.6 Non-Axisymmetric Mean Flames

In the previous section, the results indicated that asymmetric modes in the disturbance field have no effect or role in the global flame response of axisymmetric mean flames. An important observation from this result relates to comparisons of the forced response sensitivities of axisymmetric and non-axisymmetric flames. For example, single flames are nearly axisymmetric when placed in circular geometries. However, a single flame becomes non-axisymmetric when placed in a non-circular geometry, such as a square or sector combustor. In addition, multiple nozzles

configurations generally lead to strong flame-flame interactions, whose shapes are decidedly not axisymmetric [115]. An illustrative example of this point is shown in Figure 18, showing a side view and end-on visualization of a 5-flame configuration housed in a circular combustor [145]. Note the nearly square shape of the central flame. *Thus, the sensitivity of the flame to helical modes is fundamentally different in axisymmetric or non-axisymmetric environments.* In this section we consider the effects of mean flame non-axisymmetry and hence how asymmetric modes in the disturbance field affect global flame response.

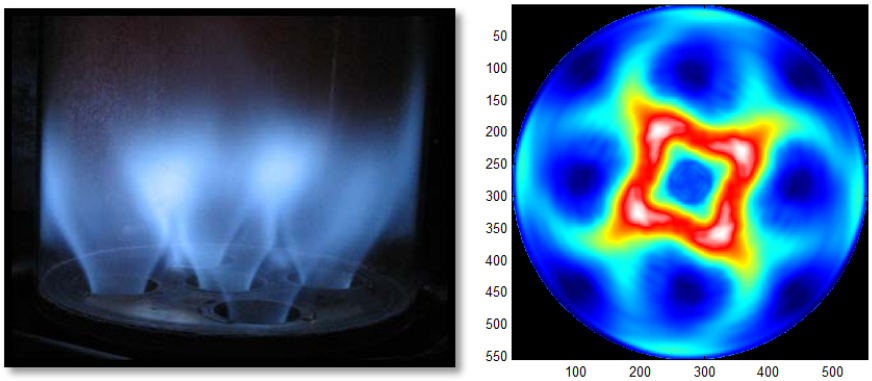

Figure 18 : Side and end-on view of a combustor with five swirling nozzles, showing the non-circular shape taken by the flames. Images reproduced from Ref. [145].

3.6.1 Weak Asymmetry

In this sub-section, we consider mean flame/flow with a weak non-axsiymmetry controlled by the small parameter η. Using Eq.(3.8) we have:

$$u_i(t,r,\theta) = \bar{U}_i(r) + \eta U_{\eta,i}(r,\theta) + \varepsilon u_i'(r,\theta,t) \tag{3.72}$$

$$\xi(r,\theta) = \bar{\xi}_0(r) + \eta \bar{\xi}_\eta(r,\theta) + \varepsilon \xi'(r,\theta,t) \tag{3.73}$$

The flame position fluctuations (in frequency domain) are then decomposed as:

$$\hat{\xi}'(\omega,r,\theta) = \hat{\xi}_0'(\omega,r,\theta) + \eta \hat{\xi}_\eta'(\omega,r,\theta) \tag{3.74}$$

Note that the axial coordinate *z* is not included in Eq.(3.72) since it is considered at the flame location given by $z = \xi(r,\theta)$. The strictly axisymmetric mean flame surface is governed by the equation (from Eq.(3.34)):

$$\begin{aligned} \bar{U}_z - \bar{U}_r \frac{d\bar{\xi}_0}{dr} &= s_L \sqrt{1+\left(\frac{d\bar{\xi}_0}{dr}\right)^2} \\ \frac{d\bar{\xi}_0(r)}{dr} &= \cot\left(\psi(r)\right) \end{aligned} \tag{3.75}$$

The non-axisymmetric correction to the mean flame is governed by:

$$\left(\vec{\bar{U}}_t \cdot \vec{\nabla}\right)\bar{\xi}_\eta = U_{\eta,z} - U_{\eta,r}\frac{\partial\bar{\xi}_0(r)}{\partial r} = \frac{U_{\eta,n}(r,\theta)}{\sin\psi(r)} \tag{3.76}$$

Where the subscript *n* corresponds to the normal component to the axisymmetric mean flame. This equation indicates that the asymmetries in the mean flame surface are governed by the normal component of the asymmetric part of the mean flow. Similarly, the flame wrinkling can be decomposed into its respective governing equations as:

$$i2\pi St\hat{\xi}_0' + \left(\vec{\bar{U}}_t \cdot \vec{\nabla}\right)\hat{\xi}_0' = \hat{u}_z' - \hat{u}_r'\frac{\partial\bar{\xi}_0(r)}{\partial r} = \frac{\hat{u}_n'}{\sin\left(\psi(r)\right)} \tag{3.77}$$

$$i2\pi St\hat{\xi}_\eta' + \left(\vec{\bar{U}}_t \cdot \vec{\nabla}\right)\hat{\xi}_\eta' = -\left(\vec{\hat{u}}' \cdot \vec{\nabla}\right)\bar{\xi}_\eta - \left(\vec{U}_\eta \cdot \vec{\nabla}\right)\hat{\xi}_0' - s_L \sin\left(\psi(r)\right)\left[\vec{\nabla}\bar{\xi}_\eta \cdot \vec{\nabla}\hat{\xi}_0'\right] \tag{3.78}$$

As seen earlier, Eq.(3.77) indicates that the leading order flame wrinkling is generated by the normal component of the flow fluctuations. However, in the case of Eq.(3.78) there are multiple sources of disturbances in the RHS. The first term on the right hand side indicates the interaction of mean flame asymmetries with flow disturbances. The second term indicates the interaction of mean flow asymmetries with the leading order local flame wrinkling. The third term is due to normal propagation at the mean flame asymmetries interacting with the leading order local flame wrinkling. Note that all three

terms contribute to the interaction of helical modes in the disturbance flow with the asymmetries in the mean flame. This is better explained using an example problem presented in Chapter 5.

3.6.2 Strong Asymmetry

In order to consider this case, the general solution to Eq.(3.6) is required. This requires the use of numerical methods. The spatial derivatives are discretized using a Weighted Essentially Non-Oscillatory (WENO) [146] scheme designed for Hamilton-Jacobi equations. This scheme is uniformly fifth order accurate in regions where the spatial gradients are smooth and third order accurate in discontinuous regions. Derivatives at the boundary nodes are calculated using fifth order accurate upwind-differencing schemes so that only the nodes inside the computational domain were utilized. A Total Variation Diminishing (TVD) Runge-Kutta scheme [147], up to third order accurate, was used for time integration and Local Lax-Friedrich (LLF) scheme, was used for improved stability [146]. These are detailed in Appendix B.

The spatial grid is chosen based on resolving $1/100^{th}$ of the smallest length scale and the time-step is chosen to capture atleast $1/1000^{th}$ of the forcing frequency. Note that the spatial grid is two-dimensional with both the radial and azimuthal directions. A typical grid (radial x azimuthal) ranges between 500x1000 to 1000x1000 grid points. The numerical solver was developed in the C language using OpenMP for parallel computing. Results using this numerical solver for example calculations are presented in Chapter 5.

3.7 Disturbance Field Decomposition

The analytical form of the disturbance field used as input to the flame response model is an integral piece in both deriving the flame wrinkling behavior as well as the global heat

release fluctuations. A small amplitude disturbance field can be decomposed into three canonical types – (i) acoustic, (ii) vortical, and (iii) entropy [148, 149]. The disturbances in may be expanded as:

$$\begin{aligned} \vec{\Omega}' &= \vec{\Omega}'_A + \vec{\Omega}'_V + \vec{\Omega}'_S \\ p' &= p'_A + p'_V + p'_S \\ S' &= S'_A + S'_V + S'_S \end{aligned} \tag{3.79}$$

Here, $\vec{\Omega}'$ is the vorticity vector disturbance, p' is the pressure disturbance and s' is the entropy disturbance. The subscripts A,V,S denote acoustic, vortical and entropy contributions. In the linear approximation, for uniform and homogeneous mean quantities, these three disturbances propagate independent of each other and are decoupled [148]. This implies:

$$\begin{aligned} \vec{\Omega}' &= \vec{\Omega}'_V \\ p' &= p'_A \\ S' &= S'_S \end{aligned} \tag{3.80}$$

Hence, this implies that the velocity fluctuations due to acoustic disturbances and vorticity disturbances will propagate independently and hence independently lead to flame response. The acoustic disturbances propagate at the speed of sound (c) while vortical disturbances propagate on the order of the local flow velocity ($U_{c,v} \sim U_0$). Here, U_0 is a characteristic flow velocity. This leads to a significant difference in the acoustic and vortical disturbance length scales for low Mach number flows ($M = U_0/c$). In this thesis, we consider low Mach number flows where the disturbance field is imposed on the flame and that the effect of the flame on the disturbance field is not considered.

Using the linearized governing equations for wave phenomena and momentum, the following form of the velocity disturbances is obtained:

$$\frac{u'_A(x,t)}{U_0} = \mathrm{Re}\left[\varepsilon_A \exp\left(i\omega\left(t-\frac{x}{c}\right)\right)\right]$$
$$\frac{u'_V(x,t)}{U_0} = \mathrm{Re}\left[\varepsilon_V \exp(-\alpha x)\exp\left(i\omega\left(t-\frac{x}{U_{c,v}}\right)\right)\right] \tag{3.81}$$

Here, the acoustic and vortical amplitude are in general different, and the parameters α and $U_{c,v}$ are typically functions of the frequency ω:

$$\alpha = \frac{U_0}{2\nu}\left(\sqrt{\frac{\left(1+\Gamma_V^2\right)^{1/2}+1}{2}}-1\right)$$
$$U_{c,v} = \frac{U_0\Gamma_V}{\sqrt{2\left(\left(1+\Gamma_V^2\right)^{1/2}-1\right)}} \tag{3.82}$$

Here, $\Gamma_V = 4\omega\nu/U_0^2$ and ν is the kinematic viscosity. In the low frequency limit, the disturbances can be reduced to the form:

$$\frac{\hat{u}'_A}{U_0} = \mathrm{Re}\left[\varepsilon_A \exp\left(i\omega\left(t-\frac{x}{c}\right)\right)\right]$$
$$\frac{\hat{u}'_V}{U_0} = \mathrm{Re}\left[\varepsilon_V \exp\left(i\omega\left(t-\frac{x}{U_{c,v}}\right)\right)\right] \tag{3.83}$$

Using the analytical forms of the disturbance fields presented here, the example calculations can be performed for the two non-axisymmetric fields. These example calculations are described in detail in the next two chapters.

CHAPTER 4

EXAMPLE CALCULATIONS: TRANSVERSE ACOUSTIC DISTURBANCES

This chapter utilizes the formulation from Chapter 3 to specifically consider the response of premixed flames to transverse acoustic disturbances.

4.1 Mean Flow and Mean Flame

In order to show explicit results, consider an axially uniform mean velocity field U_0, and a solid body azimuthal field, given by

$$\bar{U}_r = 0; \bar{U}_\theta = 2\pi St(\Omega/\omega)r = 2\pi St\sigma r; \bar{U}_z = 1 \tag{4.1}$$

While a variety of different swirl profiles are experimentally observed, such as Rankine, Oseen, solid body, and so forth, we particularly focus on a solid body flow field, as this result is analytically tractable and enables relatively simple analytical expressions which provide insight into the more general results described in Chapter 3. Note that the velocity field here has been normalized by the characteristic velocity U_0. The Strouhal number St is as defined in Eq.(3.17). The angular rotation rate of the mean flow field is then given by Ω and the dimensionless rotation rate by $\sigma = \Omega/\omega$. The mean flame shape from solving Eq.(3.34) is then given by:

$$\bar{\xi}(r) = (r - R)\cot\psi \tag{4.2}$$

Using Eq. (4.1) in Eq.(3.36), we obtain the following expressions for the linear spiral propagation path of disturbances from the flame base:

$$r = \left(\frac{s_L \cos\psi}{2\pi St\sigma}\right)\theta \tag{4.3}$$

4.2 Flame Wrinkling and Global Flame Response

Based on Eq.(3.83), the general transverse acoustic disturbance field is chosen as:

$$\hat{u}'_x = D_f \exp\left(-i2\pi\chi x\right) + D_b \exp(i2\pi\chi x) \tag{4.4}$$

The transverse velocity is along the x-coordinate direction which is a one-dimensional transverse direction to the main axial flow for the swirl-stabilized flame (see Figure 16). Here, the amplitudes D_f and D_b are the amplitudes of the forward traveling and backward traveling wave. Their relative values are used to control the nature of disturbance as (i) pure traveling wave for $D_f = 1, D_b = 0$ and (ii) pure standing wave for $D_f = D_b = 1$. The parameter χ controls the compactness of the flame length scale relative to the acoustic wavelength, and is defined as:

$$\chi = \frac{L_f}{\lambda_a} = St.M \tag{4.5}$$

Where $M = U_0/c$ is the Mach number of the flow. First consider the case of a compact flame, in the limit of $\chi \to 0$. Essentially the acoustic field becomes a spatially uniform bulk transverse forcing. The cylindrical coordinate velocity components are given by:

$$\begin{aligned} \hat{u}'_r &= \cos\theta \\ \hat{u}'_\theta &= \sin\theta \end{aligned} \tag{4.6}$$

Without any loss of generality, we can omit the constants D_f, D_b. Note that for the axisymmetric mean flow/flame assumed here, the $\hat{u}'_\theta$ component has no influence, as seen from Eq.(3.35). The azimuthal mode representation of Eq.(4.6) is given by:

$$\begin{aligned} \hat{B}_{r,m\neq\pm1} &= 0 \\ \hat{B}_{r,m\pm1} &= \frac{1}{2} \end{aligned} \tag{4.7}$$

Applying this to Eq.(3.38) leads to the solution:

$$\hat{\xi}'(\tilde{r},\theta)=\frac{i\cot\psi}{2\pi St\left(\sigma^2-1\right)}\left[\begin{array}{l}\cos\theta\left[i-e^{-i2\pi St_2\tilde{r}}\left\{i\cos(2\pi St_{\Omega,2}\tilde{r})-\sigma\sin(2\pi St_{\Omega,2}\tilde{r})\right\}\right]\\+\sin\theta\left[\sigma-e^{-i2\pi St_2\tilde{r}}\left\{i\sin(2\pi St_{\Omega,2}\tilde{r})+\sigma\cos(2\pi St_{\Omega,2}\tilde{r})\right\}\right]\end{array}\right] \quad (4.8)$$

Where

$$St_2=\frac{St}{\cos^2\psi}$$
$$St_{\Omega,2}=St_2\sigma \quad (4.9)$$

And

$$\tilde{r}=\left(\frac{r-R}{\tan\psi}\right) \quad (4.10)$$

As seen from Eq.(3.43) and Eq.(3.44), only the symmetric mode $m=0$ contributes to the global flame response. Since the amplitude of the symmetric mode is zero, the global flame response in zero for the compact flame case. This is despite non-zero local flame wrinkling and regardless of the swirl parameter σ, flame angle ψ or Strouhal number St. This can also be directly seen from the nature of the spatial dependence of the forcing function in Eq.(4.6). The spatial distribution shows that opposite halves of the flame always have equal normal component of velocity fluctuation at any instant of time, but of opposite sign. This implies that the change in area at a point in one half is cancelled by the change in area in the opposite half, leading to no net change in area. Note that, as mentioned earlier, this argument applies only to axisymmetric flames.

The solution in Eq.(4.8) may also be written as:

$$\hat{\xi}'(\tilde{r},\theta)=\mathscr{W}(\tilde{r},\theta)\exp\left(i\varphi(\tilde{r},\theta)\right) \quad (4.11)$$

Where

$$\mathscr{W}(\tilde{r},\theta)=\cot\psi\left[\frac{1}{\tau_+^2}\sin^2\frac{\tau_+\tilde{r}}{2}+\frac{1}{\tau_-^2}\sin^2\frac{\tau_-\tilde{r}}{2}+\frac{2}{\tau_+\tau_-}\sin\frac{\tau_+\tilde{r}}{2}\sin\frac{\tau_-\tilde{r}}{2}\cos(2\theta-2\pi\sigma\tilde{r})\right]^{1/2} \quad (4.12)$$

$$\tan\left[\varphi(\tilde{r},\theta)\right]=\frac{\frac{1}{\tau_+}\cos\left(\theta-\frac{\tau_+\tilde{r}}{2}\right)\sin\left(\frac{\tau_+\tilde{r}}{2}\right)+\frac{1}{\tau_-}\cos\left(\theta+\frac{\tau_-\tilde{r}}{2}\right)\sin\left(\frac{\tau_-\tilde{r}}{2}\right)}{\frac{1}{\tau_+}\sin\left(\theta-\frac{\tau_+\tilde{r}}{2}\right)\sin\left(\frac{\tau_+\tilde{r}}{2}\right)-\frac{1}{\tau_-}\sin\left(\theta+\frac{\tau_-\tilde{r}}{2}\right)\sin\left(\frac{\tau_-\tilde{r}}{2}\right)} \quad (4.13)$$

Here, $\tau_\pm=2\pi St_2\left(1\pm\sigma\right)$.

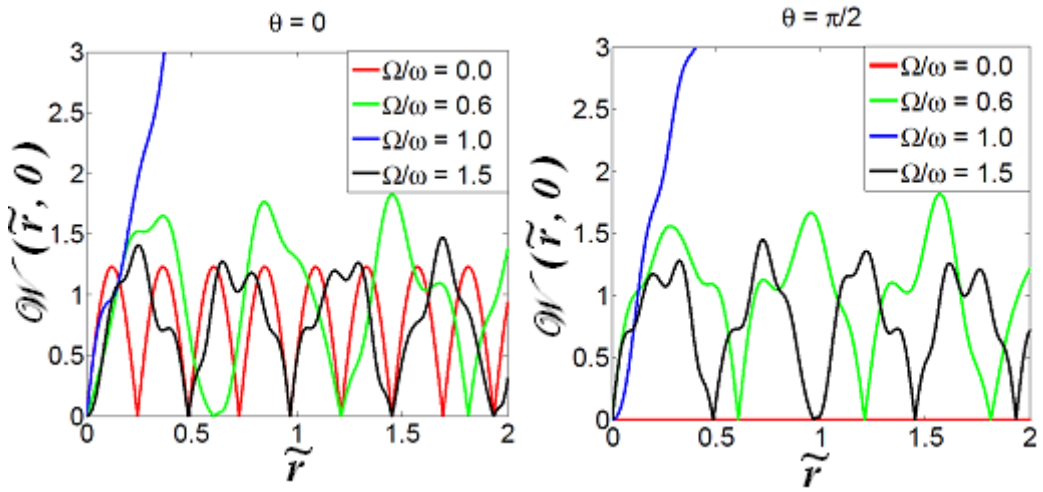

(a) **(b)**

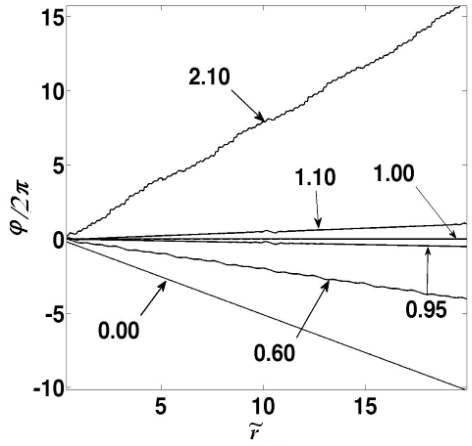

(c)

Figure 19 : Amplitude variation $\mathscr{W}$ along the flame for different values of $\sigma=\Omega/\omega$, with downstream radial distance at (a) $\theta=0$, (b) $\theta=\pi/2$; (c) Phase variation (φ) for different values of $\sigma=\Omega/\omega$.

The apparent convection speed of wrinkles measured at a fixed azimuthal position, θ, is modified due to the interference patterns created by the swirl transport component. This apparent convection speed is obtained from the slope of the phase dependence upon frequency, shown later.

The presence of transverse excitation introduces non-axisymmetric wrinkling on the flame surface, as illustrated in Figure 19(a). In the absence of swirl, these non-axisymmetric wrinkles convect axially downstream; they are simply not axisymmetric. The superposition of swirl onto a non-axisymmetric problem introduces fundamentally new features for the flame response.

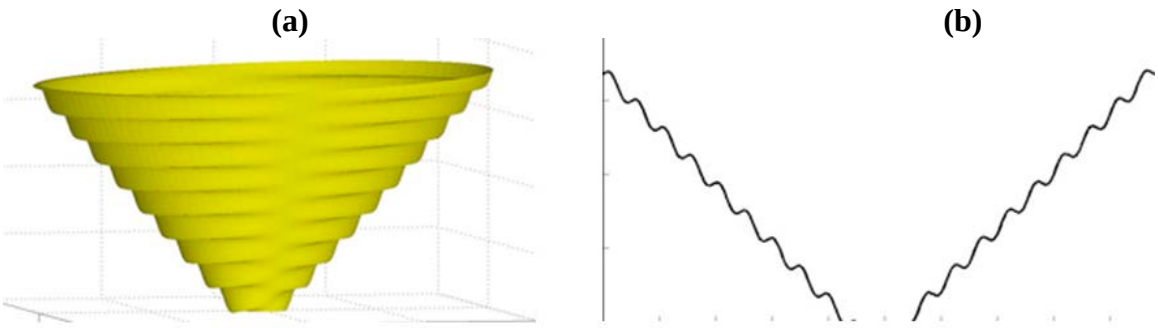

Figure 20 : Instantaneous flame shape visualization for ψ = 14^o, σ = Ω/ω = 0.00 showing; (a) flame surface, (b) flame branches at θ = 0,π.

We start first with the no swirl case, σ=0, as a baseline. Figure 20(a) illustrates a three dimensional view of the instantaneous flame surface, as well as a slice of the flame surface at θ =0 and π. Notice that that even in the absence of swirl, the flame wrinkling is non-axisymmetric. There is no wrinkling at the "grazing" angles $\theta=\pi/2$ and $3\pi/2$, and the wrinkles are out of phase at θ =0 and π. The latter can be seen from Figure 20(b). The phase of the flame wrinkling is given by Eq.(4.13) for $\theta=0$ and π, is shown in Figure 19 (c). Note that since the phase decreases with downstream distance, it corresponds to

downstream motion of the wrinkles. The spatial dependence of the amplitude of flame wrinkling, $\mathscr{W}$, is shown in Figure 19(a) and Figure 19(b). Note the spatially modulated character of the flame wrinkling amplitude which is due to interference between wrinkles excited at the flame attachment point and by the local disturbance field.

(a) **(b)**

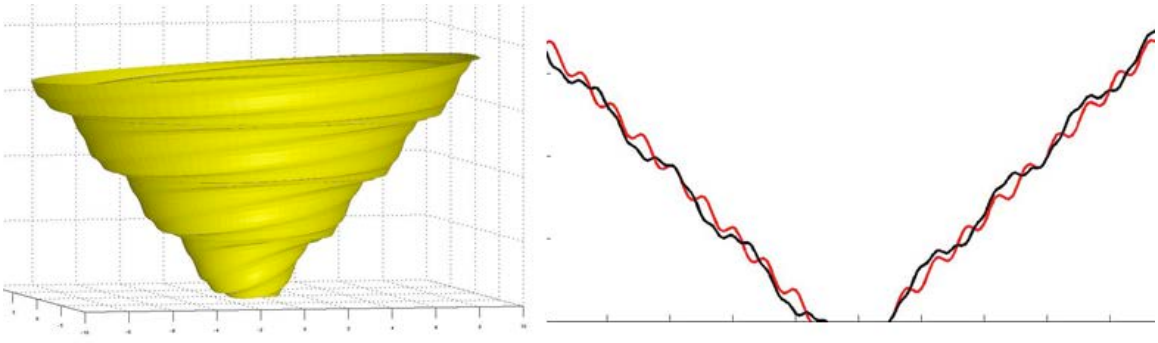

Figure 21 : Instantaneous flame shape visualizations for ψ = 14^o, $\sigma = \Omega/\omega$ = 0.60 showing; (a) flame surface, (b) flame branches at θ = 0, π; black : σ = 0.60, red : σ = 0.00.

We next consider a higher swirl case, σ=0.6. An image of the computed flame surface is shown in Figure 21(a), which shows that the flame is wrinkled at the grazing incidence angles, $\theta=\pi/2$ and $3\pi/2$, even though the normal perturbation field is zero. This occurs because swirl convects wrinkles created at other azimuthal angles into these planes. This image clearly shows a more complex interference pattern along the flame sheet. This can also be seen from the flame wrinkling amplitude, $\mathscr{W}$, shown in Figure 19(a) and Figure 19(b). Note also the change in periodicity of the nodes in flame response from this figure. The axial cut of flame wrinkling is shown in Figure 21(b). For reference, the red curve shows the baseline $\sigma=0$ case at the same instant of time. Note that there are multiple scales of wrinkling and that the effective wrinkling wavelength has increased

relative to the $\sigma=0.6$ case. Furthermore, Figure 19(c) shows that the rate of axial phase roll-off is shallower than that of the baseline case, indicating a faster "effective" axial convection speed of this cut. It is important to emphasize, however, that the rate of phase roll-off corresponds to a *trace* velocity, not a *group* velocity, since it is obtained from an azimuthal cut in which wrinkles are rotating into and out of. Recall that the trace velocity does not correspond to the propagation speed of a disturbance and can be positive, negative, and even have infinite values for finite propagation speed disturbances. This result has important implications on interpretations of sheet imaging of swirling flames, such as Mie scattering or planar laser induced fluorescence (PLIF), as it shows that the axial phase speed of disturbances along these cuts should not always be interpreted as physical convection velocities.

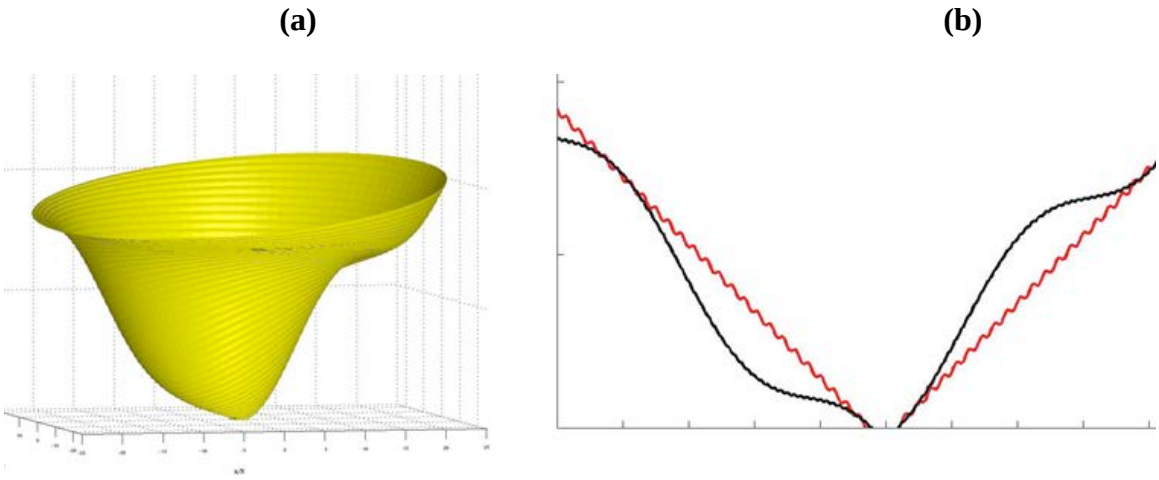

Figure 22 : Instantaneous flame shape visualizations for ψ = 14^o, $\sigma = \Omega/\omega$ = 0.95 showing; (a) flame surface, (b) flame branches at θ = 0, π; black : σ = 0.95, red : σ = 0.00.

We next consider σ=0.95, a value less than unity but very close, corresponding to near frequency matching. As shown in Figure 22(a), the flame surface exhibits a much larger scale helical motion. This longer wrinkling wavelength can also be seen in Figure 22(b),

by comparing this case to the no swirl result. Moreover, Figure 19(c) shows that the phase roll-off rate is nearly flat, corresponding to a very high axial trace velocity of the wrinkle.

(a) **(b)**

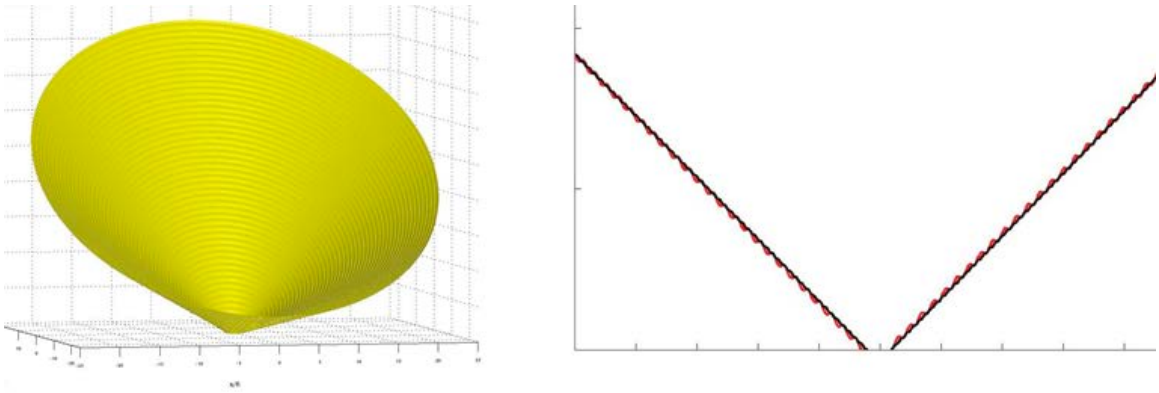

Figure 23 : Instantaneous flame shape visualizations for $\psi = 14^{o}$, $\sigma = \Omega/\omega = 1.00$ showing; (a) flame surface, (b) flame branches at $\theta = 0, \pi$; black : $\sigma = 1.00$, red : $\sigma = 0.00$.

We next consider the frequency matching case, σ=1.0. As shown in Figure 23(a), there is no periodic wrinkling on the flame surface. Rather the flame exhibits a solid body rotation of the tilted conical flame surface. The degree of off-axis rotation is controlled by the excitation amplitude. As shown in Figure 23(b), the phase-axial dependence is flat. These results show that as the swirl velocity is increased, or the excitation frequency decreased, that the scale of flame wrinkling increases up to an infinite value. This is also manifested through the phase of the wrinkles in the axial cuts, which as shown in Figure 19(c), monotonically decrease toward zero. The amplitude of wrinkling, $\mathscr{Y}$, does not oscillate but grows monotonically with downstream distance, as illustrated in Figure 19(a) and Figure 19(b).

(a) **(b)**

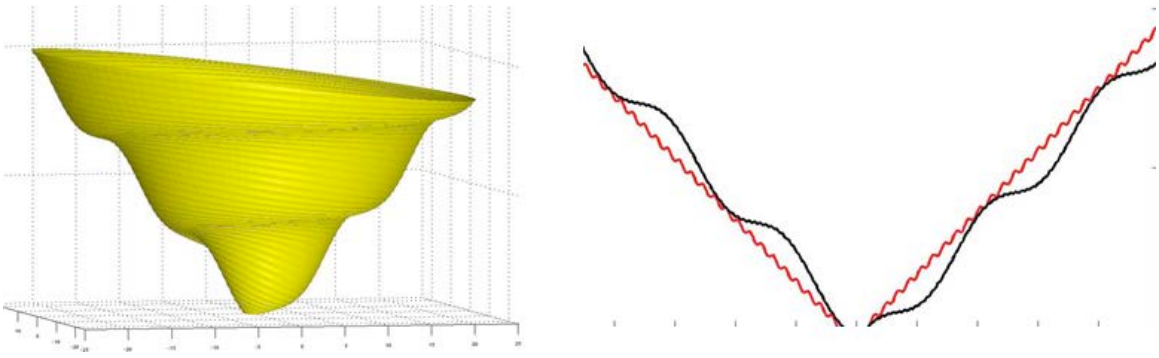

Figure 24 : Instantaneous flame shape visualizations for ψ = 14°, $\sigma = \Omega/\omega$ = 1.10 showing; (a) flame surface, (b) flame branches at θ = 0, π; black : σ = 1.10, red : σ = 0.00.

We next consider a dimensionless rotation rate which is greater than unity, σ=1.1, see Figure 24(a). Note that finite-scale flame wrinkling is present again. However, as shown in Figure 19(c), the phase now *increases* with downstream distance; i.e., the apparent direction of motion of wrinkles is now upstream. It is important to note that the flame wrinkles are not actually moving backward. Rather, they are moving along the characteristic curves given by at a velocity of $\vec{u}_t$. As discussed earlier, wrinkle motion along these axial cuts of the flame should be interpreted as trace velocities, not as convection speeds of actual flame wrinkles. Returning to Figure 19(c), this positive phase-axial distance behavior is analogous to the phenomenon of aliasing in spectral analysis, where the wrinkle is rotating through the axial cut faster than the period of oscillation. A familiar example is that of the apparent backward rotation rate of a vehicle's tire rims (as seen in films), despite the vehicle's forward motion.

We last consider an even faster rotation rate, σ=2.1. As shown in Figure 25(a), the wrinkling wavelength has further decreased. Figure 19(c) shows that the slope of the

phase continues to increase. Thus, we can see that beyond the frequency matching condition, the wrinkling wavelength decreases monotonically.

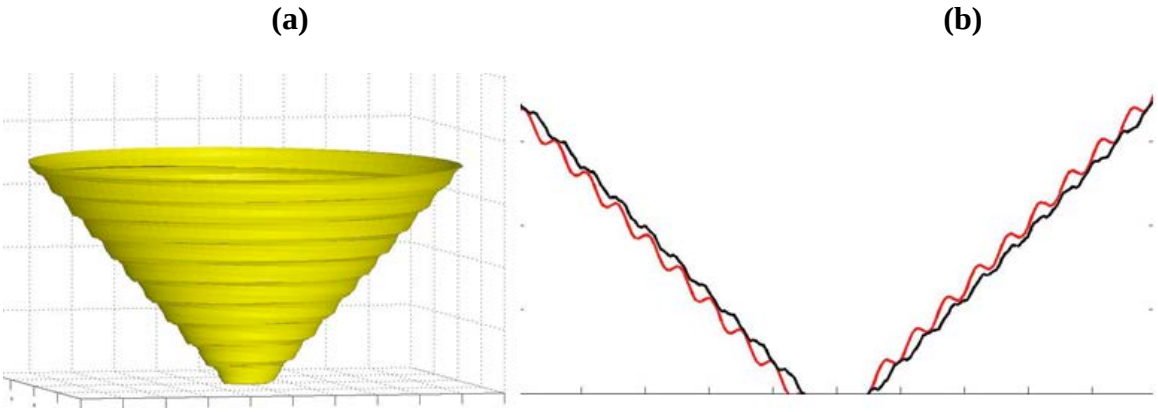

Figure 25 : Instantaneous flame shape visualizations for ψ = 14^{o}, $\sigma = \Omega/\omega$ = 2.10 showing; (a) flame surface, (b) flame branches at θ = 0, π; black : σ = 2.10, red : σ = 0.00.

Having considered the local flame wrinkling features for the compact flame case, we next consider the non-compact flame case. The transverse forcing expressed in Eq.(4.4) must be transformed from Cartesian coordinates to cylindrical coordinates for use with the model:

$$\begin{aligned} \hat{u}_r' &= \cos\theta\left[D_f \exp\left(-i2\pi\chi r\cos\theta\right) + D_b \exp\left(i2\pi\chi r\cos\theta\right)\right] \\ \hat{u}_\theta' &= \sin\theta\left[D_f \exp\left(-i2\pi\chi r\cos\theta\right) + D_b \exp\left(i2\pi\chi r\cos\theta\right)\right] \end{aligned} \tag{4.14}$$

Note that for the axisymmetric mean flow/flame assumed here, the $\hat{u}_\theta'$ component has no influence, as seen from Eq.(3.35). Before we proceed to apply the model, the analytical form of $\hat{u}_r'$ needs to expressed in terms of its helical modes as described by Eq.(2.2). This is facilitated by the use of the *Jacobi-Anger* expansion [132]:

$$e^{i\kappa\cos\theta} = \sum_{m=-\infty}^{\infty} i^m J_m(\kappa) e^{im\theta} \tag{4.15}$$

Consider only the forward wave component with $D_f = 1, D_b = 0$ (derivation for the backward wave component is similar). Applying the expansion to $\hat{u}_r'$ in Eq.(4.14) leads to:

$$\hat{u}_r' = \cos\theta \sum_{m=-\infty}^{\infty} i^m J_m\left(-2\pi\chi r\right) e^{im\theta} = \sum_{m=-\infty}^{\infty} \left[\frac{J_{m-1}\left(-2\pi\chi r\right) - J_{m+1}\left(-2\pi\chi r\right)}{2}\right] i^{m-1} e^{im\theta} \quad (4.16)$$

This leads to the following coefficients:

$$\begin{aligned} \hat{B}_{r,0}(r, St) &= \left[\frac{J_{-1}\left(-2\pi\chi r\right) - J_1\left(-2\pi\chi r\right)}{2}\right] i^{-1} = i\varepsilon J_1\left(-2\pi\chi r\right) \\ \hat{B}_{r,m}(r, St) &= \left[\frac{J_{m-1}\left(-2\pi\chi r\right) - J_{m+1}\left(-2\pi\chi r\right)}{2}\right] i^{m-1} \end{aligned} \quad (4.17)$$

Applying this to Eq.(3.38) leads to the solution:

$$\hat{\xi}_{r,m}'(\tilde{r}) = \frac{1}{\cos^2\psi}\left[\frac{J_m\left(-2\pi\chi_{T,m}\tilde{r} - 2\pi\chi\, R/L_f\right) - J_m\left(-2\pi\chi\, R/L_f\right)}{2\pi\chi_{T,m}}\right] e^{i\frac{\pi}{2}} e^{im\left(\frac{\pi}{2}\right)} e^{-i2\pi St_2\tilde{r}(1+m\sigma)} \quad (4.18)$$

where R is the center-body radius, L_f is the flame height and the parameters are defined as:

$$\chi_{T,m} = \chi\tan\psi - St_2 - mSt_{\Omega,2} \quad (4.19)$$

The Strouhal numbers St_2 and $St_{\Omega,2}$ have been defined earlier in Eq.(4.9). The parameter $\chi_{T,m}$ relates these Strouhal numbers to the asymmetry mode m and the non-compactness parameter χ. Note that, for the case of the transverse one-dimensional forcing, the modal amplitudes $\hat{B}_{r,m}$ is non-zero for all mode numbers m. This indicates the local flame wrinkles occurs due to all mode numbers. An important special case occurs in the limit of $\chi_{T,M} \to 0$, which results in the flame wrinkling that grows linearly, given by:

$$\hat{\xi}'_{r,m}(\tilde{r}) \to \frac{\tilde{r}}{2\cos^2\psi}\left[J_{m-1}\left(-2\pi\chi\, R/L_f\right) - J_{m+1}\left(-2\pi\chi\, R/L_f\right)\right] e^{i\frac{\pi}{2}} e^{im\left(\theta+\frac{\pi}{2}\right)} e^{-i2\pi\chi\tan\psi\tilde{r}} \quad (4.20)$$

The limiting condition is obtained when the parameters satisfy the condition given by:

$$M\sin\psi\cos\psi = (1+m\sigma) \quad (4.21)$$

Despite the presence of all helical modes, only the symmetric mode $m=0$ contributes to the global flame response (as seen from Eq.(3.43) and Eq.(3.44)). For the transverse transfer function defined as:

$$F_T = \left(\hat{A}'/\bar{A}\right)\Big/\left(\hat{u}'_{ref}/U_0\right) \quad (4.22)$$

We obtain:

$$F_T = 2\cot\psi\left[\hat{\mathscr{I}}_o\left(1+\frac{1}{i2\pi St_2}\right) - \frac{1}{i2\pi St_2}\left(\frac{1-J_0(2\pi\chi\tan\psi)}{2\pi\chi}\right)\right]$$

where (4.23)

$$\hat{\mathscr{I}}_o = \exp\left(-i2\pi St_2\right)\int_{\tilde{r}=0}^{\tilde{r}=\tan\psi}\left[J_1(2\pi\chi\tan\psi\tilde{r})\exp\left(-i2\pi St_2\tilde{r}\right)\right]d\tilde{r}$$

Note that the only controlling parameters for the global flame response are the non-compactness parameter χ, the Strouhal number St_2 and the flame angle ψ. The expression also indicates the presence of two different scales of interference in the Strouhal number space, one due to the exponential term and the other due to the Bessel term. This is primarily due to the unique spatial distribution of the non-compact transverse forcing as seen by the conical flame surface. These aspects are depicted in Figure 26.

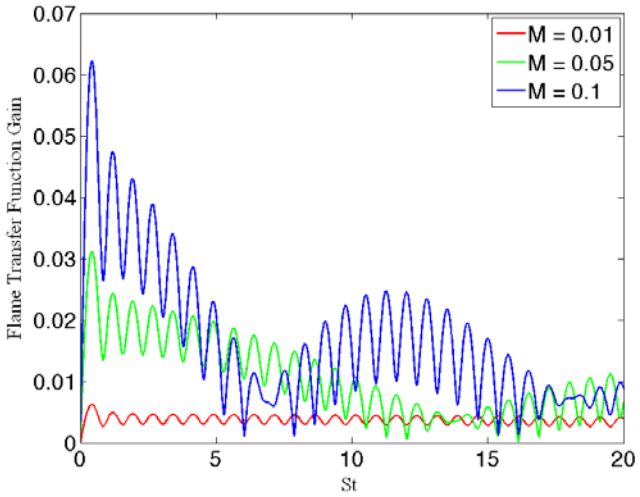

Figure 26 : Flame transfer function gain for a nominally axisymmetric flame in a non-compact transverse disturbance field. The non-compactness is controlled by the Mach number, but also varies along the x-axis with Strouhal number.

Note how all the curves start at zero for $St = 0$, for the reasons discussed earlier. They then rise and oscillate with the two scales mentioned above. Note also that larger transfer function gains are achieved for shorter length scale disturbances, parameterized here by *M*.

These results have important implications for our understanding of flame response mechanisms during transverse instabilities. Consider the potential pathways through which transverse acoustic waves excite the flame (Figure 5(b)). Two of these pathways are directly acoustic in origin - transverse acoustic motions associated with the natural frequencies/mode shapes of the combustion system, and longitudinal oscillations in the nozzle due to the oscillating pressure difference across the nozzle. These longitudinal fluctuations should not be confused with longitudinal modes of the combustor but, rather, are *longitudinal motions associated with the dominantly transverse modes*. In addition, these transverse and longitudinal acoustic disturbances also excite vortical flow disturbances. These include excitation of the shear layers, swirl number fluctuations, and

oscillations in the vortex breakdown bubble [51, 74, 108]. As such, the receptivity of these flow instabilities to both transverse and longitudinal acoustic oscillations must be considered.

These disturbance pathways all play a role in exciting the flame, but are difficult to separate in real systems. However, the results of this study provide insight into the role of "direct" transverse excitation path on the local and global response of the flame. Assume for the moment that the velocity fluctuations induced by all the pathways are of similar magnitude (e.g., see measurements by O'Connor [45]). These results suggest, then, that this direct path leads to flame fluctuations that are locally comparable to the other pathways. This implies that the influence of transverse sound waves should be clearly present in measurements of flame front fluctuations. It also shows, however, that interpretation of local flame wrinkle dynamics using planar sheet imaging approaches is problematic. In order to better understand these, the next subsection presents a comparison between the transverse flame transfer function and longitudinal flame transfer function.

4.3 Relative Importance of Transverse and Longitudinal Flame Transfer Functions

In addition to the transverse forcing transfer function presented in the previous section, consider the longitudinal transfer function introduced by the following axially convecting longitudinal disturbance field:

$$\hat{u}'_z = \sin\psi \exp\left(-i2\pi\chi\tilde{r}\right) \tag{4.24}$$

Using similar procedure outlines in the previous section, the longitudinal flame transfer function is obtained as:

$$F_L = \frac{k_M}{2\pi^2(1-k_M)St_2^2}\left(1-k_M-(1-2\pi i\,St_2)\;e^{2\pi i St_2}+(k_M-2\pi i\,St_2)\,e^{2\pi i St_2/k_M}\right) \quad (4.25)$$

Here, $k_M = 1/M\cos^2\psi$ and St_2 is as defined earlier in Eq.(4.9). Before we proceed to compare the transfer functions, let us consider the low and high frequency limits.

In the limit of $St \to 0$, we have:

$$\begin{aligned} |F_L| &\to 1 \\ |F_T| &\to 0 \end{aligned} \quad (4.26)$$

In the limit of $St \to \infty$, for the longitudinal transfer function, we have

$$|F_L| \to \frac{1}{St}\frac{2\cos^2\psi}{\pi(1-M\cos^2\psi)}\left|\sin\left(\pi\,StM-\frac{\pi\,St}{\cos^2\psi}\right)\right| \sim O\left(\frac{1}{St}\right) \quad (4.27)$$

For the case of constant Mach number, the corresponding limit for the transverse transfer function can also be evaluated as:

$$|F_T| \to \frac{1}{St\sqrt{St}}\frac{1}{\sqrt{M}}\frac{\cot\psi\cos^2\psi}{\pi^2\sqrt{\tan\psi}}\left|\cos\left(2\pi\chi\tan\psi-\frac{3\pi}{4}\right)\right| \sim O\left(\frac{1}{St\sqrt{St}}\right) \quad (4.28)$$

Now, consider the limit where $St \to \infty$ but the compactness parameter $\chi = StM$ is kept constant. Therefore,

$$\begin{aligned} F_T &\to \frac{i\cot\psi\cos^2\psi}{\pi St}\left[J_1(2\pi\chi\tan\psi)\exp\left(-\frac{i4\pi\mathrm{St}}{\cos^2\psi}\right)-\cot\psi\left(\frac{1-J_0(2\pi\chi\tan\psi)}{2\pi\chi}\right)\right] \\ \Rightarrow |F_T| &\sim O\left(\frac{1}{St}\right) \end{aligned} \quad (4.29)$$

Now, let us consider comparison plots for the two transfer functions. An important parameter in making this comparison is the Mach number of the flow. Shown in Figure 27 is the comparison between $|F_T|$ and $|F_L|$ for (a) $M = 0.1$ and (b) $M = 0.3$. Note that for low Strouhal number, $|F_L|$ is greater than $|F_T|$. This can be attributed to the limit

shown in Eq.(4.26). However, as the Strouhal number is increased, the envelope of $|F_T|$ increases and remains constant while that of $|F_L|$ decreases. At an intermediate Strouhal number, the $|F_T|$ and $|F_L|$ values are comparable. As can be seen from Figure 27(a) and Figure 27(b), this intermediate *St* value is different and hence dependent on Mach number. Beyond this intermediate value, both transfer functions decrease with *St*. However, $|F_T|$ decreases faster than $|F_L|$ as can be seen from Eq.(4.28) and Eq.(4.27), respectively. This indicates that $|F_T|$ can be neglected for large *St* when compared to $|F_L|$.

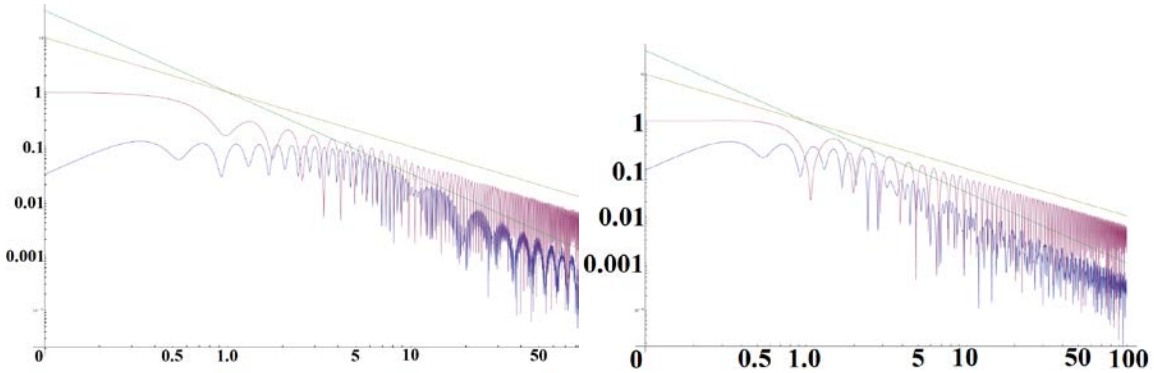

(a) **(b)**

Figure 27 : Comparison of $|F_T|$ (blue) and $|F_L|$ (pink) for (a) $M = 0.1$ and (b) $M = 0.3$. Asymptotic behavior is shown in yellow ($1/St$) for $|F_L|$ and green ($1/St^{1.5}$) for $|F_T|$.

Next, consider the comparison between $|F_T|$ and $|F_L|$ for constant values of the compactness parameter, χ. Figure 28(a) shows the comparison for a very compact flame, $\chi = 0.1$. This indicates the $|F_T|$ is always lower than $|F_L|$ for all values of *St*. The asymptotic behavior for both curves is seen to be $1/St$, as also shown earlier in Eq.(4.27) and Eq.(4.29). For the case of $\chi = 1.0$ shown in Figure 28(b), $|F_T|$ is greater than $|F_L|$ for low values of *St*. Note however that for values of *St* close to zero, $|F_L|$ is still greater than

$|F_T|$, due to differences in their low-*St* limit. As the flame becomes highly non-compact, $|F_T|$ is greater than $|F_L|$ over a much larger *St* range. This can be seen in Figure 28(c) for the case of $\chi = 10.0$. This indicates that the importance of $|F_T|$ increases with increasing Mach number.

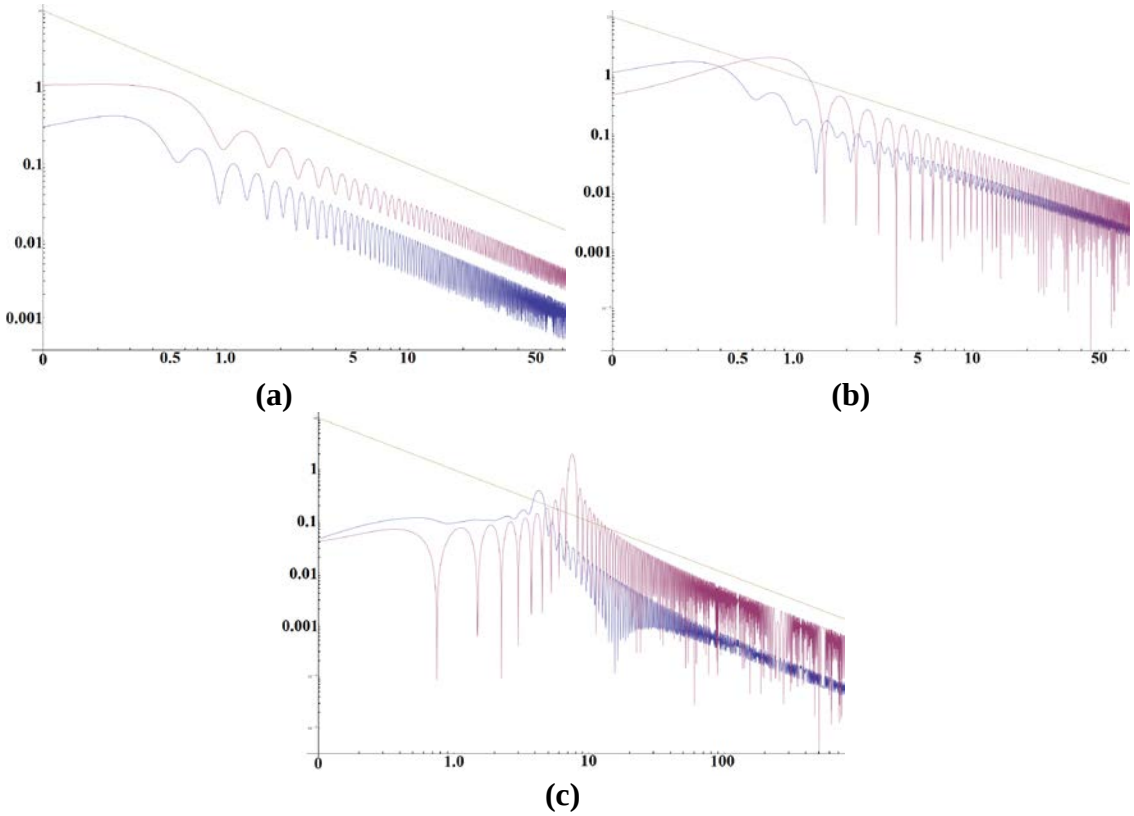

Figure 28 : Variation of $|F_T|$ (blue) and $|F_L|$ (pink) for constant values of the compactness parameter, where (a) $\chi = 0.1$, (b) $\chi = 1.0$ and (c) $\chi = 10.0$. Yellow line indicates asymptotic behavior 1/*St*.

An important feature of the $|F_T|$ curves is the "kneeing" behavior of the envelope. The $|F_L|$ transfer function envelope is seen to decrease continuously from low values of *St*, however in contrast, the $|F_T|$ transfer function shows 2 distinct regions: one with a constant envelope and one with a decreasing envelope. The demarcating *St* at which this happens is the "kneeing" Strouhal number. This *St* value also corresponds to the region

where the two transfer functions are comparable and hence it is important to understand its dependence on Mach number. Figure 29(a) shows the variation of $|F_T|$ for different Mach numbers and hence the variation of the "kneeing" *St*. This *St* is plotted as a function of Mach number in Figure 29(b). This plot indicates that the kneeing *St* varies inversely as the Mach number. In other words, for higher Mach number flows, both $|F_T|$ and $|F_L|$ are comparable at decreasing *St* values.

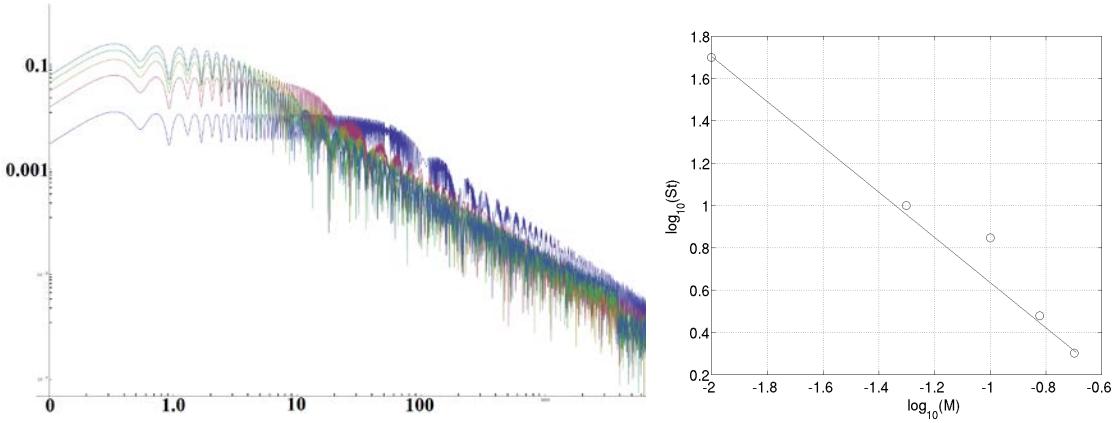

(a) **(b)**

Figure 29 : (a) Variation of $|F_T|$ for different Mach numbers, Violet: 0.01, Pink: 0.05, Yellow: 0.1, Green: 0.15, Blue: 0.2. (b) Variation of "kneeing" St with Mach number. Best fit indicates $St \sim 0.5M^{-1}$.

In this Chapter, the example calculations for transverse acoustic disturbances illustrated the non-axisymmetric nature of the local flame wrinkling features and the cancellation effects seen for global flame response. This begged the question as to whether transverse acoustic disturbances have any relative importance with reference to longitudinal disturbances. This question was answered with an example comparison between the two transfer functions indicating that both Strouhal number and mean flow Mach number were important control parameters.

CHAPTER 5

EXAMPLE CALCULATIONS: HELICAL FLOW DISTURBANCES

In this chapter we consider example calculations for the helical flow disturbances. The same mean flow and flame shape from Chapter 4 has been used.

5.1 Local Flame Response

Helical disturbances in the flow are vortical and hence, we consider an axially convecting disturbance whose variation along the flame surface is given by (from Eq.(3.81)):

$$\hat{u}'_{z,m}(\tilde{r},\theta)\Big|_{flame} = \exp(\tilde{\alpha}\tilde{r})\exp\left(-i2\pi \mathrm{St}\frac{1}{k_c}\tilde{r} + im\theta\right) = \exp\left(-i\left(2\pi \mathrm{St}_c + i\tilde{\alpha}\right)\tilde{r} + im\theta\right) \quad (5.1)$$

Where $k_c = U_c/U_0$ equals the phase speed of the disturbance normalized by the axial flow velocity and $St_c = fL_f/U_c$ is a Strouhal number based on this speed.

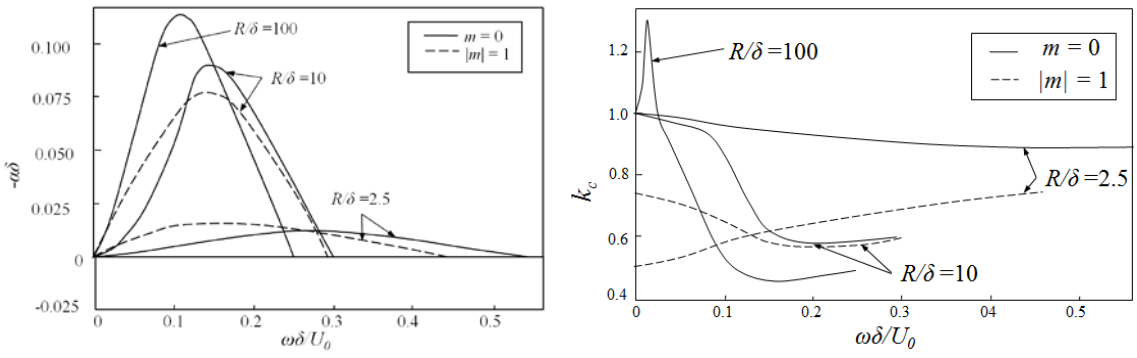

(a) **(b)**

Figure 30 : Dependence of the spatial instability (a) growth rate and (b) phase speed upon the dimensionless frequency of excitation for a non-swirling jet, where R/δ denotes the ratio of burner radius to boundary layer thickness. Adapted from Michalke [109].

The parameter $\tilde{\alpha}$ is the non-dimensional growth/decay rate of the disturbance amplitude projected along the flame, where $\tilde{\alpha} = \alpha L_f$. Hydrodynamic stability calculations show that both α and k_c are a function of mode number, boundary layer thickness, and frequency. For example, results from Michalke's calculations [109] for a non-swirling jet are reproduced in Figure 30.

The flame shape solution is obtained from Eq.(3.38) as,

$$\hat{\xi}'_m(\tilde{r}) = \frac{1}{\cos^2\psi}\left[\frac{e^{i(2\pi\chi_L)\tilde{r}} - e^{\tilde{\alpha}\tilde{r}}}{\left(i2\pi\chi_L - \tilde{\alpha}\right)}\right] e^{-i(2\pi St_c)\tilde{r}} \tag{5.2}$$

Where

$$\chi_L = St_2\left(\frac{1}{k_c}\cos^2\psi - m\sigma - 1\right) \tag{5.3}$$

The parameter St_2 is the Strouhal number based on the component of tangential flame wrinkle propagation speed along the forcing direction, given by $U_{t,z} = U_0\cos^2\psi$, similar to results from Preetham *et al.* [44]. Note that the flame response amplitude in Eq.(5.2) depends upon the parameter χ_L. The parameter can be expressed in the form:

$$\chi_L = St_2\left(\frac{1}{k_{c,L}} - m\sigma - 1\right) = St_c - St_2 - mSt_{\Omega,2} \tag{5.4}$$

where $k_{c,L}$, is the phase speed of forcing normalized by the component of the wrinkle propagation speed along the wave propagation direction.

Note that the parameter χ_L is a function of the three different Strouhal numbers involved. These three Strouhal number ($St_c, St_2, St_{\Omega,2}$) relate the four relevant time-scales, which are due to swirl (Ω), phase speed of forcing (U_c), axial wave propagation along the

flame surface ($\bar{U}_{t,z}$) and forcing frequency (ω). The Strouhal number from swirling is combined with the mode number m and occurs as $mSt_{\Omega,2}$, which indicates that swirl only influences the flame response through helical modes.

The above expressions show that the flame response to a given velocity fluctuation is a strong function of its azimuthal distribution. For a given $\tilde{\alpha}$, the mode leading to the largest flame wrinkling magnitude corresponds to the one that minimizes χ_L. The mode associated with the χ_L=0 condition is:

$$m_0 = \frac{St_c - St_2}{St_{\Omega,2}} \tag{5.5}$$

This condition can also be obtained from Eq.(3.42), using the characteristic functions for the assumed flow field and forcing: $g(s) = 2\pi \cos^2 \psi St_{\Omega,2} s$ and $\varphi(s) = \cos^2 \psi St_c s$. Note that this equation is valid only for swirling flows ($St_{\Omega,2} \neq 0$). In case of non-swirling flows, Eq.(5.5) becomes $St_c = St_2$, similar to that derived by Preetham *et al.* [44]. Similarly, it can be shown that this same helical mode, m_0, leads to the largest fluctuations in local flame surface area, proportional to $\left(\partial \hat{\xi}'_m / \partial r\right)$. Thus, for a general swirling flow ($St_{\Omega,2} \neq 0$), a non-axisymmetric mode dominates the flame response amplitude when the axial phase speed of the vortex is different from the mean flow velocity, $St_c \neq St_2$. This is significant given the fact that from Eq.(3.43), only the axisymmetric mode contributes to the global flame area. Thus, different measures of the flame response (local wrinkling/heat release and global heat release) have very different sensitivities to different azimuthal modes.

The corresponding flame motion for $\chi_L = 0$ is:

$$\hat{\xi}'_m(\tilde{r}) = \frac{1}{\cos^2\psi}\left[\frac{\exp(\tilde{\alpha}\tilde{r})-1}{\tilde{\alpha}}\right]e^{-i(2\pi St_c)\tilde{r}} \tag{5.6}$$

The flame response variation is shown in Figure 31 for a spatially damped, neutrally stable, and growing disturbance mode.

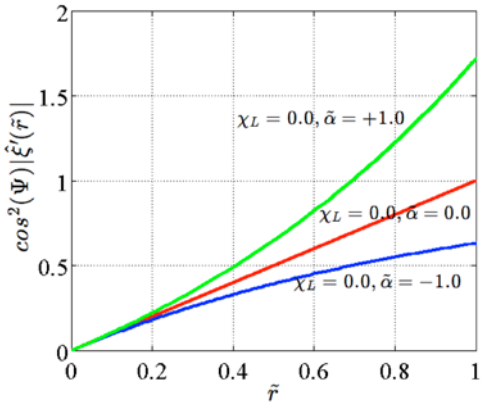

Figure 31 : Radial variation of the flame wrinkling amplitude for spatially damped, neutrally stable, and growing disturbance modes, for $\chi_L = 0$.

Consider the case of $\tilde{\alpha} = 0$ (neutrally stable), for which we have:

$$\hat{\xi}'_m(\tilde{r}) = \frac{\tilde{r}}{\cos^2\psi}e^{-i2\pi St_c\tilde{r}} \tag{5.7}$$

Note that, for this case, the flame response amplitude grows monotonically downstream in a linear manner and the flame response mode depicts a solid body rotation of a tilted conical flame surface. The degree of off-axis rotation is a function of the excitation amplitude. In this case, there is no interference between wrinkles excited along the flame at different times and spatial locations - rather, they constructively superpose to cause the magnitude of flame wrinkling to grow monotonically with downstream distance. The radial phase depends only on the parameter $St_c = fL_f/U_c$. We may also rewrite Eq.(5.4) as,

$$\chi_L = St_{\Omega,2}(m_0 - m) \tag{5.8}$$

This representation of the parameter better aids in understanding the flame's relative sensitivity to different co- and counter-rotating helical modes. Simply put, mode numbers closer to the value m_0 would give a lower value of χ_L and hence a higher flame motion response amplitude. For example, consider the case where $St_c > St_2$, i.e., $U_c < \bar{U}_{t,z}$, which implies that $m_0 > 0$. For this case, a counter-swirling helical mode, $+m$, has a corresponding lower value of χ_L compared to its co-swirling mode, $-m$, leading to larger magnitude of flame wrinkling. The opposite behavior occurs if the axial phase speed of the helical disturbance is greater than the axial component of the mean tangential velocity, i.e., $U_c > \bar{U}_{t,z}$. Finally, the flame responds identically to co- or counter-swirling modes when the flow is either not swirling, or when $U_c = \bar{U}_{t,z}$.

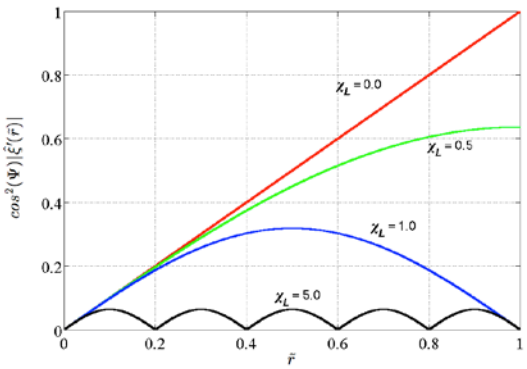

Figure 32 : Radial variation of flame response amplitude with χ_L for $\tilde{\alpha} = 0$, from Eq.(5.2).

We next present several plots to illustrate these results. The spatial variation of the flame response amplitude is shown in Figure 32. As the value of χ_L increases, the amplitude modulates in space and its maxima decreases as $1/\pi\chi_L$. Note that negative values of χ_L show the exact same behavior as their corresponding positive values. Equation (5.2) shows that the flame response amplitude depends only upon χ_L and the

flame angle ψ, while the phase of the flame response depends on both χ_L and St_c. At a given azimuthal location, the axial/radial phase varies linearly with downstream distance with a slope given by $\pi\chi_L - 2\pi St_c$. Thus, for the limiting case of $\chi_L/St_c = 2$, the flame response fluctuations at all radial locations (for a given azimuthal location on the flame surface are in phase with each other. When $\chi_L/St_c > 2$, the phase roll-off is positive, indicating an apparent negative phase speed. These spatial phase characteristics in the radial direction for different values of χ_L/St_c are shown in Figure 33.

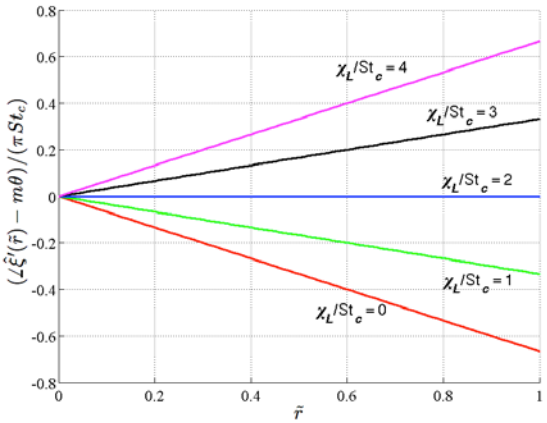

Figure 33 : Phase variation for flame wrinkling (from Eq.(5.2)) for different values of χ_L/St_c with $\tilde{\alpha} = 0$.

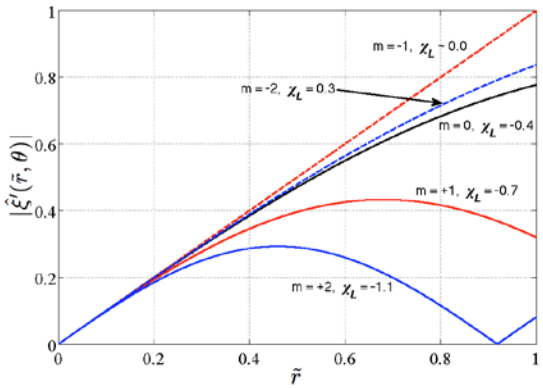

Figure 34 : Amplitude dependence upon radial location for different modes for $\psi = 24^o$, $k_c = 0.9$, $\tilde{\alpha} = 0$, $St = 0.45$, $\sigma = 0.4$, where $m_0 = -1$.

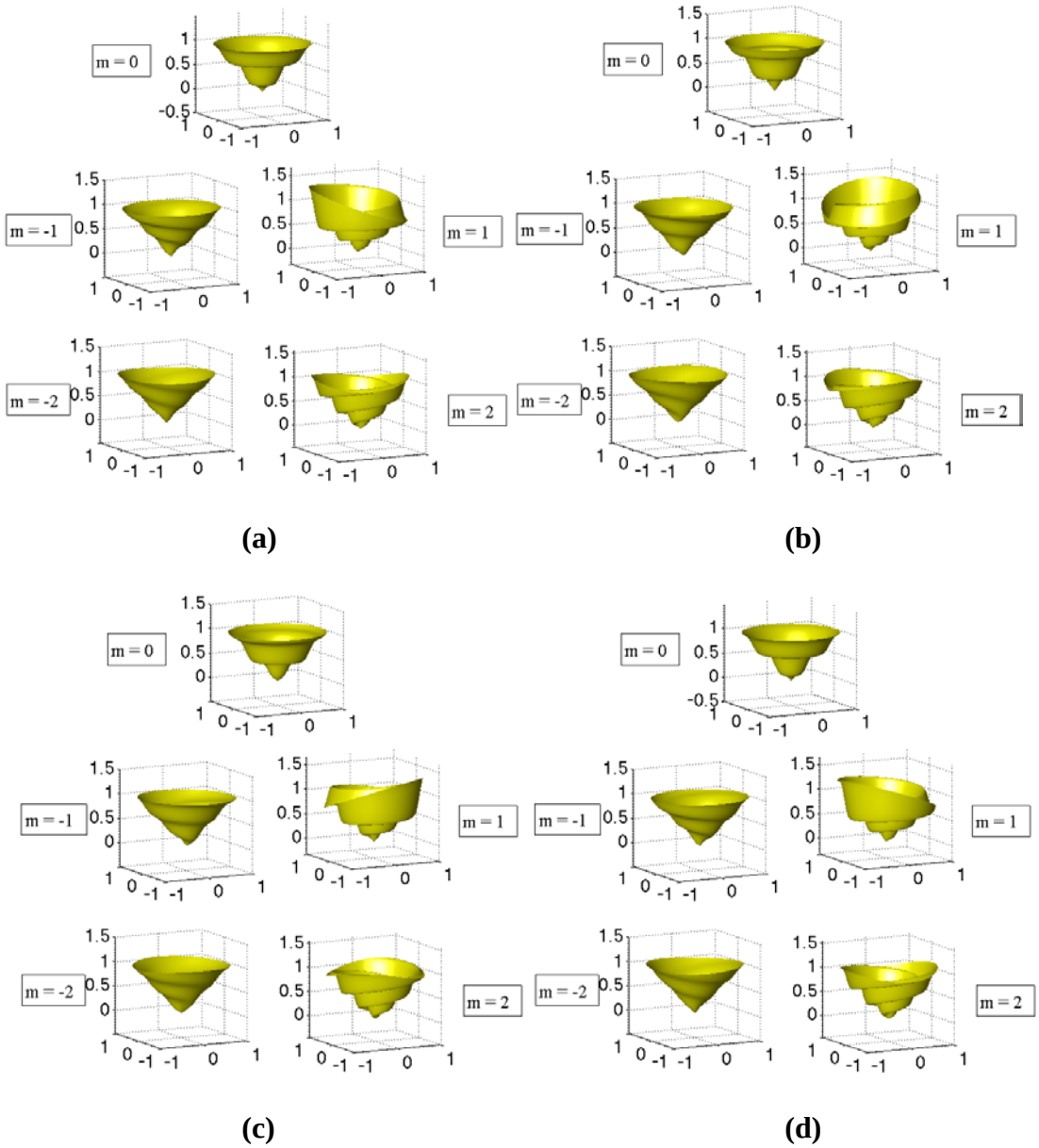

Figure 35 : Flame surface plots over different instants in a time period, showing the wrinkling due to different helical modes: (a) *t/T* = 0.0, (b) *t/T* = 0.3; (c) *t/T* = 0.6; (d) *t/T* = 0.9; for $\psi = 24^o, k_c = 0.5, \tilde{\alpha} = 0, St = 1.25, \sigma = 0.6$. Surface wrinkling has been exaggerated to highlight features.

Finally, let us consider the three-dimensional spatial wrinkle pattern on the flame surface for different mode numbers, and their respective amplitudes. Figure 34 shows the amplitude variation for the different modes for a case where $m_0 = -1$, and as expected the co-swirling modes dominate their counter-swirling counterparts. Figure 35 shows

instantaneous plots of the flame surfaces for the different modes, at different instances in a periodic cycle. It shows the different wrinkling patterns and wavelengths excited on the flame by the different helical modes. Next, we consider explicit solutions for sound generation.

5.2 Sound Generation

For the illustrative results in this section, the helical flow disturbance example of the previous section is considered. Before proceeding, we define the following for ease of notation:

$$\hat{\mathscr{P}}_m'\left(\theta_0,\phi_0,\omega\right)=\hat{p}_m'\left(\vec{x}_0,\omega\right)\frac{R_0\sin\psi}{2\pi e^{ikR_0}} \tag{5.9}$$

For the purpose of this study, we shall be using a negligible center-body radius in order to depict the qualitative features of the generated sound. Thus, using Eq.(5.9) and Eq.(3.47), we have:

$$\begin{aligned}&\hat{\mathscr{P}}_m'\left(\theta_0,\phi_0,\omega\right)\\&=\frac{e^{im\left(\theta_0+\pi\right)}}{\chi_L}\int_{\tilde{r}=0}^{1}\left[J_m\left(kL_f\tilde{r}\tan\psi\sin\phi_0\right)\left\{\begin{matrix}\left(\chi_L-St_c\right)e^{i2\pi\chi_L\tilde{r}}\\+St_c\end{matrix}\right\}e^{-ikL_f\tilde{r}\cos\phi_0-i2\pi St_c\tilde{r}}\right]\tilde{r}d\tilde{r}\end{aligned} \tag{5.10}$$

Some general inferences can be drawn from these equations. The axisymmetric $m=0$ mode radiates far-field sound that is independent of swirl, whereas the pressure field radiated by the helical modes ($m\neq 0$) is a function of swirl number. For these helical modes, the bias due to the direction of swirl can be seen in the differences it introduces in the values of χ_L and, hence, on the far-field pressure. The effects of different physical time-scales, swirl and helical mode number are all contained in the parameter χ_L,defined in Eq.(5.4).

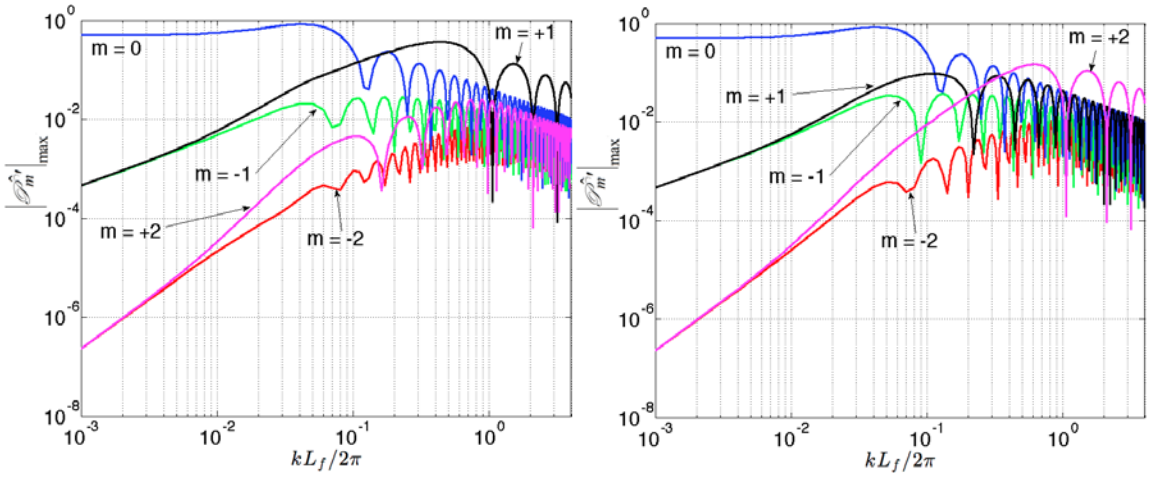

Figure 36 : Dependence of maximum pressure amplitude variation $\left|\hat{\mathscr{P}}'_m\right|_{\max}$ upon compactness parameter kL_f for several modes, for $\psi = 24^o, k_c = 0.5, M = 0.1$, (a) $\sigma = 0.6$, where $m_0 = +1$ and (b) $\sigma = 0.3$, where $m_0 = +2$. Note that ϕ_0 value where the plotted maximum pressure amplitude occurs varies with kL_f.

There are significant differences in both peak sound emissions, $\left|\hat{\mathscr{P}}'_m\right|_{\max}$, and directivity for the different modes. We start by consider the peak sound emissions, by plotting the magnitude of the unsteady pressure at the angle, ϕ_0, where its magnitude peaks as a function of compactness parameter, kL_f. In this calculation, the Mach number ($M = U_0/c$), swirl parameter ($\sigma = \Omega/\omega$), flame angle (ψ) and $k_c = U_c/U_0$ are kept constant as kL_f varies, implying that all Strouhal numbers increase proportionally to kL_f. This is in contrast to, for example, kL_f varying at fixed *St*. Results are shown for two different conditions, corresponding to $m_0 = +1$ and $m_0 = +2$, respectively, in Figure 36. Both plots show that the $m = 0$ mode dominates the far-field pressure for kL_f <<1, since all other modes provide zero net unsteady heat release. The magnitudes of the first and second helical modes rise monotonically as kL_f and $\left(kL_f\right)^2$ respectively, as can also

be anticipated by the multi-pole expansion discussed earlier. The far-field sound from the $m = 0$ mode asymptotes to:

$$\left|\hat{\mathscr{P}}'_{m=0}\right|_{\max} \xrightarrow{kL_f << 1} \frac{1}{2} \tag{5.11}$$

Returning to Figure 36(a), while the $m = 0$ mode dominates for very small kL_f, for $kL_f/2\pi > 0.2$, the dominant far-field pressure mode becomes *m*= +1, which equals m_0 (dominant flame wrinkling, see Eq.(5.5)) for the parameter values used in this case. Note also the fact that the counter-swirling modes ($m > 0$) dominate their co-swirling ($m < 0$) counterparts. This again, is because of the fact that for these parameters, the dominant flame response mode $m_0 = +1$ is a counter-swirling mode. These features are reinforced by the second example shown in Figure 36(b) where parameter values are selected so that $m_0 = +2$. In this case, the $m = +2$ mode dominates the far-field pressure for $kL_f/2\pi > 0.4$. However, note also that the dominant mode is a function not only of m_0, but also of kL_f. For kL_f <<1, the *m*=0 mode similarly dominates, while for an intermediate kL_f range, the *m*=1 mode dominates. These points illustrate that far-field sound radiation is a function of local source strength and acoustic interference phenomenon. Thus, since the *m*=0 mode creates the least destructive interference, it dominates the far-field sound in the kL_f <<1 case, even though its local source strength is not as strong as the *m*=1 or 2 modes. In contrast, though the *m*=2 mode, by virtue of its equality with m_o for this example, has the largest local source strength by virtue of having the largest magnitudes of local heat release fluctuations, cancelation makes it a weak sound radiator for kL_f <<1. Only when kL_f ~O(1), does this strong local source

dominate the far-field pressure. Also, because of the dependence of the sound radiation on multiple parameters, including kL_f, *St*, and m_0, the dependence of the character of these curves at $kL_f >> 1$ upon the assumed relationship between these quantities should be emphasized. Thus, the oscillatory behavior and low sound emissions that are evident at higher kL_f values in this plot occurs because the corresponding Strouhal number is associated with a node in global heat release at that particular kL_f value.

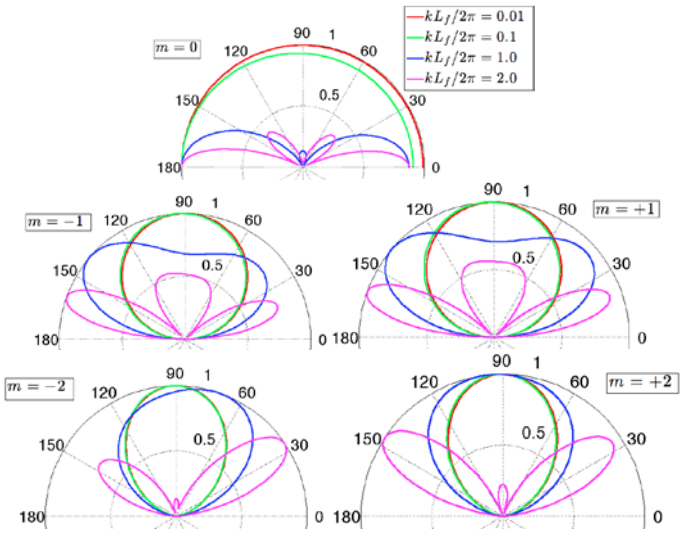

Figure 37 : Directivity plots showing modal dependence of the normalized far-field pressure amplitude in the spherical coordinate direction ϕ_0 for different values of $kL_f/2\pi$ with $\psi = 24^o, k_c = 0.5, M = 0.1, \sigma = 0.6$. The axial flow direction is from left to right in each of the polar plots.

Next, consider the directivity of sound for different helical modes. Figure 37 shows the variation in far-field pressure amplitude $\left|\hat{\mathscr{P}}_m'\right| / \left|\hat{\mathscr{P}}_m'\right|_{\max}$ as a function of the spherical coordinate $0 < \phi_0 < \pi$, for different values of kL_f. Note that there is no directivity along the coordinate θ_0, since it only controls the phase. For compact flames, the $m = 0$ mode radiates sound nearly omni-directionally, as suggested by Eq.(3.51). The $m = \pm 1$ modes radiate sound as $\sin\phi_0$ and so peak in sound emissions at $\phi_0 = 90^o$, since

they are dominated by the dipole component shown in Eq.(3.54). Similarly, the $m = \pm 2$ modes radiate sound as $\sin^2 \phi_0$, as shown in Eq.(3.69), and also peak in sound emissions at $\phi_0 = 90^o$. For each of the modes, the directivity pattern changes as dimensionless frequency increases, and exhibits angles of local maxima and minima due to phase interference effects.

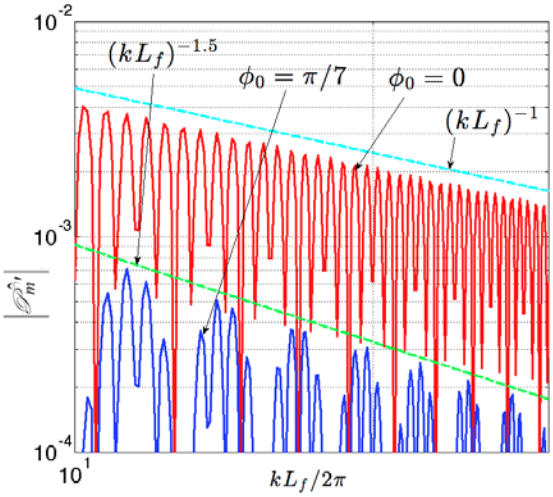

Figure 38 : Variations in sound pressure amplitude for $kL_f \gg 1$ at two polar angles, ϕ_0, excited by the $m = 0$ mode with $\psi = 24^o$, $k_c = 0.5$, $M = 0.1$ and $\sigma = 0.6$.

Next, consider the high frequency, $kL_f \gg 1$ limit. The limiting behavior on and off axis must be considered separately. For on-axis sound radiation, i.e., $\phi_0 = 0, \pi$, the Bessel function is zero when $m \neq 0$ and thus we confine attention to the $m = 0$ case. In this case, high frequency, on-axis sound radiation from the axisymmetric mode, *m*=0 mode scales as $\left(kL_f\right)^{-1}$, as also shown in Figure 38 for the $\phi_0 = 0$. Helical modes do not radiate on-axis sound. Off-axis sound radiation limiting behavior can be evaluated using methods for rapidly oscillating integrals and the limiting behavior of the Bessel function for large arguments:

$$J_m(x) \xrightarrow{x\to\infty} \sqrt{\frac{1}{2\pi x}}\left\{ e^{i\left(x-\frac{m\pi}{2}-\frac{\pi}{4}\right)} + e^{-i\left(x-\frac{m\pi}{2}-\frac{\pi}{4}\right)} \right\} \tag{5.12}$$

This can be used to show that high frequency, off-axis sound radiation from all modes, axisymmetric and non-axisymmetric, scales as $\left(kL_f\right)^{-3/2}$, as also shown in Figure 38.

Finally, consider the total sound power radiated by these flames. Based on the transformations in Eq.(3.27) and Eq.(5.9), the normalized sound power computed here is given by:

$$\mathscr{P}_m = P_m\left(\frac{4\rho c^3 \sin^2\psi}{\omega^2 \overline{q}^2 (\gamma-1)^2}\right) = \int_{\phi_0=0}^{\pi} \left|\hat{\mathscr{P}}_m'(\phi_0,\omega)\right|^2 \sin\phi_0 d\phi_0 \tag{5.13}$$

Using Eq.(5.10) in Eq.(5.13):

$$\begin{aligned} &\mathscr{P}_m (\eta_1-\eta_2)^2 \left(kL_f\right)^4 \\ &= \int_{\phi_0=0}^{\pi}\int_{\tilde{r}_1=0}^{kL_f}\int_{\tilde{r}_2=0}^{kL_f} J_m(\vartheta\tilde{r}_1) J_m(\vartheta\tilde{r}_2) \left\{ \begin{array}{l} \eta_1^2 e^{i\beta_1(\tilde{r}_1-\tilde{r}_2)} + \eta_2^2 e^{i\beta_2(\tilde{r}_1-\tilde{r}_2)} \\ -\eta_1\eta_2 \left(\begin{array}{l} e^{i(\beta_1\tilde{r}_1-\beta_2\tilde{r}_2)} \\ +e^{i(\beta_2\tilde{r}_1-\beta_1\tilde{r}_2)} \end{array} \right) \end{array} \right\} \tilde{r}_1\tilde{r}_2 d\tilde{r}_1 d\tilde{r}_2 \sin\phi_0 d\phi_0 \end{aligned} \tag{5.14}$$

where

$$\begin{aligned} &\vartheta = \tan\psi \sin\phi_0 \qquad \eta_1 = \frac{\cos^2\psi}{k_c} \qquad \eta_2 = (1+m\sigma) \\ &\beta_1 = \frac{\eta_1}{M\cos^2\psi} - \cos\phi_0 \qquad \beta_2 = \frac{\eta_2}{M\cos^2\psi} - \cos\phi_0 \end{aligned} \tag{5.15}$$

Typical results of numerical quadrature of Eq.(5.14) are shown in Figure 39 for the same conditions used in Figure 36. Most of the trends shown here mirror those shown in Figure 36. The $m=0$ mode dominates the compact flame sound emissions, with an asymptotic limit given by:

$$\mathscr{P}_{m=0} \xrightarrow{kL_f \ll 1} \frac{1}{2} \tag{5.16}$$

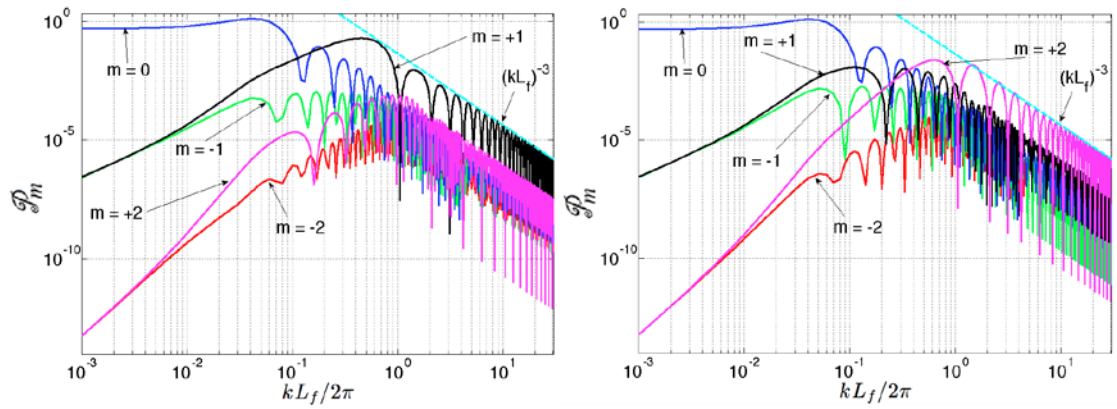

Figure 39 : Sound power variation $\mathscr{P}_m$ with compactness parameter kL_f and different mode numbers, for $\psi = 24^o, k_c = 0.5, M = 0.1$ and (a) $\sigma = 0.6$, where $m_0 = +1$ and (b) $\sigma = 0.3$, where $m_0 = +2$.

Similarly, the total sound power scales as $\left(kL_f\right)^2$ and $\left(kL_f\right)^4$ for |*m*|= 1 and 2 modes, respectively. Note how both positive and negative *m* values of the same index converge to the same limit at low kL_f, but then diverge as the flame becomes non-compact. The total sound power peaks at some intermediate kL_f value and then starts to roll off. The $kL_f >> 1$ limits can be evaluated to show that the total sound power scales as $\left(kL_f\right)^{-3}$ for all *m* values, as depicted in Figure 39. Finally, the oscillatory behavior and low sound power emissions at higher kL_f values in this plot occurs for the same reasons as discussed in the context of Figure 37 - namely, that the corresponding Strouhal number at that particular kL_f value is associated with a zero global flame area response.

5.3 Effects of Mean Flame Asymmetry

In this section, we consider the same example used in Section 5.1, to: (i) illustrate the effect of weak non-axisymmetries on the flame response results earlier in this thesis,

and (ii) illustrate the effect of strong asymmetries. Consider the following non-axisymmetric flow field (following Eq.(4.1)):

$$\begin{aligned}\bar{U}_r &= 0 \\ \bar{U}_\theta &= 2\pi St(\Omega/\omega)r = 2\pi St\sigma r \\ \bar{U}_z &= 1+\eta U_{\eta,z}(\theta)\end{aligned} \tag{5.17}$$

Here, the mean flow asymmetries are considered only in the axial flow for illustration purposes. This mean flow asymmetry can be expressed in terms of its asymmetric modes as:

$$U_{\eta,z}(r,\theta) = A^u_{\eta,z,0}(r) + \sum_{n\geq 0} A^u_{\eta,z,n}(r)\cos n\theta + B^u_{\eta,z,n}(r)\sin n\theta \tag{5.18}$$

From Eq.(3.75), we have:

$$\bar{\xi}_0(r) = (r-R)\cot\psi = \tilde{r} \tag{5.19}$$

Using Eq.(3.76), the governing equation for the mean flame asymmetry is given by:

$$s_L\cos\psi\frac{\partial\bar{\xi}_\eta}{\partial r} + St_\Omega\frac{\partial\bar{\xi}_\eta}{\partial\theta} = U_{\eta,z}(r,\theta) \tag{5.20}$$

The solution is given by:

$$\bar{\xi}_\eta(\tilde{r},\theta) = A^\xi_{\eta,z,0}(\tilde{r}) + \sum_{n\geq 0} A^\xi_{\eta,z,n}(\tilde{r})\cos n\theta + B^\xi_{\eta,z,n}(\tilde{r})\sin n\theta \tag{5.21}$$

Where

$$\begin{aligned}A^\xi_{\eta,z,0}(\tilde{r}) &= \frac{1}{\cos^2\psi_0}\int_{s=0}^{s=\tilde{r}} A^u_{\eta,z,0}(R+s\tan\psi_0)ds \\ A^\xi_{\eta,z,n}(\tilde{r}) &= \frac{1}{\cos^2\psi_0}\int_{s=0}^{s=\tilde{r}}\begin{bmatrix}A^u_{\eta,z,n}(R+s\tan\psi_0)\cos(nSt_{\Omega,2}(s-\tilde{r})) \\ +B^u_{\eta,z,n}(R+s\tan\psi_0)\sin(nSt_{\Omega,2}(s-\tilde{r}))\end{bmatrix}ds \\ B^\xi_{\eta,z,n}(\tilde{r}) &= \frac{1}{\cos^2\psi_0}\int_{s=0}^{s=\tilde{r}}\begin{bmatrix}B^u_{\eta,z,n}(R+s\tan\psi_0)\cos(nSt_{\Omega,2}(s-\tilde{r})) \\ -A^u_{\eta,z,n}(R+s\tan\psi_0)\sin(nSt_{\Omega,2}(s-\tilde{r}))\end{bmatrix}ds\end{aligned} \tag{5.22}$$

and $St_{\Omega,2} = St_{\Omega} / \cos^2 \psi_0$. Now consider the axial velocity fluctuation given by (from Eq.(5.1) with $\tilde{\alpha} = 0$):

$$\hat{u}'_{z,m}(\tilde{r},\theta)\Big|_{flame} = \exp\left(-\frac{i2\pi \mathrm{St}}{k_c}\tilde{r} + im\theta\right) \tag{5.23}$$

The leading order local flame wrinkling solution for Eq.(3.77) is given by:

$$\hat{\xi}'_{0,m}(\tilde{r},\theta) = \frac{1}{\cos^2\psi}\left[\frac{\sin(\pi\chi_L\tilde{r})}{(\pi\chi_L)}\right] e^{-i2\pi St_2\tilde{r} - i2\pi m St_{\Omega,2}\tilde{r} + i\pi\chi_L\tilde{r}} \tag{5.24}$$

The parameters in this equation have been defined earlier in Eq.(5.3). In order to determine the correction to the leading order flame wrinkling behavior, Eq.(3.78) must be solved using Eqs.(5.22)-(5.24) as inputs. First the forcing function in the RHS needs to be determined. The three terms in the RHS need to be evaluated individually before the total forcing function is calculated. For the first term:

$$\begin{aligned} &\hat{u}'_z \neq 0; \hat{u}'_r = \hat{u}'_\theta = 0 \\ &\overline{\xi}_\eta = \overline{\xi}_\eta(r,\theta) \\ &\Rightarrow -\left(\vec{\hat{u}}' \cdot \vec{\nabla}\right)\overline{\xi}_\eta = 0 \end{aligned} \tag{5.25}$$

For the second term:

$$\begin{aligned} &U_{\eta,z} \neq 0; U_{\eta,r} = U_{\eta,\theta} = 0 \\ &\hat{\xi}'_0 = \hat{\xi}'_0(St,r,\theta) \\ &\Rightarrow -\left(\vec{U}_\eta \cdot \vec{\nabla}\right)\hat{\xi}'_0 = 0 \end{aligned} \tag{5.26}$$

For the third term:

$$-s_L \sin\left(\psi(r)\right)\left[\vec{\nabla}\overline{\xi}_\eta \cdot \vec{\nabla}\hat{\xi}'_0\right] = -\sin^2\psi\left[\frac{\partial\overline{\xi}_\eta}{\partial r}\frac{\partial\hat{\xi}'_0}{\partial r} + \frac{1}{r^2}\frac{\partial\overline{\xi}_\eta}{\partial\theta}\frac{\partial\hat{\xi}'_0}{\partial\theta}\right] \tag{5.27}$$

In order to evaluate the third term above, consider only the *n*-th mode asymmetry in the mean flame shape (Eq.(5.21)) and the *m*-th mode flame response in the leading order

flame wrinkling (Eq.(5.24)). We shall denote this interaction by $RHS_{n,m}$. We can rewrite Eq.(5.21), in the form:

$$\bar{\xi}_\eta\left(\tilde{r},\theta\right) = A^{\xi}_{\eta,z,0}(r) + \frac{1}{2}\sum_{n\neq 0}\left[A^{\xi}_{\eta,z,n}(r) + sign(n) iB^{\xi}_{\eta,z,n}(r)\right]e^{in\theta} \tag{5.28}$$

Using this, we have:

$$RHS_{n,m} = -e^{i(n+m)\theta}\sin^2\psi_0\begin{pmatrix}\frac{d}{dr}\left[\left(A^{\xi}_{\eta,z,n}(r) - iB^{\xi}_{\eta,z,n}(r)\right)\right]\frac{d}{dr}\left[\hat{\xi}'_{0,m}(\tilde{r})\right] + \\ \frac{1}{r^2}\left[-nm\left(A^{\xi}_{\eta,z,n}(r) - iB^{\xi}_{\eta,z,n}(r)\right)\hat{\xi}'_{0,m}(\tilde{r})\right]\end{pmatrix} \tag{5.29}$$

The resulting flame response correction due to this forcing function can be expressed as $\hat{\xi}'_{\eta,n,m}$, where (from Eq.(3.78)):

$$i2\pi St\hat{\xi}'_{\eta,n,m} + \left(\vec{\bar{U}}_t(r)\cdot\vec{\nabla}\right)\hat{\xi}'_{\eta,n,m} = RHS_{n,m} \tag{5.30}$$

Note that this corresponds to a system where the forcing function has a combined azimuthal mode $\left(n+m\right)$. Note that Eq.(3.77), Eq.(3.78) and Eq.(5.30) are similar in their operators in their respective LHS. Hence, their mathematical behavior for their respective RHS would also be similar for the same forcing function. We have seen earlier (Chapter 3) that only the symmetric mode of the forcing function contributes finitely to the global flame response. Hence for cases where $n+m=0$, the global response is finite. This implies that the asymmetries in the mean flow ($n\neq 0$) can interact with helical modes in the disturbance field ($m\neq 0$) leading to changes in the global flame response. Thus, for asymmetric mean flames, helical modes are important from a global flame response perspective. The importance of a particular helical mode is dictated by the presence of a corresponding mode of opposite sign in the asymmetric mean flame/flow.

For the purposes of illustration, consider an example flow field where:

$$A^{u}_{\eta,z,0} = 0$$
$$A^{u}_{\eta,z,n} = B^{u}_{\eta,z,n} = 1 \tag{5.31}$$

From a global flame response perspective, only the cases where $n+m=0$ are considered. Hence, we first consider the asymmetric modes $n=-m$ in Eq.(5.22):

$$A^{\xi}_{\eta,z,-m}(\tilde{r}) = \frac{1+\sqrt{2}\sin\left(mSt_{\Omega,2}\tilde{r} - \pi/4\right)}{mSt_{\Omega}}$$
$$B^{\xi}_{\eta,z,-m}(\tilde{r}) = \frac{\sqrt{2}\sin\left(mSt_{\Omega,2}\tilde{r} + \pi/4\right)-1}{mSt_{\Omega}} \tag{5.32}$$

Using Eq.(5.24), Eq.(5.29) and Eq.(5.32) in Eq.(5.30), we have the solution:

$$e^{i2\pi St_2\tilde{r}}\hat{\xi}'_{\eta,-m,m}(\tilde{r}) = I_1 + I_2 + \frac{im\tan^2\psi_0}{4\pi St_{\Omega}\chi_L}\left(I_3 + I_4 + I_5 + I_6\right) \tag{5.33}$$

The integrals are defined as:

$$I_1 = -\int_0^{\tilde{r}/\cos^2\psi_0} \frac{1}{2}\left(1 - \frac{St_2(1+m\sigma)}{\chi_L}\right)e^{i\alpha_1 s}ds = \frac{1}{2i\alpha_1}\left(1 - \frac{St_2(1+m\sigma)}{\chi_L}\right)\left(1 - e^{i\alpha_1 \tilde{r}/\cos^2\psi_0}\right) \tag{5.34}$$

$$I_2 = \int_0^{\tilde{r}/\cos^2\psi_0} \frac{1}{2}\left(\frac{St_2(1+m\sigma)}{\chi_L}\right)e^{i\alpha_2 s}ds = \frac{1}{2i\alpha_2}\left(\frac{St_2(1+m\sigma)}{\chi_L}\right)\left(e^{i\alpha_1 \tilde{r}/\cos^2\psi_0} - 1\right) \tag{5.35}$$

$$I_3 = \int_0^{\tilde{r}/\cos^2\psi_0}\left[\frac{e^{i(\alpha_3+\alpha_4+\alpha_5)s}}{\left(R + s\cos\psi_0\sin\psi_0\right)^2}\right]ds \tag{5.36}$$

$$I_4 = -\int_0^{\tilde{r}/\cos^2\psi_0}\left[\frac{e^{i(\alpha_5+\alpha_3-\alpha_4)s}}{\left(R + s\cos\psi_0\sin\psi_0\right)^2}\right]ds \tag{5.37}$$

$$I_5 = -\int_0^{\tilde{r}/\cos^2\psi_0}\left[\frac{e^{i(\alpha_5-\alpha_3+\alpha_4)s}}{\left(R + s\cos\psi_0\sin\psi_0\right)^2}\right]ds \tag{5.38}$$

$$I_6 = \int_0^{\tilde{r}/\cos^2\psi_0}\left[\frac{e^{i(\alpha_5-\alpha_3+\alpha_4)s}}{\left(R + s\cos\psi_0\sin\psi_0\right)^2}\right]ds \tag{5.39}$$

Where

$$\begin{aligned}
\alpha_0 &= -2\pi St_2(1+m\sigma)+2\pi St\sigma m \\
\alpha_1 &= \left(2\pi\chi_L\cos^2\psi_0+\alpha_0\cos^2\psi_0+2\pi St\right) \\
\alpha_2 &= \left(\alpha_0\cos^2\psi_0+2\pi St\right) \\
\alpha_3 &= 2\pi St\sigma m\cos^2\psi_0 \\
\alpha_4 &= \pi\chi_L\cos^2\psi_0 \\
\alpha_5 &= \alpha_0\cos^2\psi_0-\pi mSt\sigma\cos^2\psi_0+\pi\chi_L\cos^2\psi_0
\end{aligned} \tag{5.40}$$

And

$$\int_0^{\tilde{r}/\cos^2\psi_0}\left[\frac{\cos\psi_0\sin\psi_0 e^{i\beta s}}{\left(R+s\cos\psi_0\sin\psi_0\right)^2}\right]ds=\left\{\left[\frac{1}{R}-\frac{e^{i\beta\,\tilde{r}/\cos^2\psi_0}}{r}\right]+i\beta e^{\frac{i\beta R}{\cos\psi_0\sin\psi_0}}\left[\begin{array}{l}Ei\left(\dfrac{i\beta r}{\cos\psi_0\sin\psi_0}\right)\\ -Ei\left(\dfrac{i\beta R}{\cos\psi_0\sin\psi_0}\right)\end{array}\right]\right\} \tag{5.41}$$

$$Ei(x)=-\int_{-x}^{\infty}\frac{e^{-s}}{s}ds$$

Using these solutions for weak asymmetries, we apply them to example flames shapes that have: (i) Elliptic cross-section and (ii) Square cross-section. These are performed using a numerical solver, detailed in Appendix B, where the numerical methods and the parallel system used for its computations are detailed.

The effects of mean flame asymmetry are understood by comparing the Flame Transfer Function (*FTF*) which in these examples is defined as:

$$FTF=\frac{\hat{A}'/\bar{A}}{\varepsilon} \tag{5.42}$$

5.3.1 Example Calculations: Elliptic cross-section

Single flames in axisymmetric geometries are axisymmetric. However, when such a flame is confined in a non-axisymmetric combustor, like those with rectangular cross-sections, flame asymmetries are possible. Specifically if the confinement is significant in

one direction compared to the other, the single flame shapes can deviate from a circular cross-section to that of an ellipse. The asymmetric mean flame for this example is given by:

$$\overline{\xi}(\tilde{r},\theta) = \overline{\xi}_0(\tilde{r})\sqrt{1-\eta\cos^2\theta} \tag{5.43}$$

Here, $\overline{\xi}_0(\tilde{r}) = \tilde{r}$ from Eq.(5.19). The azimuthal variation in position is shown in Figure 40 for different values of the asymmetry parameter η. Note that for $\eta = 0$ we retrieve the axisymmetric mean flame given by Eq.(5.19). As this value is increased, the cross-section eccentricity increases. Note that the elliptic cross-section is valid only for $0 < \eta \leq 0.5$. For $0.5 < \eta \leq 1.0$, the flame shape is akin to that of two interacting flames. In this analysis, we shall focus on $\eta < 0.5$.

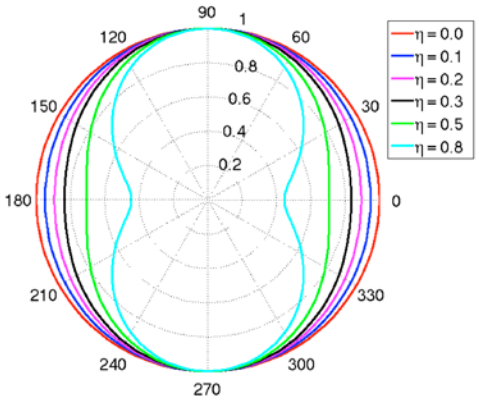

Figure 40 : Elliptic flame cross-section denoted by $\overline{\xi}(\tilde{r},\theta)/\overline{\xi}_0(\tilde{r})$ for varying η.

For the case of weak asymmetries, the mean flame shape correction can be expressed as (using Taylor expansion to first order):

$$\overline{\xi}_\eta(r,\theta) = \tilde{r}\left(-\frac{1}{4}-\frac{1}{4}\cos 2\theta\right) \tag{5.44}$$

Hence, we have:

$$A^{\xi}_{\eta,z,0}(\tilde{r}) = A^{\xi}_{\eta,z,n=2}(\tilde{r}) = -\frac{1}{4}\tilde{r}$$
$$A^{\xi}_{\eta,z,n\neq 0,2}(\tilde{r}) = B^{\xi}_{\eta,z,n}(\tilde{r}) = 0 \qquad \forall n \geq 0 \tag{5.45}$$

Since we are specifying the mean flame shape here, the mean flow field can be obtained using Eq.(5.20):

$$U_{\eta,z}(r,\theta) = -\left(\frac{\cos^2\psi}{4}\right) - \left(\frac{\cos^2\psi}{4}\right)\cos 2\theta + St_{\Omega}\left(\frac{\tilde{r}}{2}\right)\sin 2\theta \tag{5.46}$$

This results in the following asymmetric mode coefficients:

$$A^{u}_{\eta,z,0}(\tilde{r}) = A^{u}_{\eta,z,n=2}(\tilde{r}) = -\left(\frac{\cos^2\psi}{4}\right)$$
$$B^{u}_{\eta,z,n=2}(\tilde{r}) = St_{\Omega}\frac{\tilde{r}}{2} \tag{5.47}$$
$$A^{u}_{\eta,z,n\neq 0,2}(\tilde{r}) = B^{u}_{\eta,z,n\neq 2}(\tilde{r}) = 0 \qquad \forall n \geq 0$$

These equations show that for a weakly asymmetry flame with an elliptic cross-section, there exists only the asymmetric modes: $n = 0, \pm 2$. For a symmetric mode $m = 0$ in the disturbance field, the global flame response is corrected due to the $n = 0$ mode in the mean non-axisymmetry. The $n = \pm 2$ mode in the mean flow/flame asymmetry interacts with the helical modes $m = \mp 2$ in the flow disturbance, leading to a finite global flame response. For the example calculations presented next, we consider three cases: (i) Effect of η on the *FTF* amplitude, (ii) Effect of swirl (St_{Ω}) on the *FTF* amplitude and (iii) Effect of Flame angle on the *FTF* amplitude

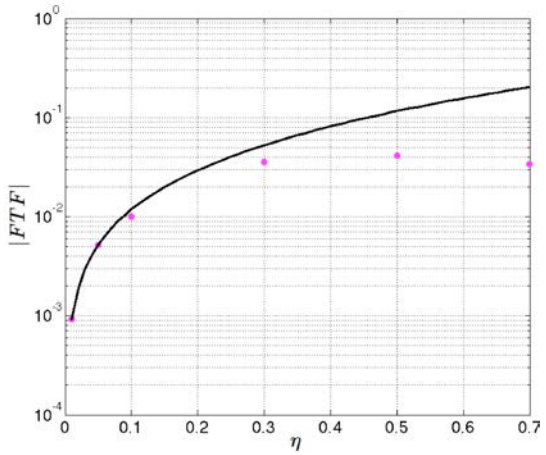

Figure 41 : Comparison of *FTF* amplitude for an elliptic flame computed using analytical solution in Eq.(5.33) (black curve) and numerical solver (pink circles) for increasing values of η. Flow disturbance contains the $m = 2$ mode with $St_2 = 2.0$ and $k_c = 0.8$. Note that $St_2 = fL_f / U_0 \cos^2 \psi$.

First consider the effect of η on the *FTF* as shown in Figure 41. The flow disturbance comprises of a helical mode of $m = 2$. As seen in the figure, for low values of η, the *FTF* amplitude is low as expected and increases with increasing value of η. For values of $\eta < 0.1$, there is a reasonable match between the *FTF* obtained using the numerical solver and that obtained using the asymptotic solution shown in Eq.(5.33).

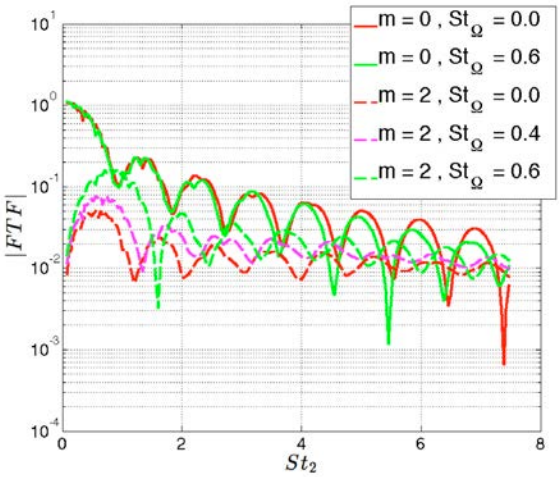

Figure 42 : Comparison of *FTF* amplitude for an elliptic flame, for different values of St_Ω for an elliptic flame with $\eta = 0.5, \psi = 15^o$, in response to a flow disturbance helical mode of $m = 2$ and $k_c = 0.8$. Note that $St_2 = fL_f / U_0 \cos^2 \psi$.

Next, consider the effect of swirl number on the FTF amplitude. This is shown in Figure 42 for the elliptic flame of $\eta = 0.5$. The solid curves denote the response of this asymmetric flame to a symmetric flow disturbance (*m*=0). Note that the low Strouhal number transfer function begins from unity and then decreases with increasing Strouhal number. In the case of perfectly axisymmetric mean flames, we showed earlier (Chapter 3) that the swirl component had no effect on the global *FTF* amplitude. However, for the case of asymmetric mean flames, this is not true. This is shown by the comparison of the *FTF* amplitude for two different values of St_Ω. The non-swirling case is indicated by the solid red curve and the swirling case ($St_\Omega = 0.6$) is indicated by the solid green curve. As the value of St_2 is increased, the *FTF* amplitudes deviate from each. This deviation indicates both a change in the interference Strouhal numbers and also a change in the amplitude. This can be attributed to the change in interference effects introduced by the transport of wrinkles on the asymmetric flame surface by the swirling flow. Finally, the effect of flame angle on the results is shown in Figure 43.

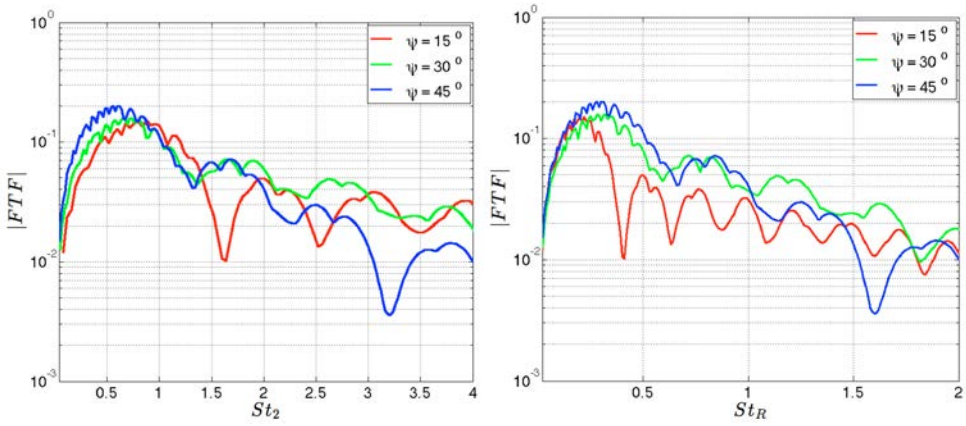

(a) **(b)**

Figure 43 : Effect of Flame angle on the *FTF* amplitude variation for an elliptic flame with $\psi = 15^o, St_\Omega = 0.5, \eta = 0.5, m = 2$ and $k_c = 0.8$. (a) Variation with $St_2 = fL_f / U_0 \cos^2 \psi$ and (b) Variation with $St_R = fR/U_0$.

5.3.2 Example Calculations: Square cross-section

In this sub-section, we consider example calculations for a flame with a square cross-section. Such an asymmetry is possible in the case of flame-flame interactions, such as shown earlier in Figure 18. The asymmetric mean flame for this example is given by:

$$\overline{\xi}(\tilde{r},\theta) = \overline{\xi}_0(\tilde{r})\left[\left(\cos\theta\right)^{2+2\eta} + \left(\sin\theta\right)^{2+2\eta}\right]^{1/(2+2\eta)} \tag{5.48}$$

Here, $\overline{\xi}_0(\tilde{r}) = \tilde{r}$ from Eq.(5.19). Note that η must be an integer for the expression to be valid. Hence, unlike the elliptic flame case, a weak asymmetry analysis cannot be performed for this flame due to the analytical nature of Eq.(5.48). A representative asymmetric mean flame shape is shown in Figure 44 for $\eta = 1$.

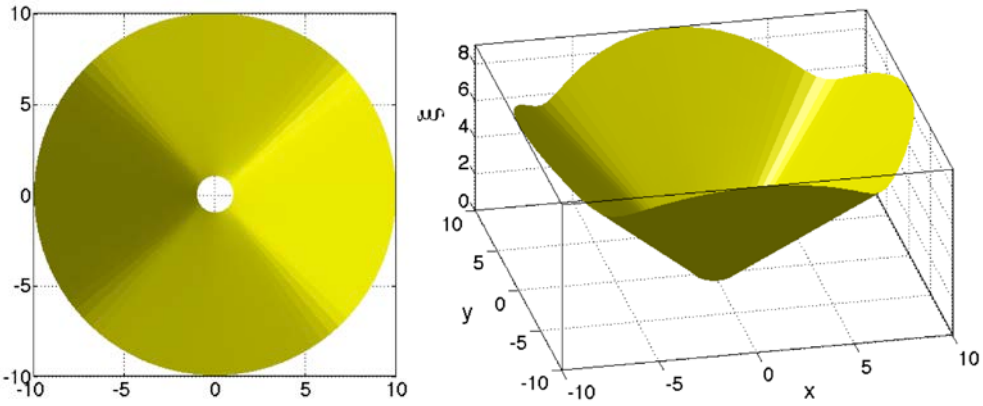

(a) **(b)**

Figure 44 : Flame surface for $\eta = 1$, showing (a) view along the axial flow direction and (b) isometric view from the side, with surface shading indicating the asymmetry of the mean flame surface. The hole in the center corresponds to the centerbody rim. The outer radial extent of the domain is 10 times the centerbody radius.

The azimuthal variation is shown in Figure 45(a). Note that the periodicity is of order $n = 4$. This is also reflected in Figure 45(b) which shows the modal coefficients. Note that modes that are multiples of $n = 4$ have dominant amplitudes compared to the other modes.

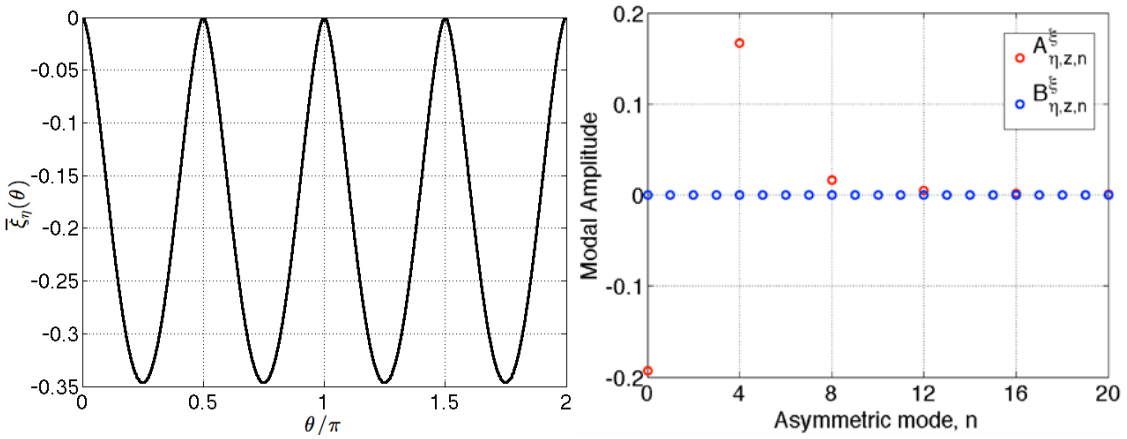

(a) **(b)**

Figure 45 : Square flame with $\eta = 1$ showing (a) Azimuthal variation of the mean flame shape and (b) Asymmetric modal coefficients.

The modal coefficients are given by:

$$A^{\xi}_{\eta,z,n=0}(\tilde{r}) = -0.1931\tilde{r} \qquad A^{\xi}_{\eta,z,n=4}(\tilde{r}) = 0.1667\tilde{r} \qquad A^{\xi}_{\eta,z,n=8}(\tilde{r}) = 0.0167\tilde{r}$$
$$B^{\xi}_{\eta,z,n}(\tilde{r}) \approx 0.0 \tag{5.49}$$

Note that only the $n = 0$ and $n = 4$ modes are significant and all other modes are an order of magnitude lower or more.

For a symmetric mode $m = 0$ in the disturbance field, the global flame response is corrected due to the $n = 0$ mode in the mean non-axisymmetry. The $n = \pm 4$ modes in the mean flow/flame asymmetry interacts with the helical modes $m = \mp 4$ (and its multiples respectively) in the flow disturbance, leading to a finite global flame response. In the example calculations we consider only the $\eta = 1.0; m = 0, 4$ modes.

Figure 46 shows the effect of swirl on the *FTF* amplitude for an axisymmetric flow disturbance (*m*=0). As the value of St_Ω is increased, the *FTF* amplitude shows little difference. However, in comparison with the reference case, the asymmetric mean flame case shows a shift in the interference location. This change is attributed directly to the asymmetry of the mean flame interacting with the swirl transport of wrinkles.

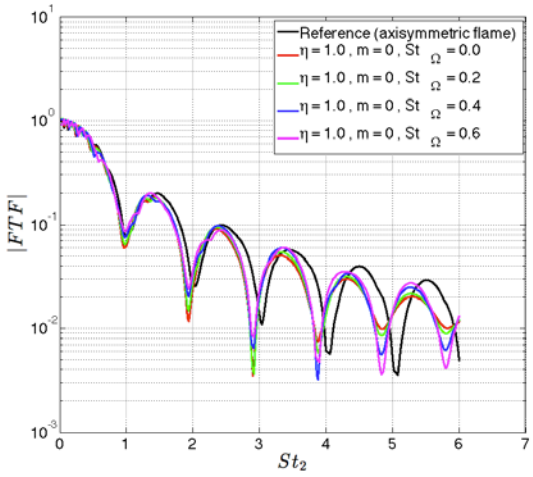

Figure 46 : Comparison of *FTF* amplitudes for a square flame responding to a symmetric flow disturbance, for different values of swirl parameter St_Ω and $k_c = 0.8$. Note that $St_2 = fL_f / U_0 \cos^2 \psi$.

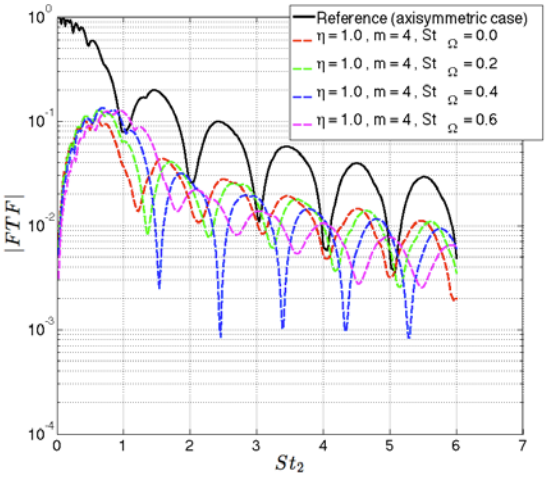

Figure 47 : Comparison of *FTF* amplitudes for a square flame responding to helical flow disturbance of mode *m*=4, for different values of swirl parameter St_Ω and $k_c = 0.8$. Note that $St_2 = fL_f / U_0 \cos^2 \psi$.

In contrast, consider the comparison shown in Figure 47. This figure shows the *FTF* amplitude under the presence of a helical flow disturbance ($m = 4$). As mentioned in earlier chapters, the asymmetric mode helical flow disturbance has no finite *FTF* amplitude for axisymmetric flames. However, the plots clearly show the finite *FTF* amplitudes. As the swirl number is increased, the interference pattern in Strouhal space is changed. Specifically there is a shift in the curves to the left and a decrease in amplitude. Depending upon the Strouhal number in question, the *FTF* amplitude is comparable to

the reference case, indicating the importance of helical modes in controlling global *FTF* of asymmetric mean flames. Finally, the effect of flame angle on the results is shown in Figure 48.

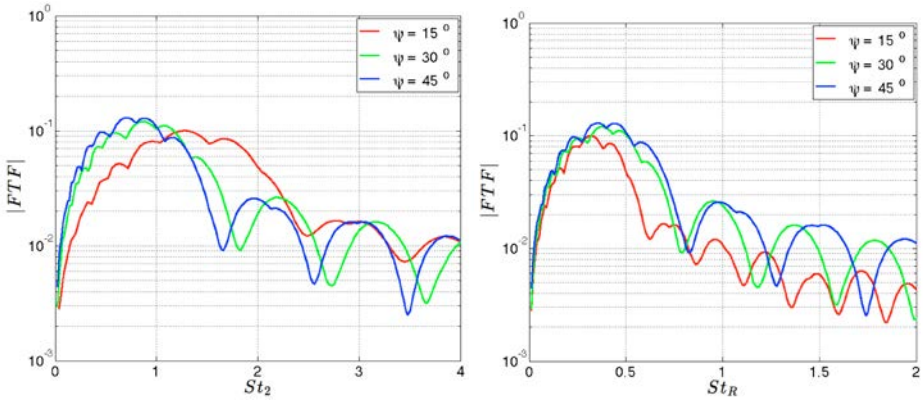

(a) **(b)**

Figure 48 : Effect of flame angle of a square flame on the *FTF* amplitude variation for $St_\Omega = 0.5, \eta = 1, m = 4$ and $k_c = 0.8$. Note that $St_2 = fL_f / U_0 \cos^2 \psi$. (a) Variation with $St_2 = fL_f / U_0 \cos^2 \psi$ and (b) Variation with $St_R = fR/U_0$.

These results clearly indicate the variation of the *FTF* amplitude due to different helical modes in the disturbance field for different control parameters. For low Strouhal number, the symmetric contribution to the *FTF* is dominant and the contribution from the asymmetric helical modes is negligible. However for intermediate Strouhal numbers, these asymmetric helical modes in the flow disturbance lead to significant *FTF* that are comparable to that due to the symmetric flow disturbance. Additionally, the *FTF* interference patterns are affected by the extent of swirl in the mean flow.

Having considered example calculations using the model, we now proceed to applying this model to experimental data in order compare predictions with measured values. This comparison study is divided into two chapters with Chapter 6 focusing on local flame response and Chapter 7 focusing on global flame response.

CHAPTER 6

COMPARISON WITH EXPERIMENTS:

LOCAL FLAME RESPONSE PREDICTIONS

In this chapter we consider the application of the model in capturing local flame response characteristics. A transversely forced, two-dimensional bluff-body stabilized flame is considered since both flame and flow data is available with both spatial and temporal resolution, which facilitates a local flame response comparison. The details of the experimental setup and diagnostics are mentioned in Ref. [150]. The data were obtained by researchers at Energy Research Consultants and analyzed by Benjamin Emerson at the Georgia Tech Combustion Lab. This chapter presents the use of this data to compare measurements and model predictions. The rest of this chapter shall first detail the features of the experiment, the physics of the flow and the flame and finally, the comparison study.

The experiment measured the response of bluff body stabilized flames to transverse acoustic waves, with specific focus on modeling the relationship between the unsteady flow field and flame response. The transverse acoustic motions both directly perturb the flame, and lead to asymmetric rollup of the two shear layers separating from the bluff body. The velocity induced by these concentrated regions of high vorticity leads to synchronized roll-up of the flame sheet and heat release oscillations. A number of studies have shown the significance of the shear layer vortices in exciting instabilities in bluff-body stabilized flames [67, 68, 151, 152]. The general picture that has emerged from these is shown in Figure 49 [153], showing the flame being wrinkled by flow perturbations arising from both vortical disturbances and acoustic waves.

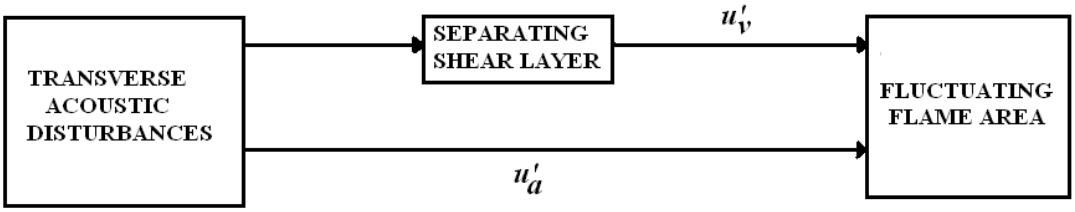

Figure 49 : Physical processes by which acoustic sources lead to flow oscillations that cause flame area (and hence heat release) fluctuations. Reproduced from Ref. [150].

It has generally been hypothesized that the acoustic velocity disturbances are not the leading order cause of flame wrinkling. Rather, it is the vortical disturbances, which are themselves excited by the sound waves that disturb the flame [123]. The results from this study are consistent with this general picture, but we do show that the acoustic velocity disturbances do exert a non-negligible effect on the flame response. Moreover explaining certain features of the measured flame dynamics, such as the short length scale undulations in flame wrinkle amplitude, requires incorporating acoustic velocity field effects. These features shall be shown using the measured data in a later section of this chapter.

6.1 Experimental Data

Before we consider details of the model equations and the comparison study, it is important to understand the key experimental features. The mean flow considered was 50 and 100m/s with a preheating temperature for the mixture ranging from 477-755K. Both uniform and stratified mixtures were considered with stratification in the transverse direction to the main flow.

6.1.1 General Features of the Flame and Flow

This section presents representative characteristics of the measured flame and flow dynamics. Results have been reproduced from Emerson *et al.* [150]. Start with the time

averaged flow field features. Typical axial velocity profiles are shown in Figure 50(a). The figure plots the axial variation of the velocity at transverse locations corresponding to the bluff body symmetry centerline and at an offset of one bluff body diameter. At the offset location, the axial velocity is seen to be roughly uniform. At the centerline, the recirculation zone is evident through the negative velocity which persists for 3 diameters downstream. Further downstream, the centerline velocity monotonically increases. Figure 50(b) also plots the transverse variation of the axial velocity at several axial stations inside and downstream of the recirculation zone. These data show the high gradients in flow velocity near the flow separation point which smooth out with downstream distance, which is a typical feature of the wake behind a bluff-body.

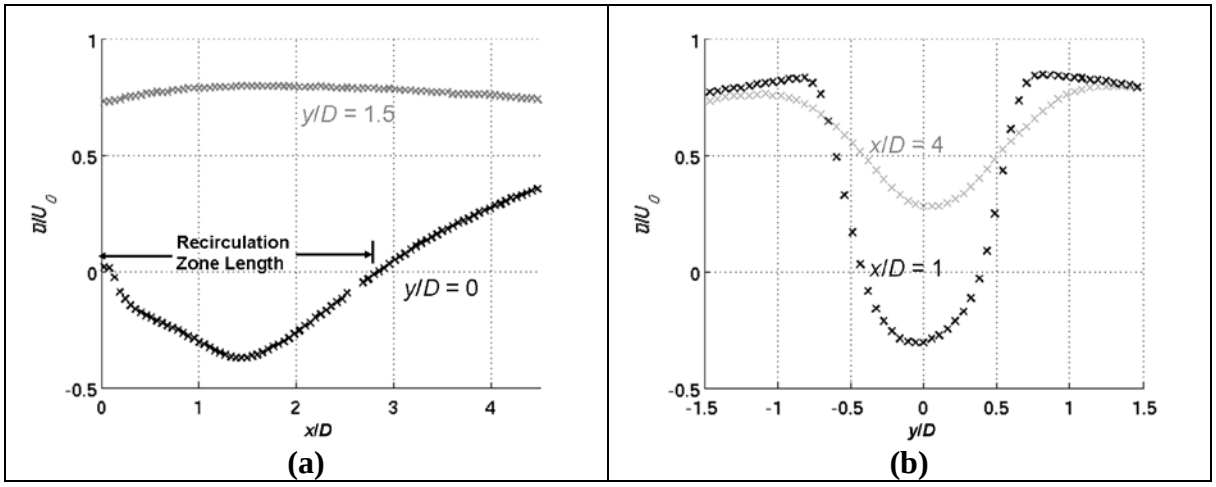

Figure 50 : Variations in the time averaged axial velocity along (a) axial and (b) transverse cuts, for 477K approach flow at 50 m/s, 450Hz out of phase forcing and uniform fuel. Reproduced from Ref. [150].

Figure 51 plots the spatial distribution of the axial and transverse unsteady velocity and Figure 52 provides a cut of the magnitude and phase of the transverse velocity at a fixed transverse position. The figures show large axial velocity fluctuations very close to the bluff-body in the shear layers that decay quickly downstream. The transverse velocity

component dominates over the bulk of the flow, as shown in Figure 51(b). Also, there is an interesting, non-monotonic spatial distribution of the transverse velocity amplitude, particularly evident in Figure 52(a). Finally, the axial phase roll-off in Figure 52(b) indicates the convective nature of the velocity disturbances.

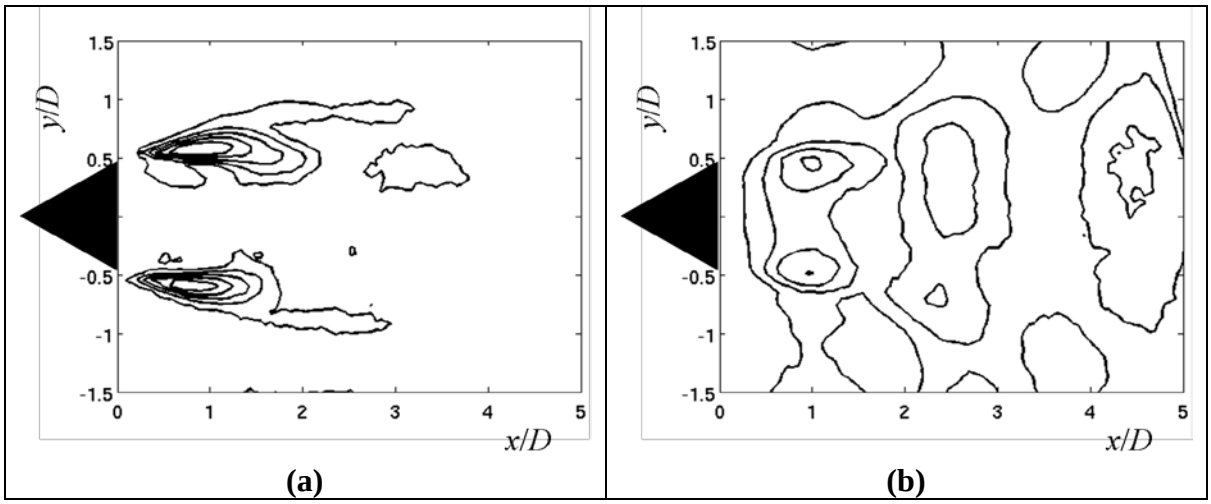

Figure 51 : Contours of unsteady (a) axial velocity magnitude and (b) transverse velocity magnitude for 477K approach flow at 50 m/s, 450Hz out of phase forcing and uniform fuel. The five contour values for $|u'|/U_0$ and $|v'|/U_0$ range evenly from 0.05 to 0.2. Reproduced from Ref. [150].

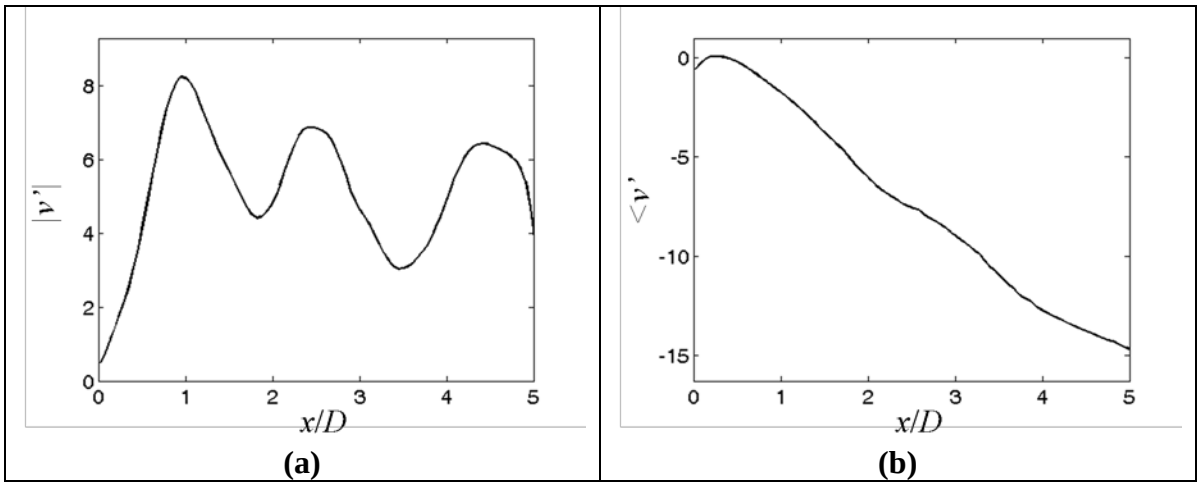

Figure 52 : (a) Magnitude and (b) phase of the unsteady, transverse velocity at y/D = 0.5 for 477K approach flow at 50 m/s, 450Hz out of phase forcing and uniform fuel. Reproduced from Ref. [150].

These points are important from a flame response viewpoint, as understanding the velocity disturbance field is critical to understanding the velocity-coupled flame

response. The PIV data have shown that the transverse acoustic waves result in axial velocity disturbances, as well as an undulating pattern of transverse velocity disturbances. Furthermore, the fact that the velocity disturbances are convecting downstream demonstrates that the disturbance field is not purely acoustic. In fact the acoustic field stimulates the unsteady hydrodynamic response of the flow. The downstream convection of the resulting vortical structures turns out to be largely responsible for the interference patterns in the transverse velocity.

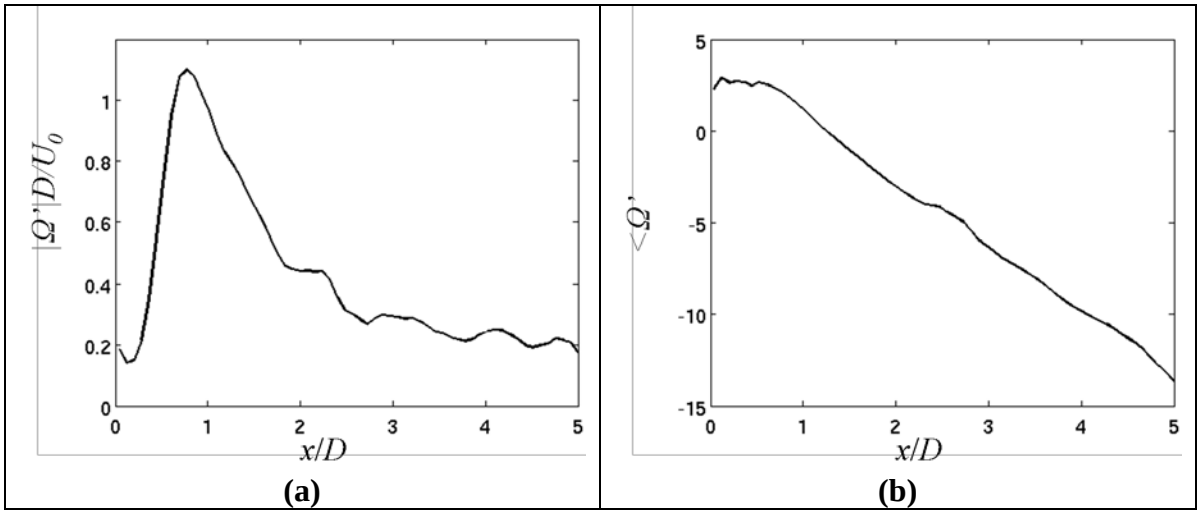

Figure 53 : (a) Magnitude and (b) phase of the unsteady vorticity at y/D = 0.5 for 477K approach flow at 50 m/s, 450Hz out of phase forcing and uniform fuel. Reproduced from Ref. [150].

Further insight into the vortical field features can be obtained from Figure 53, which plots the axial dependence of the unsteady vorticity amplitude and phase at the forcing frequency. Note that vorticity rises and peaks shortly behind the bluff body, and then decays downstream. Also, note the nearly linear decrease of the phase with axial position, which shows that the unsteady vorticity is convecting downstream. Finally, the interference pattern shown in the transverse velocity disturbance in Figure 52(a) is not present in the unsteady vorticity alone. Again, it is the superposition of the vortically

induced velocity field with the acoustic field that causes the interference pattern in the velocity, as shown later in this chapter. We next consider the flame dynamics, using the nomenclature presented in Figure 54.

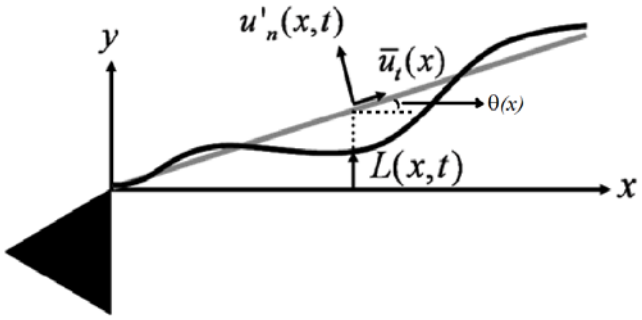

Figure 54 : Co-ordinate system and schematic of a bluff-body stabilized flame.

Figure 55 overlays the ensemble averaged velocity vectors with the ensemble averaged flame position, as well as the up and downstream extent of the flame brush for both velocity data sets. The slower widening of the flame brush in the 100 m/s case is evident from these data. The velocity field along this upstream edge of the flame brush will be used as inputs to the flame response model.

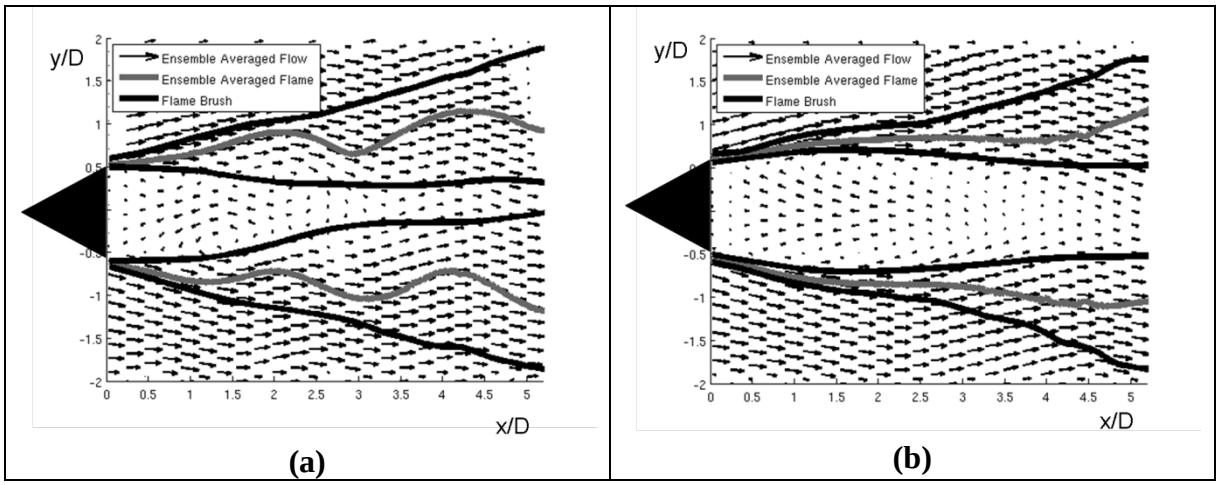

Figure 55 : Sample ensemble averaged fields obtained from PIV with flame brush and phase-averaged flame position overlaid. Conditions shown were (a) 477K approach flow at 50 m/s, 450Hz out of phase forcing and (b) 755K approach flow at 100 m/s, 450 Hz out of phase forcing. Reproduced from Ref. [150].

The much longer convective wavelength of the flame wrinkle in the 100 m/s case than in the 50 m/s case is also clearly evident in Figure 55. This reflects the fact that the length scale of harmonically forced, convecting flow features scales inversely with flow velocity.

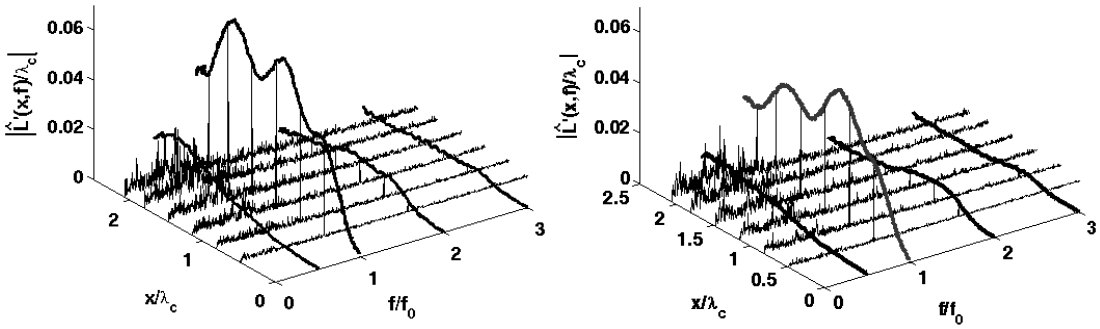

(a) **(b)**

Figure 56 : Spectrum of flame sheet fluctuations at different downstream locations for (a) 50 m/s, 477K and (b) 50 m/s, 644K. The *x*-coordinate corresponds to the downstream axial location, where *x* = 0 corresponds to the bluff body trailing edge. Reproduced from Ref. [150].

Typical spatial characteristics of flame-front position spectra (both amplitude and phase) under the influence of acoustic excitation are shown in Figure 56. The axial coordinate is normalized by the convective wavelength, $\lambda_c = U_0 / f_0$, where U_0 is the characteristic mean flow velocity calculated as:

$$U_0 = \frac{\int_{\text{bluff-body lip}} \bar{u}(x=0, y)dy}{\int_{\text{bluff-body lip}} dy} \tag{6.1}$$

The convective wavelength is the distance that a disturbance propagating at the mean flow velocity travels in one acoustic period. The figures also indicate the spatial envelope of the flame response at $f = f_0$, as well as at several harmonics and the sub-harmonic, $f = f_0/2$, $2f_0$, and $3f_0$. At locations closer to the bluff body (located at

$x/\lambda_c = 0$), the flame responds mainly at the frequency of excitation, f_0. Moving downstream, the response at $f = f_0$ grows, reaches a maximum, and then begins to oscillate. Note that the viewing window is not long enough at these much higher velocities to see the downstream decay of the flame response at f_0 due to nonlinear effects. These data also show the growing magnitude of the sub-harmonic and first harmonic.

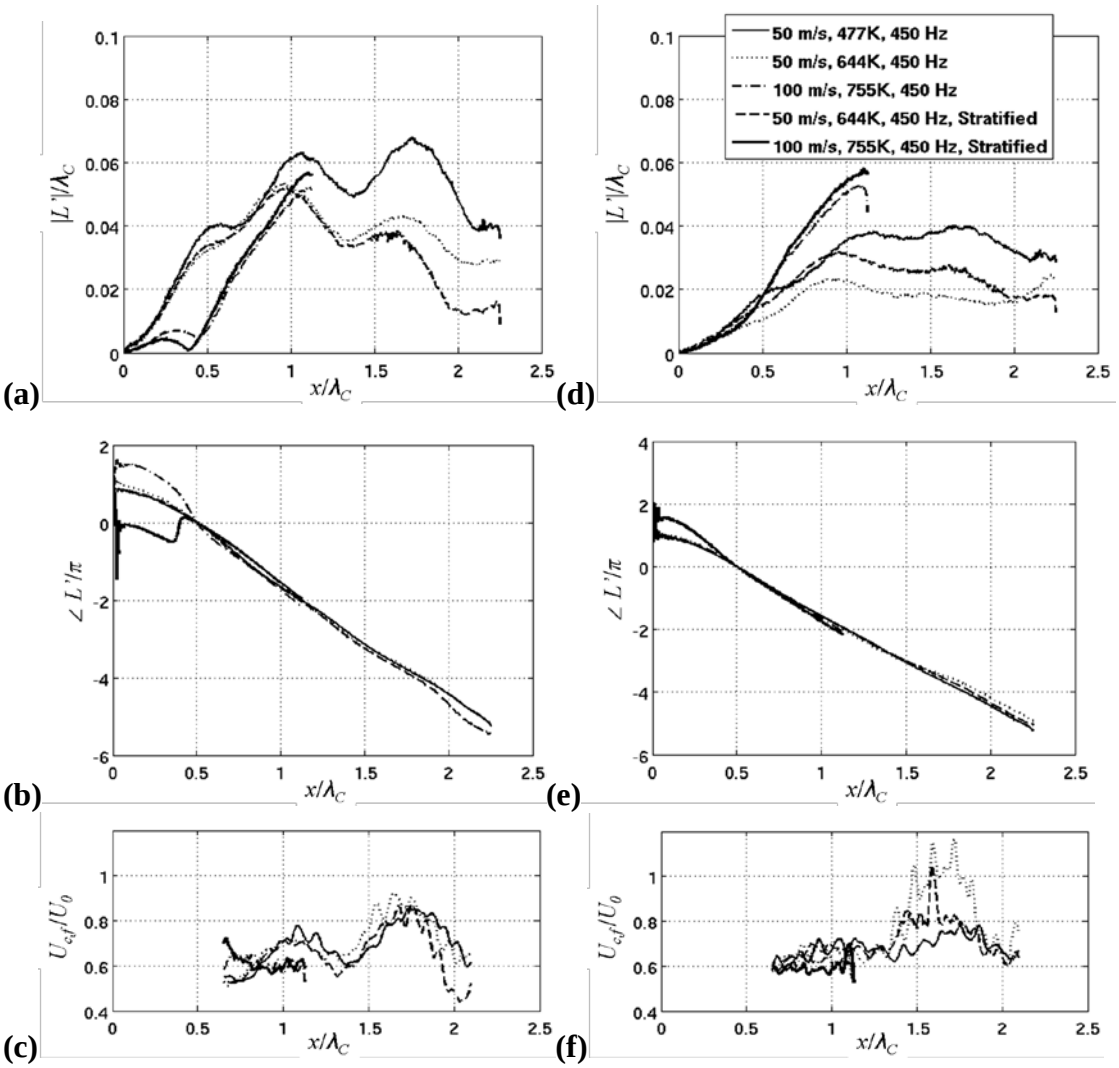

Figure 57 : Overlays of flame response for 450 Hz forcing at all flow conditions, showing (a) gain from out of phase forcing, (b) phase from out of phase forcing, (c) convective velocity from out of phase forcing, (d) gain from in-phase forcing, (e) phase from in-phase forcing, (f) convective velocity from in-phase forcing. Error bars not shown for clarity on this plot. Reproduced from Ref. [150].

Figure 57(a) and Figure 57(b) overlay a number of gain plots at different velocities, inlet temperatures, and speaker excitation phasing at the forcing frequency. Most of these flame response data suggest an interference pattern, reflected in the ripple in the amplitude plots, discussed later in this chapter. Most curves show similar qualitative behavior for both amplitude and phase. In addition, the 100 m/s and 755K preheating case show a near-field behavior that is distinct from all the other cases, as well as previously reported trends in the literature. Specifically, the flame response amplitude rises with downstream distance, peaks, falls to nearly zero at about half a convective wavelength downstream, and then grows monotonically. As shown later in this chapter, these are a manifestation of the simultaneous excitation of the flame by acoustic and vortical velocity disturbances, which are of comparable magnitudes near the bluff body. Because these two velocity disturbance sources have very different axial phase characteristics, they lead to a "node" in the flame response [154].

We next turn to the axial character of the phase. Figure 57(b) and Figure 57(e) overlay the corresponding axial dependence of the flame edges. From this plot it is clear that all the phase results have, for the most part, a roughly constant axial phase slope. This suggests an approximately constant convective velocity for flame wrinkle disturbances. An effective propagation speed of the *flame wrinkle*, which should not be confused with the propagation speed of the *vortical disturbance* or *mean flow*, can be computed from the relation $U_{c,f} = 2\pi f_0 \Big/ \left[d\left(\angle \hat{L}' \right) \Big/ dx \right]$. These plots are shown in Figure 57(c) and Figure 57(f) showing that the flame wrinkles move downstream at a velocity of roughly $0.7U_0$.

Several observations from this data set should be made. First, it reinforces the notion that transverse flow excitation leads to excitation of a convecting train of vortical flow

features. Indeed, while acoustic flow oscillations may be ultimately responsible for the flow oscillations, it is the vortices that they excite that dominate the flow field. Next, these data show that the flow oscillations excite wrinkles on the flame that convect downstream, with a magnitude that varies spatially. Specifically, the wrinkles start with low amplitude and grow with downstream distance before reaching a maximum. The wrinkle amplitude can then be modulated with downstream distance as it decays. Very significantly, these flame dynamics results show important similarities to the flame dynamics observed in much lower velocity, even laminar cases and in flames with much higher density ratios. This shows that while critical flow dynamics may change strongly with flow velocity and flame density ratio, that the flame response features do not. In the next section, we focus on the specifics of the velocity at the flame location.

6.1.2 Flow Disturbances at the Flame

Of particular interest to solving the flame dynamics equations are the disturbance velocity values just upstream of the flame front. As such, this section particularly focuses on the velocity disturbance features along the upstream edge of the flame brush indicated in Figure 55 (note that measurements of the fluctuating velocity at the time averaged flame position biases the upstream disturbance velocity estimate, because the time averaged flame position lies in locations that lie in the hot products at some time instants). Specifically, we determined the velocity at each phase of the cycle directly from its value just upstream of the ensemble averaged flame from the measurements, i.e., $u_n(x, y = \bar{L}(x) + L'(x,t), t)$.

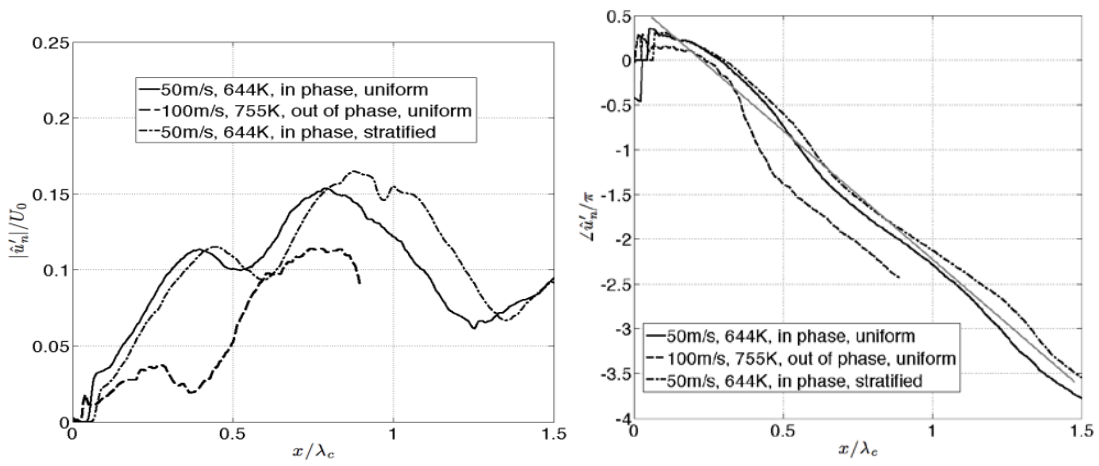

(a) **(b)**

Figure 58 : Normal component of velocity fluctuations as experienced by the flame (input to the linear model) from PIV measurement showing (a) magnitude and (b) phase, grey straight line indicates a phase roll-off at $U_{c,v}/U_0$ = 0.67.

Typical results showing the axial dependence of the non-dimensional normal velocity disturbance, $\hat{u}_n'/U_0$ are shown in Figure 58. The velocity field magnitude is quite small near the flameholder and grows with downstream distance. This presumably reflects the amplification of the disturbances in the convectively unstable shear layer. Farther downstream, the velocity field magnitude varies in a non-monotonic manner, as previously discussed in the context of Figure 52. These undulations in magnitude suggest interference effects. The phase rolls off monotonically at a nearly constant slope. For reference, a line is drawn in corresponding to the phase variation of a disturbance propagating at a constant velocity of $U_{c,v}/U_0 = 0.67$.

These interference patterns in velocity magnitude appear to be a manifestation of the superposition of acoustic and vortical velocity disturbances, which have substantially different axial phase speeds. To demonstrate, consider the sum of the following two disturbances, one with uniform axial phase and the second associated with a disturbance convecting axially at a velocity of $U_{c,v}$:

$$\frac{u_n'}{U_o} = \varepsilon_a \cos\left(2\pi f_o t\right) + \varepsilon_v \cos\left(2\pi f_o\left(t - \frac{x}{U_{c,v}}\right) + \psi_v\right) \tag{6.2}$$

Using trigonometric identities, this can be written as:

$$\frac{u_n'}{U_o} = \mathscr{A}(x)\cos\left(2\pi f_o t + \varphi(x)\right)$$

where

$$\mathscr{A}(x) = \sqrt{\varepsilon_a^2 + \varepsilon_v^2 + 2\varepsilon_a\varepsilon_v \cos\left(\psi_v - 2\pi f_0 \, x/U_{c,v}\right)} \tag{6.3}$$

$$\varphi(x) = \tan^{-1}\left[\frac{\varepsilon_v \sin\left(\psi_v - 2\pi f_0 \, x/U_{c,v}\right)}{\varepsilon_a + \varepsilon_v \cos\left(\psi_v - 2\pi f_0 \, x/U_{c,v}\right)}\right]$$

Thus, the velocity magnitude varies spatially as $\mathscr{A}(x)$. The interference wavelength is given by $U_{c,v}/f_0$ and the depth of modulation in amplitude (peak to peak) is $\left(\varepsilon_a + \varepsilon_v\right) - \left|\varepsilon_a - \varepsilon_v\right|$. The local maxima are located at:

$$\frac{x}{\lambda_c} = \frac{U_{c,v}}{U_o}\left|\frac{\psi_v}{2\pi} - n\right| \tag{6.4}$$

where $n \geq 0$ are integers. Following this idea, we can fit the velocity data to the more general form shown in Eq.(6.5), which allows for spatial variation in amplitude of the acoustic and vortical disturbance.

$$\frac{\hat{u}_n'}{U_o} = \varepsilon_a(x) + \varepsilon_v(x)\exp\left(i\psi_v - i2\pi f_o \frac{x}{U_{c,v}}\right) \tag{6.5}$$

We next present two examples from the 50 m/s data where we fit this expression to the velocity data. The requisite parameters were determined in the following manner: The phase velocity $U_{c,v}$ value was extracted from the measured axial phase variation of the unsteady vorticity. The phase ψ_v was determined from the location of the interference

maxima/minima, following Eq.(6.4). The amplitudes ε_a and ε_v were then manually determined in order to yield the best fit.

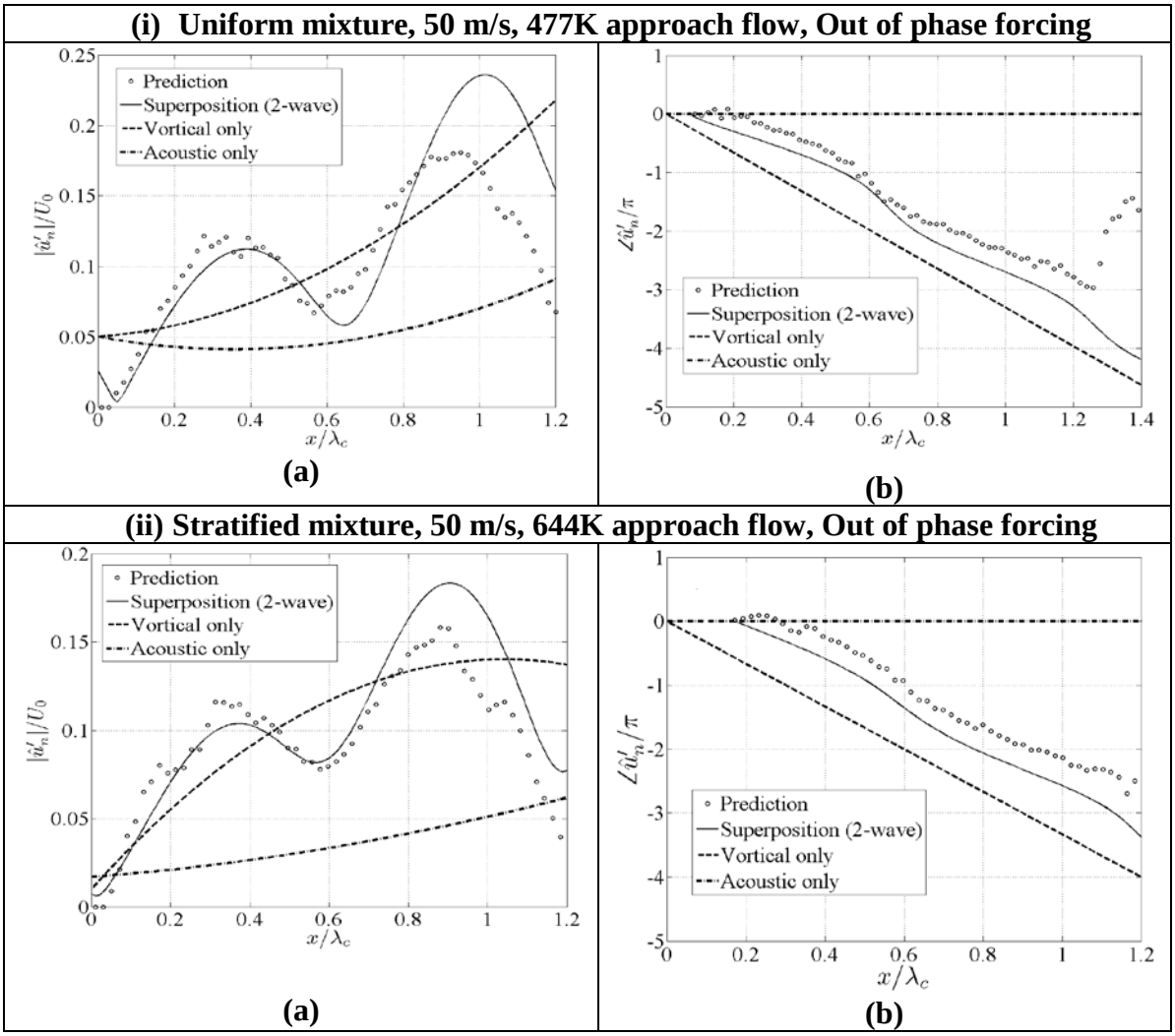

Figure 59 : Velocity decomposition based fitting of predicted velocity field for cases: (i) Uniform mixture, 50 m/s, 477K approach flow, Out of phase forcing and (ii) Stratified mixture, 50 m/s, 644K approach flow, Out of phase forcing. Comparisons for (a) magnitude and (b) phase.

Figure 59 illustrates the actual predicted velocity field, as well as the fit values of ε_a and ε_v. The prediction methodology is described later in this chapter. Note how the acoustic and vortical disturbance fits have similar magnitudes near the bluff body, but that the vortical disturbance is roughly twice the acoustic farther downstream. Thus, the

vortical component dictates the overall magnitude of the velocity fluctuations, but the acoustic component is needed to understand the modulation in amplitude. Moreover, although the vortical disturbances are dominant, the acoustic disturbances are not negligible. We will return to this point to interpret the similar presence of undulations in the flame gain curves.

Thus, this decomposition validates the general idea put forth in the introduction that the dominant source of flow fluctuations at the excitation comes from the convecting vortical field. While these vortical oscillations are excited by the acoustic field, which serves as the "clock", the convectively unstable shear layer responds strongly to this excitation and leads to synchronized rollup of the shear layer at this frequency.

6.2 Model Equations

In this section, we derive the model equations that are used for the comparison study. Using the coordinate system described in Figure 54, the following transformation is applied to the *G*-equation (Eq.(3.4)):

$$G(x,y,t) = L(x,t) - y \tag{6.6}$$

Hence, substituting in Eq.(3.4), we have:

$$\frac{\partial L}{\partial t} + u\frac{\partial L}{\partial x} - v = s_L\sqrt{\left(\frac{\partial L}{\partial x}\right)^2 + 1} \tag{6.7}$$

This equation describes the simultaneous wrinkling of the flame by broadband turbulent fluctuations and harmonic oscillations. In order to focus on the flame response at the forcing frequency, this equation needs to be ensemble averaged. First, each fluctuating variable is expanded in a triple decomposition; e.g., for the axial velocity:

$$u = \bar{u} + u' + \tilde{u} \tag{6.8}$$

where $\bar{u}$ denotes the time average, $u' = \langle u - \bar{u} \rangle$, the fluctuating ensemble average and $\tilde{u}$ denotes the randomly oscillating component, whose time and ensemble averages are both zero, i.e. $\overline{(\tilde{u})} = \langle \tilde{u} \rangle = 0$. Applying this to Eq.(6.7), we have:

$$\frac{\partial \langle L \rangle}{\partial t} + \langle u \rangle \frac{\partial \langle L \rangle}{\partial x} - \langle v \rangle = s_T \sqrt{\left(\frac{\partial \langle L \rangle}{\partial x} \right)^2 + 1} \tag{6.9}$$

This equation is essentially *a* definition of the turbulent flame speed, s_T [155]. The reader is referred to several focused treatments of this subject for further discussion on this approach and the relationship of this turbulent flame speed to that obtained in the absence of harmonic forcing [127, 156, 157].

As discussed earlier, acoustic disturbances (u_a') lead to the synchronized rollup of the separating shear layer into concentrated vortices. These vortical fluctuations (u_v') propagate in the flow direction at a velocity that is proportional to the mean flow velocity. The associated flame response is then influenced by this disturbance field through three parameters: (1) the spatial amplitude of the respective disturbances, $\varepsilon_a = u_a'/U_0$ and $\varepsilon_v = u_v'/U_0$, (2) the frequency of the disturbance, f_0, and (3) the velocity of the disturbances, *c* and $U_{c,v}$. There are two additional parameters that influence the flame response and are directly associated with the flame itself. The first is the angle of the flame front with respect to the mean velocity, θ. The second parameter is the response of the flame attachment point to the excitation. Based upon the visualization results obtained, it has been assumed that the flame remains firmly attached to the bluff body separation point and does not oscillate in response to the excitation, i.e., $L'(x = 0, t) = 0$.

Prior work has shown that the flame dynamics are linear in disturbance amplitude near the attachment point and that nonlinear effects grow in prominence with increasing amplitude of excitation and downstream distance [158]. These nonlinear effects are due to "kinematic restoration" [159], and reflect the propagation of the flame normal to itself at the local burning velocity. In the prior study by Shanbhogue *et al.* [158] with similar viewing windows using flow velocities in the 2-5 m/s range, nonlinear effects had sufficient time to accumulate and had to be accounted. While nonlinear effects are certainly important at axial locations on the flame that are sufficiently far downstream, they are negligible over the residence times for which the flame wrinkles are in the viewing window. The non-linear contributions to the dynamics are compared with the linear contributions later in this chapter, to illustrate their relative roles.

The linearized flame dynamics can be determined by expanding the ensemble averaged velocity into its time average and fluctuating component:

$$\begin{aligned} \langle u(x,t)\rangle &= \overline{u}(x) + u'(x,t) \\ \langle v(x,t)\rangle &= \overline{v}(x) + v'(x,t) \\ \langle L(x,t)\rangle &= \overline{L}(x) + L'(x,t) \end{aligned} \tag{6.10}$$

Using this decomposition in Eq.(6.9), and linearizing, we obtain the following equations for the mean and fluctuating components:

$$\overline{u}(x)\sin\theta(x) - \overline{v}(x)\cos\theta(x) = s_T(x) \tag{6.11}$$

$$\frac{\partial L'(x,t)}{\partial t} + \overline{u}_t(x)\cos\theta(x)\frac{\partial L'(x,t)}{\partial x} = \frac{u_n'(x,t)}{\cos\theta(x)} \tag{6.12}$$

Where it has been assumed that s_T is not varying in time (see discussion and limitations of this assumption in Shin and Lieuwen [155]). Fuel/air ratio stratification effects are

implicitly incorporated in the analysis through the measured time averaged quantities in these two equations, such as the local flame angle $\theta(x)$.

The following definitions are used:

$$\frac{d\overline{L}(x)}{dx} = \tan\theta(x) \tag{6.13}$$

$$\overline{u}_t(x) = \overline{u}(x)\cos\theta(x) + \overline{v}(x)\sin\theta(x) \tag{6.14}$$

$$u_n'(x,t) \equiv \left[v(x, y = \langle L(x,t) \rangle, t)\cos\theta(x,t) - u(x, y = \langle L(x,t) \rangle, t)\sin\theta(x,t) \right]' \tag{6.15}$$

These terms u_n', $\overline{u}_t$, θ, and $L(x,t)$ are also depicted in Figure 54. The time averaged equation, shown in Eq.(6.11), states that the turbulent flame speed s_T matches the local normal component of the mean velocity field. The unsteady equation, shown in Eq.(6.12) , describes axial disturbance convection on the left side and the excitation due to disturbances on the right. This operator shows that wrinkles on the flame propagate at the tangential mean velocity $\overline{u}_t$, shown in Eq.(6.14). The wrinkles are generated by the normal component of the fluctuating velocity u_n' shown in Eq.(6.15) . The $\cos\theta$ term is an artifact of the coordinate system, and is the angle between the chosen coordinate system and a local flame-fixed coordinate system.

Since the analysis is performed for data at the forcing frequency, it is useful to consider the equations in the Fourier domain. The Fourier transform of Eq.(6.12) is given by:

$$i2\pi\left(\frac{\hat{L}'\left(x/\lambda_c, f_0\right)}{\lambda_c}\right) + \frac{\overline{u}_t}{U_0}\cos\theta\frac{d}{d\left(x/\lambda_c\right)}\left(\frac{\hat{L}'\left(x/\lambda_c, f_0\right)}{\lambda_c}\right) = \frac{1}{\cos\theta}\left(\frac{\hat{u}_n'}{U_0}\right) \tag{6.16}$$

where the over-hats "^", denote the corresponding complex quantity in the frequency domain, and U_0 is calculated using Eq.(6.1). This equation is a two-dimensional version

of Eq.(3.16), and will serve as the key tool for comparison of measured and predicted flame response characteristics.

There are two ways in which data and measurements can be compared using this equation. First, the measured flame edge data, $\hat{L}'(x/\lambda_c, f_0)$, can be used as an input to the left side of Eq.(6.16) to predict a value for the normal velocity component, $\hat{u}_n'$.

$$\overbrace{\left(\frac{\hat{u}_n'}{U_0}\right)}^{predicted} = i2\pi\cos\theta \underbrace{\left(\frac{\hat{L}'}{\lambda_c}\right)}_{measured} + \underbrace{\frac{\overline{u}_t}{U_o}}_{measured}\cos^2\theta \underbrace{\frac{d}{d\left(x/\lambda_c\right)}\left(\frac{\hat{L}'}{\lambda_c}\right)}_{measured} \tag{6.17}$$

While from a practical point of view, prediction of flame position from a known (or assumed) velocity field is the more interesting scenario, this approach of predicting the velocity from the measured flame position is more useful for model validation purposes. The reason for this is that Eq.(6.17) directly relates the *local* flame position and slope to the *local* velocity field. Thus, errors/uncertainties in the flame position and velocity field at other locations do not corrupt predictions/data at the point of comparison.

Alternatively, the measured fluctuating velocity field is used as an input on the right side of Eq.(6.16) to predict the flame edge response. This is given by:

$$\overbrace{\left(\frac{\hat{L}'}{\lambda_c}\right)}^{predicted} = \exp\left(-\int \underbrace{\frac{i2\pi}{\left(\frac{\overline{u}_t(x)}{U_0}\right)\cos\theta(x)}}_{measured} d\left(\frac{x}{\lambda_c}\right)\right) \int_{s=0}^{s=\frac{x}{\lambda_c}} \left[\underbrace{\frac{\hat{u}_n'(s)}{\overline{u}_t(s)\cos^2\theta(s)}}_{measured} \exp\left(\int \underbrace{\frac{i2\pi ds}{\left(\frac{\overline{u}_t}{U_0}\right)\cos\theta}}_{measured}\right)\right] ds \tag{6.18}$$

This is the more interesting comparison because generally it is the flame position which must be calculated. However, from a validation point of view, this approach is problematic because the predicted flame position is a convolution of velocity field

disturbances at all upstream positions. Thus, errors in measurement at one point (i.e., near the bluff body) corrupt the predicted flame position not only at that point, but also at all downstream positions.

6.3 Comparison of Measurements and Model

This section presents comparisons of the measured flame and flow field characteristics using the linear flame dynamics model. Before we proceed to discussing the comaprisons, an important point regarding the experimental data and its usage must be mentioned. The measurements for both velocity and flame edge are prone to large errors close to the edge of their respective image boundaries at the edge of the laser sheet. Where the flame edge data is used as input, the predictions use only local data and the velocity field prediction is only shown farther downstream. Where the velocity field is used as an input, the flame edge prediction is initiated at the bluff-body. The velocity data in the region $x/\lambda_c<0.1$, is extrapolated from points close to $x/\lambda_c>0.1$ based on a polynomial fit of their behavior. These extrapolated values are not used for the *local* comparison in the velocity field validation study.

6.3.1 Application of Linear Model

Recall that either velocity or flame position can be used as model inputs. These two approaches present different perspectives on the same measured data sets and comparisons are presented using both in Figure 60 and Figure 61. Subplots (a) and (b) in each figure use the flame edge as input and the velocity field magnitude and phase is the prediction. Subplots (c) and (d) use the velocity field as the input to predict the gain/phase of the flame.

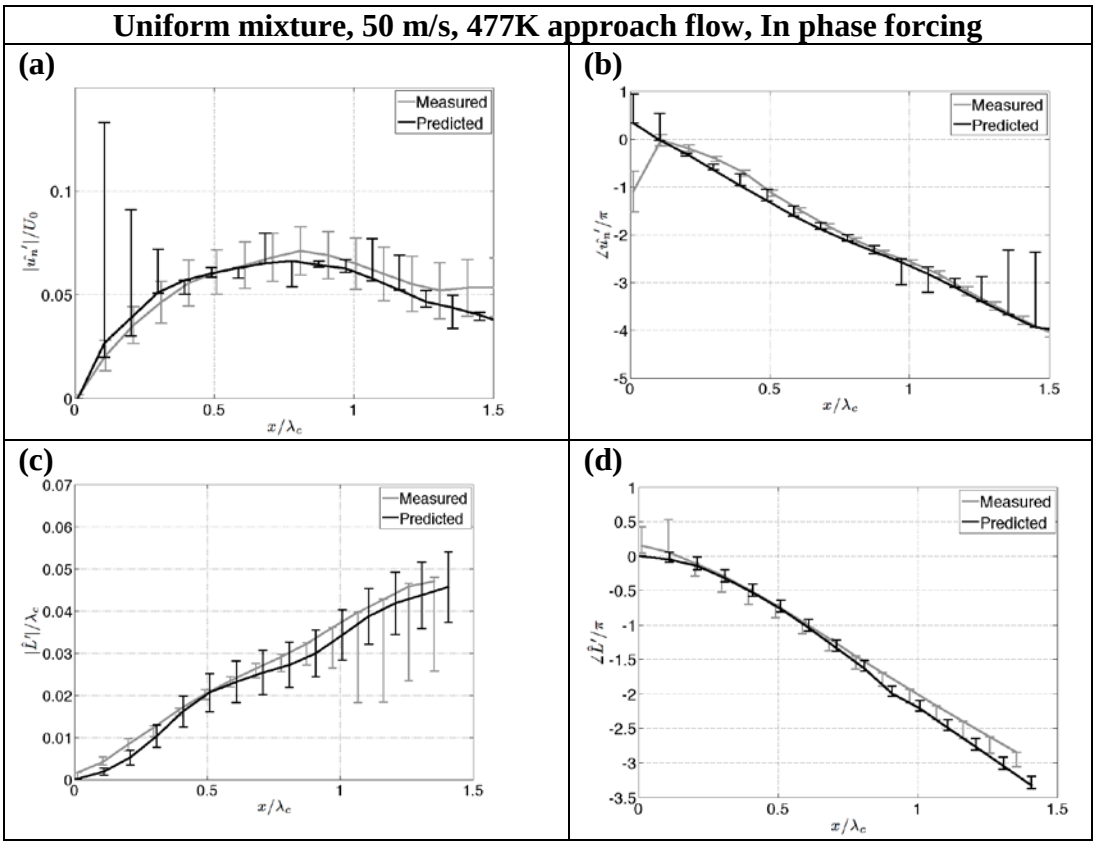

Figure 60 : Velocity validation study for Uniform mixture, 50 m/s, 477K approach flow, In phase forcing, using Eq.(6.17) with flame edge as input : (a) amplitude comparison, (b) corresponding phase comparison; Flame edge validation study using Eq.(6.18) with velocity as input : (c) amplitude comparison, (d) corresponding phase comparison.

Start with Figure 60, which corresponds to a spatially uniform reactant mixture, in-phase forcing case. Uncertainty bars are also indicated for both the direct measurement of velocity or flame position, as well as the propagated uncertainty that, for example, the measured flame position leads to for predicted velocity, and vice-versa. The figure shows the monotonically growing uncertainty in measured flame position, due to growing three dimensional effects. Note the one spot with large propagated uncertainty in the predicted unsteady velocity field occurs near the flame holder (a). This large uncertainty is due to the low amplitude of flame wrinkling (c) near the bluff body. As shown in Shanbhogue *et al.* [158], the slope of this magnitude curve in (c) is directly proportional

to the fluctuating velocity in (a). As such, the small uncertainty in flame position leads to a large uncertainty in slope, $d\left|\hat{L}'\right|/dx$, and, therefore, velocity near the flame holder.

Comparing the predictions and measurements shows that the agreement is very good. For example, the key features of the disturbance velocity field, such as its general spatial character, and the location and magnitude of the peak, are well predicted in Figure 60(a). Similarly, the velocity phase roll-off is captured very well. The corresponding flame features in (c) and (d) are also well captured. In this particular case, the flame wrinkling amplitude monotonically rises with downstream distance. Both this general feature, as well as the slope of the rise is well captured by the predicted result. Similarly, the monotonic rolloff in phase of flame wrinkling, as well as its slope, is well captured.

Consider next Figure 61, which corresponds to a spatially uniform reactant mixture, out of phase forcing case. The qualitative agreement is similarly good in this case, although there are larger quantitative differences observed downstream. For example, the general spatial character of the disturbance velocity amplitude and phase are well predicted. The quantitative agreement is quite good over the first half of the measurement window as well, although downstream of the velocity amplitude peak the results show a growing quantitative difference in phase, although the amplitude agreement continues to be good. Similarly, the corresponding flame magnitude and phase features in (c) and (d) are also well captured qualitatively. Similar to the velocity phase, the flame magnitude results show a growing difference between predictions downstream of the velocity amplitude peak. The monotonic rolloff in phase of flame wrinkling as well as its slope is well captured. Similar comparisons were performed at all other conditions as well and are shown in Appendix C.

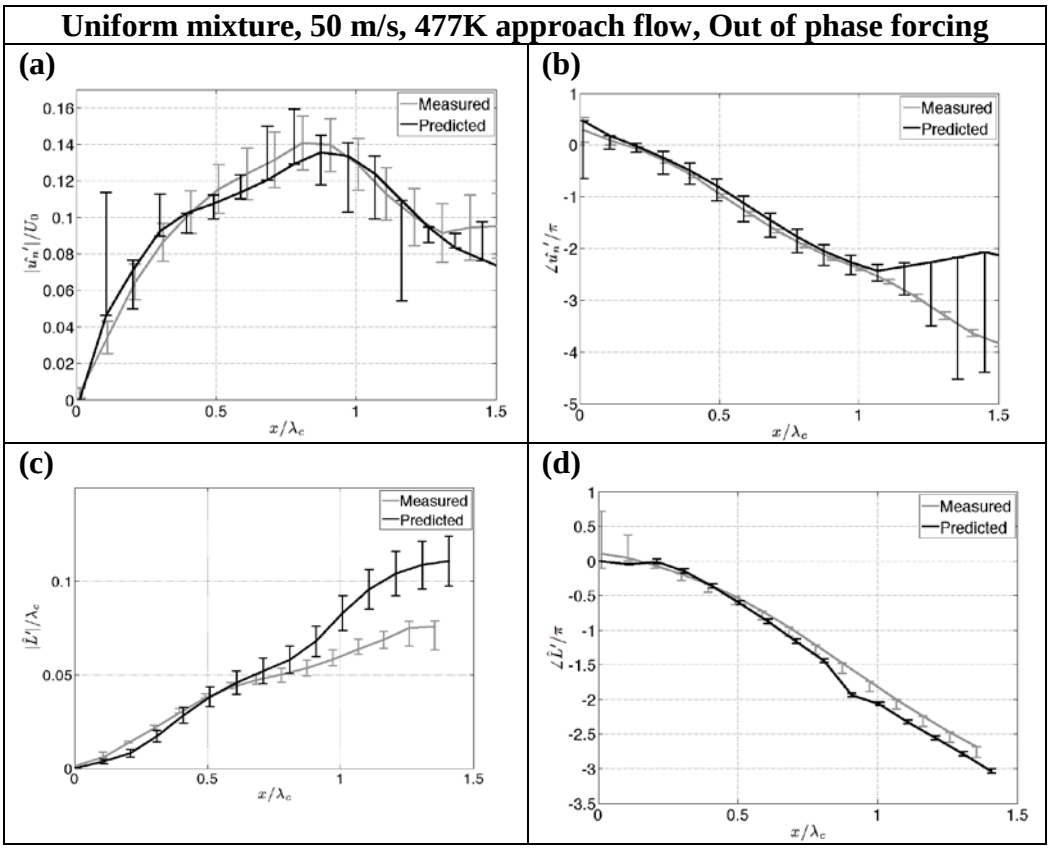

Figure 61 : Velocity validation study for Uniform mixture, 50 m/s, 477K approach flow, Out of phase forcing, using Eq.(6.17) with flame edge as input : (a) amplitude comparison, (b) corresponding phase comparison; Flame edge validation study using Eq.(6.18) with velocity as input : (c) amplitude comparison, (d) corresponding phase comparison.

6.3.2 Flame Response Content

The decomposition of the flow field into acoustic and vortical components was presented in Section 6.1.2. We now show how this velocity field decomposition provides a useful interpretation of the flame response and its sensitivity to the axial phase characteristics of the disturbance field. This is obtained by calculating the flame wrinkling induced by the calculated acoustic and vortical components.

Figure 62 plots the actual measured flame data, the flame wrinkling associated with the 2-wave fit, and then the contributions from the acoustic and vortical component. Mirroring the discussion of the velocity field, these results show that the undulation in the

gain is due to the acoustic component, but that the majority of the flame response can be understood by simply considering the vortical component. The phase of the flame response is modeled accurately and is seen to be roughly the same as that of the vortical component. The acoustic contribution creates a short length scale interference pattern due to its large phase speed, while the vortical contribution creates a much larger scale pattern due to a phase speed that is roughly of the order of the mean flow velocity.

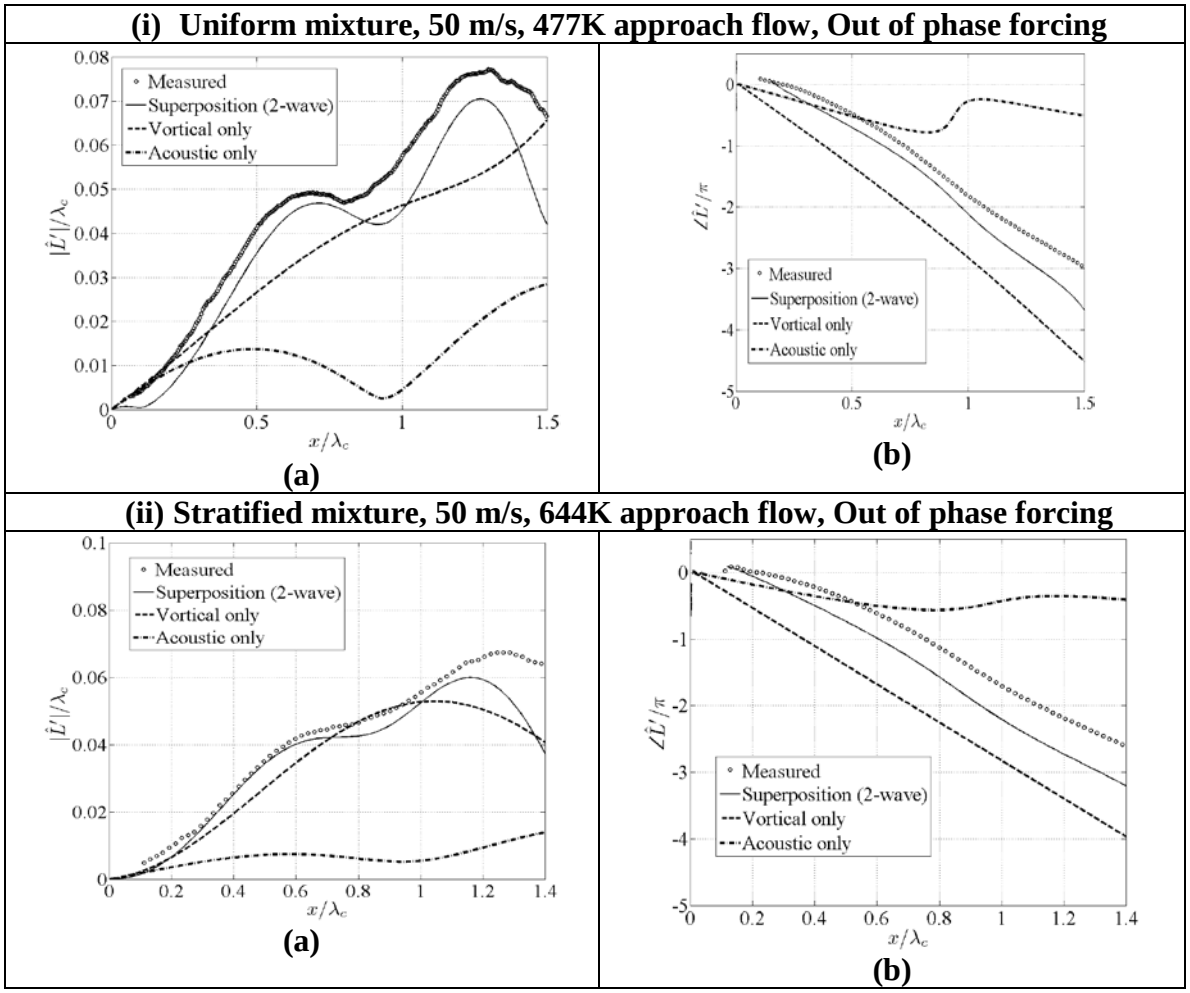

Figure 62 : Flame response prediction from analytical solution of Eq.(6.18) for cases shown as (i) Uniform mixture, 50 m/s, 477K approach flow, Out of phase forcing and (ii) Stratified mixture, 50 m/s, 644K approach flow, Out of phase forcing, comparing (a) amplitude and (b) phase.

In order to explain the interference "wavelength" of wrinkles on the flame, consider a velocity disturbance field of the form:

$$\frac{\hat{u}_n'}{U_0} = \varepsilon \exp\left(-\frac{i2\pi\left(x/\lambda_c\right)}{\left(U_{c,v}/U_0\right)} \right) \tag{6.19}$$

Where $\lambda_c = U_0/f$ is the convective wavelength and $U_{c,v}$ is the phase speed of the disturbance. The flame response to this disturbance, in a constant mean flow field U_0 (flame angle θ is constant) is given by (using Eq.(6.18)):

$$\frac{\hat{L}'(x)}{\lambda_c} = \frac{\varepsilon \sin\left(\pi\left[1-\cos^2\theta\left(\frac{U_0}{U_{c,v}} \right) \right] \frac{x}{\lambda_c \cos^2\theta} \right)}{\pi\left[1-\cos^2\theta\left(\frac{U_0}{U_{c,v}} \right) \right]} \exp\left(-i\pi \frac{x}{\lambda_c} \left\{ \frac{1}{\left(\frac{U_0}{U_{c,v}} \right)} + \frac{1}{\cos^2\theta} \right\} \right) \tag{6.20}$$

From this expression, we can see that the flame wrinkling wavelength, is given by:

$$\frac{\lambda_{flame}}{\lambda_c} = 2\left\{ \frac{1}{\cos^2\theta} - \frac{1}{\left(U_{c,v}/U_0\right)} \right\}^{-1} \tag{6.21}$$

Consider an acoustic disturbance, where $U_{c,v} \sim O(c)$. In the case where $M = U_0/c \ll 1$, we have $\lambda_{flame} \approx \lambda_c$. In contrast, a vortical disturbance, where $U_{c,v} \sim O\left(U_0\right)$ leads to a much longer wavelength; e.g., $U_{c,v} = 0.67U_0$ (mentioned earlier). Both of these points are clearly evident in Figure 62. This result - a broad peak with a length scale encompassing several convective wavelengths, which has shorter length scale undulations superposed upon it, provides insight into data from a number of other studies in the literature. To illustrate, Figure 63 reproduces data from experiments by Shanbhogue *et al.* [158, 160] at lower flow velocities, showing similar features, again suggesting that the wrinkles are due to a smaller amplitude, fast propagating acoustic field superposed upon a larger amplitude vortical disturbance field. For those studies, the mean velocity was an order of

magnitude smaller than used here, leading to an even larger disparity in wrinkling wavelengths on the flame.

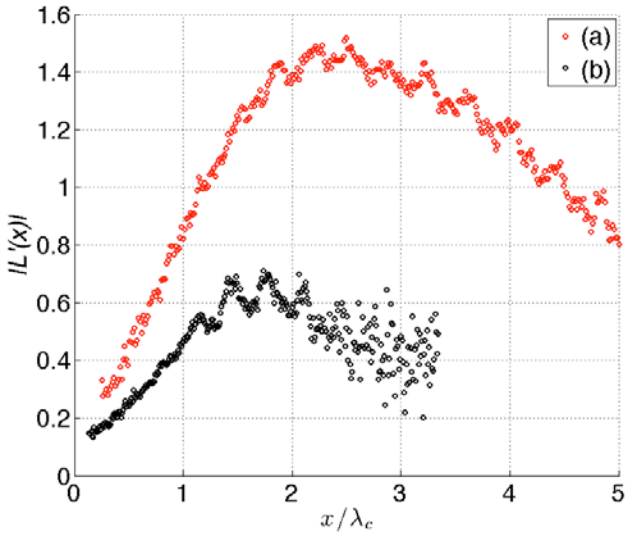

Figure 63 : Experimental data reproduced from Refs. [158, 160], showing $|L'(x)|$ for cases where (a) D = 12.7mm, f_0 = 150Hz, U_0 = 2.27m/s, u' = 0.021m/s; (b) D = 9.52mm, f_0 = 150Hz, U_0 = 3.37m/s, u' = 0.016m/s, φ = 0.77.

The interference effects which are explicitly shown in Eq.(6.20), also lead to substantially different sensitivities of the flame response to slight variations in axial phase characteristics of these two disturbance modes. Specifically, a change or uncertainty in the phase speed, $\Delta U_{c,v}$, leads to a change/ uncertainty in the flame response of:

$$\frac{\left(\Delta\hat{L}'/\hat{L}'\right)}{\left(\Delta U_{c,v}/U_{c,v}\right)} \sim -\frac{1}{\left(1-\left(U_0/U_{c,v}\right)\cos^2\theta\right)}\left(\frac{U_0\cos^2\theta}{U_{c,v}}\right) \tag{6.22}$$

In the case of a fast propagating acoustic disturbance (low Mach number), the change/uncertainty in the flame response is small, since it is directly proportional to the Mach Number, $M = U_0/c \ll 1$. On the contrary, changes/uncertainties in the vortical disturbance are amplified substantially in terms of the flame response, as the $1/\left(1-\left(U_0/U_{c,v}\right)\cos^2\theta\right)$ term has very large values when U_0 and $U_{c,v}$ are of same order.

In turn, these results show the required accuracy needed for velocity measurement for a given degree of predictive fidelity and, moreover, that these accuracy requirements differ substantially between the acoustic and vortical components. In particular, they show huge sensitivities of the flame response to errors in velocity field in case where $U_{c,v} = U_0 \cos^2\theta$.

6.3.3 Estimation of Non-linear Terms

Since we have used a linear framework for the comparison of model and experimental data, an analysis of the relative magnitudes of the neglected nonlinear terms relative to the linear terms is required. Start by expanding Eq.(6.9) in terms of time averaged and fluctuating components using Eq.(6.10), and subtract the time averaged terms to obtain Eq.(6.23). Note that s_T is calculated from measured data using Eq.(6.11). The different terms in the above equation are: (1) flame motion, (2) linear convection, (3) non-linear convection, (4) linear forcing and (5) linear kinematic restoration, (6) non-linear kinematic restoration. Note that Terms 1,2,4 and 5 form the linear model shown in Eq.(6.12).

$$\underbrace{\frac{\partial L'}{\partial t}}_{1} + \underbrace{\bar{U}\frac{\partial L'}{\partial x}}_{2} + \underbrace{u'\frac{\partial L'}{\partial x}}_{3} = \underbrace{\left(v' - u'\frac{\partial \bar{L}}{\partial x}\right)}_{4} + \underbrace{s_T \frac{\frac{\partial \bar{L}}{\partial x}}{\sqrt{\left(\frac{\partial \bar{L}}{\partial x}\right)^2 + 1}}\frac{\partial L'}{\partial x}}_{5}$$
$$+ \underbrace{\left(s_T\sqrt{\left(\frac{\partial \bar{L}}{\partial x} + \frac{\partial L'}{\partial x}\right)^2 + 1} - s_T\sqrt{\left(\frac{\partial \bar{L}}{\partial x}\right)^2 + 1} - s_T \frac{\frac{\partial \bar{L}}{\partial x}}{\sqrt{\left(\frac{\partial \bar{L}}{\partial x}\right)^2 + 1}}\frac{\partial L'}{\partial x} \right)}_{6} \tag{6.23}$$

Using the measured velocity and flame fluctuation data, the magnitude of each of these terms is plotted in Figure 64 as a function of the axial coordinate for two representative conditions. Data near the bluff body is not shown for the reasons discussed earlier. The figure shows that the non-linear terms are one to two orders of magnitude smaller than the linear terms. This validates the assumption of neglecting these non-linear terms in framing the linear model.

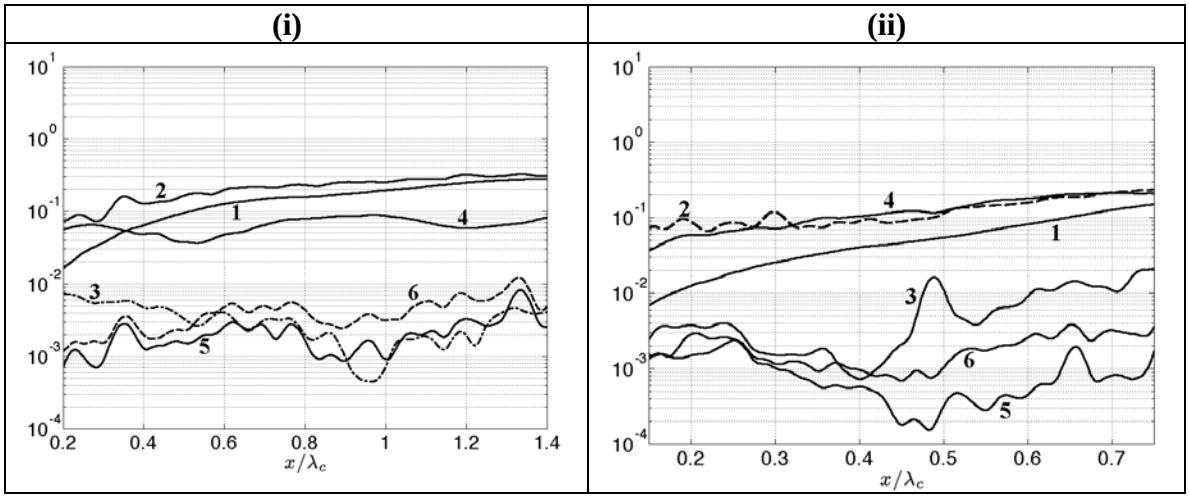

Figure 64 : Comparison of non-linear and linear terms as per Eq.(6.23) for the experimental cases (i) Uniform mixture, 50 m/s, 477K approach flow, In phase forcing and (ii) Stratified mixture, 100 m/s, 755K approach flow, In phase forcing, where, (1) unsteady term, (2) linear convection, (3) non-linear convection, (4) linear forcing, (5) linear kinematic restoration and (6) non-linear kinematic restoration.

Having considered the strength of level-set modeling for local flame response comparison for a two-dimensional flame, in the next chapter we consider a three-dimensional swirling lifted flame case.

CHAPTER 7

COMPARISON WITH EXPERIMENTS:

GLOBAL FLAME RESPONSE PREDICTIONS

In this chapter we consider the application of the model to a three dimensional swirling lifted flame. Unlike the previous chapter which considered local flame response comparisons, in this chapter we consider the global flame response of the flame subjected to transverse acoustic forcing.

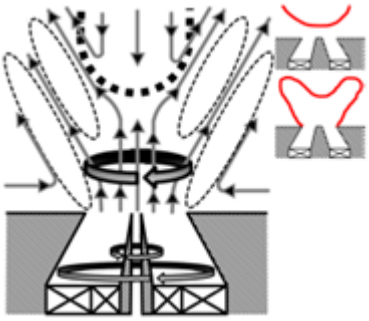

Figure 65 : Possible flow and flame configurations for two different vortex breakdown bubble structures where black dotted lines indicate edge of recirculation. (a) the bubble is lifted, (b) the bubble is merged with the centerbody wake, (c) no centerbody wake. Reproduced from Ref. [117].

The experiment considered in this chapter corresponds to the configuration sketched in Figure 65, where there is no wake region behind the centerbody and the VBB is lifted. The experiments were performed by Michael Malanoski and Michael Aguilar at the Georgia Tech Combustion Lab. The experimental configuration and details of the diagnostics are mentioned in Refs. [117, 118]. The key contribution of this chapter in the thesis has been comparison of predictions to these measurements and so the discussion below borrows content from these references. The swirling flow is setup using a DACRS nozzle (Dual Annular Counter Rotating Swirler). The lifted configuration is the result of

the low profile centerbody and coaxial jet along the centerline that develops into an annular jet around the VBB. The lifted VBB introduces a significant additional degree of freedom to the flame response problem, as described in Malanoski *et al*.[118]. The whole breakdown bubble and the stagnation point oscillate both axially and transversely due to the inherent flow instabilities in the VBB. Moreover, this region is globally unstable, meaning that it exhibits intrinsic oscillations, and so its sensitivity to external forcing is strongly amplitude dependent [161]. If the leading edge of the flame is stabilized by the stagnation point of the breakdown bubble, this also implies that the flame leading edge oscillates significantly in response to forcing. Indeed, prior investigations on a similar geometry attributed some characteristics of the unsteady heat release to the dynamics of the stagnation point and bubble motion [60, 61, 64, 65, 162]. Initial studies using this experiment have shown that the global, spatially integrated heat release response is controlled by three factors – vortical disturbances, acoustic flow disturbances, and flame leading edge motion [118]. The vortical flow motions dominate the flame response, and the flame leading edge motion is a minor contributor to the overall heat release response. This is an important result, as it shows that the significant motions of the flame leading edge actually have little dynamical significance for understanding the spatially integrated, forced response of the flame. Hence, in the model presented later in this chapter, the dynamics of the leading edge are not used for predictions. In the next section, we first consider the results from the experiment, before proceeding to model predictions.

7.1 Experimental Data

In Chapter 2, we discussed the dynamics of helical flow disturbances where the flow-field data from this experiment has been discussed. In this section, we discuss

details of the flame shape and the flow-field not discussed earlier. The results have been borrowed from Refs. [117, 118]. Before we discuss the results, a brief mention must be made of the data measurement locations. Two different planes were used for the velocity field measurements, obtained by visualizing through the front window and the other through the top window between the exhaust ports. During the first measurement, the laser sheet entered the experiment through the top window in a plane, termed the *y-z* plane, parallel to the axial flow direction (along the *z* coordinate). For the second measurement, the laser sheet entered the experiment through the front window in a plane, termed the *r-θ* plane, perpendicular to the flow direction. Two *r-θ* measurements were taken at 0.14*D* and 0.5*D* downstream from the nozzle exit.

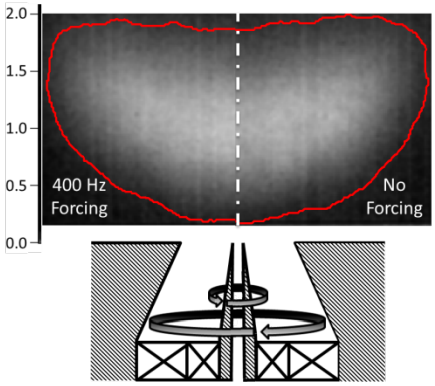

Figure 66 : Time average global flame shape with an overlay of the time average flame edge contour for unforced (right plane) and 400 Hz transverse acoustic excitation (left plane). Data reproduced from Ref. [117].

7.1.1 Time Averaged Behavior

Figure 66 presents a time averaged image of the flame under nominal and forced conditions. Note the lifted nature of the flame and the minimal impact of forcing on its time averaged character. The flame has a symmetric bowl shape with a time average standoff distance to the flame leading edge of 0.17*D*. The red contour denotes the time average flame edge which was extracted via image processing. The location of this flame

edge was used as an index in the velocity field to extract the velocity fluctuations along the surface of the flame. The velocity fluctuations were transformed into flame normal and tangential components using the time average flame angle. These are used as inputs for the model predictions presented later.

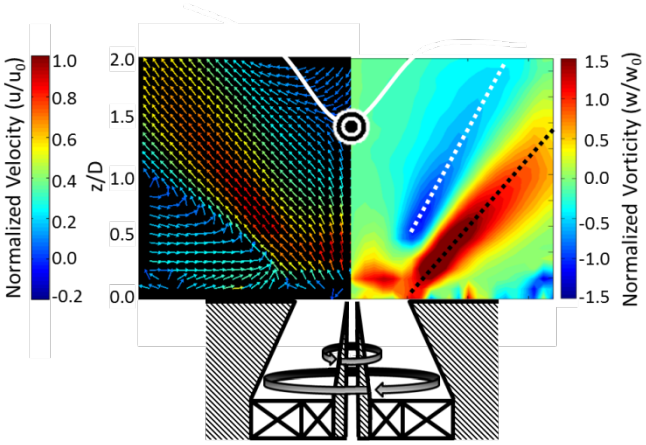

Figure 67 : Time average *y-z* velocity vector field in left plane and time average vorticity in right half plane. Solid white line traces time average zero velocity contour. Dotted white line traces time average minimum vorticity and dotted black line traces time average maximum vorticity. Data reproduced from Ref. [117].

The time average velocity field in the *y-z* plane from this counter-swirling nozzle shown in Figure 67 exhibits the expected swirl flow features illustrated in Figure 65. The velocity field, depicted on the left, and vorticity, depicted on the right, are symmetric about the centerline. The color scale on the left indicates the magnitude of the velocity normalized by a bulk nozzle exit velocity of 25 m/s. The red regions in the coaxial jet core, 0 to 0.5*D* downstream, approach 25 m/s before decelerating and stagnating upstream of the recirculated flow located about 1.5*D* downstream. On either side of the annular jet, regions of high vorticity develop from the shear between the recirculated and quiescent flow to the jet. The vorticity in the inner shear layer evolves in the counter-clockwise direction and clockwise in the outer shear layer. The time averaged centerline

stagnation point is also evident. As with the time average flame, no substantial changes occurred in the time average field for the excitation amplitudes considered here.

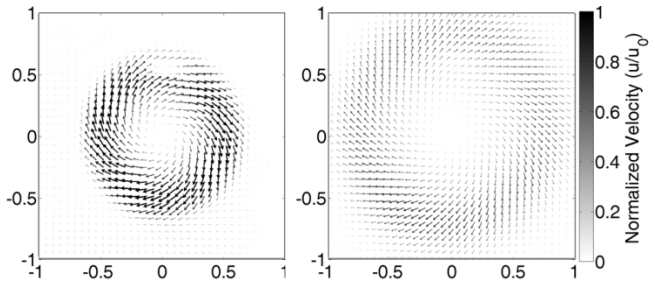

(a) **(b)**

Figure 68 : Time average *r-θ* velocity vectors for z=0.14*D* plane (a) and z=0.5*D* plane (b). Data reproduced from Ref. [117].

Unforced, time average velocity vector fields for two *r-θ* planes at axial distances of z=0.14*D* and z=0.5*D* are plotted in Figure 68. The velocity magnitude is again normalized by the nominal bulk velocity of 25 m/s. The spatial coordinates are normalized by the nozzle diameter. The bulk swirl motion, *S*=0.62, in the clockwise direction is evident from both of these planes. The radial divergence of the annular jet is evident by comparing between the 0.14*D* and 0.5*D* *r-θ* planes. The high swirl region is concentrated within a half diameter for the 0.14*D* plane and has expanded to nearly 1 diameter by the 0.5*D* plane.

7.1.2 Unsteady Behavior

In this section, we consider the unsteady dynamics in the experiment. First we consider the dynamics of the leading edge of the flame since this is a lifted flame in question. Figure 69 illustrates a number of instantaneous images of the upstream region of the flame, with an approximate location of the flame leading edge drawn in from image processing. A projection of the leading point location, the circular dot, on a circular pattern is included as well as the instance in time during the captured sequence.

The strong axial and transverse motion of the flame is evident from these images. The images indicate that the flame leading edge propagates nearly to the nozzle exit in some images and is clearly downstream in others. Additionally, the images indicate that the leading point of the flame appears to rotate around the nozzle. The image at 3 ms shows the leading edge of the flame on the right of the nozzle, while it is located on the left of the nozzle in the image at 6 ms.

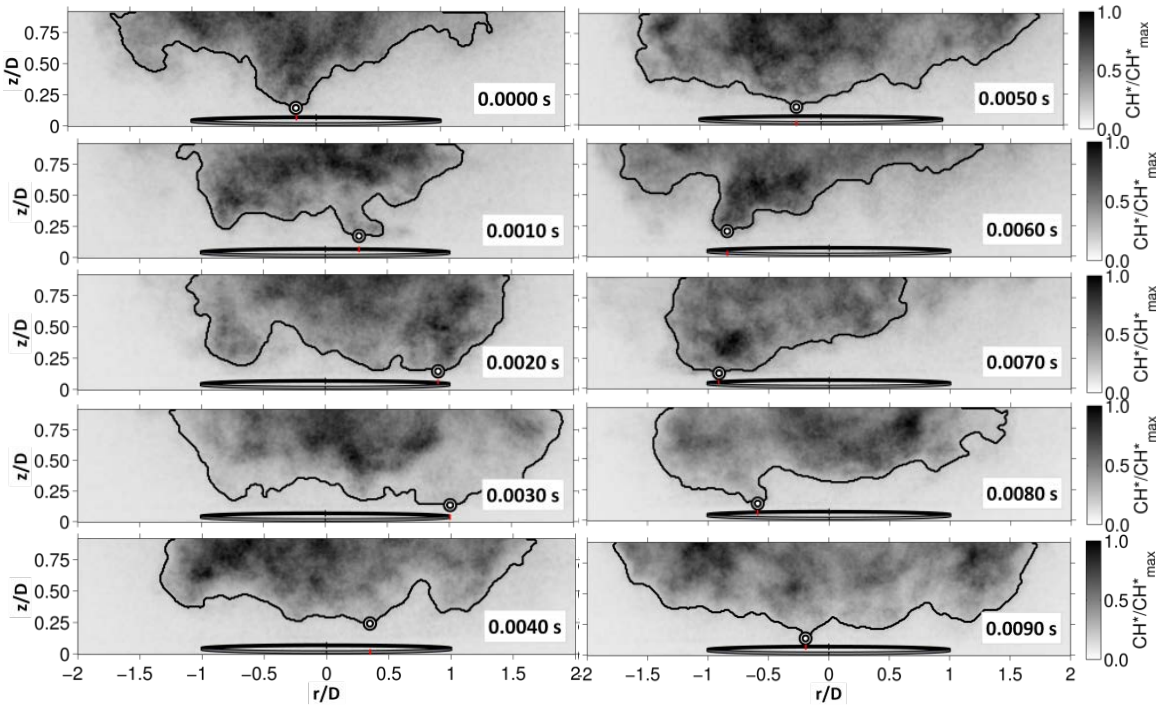

Figure 69 : Time sequence of instantaneous unforced flame leading edge. Data reproduced from Ref.[118].

The axial and transverse location of the flame leading point, defined as the farthest forward axial position of the flame edge, $\xi_b'(r,z)$, was extracted from these images. The RMS of the total motion is about 5-10 times greater than the forced motions. This indicates that the flame leading point motion is dominated by its natural motion, presumably tracking with the natural precession of the flow stagnation point. Because of

this, the overall RMS displacement exhibits negligible sensitivity to disturbance amplitude.

The formulation in Chapter 3 showed that if the mean flame shape is axisymmetric then bulk transverse disturbances produce significant local heat release oscillations and flame wrinkling, but no net heat release fluctuation; as the disturbances on each side of the flame are out of phase and cancel each other. Similarly, the *radial* oscillations in flame base position excite local wrinkling, but no global heat release oscillations. As such, it is the *axial* flame base motions which are of particular dynamical significance for the global heat release fluctuations. In this experiment, these axial motions are significantly smaller than the radial ones. Further analysis of the flame dynamics by Malanoski *et al.* [118] has showed that the contributions of flame base motion to the global heat release response was negligible in comparison to that due to acoustic motions, and vortical motions.

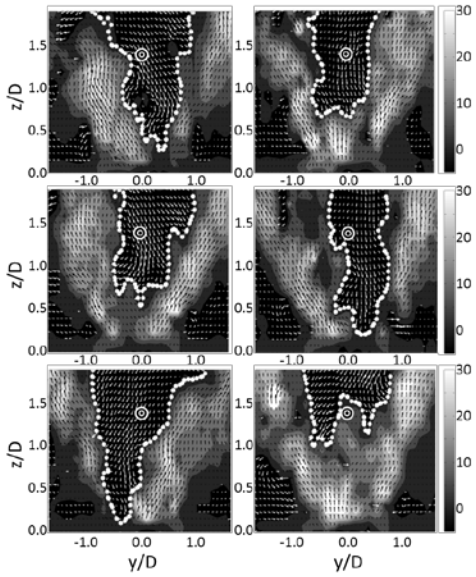

Figure 70 : Sequence of instantaneous *y-z* velocity vector fields for unforced reacting flow. Contour denotes line of zero axial velocity. The double concentric circle represents the time average position of the velocity stagnation point. The sequence is top to down in the left column, followed by the same in the right column. Data reproduced from Ref. [117].

Now consider the unsteady behavior of the flow-field in the axial direction (*y*-z plane). A sequence of instantaneous velocity vectors from the *y*-*z* plane are shown in Figure 70. Positive axial velocity is denoted by the grey to light color with black vectors while black regions with white vectors indicate regions of reversed flow. The boundary between these regions is indicated by the dotted white contour mapping the instantaneous zero axial velocity contour. The location of the instantaneous velocity stagnation point is the leading point in the reversed flow region. The time average position of the velocity stagnation point is shown with the double concentric circle at 1.4*D* downstream along the centerline. The difference between the time average location and instantaneous location of the velocity stagnation point is clear from these images and is a manifestation of the precessing, helical nature of the vortex breakdown region.

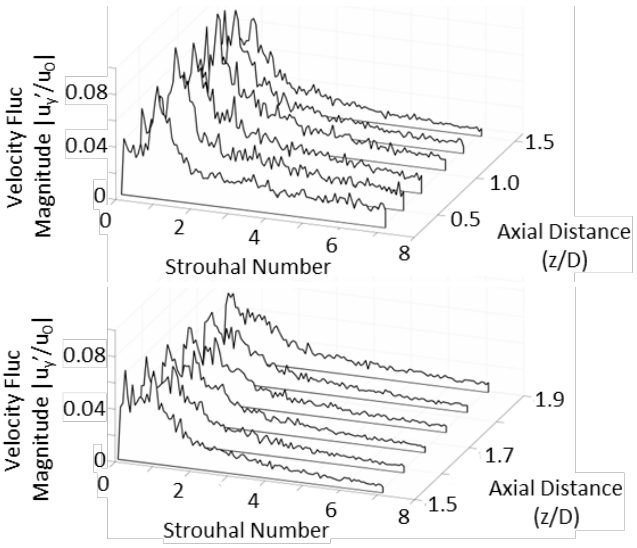

Figure 71 : Axial evolution of *y*–*z* plane ensemble averaged transverse velocity fluctuations along (a) centerline (a) and along the left VBB time average boundary (b) for unforced reacting flow. Data reproduced from Ref. [117].

Ensemble averaged spectra of the transverse velocity fluctuations along the centerline and along the left side of the time average zero velocity contour are plotted in Figure 71

as a function of downstream distance and Strouhal number. The Strouhal number is defined as $St = f / f_0$ where $f_0 = SU_0 / \pi D$.

There are significant fluctuations in the frequency range below 400 Hz, or St<2.6. The transverse velocity fluctuations along the centerline shown in Figure 71(a) are stronger closer to the nozzle exit with a peak response around 150 Hz or St=0.96. The axial velocity fluctuations, not shown here, also exhibit a spectral peak at St=0.96. The transverse fluctuations along the left VBB boundary depicted in Figure 71(b) also exhibit a significant response below 400 Hz and the peak at St=0.96 is still present, though its magnitude does decay with downstream distance. Given that this peak response occurs nearly at St=1 suggests that the peak response is related to the precession of structures around the nozzle and the decay in magnitude suggest that these structures become less coherent further downstream from the nozzle exit. An additional peak occurs along the boundary of the VBB farther downstream between 20-40 Hz. The helical mode behavior of the unsteady flow has already been detailed in Chapter 2, Section 2.3 and shall not be discussed in this chapter. Next, we shall discuss the inputs to the model framework before they are used for predictions.

7.2 Model Predictions

In this section we detail the procedure for predictions from the model using experimental data as input. First, we briefly reiterate the model equations. An axisymmetric flame/flow assumption is used in this study. The mean flame shape is governed then by:

$$\overline{u}_r \frac{\partial \overline{\xi}}{\partial r} = \overline{u}_z - s_f \left[\left(\frac{\partial \overline{\xi}}{\partial r} \right)^2 + 1 \right]^{1/2} \tag{7.1}$$

The fluctuating flame position (in frequency domain) is governed by:

$$i2\pi St\hat{\xi}' + \left[\overline{u}_{t,r}(r)\frac{\partial}{\partial r} + \frac{\overline{u}_\theta(r)}{r}\frac{\partial}{\partial \theta}\right]\hat{\xi}' = \left(\hat{u}'_z - \hat{u}'_r\frac{d\overline{\xi}(r)}{dr}\right) \tag{7.2}$$

Here,

$$\begin{aligned}\frac{\partial\overline{\xi}}{\partial r} &= \cot\psi(r)\\ \vec{\overline{u}}_t &= \vec{\overline{u}} - s_f\vec{e}_n\end{aligned} \tag{7.3}$$

where $\vec{e}_n$ is the local unit normal vector, pointing from the time averaged flame surface into the products. The flame position fluctuations can be decomposed into its azimuthal modes as:

$$\hat{\xi}'(r,\theta) = \sum_m \hat{\xi}'_m(r)e^{im\theta} \tag{7.4}$$

As mentioned in Chapter 3, for axisymmetric mean flames, a helical mode in the fluctuating flow field leads to the same mode in the flame response. The global heat release for axisymmetric mean flames can be written as:

$$\begin{aligned}\frac{\overline{Q}}{\rho h_R} &= 2\pi\int_r \frac{s_f(r)}{\sin\psi(r)}rdr\\ \frac{\hat{Q}'(\omega)}{\rho h_R} &= \sum_{m=-\infty}^{\infty}\int_{\theta=0}^{\theta=2\pi} e^{im\theta}d\theta\int_r s_f(r)\cos\psi(r)\frac{\partial\hat{\xi}'_m(r,\omega)}{\partial r}rdr\end{aligned} \tag{7.5}$$

Here h_R is the heat release per unit mass of reactants consumed, which is spatially constant due to its dependence only on equivalence ratio. $s_f(r)$ is a spatially varying displacement speed which is obtained from the mean flow and mean flame shape using Eq.(7.1). For non-axisymmetric modes ($m \neq 0$), the integral over θ is zero, which implies that only the axisymmetric ($m = 0$) mode contributes to the global flame area. An important implication of this result is that helical modes, while introducing substantial

wrinkling of the flame front, actually lead to no fluctuations in flame surface area in axisymmetric flows, a result that is also consistent with experimental observations from Moeck *et al.*[64]. This has important implications when it comes to the use of flow field data from experiments as inputs to the model.

In the next three sub-sections we shall detail the use of experimental data to obtain inputs to the model. This has been shown with the 400Hz In-Phase (IP) case as an example. The procedure detailed can be applied to the other frequencies.

7.2.1 Mean Flame Shape

The flame response model requires inputs only at the mean flame location, based on the linear analysis. In this sub-section, we present the time-averaged flame shape and hence the locations at which the model inputs are extracted. The *CH** chemiluminescence technique is used to capture the flame heat release [117]. The chemiluminescence images obtained are averaged, from which an intensity threshold is used to obtain the flame edge.

Figure 72 plots the extracted flame shapes, showing that the time-averaged flame shape is essentially the same for all forcing conditions, and also nearly symmetric. Hence, the flame shape is fit with a polynomial, also shown in the figure as the input to the model. Along with the flame shape input, the flame location coordinates are used to extract the flow field inputs to the model. Next we shall discuss the spatial distribution of the mean flow field and how this translates to its input at the flame.

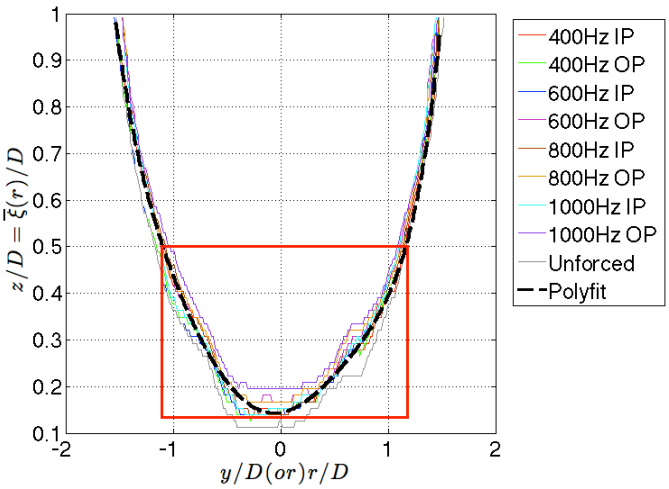

Figure 72 : Time-averaged flame edge obtained from time-averaged chemiluminescence images for the different forcing conditions in the experiment. Sample polynomial fit to the flame shape for use with the model shown as dashed black line. The red rectangular box indicates the flow field analysis domain.

7.2.2 Mean Flow

The mean flow field is critical to the model as they control wrinkle convection along the flame. We first quantify their degree of non-axisymmetry by expanding as:

$$\bar{u}_i(r,z,\theta) = H_{i,0}(r,z) + \sum_{m=1}^{\infty}\left[{}_cH_{i,m}(r,z)\cos m\theta + {}_sH_{i,m}(r,z)\sin m\theta \right] \qquad (7.6)$$

where the subscript *i* denotes the coordinate direction. The quantity $H_{i,0}(r,z)$ denotes the symmetric content in the velocity field and the quantities ${}_cH_{i,m}(r,z)$ & ${}_sH_{i,m}(r,z)$ denote non-axisymmetric contributions.

Earlier, we mentioned the use of the axisymmetric mean flow/flame model for predicting the dynamics. We shall next consider the validity of this assumption by comparing the spatial RMS amplitudes of these coefficients. For the axisymmetric contribution, this spatial RMS is defined as:

$$\bar{u}_{RMS,i,S}(z) = \sqrt{\frac{\int_r H_{i,0}^2(r,z)dr}{\int_r dr}} \tag{7.7}$$

where the subscript *S* is for symmetric. And for the non-axisymmetries, the spatial RMS is defined as:

$$\bar{u}_{RMS,i,AS}(z) = \sum_{m\neq 0} \sqrt{\frac{\int_r \left[{}_c H_{i,m}^2(r,z) + {}_s H_{i,m}^2(r,z) \right] dr}{2\int_r dr}} \tag{7.8}$$

Where the subscript *AS* is for asymmetries. Note that in Eq.(7.7) and Eq.(7.8), the respective RMS values are a function of the axial location, *z*. Hence, this comparison is performed at the two axial locations *z/D*=0.14 and *z/D*=0.5 where *r*-θ PIV data was obtained.

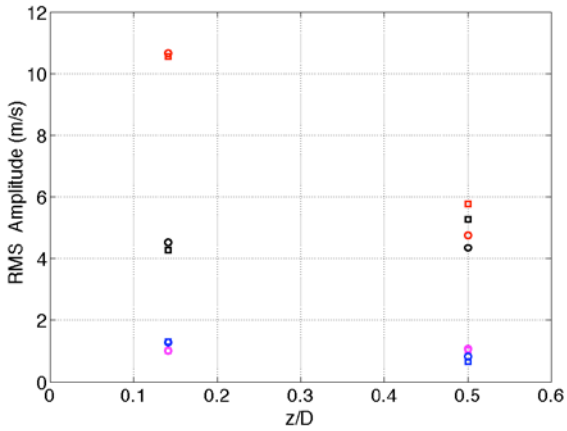

Figure 73 : RMS Amplitude comparison from time-averaged flow field of 400Hz IP (circles) and 400Hz OP (squares) cases. Symmetric contribution of radial velocity is shown in black, azimuthal velocity is shown in red and non-axisymmetric contributions are shown in magenta and blue, respectively. Estimation using Eqs.(7.7)-(7.8) applied to PIV data measured in two different planes located at *z/D*=0.14 and *z/D*=0.5.

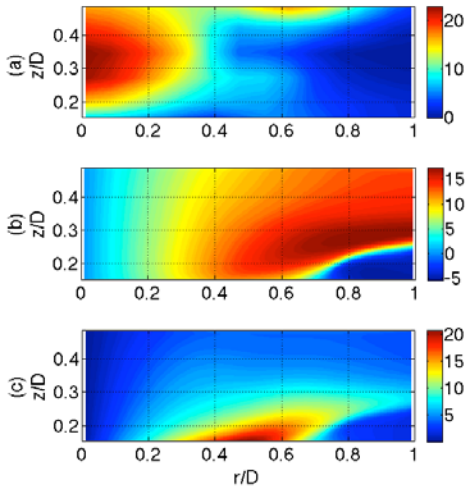

Figure 74 : Spatial variations of the time-averaged velocity components, for 400Hz IP case. (a) Axial velocity obtained directly from *r-z* PIV, (b) radial velocity and (c) azimuthal velocity, both generated using interpolation detailed in Appendix D.

An example comparison is shown in Figure 73. These plots show that, in general, the axisymmetric contribution (shown in black) is 4-10 times higher than the non-axisymmetric components. For his reason, we proceed for the rest of this discussion using the axisymmetric assumption, implying that we only need to keep $H_{i,0}(r,z)$. Henceforth, we shall denote the symmetric contribution $H_{i,0}(r,z)$ as $\overline{u}_i(r,z)$ for convenience of notation.

The symmetric contributions along the r-θ plane are available at two axial locations (z/D=0.14 and z/D=0.5) for only the radial and azimuthal components of the velocity field. The axial component, $\overline{u}_z(r,z)$, is obtained from the r-z plane. However, the model requires the complete spatial variations for all radial and axial locations along the mean flame for all components. This is generated in a domain bounded by $0.14<z/D<0.5$ and $0<r/D<1.2$ as shown in Figure 72 by the red rectangular box. In order to generate this data, an approximate interpolation procedure is applied, detailed in Appendix D. Using this procedure, the momentum equations for the symmetric mode are

used to generate the ensemble averaged flow field between the two planes of measurement. A sample result from this procedure is shown in Figure 74 for the 400Hz IP case.

The spatial variation for the time-averaged velocity field is important for the convection of wrinkles in the linear model. The displacement speed is equal to the local normal component of the time-averaged mean flow along the mean flame surface, obtained using the mean flow and mean flame shape. The model inputs are then smoothed using an appropriate polynomial fitting, before computations are performed using the model for the local flame response and then the Flame Transfer Function (FTF). An example variation of these inputs along the flame surface is shown in Figure 75 for the 400Hz IP case. Note that the extraction of mean inputs is performed for the flame surface between the *z/D*=0.14 and *z/D*=0.5 planes as indicated by the red box in Figure 72. Henceforth, the analysis and extraction of inputs shall be restricted to this region. In the next section, we detail the characteristics of the fluctuating flow field and its variation along the flame surface.

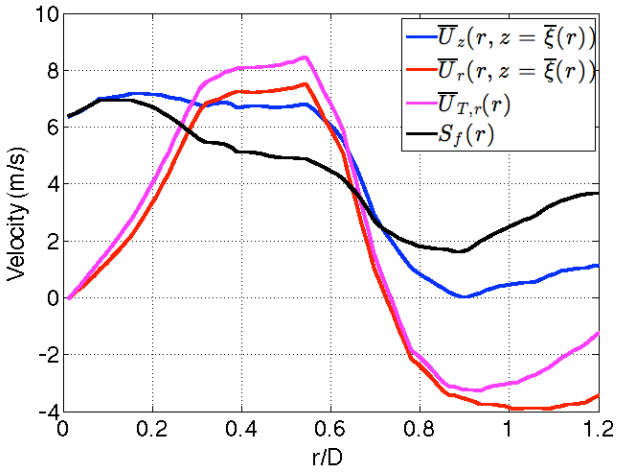

Figure 75 : Spatial variation of mean flow input parameters along the flame surface for the 400Hz IP case. The values of $\overline{U}_z$ and $\overline{U}_r$ at *r/D*=0 and *r/D*=1.2 correspond to those from the PIV measurement (*z/D*=0.14 and *z/D*=0.5).

7.2.3 Unsteady Flow

The fluctuating flow field and its helical mode decomposition are the focus of this section. The nature of the acoustic excitation field in the annulus has a direct influence on the dominant helical modes in the flow. For example, O'Connor *et al.* [45] previously reported results from another facility showing that in-phase forcing, which causes the nozzle to be located at a pressure antinode and velocity node, excited the symmetric, m=0 mode near the nozzle. In contrast, out of phase forcing, which is intrinsically asymmetric, excited a strong helical $|m|=1$ mode.

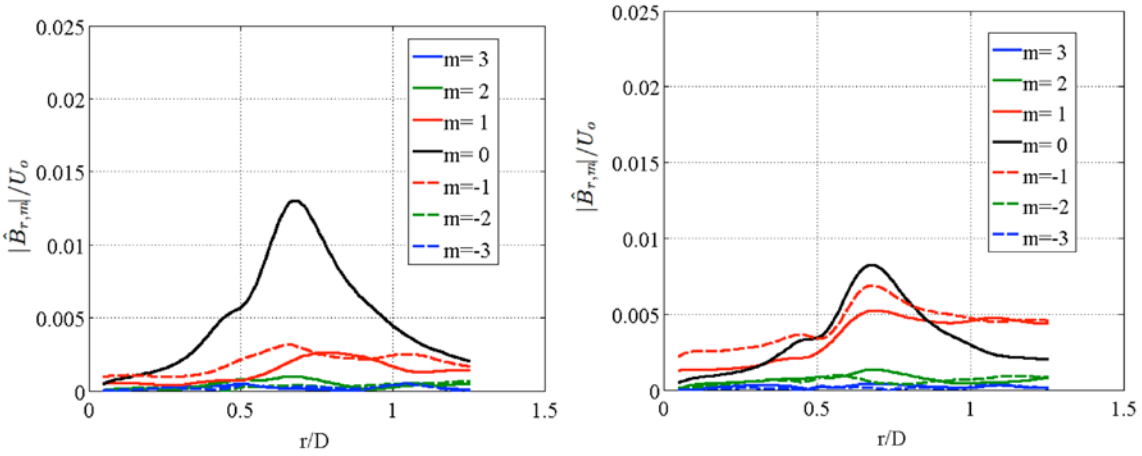

Figure 76 : Helical mode decomposition for radial velocity fluctuations for 400Hz forcing showing (a) IP and (b) OP at z/D=0.14.

As an example, we reproduce several results plotting the radial dependence of the first few helical modes extracted from the r-θ measurements described in Chapter 2. Figure 76 compares the helical modes for in-phase and out-of-phase forcing at 400Hz at z/D=0.14. Notice the dominance of the m=0 mode in the symmetric case (black curve), while the m=0 and $|m|$=1 modes are of comparable strength in the asymmetric case. Recall from an earlier section that the m=0 mode is the only required input to predict the FTF from the model under the assumption of axisymmetry of the time averaged flow and

flame. The higher strength of the *m*=0 mode in the In-Phase forcing case suggests that its FTF should be higher than that the out-of-phase case. However, this result does depend on how the *m*=0 mode evolves axially. This result also shows that the out-of-phase case will be sensitive to the degree of non-axisymmetry of the time averaged flame/flow, as helical modes influence the global unsteady heat release in non-axisymmetric flows.

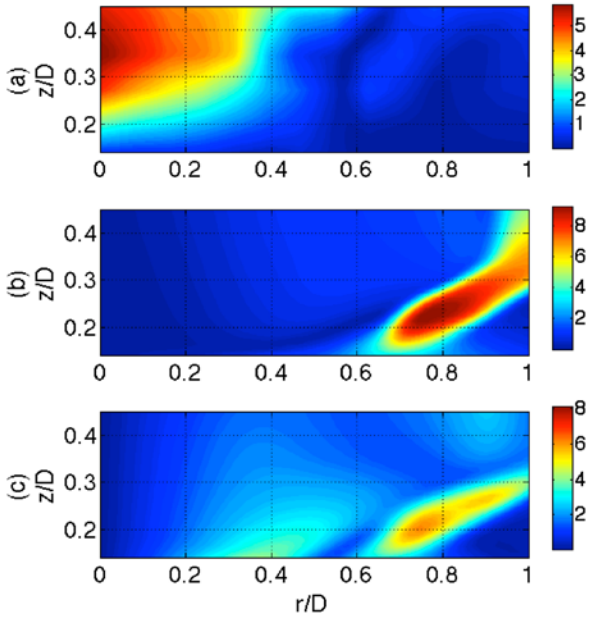

Figure 77 : Spatial variations of the symmetric mode amplitude for the velocity components ($\left|\hat{B}_{i,0}\right|$), for 400Hz IP case. (a) Axial velocity is obtained directly from *r-z* PIV, (b) radial velocity and (c) azimuthal velocity are generated using interpolation detailed in Appendix D.

Similar to the time-averaged flow field, the fluctuating flow field (and the symmetric mode) is available only at two discrete planes (*z/D*=0.14, 0.5). Hence, using the interpolation method described in Appendix D, the data between the planes can be generated. A sample result from this procedure, for the 400Hz in-phase case is shown in Figure 77. Again, while this figure shows the complete flow field, these data are only used in the model along the time averaged flame location to generate the flame transfer function.

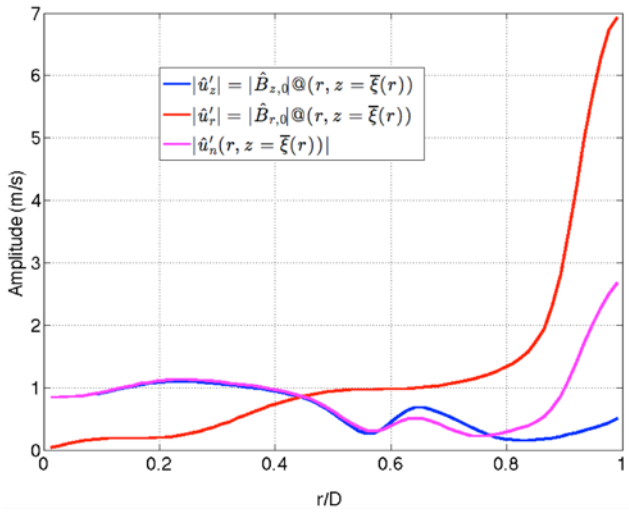

Figure 78 : Spatial variation of the amplitude of the symmetric mode (*m*=0) fluctuations along the flame for the 400Hz IP case.

As seen in Eq.(7.2), the axial and radial component of fluctuations must be specified at the mean flame. As an example, Figure 78 shows the spatial variation of these model inputs for the 400Hz in-phase case.

Using the methods described so far, the model inputs are extracted for all available cases and these are then used to obtain the FTF and compare with measurements. This is described in the next sub-section.

7.2.4 Flame Transfer Function: Comparison with Predictions

The flame transfer function (FTF) is defined as:

$$FTF = \frac{\left(\hat{Q}'(\omega)/\bar{Q}\right)}{\left(\hat{u}'_{ref}(\omega)/U_0\right)} \tag{7.9}$$

Where $\hat{Q}'(\omega)$ and $\bar{Q}$ in the numerator are defined in Eq.(7.5) and the reference velocity definition and the reference velocity measurement procedure and definition are provided in Refs. [117, 118]. Briefly, the reference velocity is defined as the integration of the instantaneous transverse velocity along the centerline in the *y*-*z* PIV plane from 1.0<*y*/*D*<2.0 from the nozzle exit. The magnitude of the frequency response at the

forcing frequency is extracted from the gain of the fast Fourier transformed fluctuations of the reference velocity. The corresponding experimental value for the numerator is obtained from the global line of sight integrated *CH** emissions, where we assume that:

$$\frac{\hat{Q}'}{\bar{Q}} \equiv \frac{\widehat{CH^*}'}{\overline{CH^*}} \tag{7.10}$$

An example of the ensemble averaged *CH** chemilumenescence spectrum is plotted in Figure 79. An estimate of the error in the magnitude and the phase in the *CH** chemiluminescence was generated from confidence intervals based on the *t*-distribution and a 95% confidence bound.

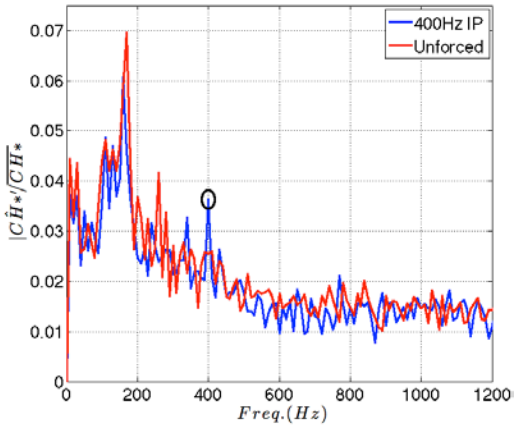

Figure 79 : Ensemble averaged spectrum from the global *CH chemiluminescence for the 400Hz IP case (blue) in comparison to the unforced case (red). The black circle indicates the response at the forcing frequency.**

The comparison between the model prediction and experiments for the amplitude of the *FTF* is shown in Figure 80(a), and for the phase of the *FTF* is shown in Figure 80(b). In general, the model comparisons fare well with the experimentally measured values. Notice that the in-phase *FTF* gains are higher than the out-of-phase *FTF* amplitudes. As mentioned earlier, this is expected from the fact that the in-phase case has dominant symmetric modes which contribute to the *FTF* whereas the out-of-phase case does not

have dominant symmetric modes, but still has a large reference velocity, as the nozzle lies in a velocity anti-node. Phase trends are also captured with the results, lying between 15-70 degrees from measurements.

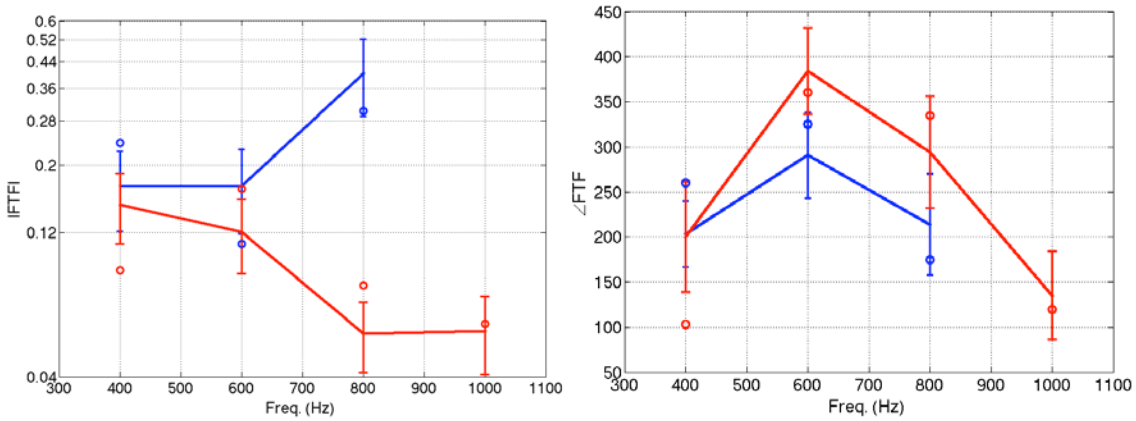

(a) **(b)**

Figure 80 : *FTF* (a) amplitude and (b) phase comparison between model prediction (circles) and experiments (solid lines with error bar) for both IP (blue) and OP (red) forcing at 400Hz.

7.2.5 Remarks

The previous section presented the results from the comparison of FTFs, however the caveats of the different assumptions must be mentioned.

(i) The mean flame was assumed to be axisymmetric, since three-dimensional spatial information was unavailable. Although the axisymmetry assumption was justified with the azimuthal mode analysis of the mean flow, this was done only at two measurement planes.

(ii) Axial velocity components were not solved for or helically decomposed. They were used directly from the axial measurement plane.

(iii) As seen from Figure 72, the flame extends beyond the domain denoted by the red box, but the analysis in this chapter considers only data within the red box. This limitation is due to the availability of experimental data only at extremes of this box.

Measurement planes further downstream must be considered to completely consider the flame response.

(iv) The Navier-Stokes interpolation procedure described in Appendix D neglected the pressure term since the required data was unavailable. The radial pressure gradients in a swirling flow are particularly significant and cannot be neglected.

(v) Finally, the turbulent flame speed was assumed constant in time, axisymmetric but varying in space. However, the turbulent flame speed is a non-axisymmetry dynamical quantity and its change in time and azimuthal space must be accounted.

The deviations between model predictions and measurements are not significant as seen in Figure 80. This indicates that the above points would lead to corrections that are relatively insignificant but non-negligible.

CHAPTER 8

CONCLUSIONS AND RECOMMENDATIONS

We now proceed to consider the key contributions to the literature from this thesis, the conclusions from the different analysis and finally, recommendations for future work.

8.1 Concluding Remarks

8.1.1 Contributions to Modeling

The first chapter presented the larger picture of thesis and where it fits in the literature. The literature survey showed that most models worked with two-dimensional symmetric disturbances and that non-axisymmetric disturbances required analytical treatment. In Chapter 2, a brief literature review on swirling flows, dynamics of transverse acoustic disturbances and helical flow disturbances showed that strong non-axisymmetric disturbances dominated such flow-fields. These were used as motivation to develop a framework that analytically tracts the response of swirling premixed flames to such flow disturbances.

In Chapter 3, a general framework is presented using the level-set equation to capture premixed flame dynamics. The level-set equation was used since a thin, thermo-diffusively stable laminar premixed flame was assumed. This assumption works in the corrugated flamelet regime shown in the Borghi diagram. The flame was assumed to be attached at its base, however the effects of flame base motion on the governing equation was presented in Appendix A. The flow disturbances were imposed in the analysis and feedback from the flame onto the flow was not considered. An important assumption made was that of small amplitude perturbations. This allows for a linear analysis where the time-averaged behavior is decoupled from the dynamics of the fluctuations. This

allowed for analytical treatment of the *G*-equation. Under these assumptions, a general solution was obtained which was used for later simplifications. This general solution is an important contribution of this thesis, since it has not been presented in the literature earlier. It serves as a simplified starting point for solutions to a generalized mean flow/flame subjected to a generalized non-axisymmetric disturbance. This then allows to obtain local flame wrinkling, local heat release, global heat release and sound generation characteristics. The sound generation model makes use of the local unsteady heat release as source term to a linear wave equation and the pressure field was then obtained using the Green's function method.

Using the general solution, simplifications were made to better understand the physics from the mathematics. The first simplification presented was the axisymmetric mean flow/flame. In such a case, the helical modes were shown to greatly influence the local flame wrinkling and hence local heat release. Specifically, a dominant mode m_0 was identified that corresponds to the mode that resulted in the maximum local flame response. In general, it was shown that this mode is non-axisymmetric and could be either co- or counter-rotating relative to the mean swirl. However, it was shown that all asymmetric helical modes cancelled out their local heat release when the globally integrated heat release was considered. This implied that irrespective of which mode was dominant, its global heat release was zero and that only the symmetric mode $m = 0$ contributed to the global heat release. This is a significant contribution from this thesis, since it emphasized the fact that despite vigorous flame flapping for the dominant mode, m_0, if $m_0 \neq 0$, it still implied that the global flame response was zero. Hence, the sensitivity of the flame to the helical modes was seen to be different. The sound

generation results also show a different sensitivity to the helical modes. Specifically, the additional parameter of importance is kL_f, which is a measure of flame compactness in reference to the acoustic wavelength. For the sound radiation in the far-field, the analysis showed that the pressure in the far-field can be directly related to a weighted moment contribution of the fluctuating change in flame surface area. This implies that even if a particular helical mode does not lead to a change in global flame area, it does contribute to the far-field pressure due to imperfect phase cancellation effects that are a function of kL_f. For small values of this parameter, it is convenient to decompose the far-field pressure using a multi-pole expansion into its monopole, dipole, quadrupole, etc. contributions. The symmetric mode $m = 0$ was the sole contributor to the leading order, monopole contribution, which is directly proportional to the global flame surface area. The $|m| = 1$ and 2 modes contribute to the dipole and quadrupole moments, respectively. This implies that the helical mode dominating the farfield sound is a function not only of m_o, but also kL_f. In the $kL_f \ll 1$ limit, the symmetric mode dominates the far-field pressure with the mode m contribution increasing as $(kL_f)^{|m|}$, as would be expected base on classical multi-pole scaling. For $kL_f \sim O(1)$, the mode dominating the farfield pressure is also a function of the dominant flame wrinkling response mode m_0. In the $kL_f >> 1$ limit, the pressure radiated by the m=0 and $|m|$>0 helical modes scale as $(kL_f)^{-1}$ and $(kL_f)^{-3/2}$, respectively. Similar results were obtained for the total sound power radiated by the flame, with the key difference being that the mode contributing to the dominant sound power emissions from the flame is a different function of kL_f than the

local pressure field. For example, the mode leading to the dominant pressure amplitude at some spherical angle could be different from the one leading to the maximum sound power radiation. The overall sound power scales as $\left(kL_f\right)^{2|m|}$ in the $kL_f \ll 1$ limit, while all modes scale equally as $\left(kL_f\right)^{-3}$ in the $kL_f >> 1$ limit.

8.1.2 Understandings from Explicit Calculations

In Chapters 4 and 5, explicit calculations were performed for example flow fields and these illustrated the general features. First, in Chapter 4, example calculations explicitly showed the features of local flame response characteristics for a premixed flame excited by transverse acoustic disturbances. This work shows the effects of swirl on a transversely forced flame, which introduces an additional degree of freedom for wrinkle motion. The presence of swirl along with the upstream axial velocity creates a helical spiral motion of the wrinkles. This leads to distinctive interference patterns on the flame surface that changes the effective wrinkling wavelength. The flame surface wrinkling also shows a strong sensitivity to the ratio between the swirling time scale and the acoustic excitation time scale, specifically seen in the apparent direction of wrinkle motion and the wrinkling wavelength. In case of axisymmetric flows, swirl was seen to have a local effect only. The global flame dynamics are independent of swirl regardless of the acoustic forcing mechanism, in the linear regime. Finally, these results provide some insight into the relative role of direct transverse excitation of the flame by acoustic waves during transverse instabilities. Specifically, they suggest that the local flame response to transverse waves is strong, and of similar magnitude to its response to the other processes. The comparison of flame transfer functions between a transversely forced flame and a longitudinally forced flame showed their relative roles for different

values of the control parameters. Specifically, it showed that a combination of flame compactness, flow Mach number and the Strouhal number was an important deciding factor.

In Chapter 5, example calculations were performed for premixed flames excited by helical flow disturbances. Unlike the transverse acoustic case, these disturbances are vortical. As mentioned earlier, a key finding from this work is that helical modes influence the flame wrinkling amplitude and heat release fluctuations differently. Starting with flame wrinkling characteristics, the analysis showed that for a general non-axisymmetric flame, a given helical mode number in the fluctuating flow field generates flame wrinkling with a different azimuthal dependence. For an axisymmetric flame, the helical modes in the fluctuating flow field generate an identical azimuthal dependence in the flame wrinkling behavior. Thus, an axisymmetric excitation field can excite a helical flame disturbance in a non-axisymmetric, swirling flow and vice-versa. In addition, it was shown that the dominant helical mode, m_o, is a function of swirl number, flow velocity, frequency, and vortex phase speed. Moving then to unsteady heat release, only the axisymmetric contribution of the flame wrinkling behavior contributes to the global area of axisymmetric flames. This stems from the simple mathematical fact that non-axisymmetric modes in the fluctuating flame response lead to area cancellation due to the 2π periodicity of these modes. This implies that in case of axisymmetric mean flames, only the axisymmetric, m=0 mode in the fluctuating flow field contributes to changes in global flame area. This implies that even if the dominant wrinkling flame response mode is non-axisymmetric, it does not contribute to the global unsteady heat release of axisymmetric flames. Thus significantly different sensitivities may be observed in single

and multi-nozzle flames in otherwise identical hardware, due to the near axisymmetry in one case and the strong non-axisymmetry in the other. In order to answer this question, analytical results were derived for weak asymmetries and a numerical solver was used to strong asymmetries in the mean flame/flow. Two example cases were considered: (i) Elliptic cross-section and (ii) Square cross-section. In both these cases, results showed that for a linear analysis, the asymmetry modes in the mean flame/flow interact with the same but opposite modes in the flow disturbance to lead to a finite global flame response. This effect is compounded especially when non-compact flames are considered, wherein, the global unsteady heat release is not considered. In this case, the Rayleigh criterion requires the local unsteady heat release to be multiplied with the local unsteady pressure before the Rayleigh Index is calculated.

8.1.3 Comparison with Experimental Data

Having considered the theoretical framework and example calculations, the level-set model is used for making predictions that are then compared with experimental measurements. For this, two different experiments are considered with different objectives: (i) two-dimensional bluff body stabilized flame for local flame response predictions and (ii) swirl stabilized lifted flame for global flame response predictions.

For the two-dimensional bluff body flame case, a key contribution is the demonstration that calculations based upon first principles, using measured velocity/flame fluctuations as inputs, can be used to quite accurately predict the spatio-temporal flame dynamics in a high turbulence flow. These are the first predictions of theory and experiment at these types of velocities/temperatures and the agreement is very encouraging. However, it is also clear that accurate prediction of flame response requires

accurate prediction of the disturbance velocity field. For example, the data clearly indicate the simultaneous presence of both acoustic and vortical disturbances whose relative magnitudes and phases change with operating conditions. The analysis of these data also shows the relative role of the transverse acoustic waves in leading to flame fluctuations. These transverse waves also excite longitudinal acoustic disturbances due to the fluctuating pressure drop they induce across the flow delivery system. Their primary role is in exciting the separating shear layer, leading to convected vortical disturbances which rollup the flame and lead to a longer length-scale pattern on the gain of the flame wrinkling. In addition, the transverse acoustic disturbances also directly disturb the flame, although with an amplitude that is about 1/2 that of the vortically-induced velocity disturbances. However, it is the superposition of these two types of disturbances that leads to the undulating character of the flame gain which is clearly shown in the data.

For the swirling flame case, global flame response predictions were made. Due to the complex three-dimensional nature of the flame and flow, simulataneous measurements were not available. However, the motive of this study was to not only to demonstrate the use of level-set models, but also to demonstrate the use of an incomplete data set in generating model inputs. An important conclusion from this result is that, with appropriate knowledge of the disturbance field, the unsteady characteristics of the flame response can be predicted. The data was available at discrete locations and the “gaps” were filled using a Navier Stokes interpolation procudure that solved the momentum equations. The mean flame shape and mean flow were assumed to be axisymmetric and this assumption was validated by comparing the symetric mode amplitude with the contribtions from the asymmetric modes. As mentioned in Chapter 3, the strongly helical

character of the disturbance field, while having important local influences on the flame, do not influence the global unsteady heat release of axisymmetric flames. This allowed for an important simplification wherein, despite the availability of the azimuthal data field, the symmetric mode was the only mode used in the analysis. In the cases considered in this thesis, this assumption was shown to provide a good comparison between predicitions and measurements.

8.2 Recommendations

This thesis provided a valuable understanding of premixed flame response to non-axisymmetric disturbances. However, several key assumptions need to be addressed.

8.2.1 Non-linear Analysis

The model presented in this thesis makes use of a linear perturbation framework. The results presented are thus only valid within this framework. However, for larger amplitudes, non-linear analysis is required and the results are susceptible to change. Firstly, the swirl parameter was shown to strongly affect the length scale of wrinkling. When nonlinear terms arising from kinematic restoration are introduced in the model, this will result in fast smoothing of shorter length-scale disturbances as the flame propagates normal to itself. Similarly, small length-scale, small curvature wrinkles will be more strongly influenced by flame stretch. As such, inclusion of either of these effects will cause swirl to have a greater influence on the global flame response than that is presented in this thesis. Secondly, the linear analysis showed that asymmetric modes in the mean flow interact *only* with helical modes of opposite sign in the flow disturbance to cause global flame response. However, in the case of non-linearity, this restriction is not valid.

Different mode numbers in the asymmetric mean flow and helical flow disturbances can interact with each other causing global flame response. This implies that the helical modes in the disturbance flow are not restricted by those in the mean flow. Finally, non-linearity in the flame response model is important in capturing limit cycle behavior. All of these features can be captured using the Numerical solver detailed in Appendix B. This can also be coupled with a linear acoustic solver (Helmholtz solver) where the unsteady heat release source is obtained from the flame response numerical solver.

8.2.2 Flame Speed Variations

Next, the constant flame speed assumption must be relaxed. First, this needs to be addressed by considering flame stretch. This brings in the flame curvature and Markstein number into the problem and thus become important control parameters. The previously mentioned changes to flame wrinkling wavelength is further affected by interactions between large disturbance amplitudes and the Markstein length.

The second, and very important factor is the consideration of turbulent flame speed effects. Swirling flows are highly turbulent in nature and hence a significant effect of turbulent flow on the flame speed must be accounted for. These require the use of a numerical level-set solver to track the flame front dynamics. Earlier work by Shin *et al.* [155] considered a bluff body stabilized flame in a non-swirling flow. In that framework, the laminar flame speed was used for instantaneous flame propagation with many different realizations available. Using this data, the turbulent flame speed could be computed. This framework can be expanded to a three dimensional swirl stabilised flame with a swirling mean flow and its corresponding turbulent flow field.

Finally, the effect of equivalence ratio fluctuations is important since these affect the flame speed greatly and hence the unsteady heat release. The role equivalence ratio fluctuations for an axisymmetric flame subjected to an axisymmetric disturbance was consdiered by Shreekrishna [125]. However, this work needs to be expanded to the framework in this thesis that considers a non-axisymmetric disturbance field. The interactions between the non-axisymmetry in the flow disturbances and the equivalence ratio fluctuations further adds to its importance.

8.2.3 Role of Azimuthal Flow Fluctuations

The axisymmetric flame model showed that the azimuthal flow fluctuations have no direct influence on the flame response. However, azimuthal flow fluctuations can couple with other flow component disturbances to indirectly cause flame response. These azimuthal flow disturbance are generated at the swirler in the nozzle annulus when axial flow fluctuations traverse the vanes of the swirler. The generated azimuthal flow fluctuations, its amplitude and phase are dependent on the geometry of the swirler vanes, frequency of forcing and the amplitude of axial flow fluctuations. For non-axisymmetric mean flames, the azimuthal flow fluctuations have a direct effect on the flame response. Apart from this direct effect, the asymmetries in the mean flow also result in differences in the way flow components couple with each other. These swirler dynamics cannot be modeled and required the use of Computational Fluid Dynamics simulations of the swirler annulus geometry. Additionally, these azimuthal flow fluctuations have a direct influence on the flame response of non-axisymmetric flames and this is also captured using CFD studies of a model combutor in conjunction with the swirler annulus section.

8.2.4 Comparison with Experiments

The application of model to experimental data, in order to make predictions was an important step in strengthening the validity of the theoretical models. In the bluff body flame case, due to spatial and temporal resolution of the data, local flame response predictions could be made. However, such a benefit was not possible for the swirling flame case. A key next step is to consider local measurements that are both spatially and temporally well resolved in multiple planes. Experimental data of both the flow and flame would provide valuable insight into the azimuthal variations in the flame response characteristics in each of the measurement planes. Another key step, is to further extend the validation to a flow field/flame shape that is more strongly-non axisymmetric. In such a non-axisymmetric configuration, the flames global heat release will be sensivitive to the asymmetric helical modes as well.

APPENDIX A

FORMULATION FOR FLAME BASE MOTION EFFECTS

The formulation presented in Chapter 3 considers a flame firmly attached to the centerbody. In this appendix, a formulation for including flame base motion effects is presented.

The flame base motion is assumed to be in both the radial direction from the circular base/holder as well as in the axial direction above the base/holder. These are a function of time and the azimuthal angle at the base and hence given by $\xi_{b,r}(t,\theta)$ and $\xi_{b,z}(t,\theta)$, respectively. The subscript *b,i* denotes the base motion along the *i* direction. The flame position as measured from the fixed base, in the lab-fixed coordinate system is given by $\xi(t,r,\theta)$. We now transform to a coordinate system in which the base is fixed. This is given as:

$$\begin{aligned} \hat{r}(r,\theta,t) &= r - \xi_{b,r}(t,\theta) \\ \hat{z}(z,\theta,t) &= z - \xi_{b,z}(t,\theta) \\ \hat{\xi}(z,\theta,t) &= \xi - \xi_{b,z}(t,\theta) \end{aligned} \tag{A.1}$$

The level set equation in its implicit form can be converted to an explicit form using the relation:

$$G = \hat{z}(z,\theta,t) - \hat{\xi}(\hat{r}(r,\theta,t),\theta,t) \tag{A.2}$$

This implies the following conversion relations:

$$\frac{\partial G}{\partial t} = \frac{\partial \hat{z}}{\partial t} - \frac{\partial \hat{\xi}}{\partial t} - \frac{\partial \hat{\xi}}{\partial \hat{r}}\frac{\partial \hat{r}}{\partial t} \tag{A.3}$$

$$\frac{\partial G}{\partial r} = -\frac{\partial \hat{\xi}}{\partial \hat{r}}\frac{\partial \hat{r}}{\partial r} \tag{A.4}$$

$$\frac{\partial G}{\partial \theta} = \frac{\partial \hat{z}}{\partial \theta} - \frac{\partial \hat{\xi}}{\partial \theta} - \frac{\partial \hat{\xi}}{\partial \hat{r}} \frac{\partial \hat{r}}{\partial \theta} \tag{A.5}$$

$$\frac{\partial G}{\partial z} = \frac{\partial \hat{z}}{\partial z} \tag{A.6}$$

The flame base motion in time can also be expressed as flame base velocities based on their time derivatives as:

$$\frac{\partial \xi_{b,r}}{\partial t} = u_{b,r} \tag{A.7}$$

$$\frac{\partial \xi_{b,z}}{\partial t} = u_{b,z} \tag{A.8}$$

Using these in the level-set equation (Eq.(3.4)) results in the following form:

$$\frac{\partial \hat{\xi}}{\partial t} + \left(u_r - u_{b,r} - \frac{u_\theta}{r} \frac{\partial \xi_{b,r}}{\partial \theta} \right) \frac{\partial \hat{\xi}}{\partial \tilde{r}} + \frac{u_\theta}{r} \frac{\partial \hat{\xi}}{\partial \theta} + s_L \sqrt{1 + \left(\frac{\partial \hat{\xi}}{\partial \hat{r}} \right)^2 + \frac{1}{r^2} \left(\frac{\partial \xi_{b,z}}{\partial \theta} + \frac{\partial \hat{\xi}}{\partial \theta} - \frac{\partial \xi_{b,r}}{\partial \theta} \frac{\partial \hat{\xi}}{\partial \hat{r}} \right)^2} \tag{A.9}$$
$$= u_z - u_{b,z} - \frac{u_\theta}{r} \frac{\partial \xi_{b,z}}{\partial \theta}$$

For the steady state flame, there is no change in time and there is no flame base motion and so the following definitions and assumptions are valid:

$$\begin{aligned} &\hat{\xi} \equiv \bar{\xi}(r, \theta) \\ &\hat{r} \equiv r \\ &\hat{z} \equiv z \\ &u_i \equiv \bar{U}_i \\ &\xi_{b,i} \equiv 0 \Rightarrow u_{b,i} \equiv 0 \end{aligned} \tag{A.10}$$

This leads to the following equation for the mean flame shape:

$$\bar{U}_r \frac{\partial \bar{\xi}}{\partial r} + \frac{\bar{U}_\theta}{r} \frac{\partial \bar{\xi}}{\partial \theta} + s_L \sqrt{1 + \left(\frac{\partial \bar{\xi}}{\partial r} \right)^2 + \frac{1}{r^2} \left(\frac{\partial \bar{\xi}}{\partial \theta} \right)^2} = \bar{U}_z \tag{A.11}$$

The dynamics under the linear assumption leads to the form:

$$\frac{\partial \hat{\xi}'}{\partial t} + \bar{U}_{t,r} \frac{\partial \hat{\xi}'}{\partial \hat{r}} + \frac{\bar{U}_{t,\theta}}{r} \frac{\partial \hat{\xi}'}{\partial \theta} = u'_{flow} - u_{base} - \frac{\bar{U}_{t,\theta}}{r} \left(\frac{\partial \xi_{b,z}}{\partial \theta} - \frac{\partial \bar{\xi}}{\partial r} \frac{\partial \xi_{b,r}}{\partial \theta} \right) \tag{A.12}$$

Where the wrinkle convection velocities are defined as:

$$\bar{U}_{t,r} = \left(\bar{U}_r + s_L \frac{\dfrac{\partial \bar{\xi}}{\partial r}}{\sqrt{1 + \left(\dfrac{\partial \bar{\xi}}{\partial r}\right)^2 + \dfrac{1}{r^2}\left(\dfrac{\partial \bar{\xi}}{\partial \theta}\right)^2}} \right) \tag{A.13}$$

$$\bar{U}_{t,\theta} = \left(\bar{U}_\theta + s_L \frac{\dfrac{1}{r}\dfrac{\partial \bar{\xi}}{\partial \theta}}{\sqrt{1 + \left(\dfrac{\partial \bar{\xi}}{\partial r}\right)^2 + \dfrac{1}{r^2}\left(\dfrac{\partial \bar{\xi}}{\partial \theta}\right)^2}} \right) \tag{A.14}$$

And the forcing terms are given by:

$$u'_{flow} = \left(u'_z - u'_r \frac{\partial \bar{\xi}}{\partial r} - \frac{u'_\theta}{r}\frac{\partial \bar{\xi}}{\partial \theta} \right) \tag{A.15}$$

$$u_{base} = \left(u_{b,z} - u_{b,r} \frac{\partial \bar{\xi}}{\partial r} \right) \tag{A.16}$$

The LHS of Eq.(A.12) is similar to equations derived in Chapter 3. In the RHS, the first forcing term given by u'_{flow} is due to flow disturbances. The second term corresponds to disturbances generated at the base due to the base motion velocity. These appear as an addition to the flow disturbance terms and are of opposite sign due to the sign convention chosen for base motion. The last term corresponds to the generation of wrinkles due to tangential transport of asymmetries in the base motion. The solution procedure for the equation is similar to that described in Chapter 3.

APPENDIX B

NUMERICAL SOLVER

In this appendix, we present the numerical methods used in the solver used for obtaining Flame Transfer Functions for the mean flame asymmetry cases presented in Chapter 5.

Consider the 2D Hamilton-Jacobi (HJ) equation of the form:

$$\frac{\partial \Phi}{\partial t} + H(r, \theta, t, \Phi_r, \Phi_\theta) = 0 \tag{B.1}$$

Let (r_i, θ_j) be the (i, j) node in the 2D $r-\theta$ grid space. Define the following:

$$\begin{aligned} \Phi_{i,j} &= \Phi(r_i, \theta_j) \\ \Delta_r^+ \Phi_{i,j} &= \Phi_{i+1,j} - \Phi_{i,j} \\ \Delta_r^- \Phi_{i,j} &= \Phi_{i,j} - \Phi_{i-1,j} \end{aligned} \tag{B.2}$$

Denote the derivatives as: $\Phi_r = \partial\Phi/\partial r$. The Weighted Essentially Non-Oscillatory (WENO) approximations to the derivatives can then be expressed as:

$$\begin{aligned} \Phi_{r,i,j}^{\pm} = \frac{1}{12}\left(-\frac{\Delta_r^+ \Phi_{i-2,j}}{\Delta r} + 7\frac{\Delta_r^+ \Phi_{i-1,j}}{\Delta r} + 7\frac{\Delta_r^+ \Phi_{i,j}}{\Delta r} - \frac{\Delta_r^+ \Phi_{i+1,j}}{\Delta r} \right) \\ \pm \Phi^{WENO}\left(\frac{\Delta_r^- \Delta_r^+ \Phi_{i\pm 2,j}}{\Delta r}, \frac{\Delta_r^- \Delta_r^+ \Phi_{i\pm 1,j}}{\Delta r}, \frac{\Delta_r^- \Delta_r^+ \Phi_{i,j}}{\Delta r}, \frac{\Delta_r^- \Delta_r^+ \Phi_{i\mp 1,j}}{\Delta r} \right) \end{aligned} \tag{B.3}$$

Where

$$\Phi^{WENO}(a,b,c,d) = \frac{1}{3} w_0 (a - 2b + c) + \frac{1}{6}\left(w_2 - \frac{1}{2} \right)(b - 2c + d) \tag{B.4}$$

And

$$\begin{aligned} w_0 &= \frac{a_0}{a_0 + a_1 + a_2}, \qquad w_2 = \frac{a_2}{a_0 + a_1 + a_2} \\ a_0 &= \frac{1}{(\varepsilon + IS_0)^2}, \qquad a_1 = \frac{6}{(\varepsilon + IS_1)^2}, \qquad a_2 = \frac{3}{(\varepsilon + IS_2)^2} \end{aligned} \tag{B.5}$$

$$
\begin{aligned}
IS_0 &= 13(a-b)^2 + 3(a-3b)^2 \\
IS_1 &= 13(b-c)^2 + 3(b+c)^2 \\
IS_2 &= 13(c-d)^2 + 3(3c-d)^2
\end{aligned}
\tag{B.6}
$$

Here, $\varepsilon \sim 10^{-6}$ is a small number chosen for preventing a zero denominator. This scheme results in a fifth order spatial accuracy for the derivative.

This form of the derivative is used in the following form of Eq.(B.1):

$$
\frac{\partial \Phi_{i,j}}{\partial t} = -\hat{H}(r_i, \theta_j, t, \Phi_{i,j}, \Phi^+_{r,i,j}, \Phi^-_{r,i,j}, \Phi^+_{\theta,i,j}, \Phi^-_{\theta,i,j}) \tag{B.7}
$$

Note that:

$$
\hat{H}(r, \theta, t, \Phi, h, h, g, g) = H(r, \theta, t, \Phi, h, g) \tag{B.8}
$$

In order to evaluate the RHS, the Local Lax-Friedrichs (LLF) scheme is used:

$$
\hat{H}^{LLF}(h^+, h^-, g^+, g^-) = H\left(\frac{h^+ + h^-}{2}, \frac{g^+ + g^-}{2}\right) - \mathrm{A}(h^+, h^-)\frac{h^+ - h^-}{2} - \mathrm{B}(h^+, h^-)\frac{g^+ - g^-}{2} \tag{B.9}
$$

Where

$$
\begin{aligned}
\mathrm{A}(h^+, h^-) &= \max_{\substack{h \in I(h^+, h^-) \\ g \in [g_{\min}, g_{\max}]}} \left| H_h(h, g) \right| \\
\mathrm{B}(g^+, g^-) &= \max_{\substack{g \in I(g^+, g^-) \\ h \in [h_{\min}, h_{\max}]}} \left| H_g(h, g) \right|
\end{aligned}
\tag{B.10}
$$

Here,

$$
\begin{aligned}
H_h &= \frac{\partial H}{\partial(\Phi_r)} \\
H_g &= \frac{\partial H}{\partial(\Phi_\theta)} \\
I(a,b) &= \left[\min(a,b), \max(a,b)\right]
\end{aligned}
\tag{B.11}
$$

Now, the time stepping is performed using a third order Total Variation Diminishing (TVD) scheme:

$$
\begin{aligned}
&\frac{d\Phi}{dt} = L\left(\Phi\right) \\
&\Phi^{(1)} = \Phi^{(n)} + \Delta t L\left(\Phi^{(n)}\right) \\
&\Phi^{(2)} = \Phi^{(1)} + \frac{\Delta t}{4}\left[-3L\left(\Phi^{(n)}\right) + L\left(\Phi^{(1)}\right)\right] \\
&\Phi^{(n+1)} = \Phi^{(1)} + \frac{\Delta t}{12}\left[-L\left(\Phi^{(n)}\right) - L\left(\Phi^{(1)}\right) + 8L\left(\Phi^{(2)}\right)\right]
\end{aligned}
\tag{B.12}
$$

Here, $\Phi^{(n)}$ corresponds to the value at the *n*-th time step. Note that this time-stepping solver was created with a much larger goal of capturing non-linear effects. However, in this thesis, this numerical solver has been used for low amplitude linear cases where a single frequency is present in the flow and flame disturbances.

These numerical methods are applied to Eq.(3.6) where:

$$
\begin{aligned}
&\Phi \equiv \xi \\
&H \equiv u_r \frac{\partial \xi}{\partial r} + \frac{u_\theta}{r}\frac{\partial \xi}{\partial \theta} + s_L\left[\left(\frac{\partial \xi}{\partial r}\right)^2 + \frac{1}{r^2}\left(\frac{\partial \xi}{\partial \theta}\right)^2 + 1\right]^{1/2} - u_z
\end{aligned}
\tag{B.13}
$$

The radial/azimuthal grid used in this analysis is comprised of between 500,000 and 1 million mesh points. The OpenMP code is used to simulate this domain on parallel computing systems offered under the National Science Foundation's XSEDE program (eXtreme Science and Engineering Discovery Environment). Specifically, the systems used were:

(i) Nautilus, at the University of Tennessee that comprises of 1024 cores with 4TB memory.

(ii) Blacklight, at the Pittsburgh Supercomputing Center that comprises of 2048 cores and 16TB of memory.

Each of these systems comprised of a global shared memory in a single system image architecture that was suitable for hybrid parallel computations. The single node/blade configuration comprised of 16 computational cores. Based on scaling studies for the developed code, the scaling for OpenMP communication and the mesh size of the problem, the analysis was parallelized across 48 cores.

APPENDIX C

ADDITIONAL RESULTS FOR LOCAL FLAME RESPONSE PREDICTIONS

This appendix section presents the remainder of the results obtained from the local flame response prediction study presented in Chapter 6. Specifically, the results correspond to the 100 m/s cases and are shown in Figure 81 to Figure 84 These results also show qualitative agreement between predictions and measurements in all cases (with one exception noted below). This series of figures show that the slope of the initial rise in gain, the presence of undulations or local maxima and minima, and the number of local maxima and minima are all well captured. Most cases where quantitative disagreements are present correspond to results which exhibit local maxima/minima in magnitude of velocity or flame wrinkling. Good examples of this are shown in Figure 82 and Figure 84. As discussed earlier in Chapter 6, these local maxima/minima correspond to locations of destructive or constructive interference between disturbance sources with different phases. In addition, qualitative disagreement, namely an almost 180 degree difference in phase, was observed between the predicted and measured flame wrinkling phase in the 100 m/s, stratified mixture, in-phase forcing case, which is reproduced in Figure 83. Interestingly, for this same case, the flame wrinkling magnitude compares quite well, as well as the phase predictions for the velocity.

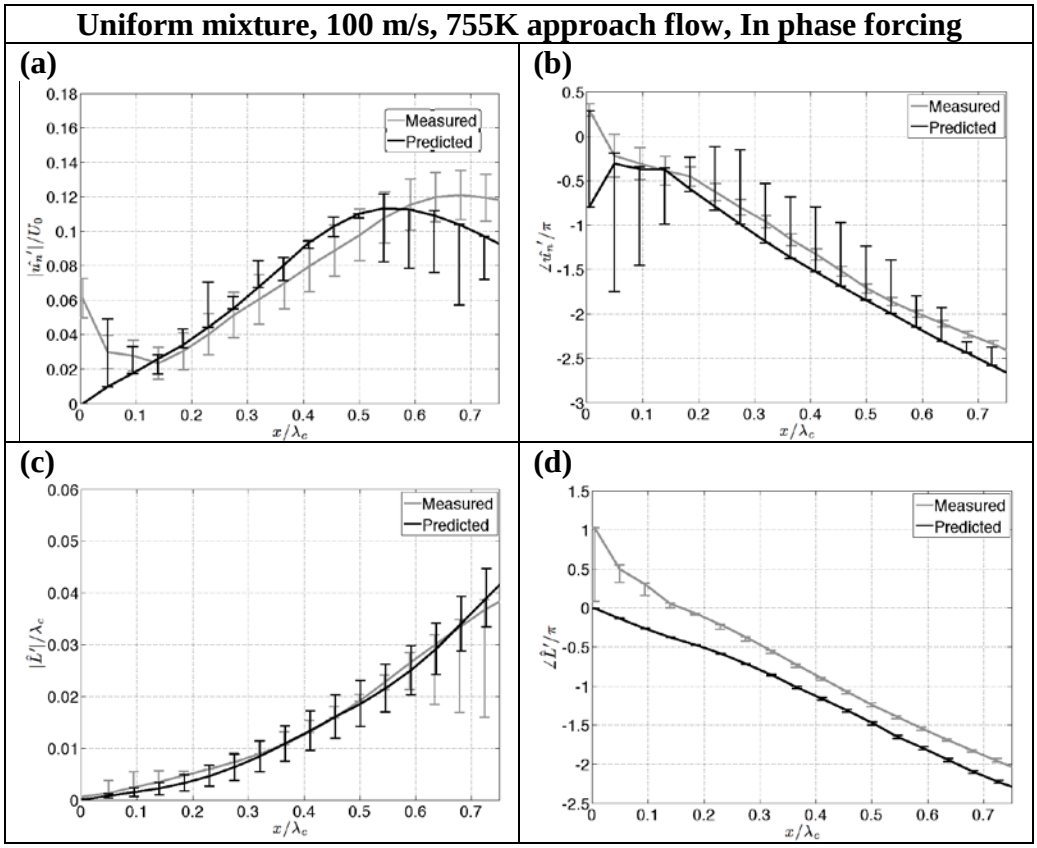

Figure 81 : Velocity validation study for Uniform mixture, 100 m/s, 755K approach flow, In phase forcing, using Eq.(6.17) with flame edge as input : (a) amplitude comparison, (b) corresponding phase comparison; Flame edge validation study using Eq.(6.18) with velocity as input : (c) amplitude comparison, (d) corresponding phase comparison.

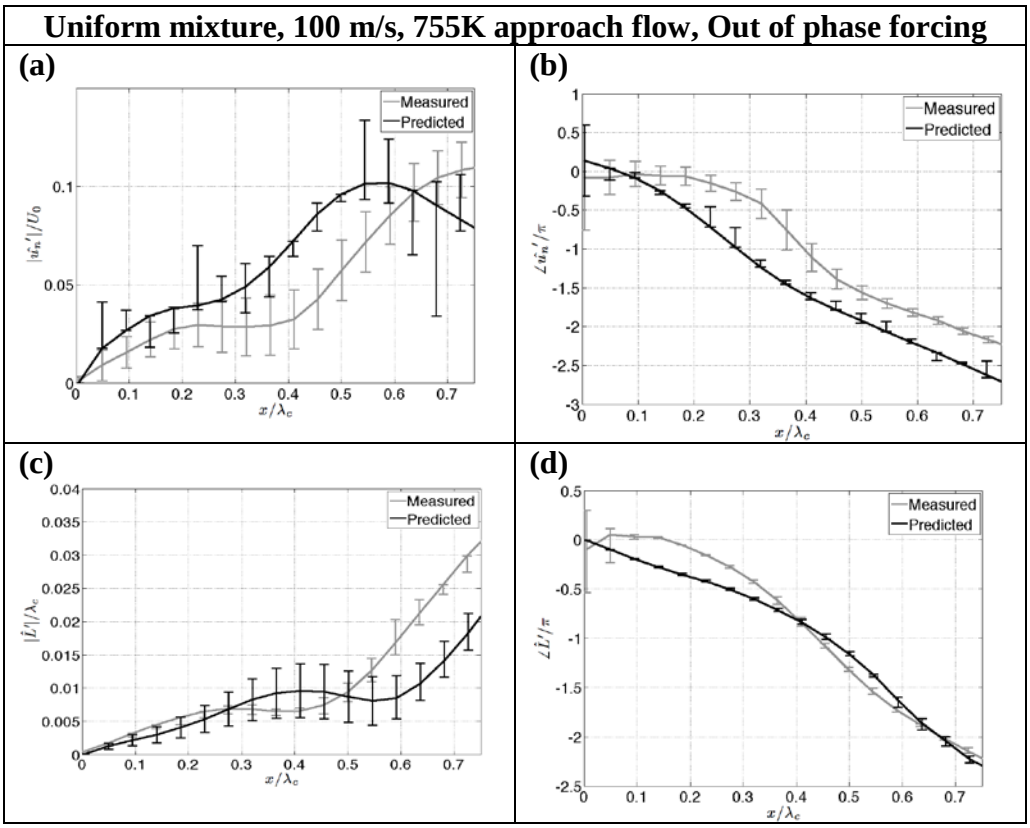

Figure 82 : Velocity validation study for Uniform mixture, 100 m/s, 755K approach flow, Out of phase forcing, using Eq.(6.17) with flame edge as input : (a) amplitude comparison, (b) corresponding phase comparison; Flame edge validation study using Eq.(6.18) with velocity as input : (c) amplitude comparison, (d) corresponding phase comparison.

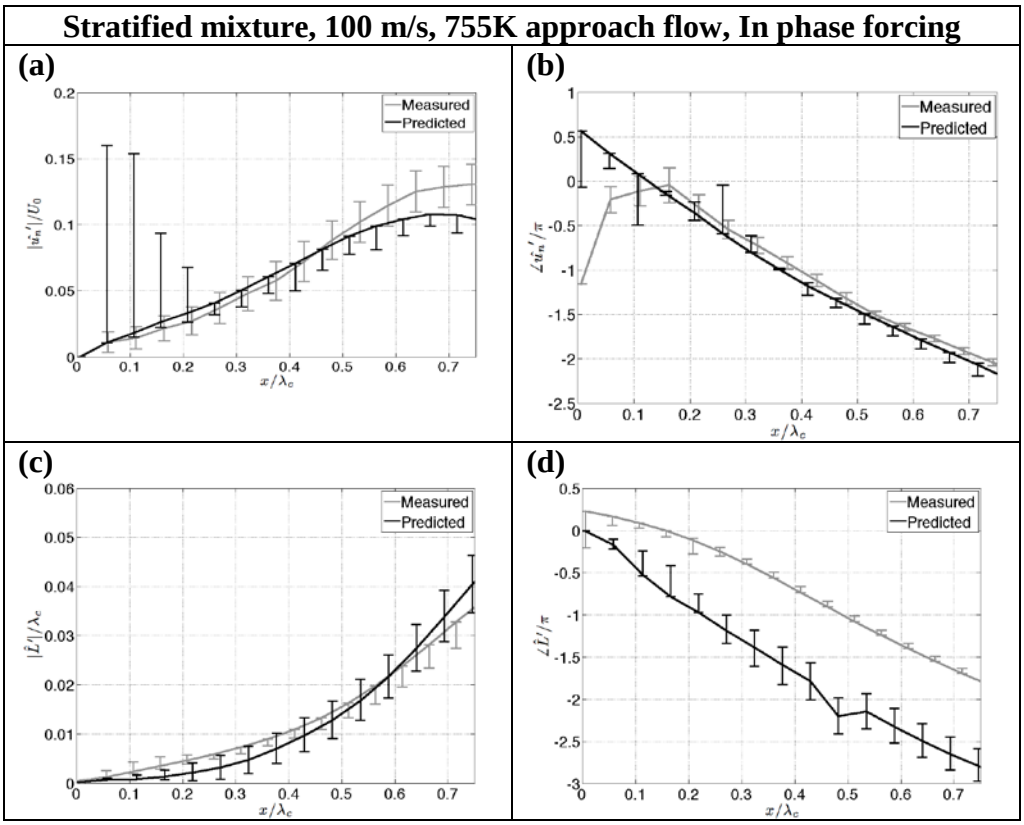

Figure 83. Velocity validation study for Stratified mixture, 100 m/s, 755K approach flow, In phase forcing, using Eq.(6.17) with flame edge as input : (a) amplitude comparison, (b) corresponding phase comparison; Flame edge validation study using Eq.(6.18) with velocity as input : (c) amplitude comparison, (d) corresponding phase comparison.

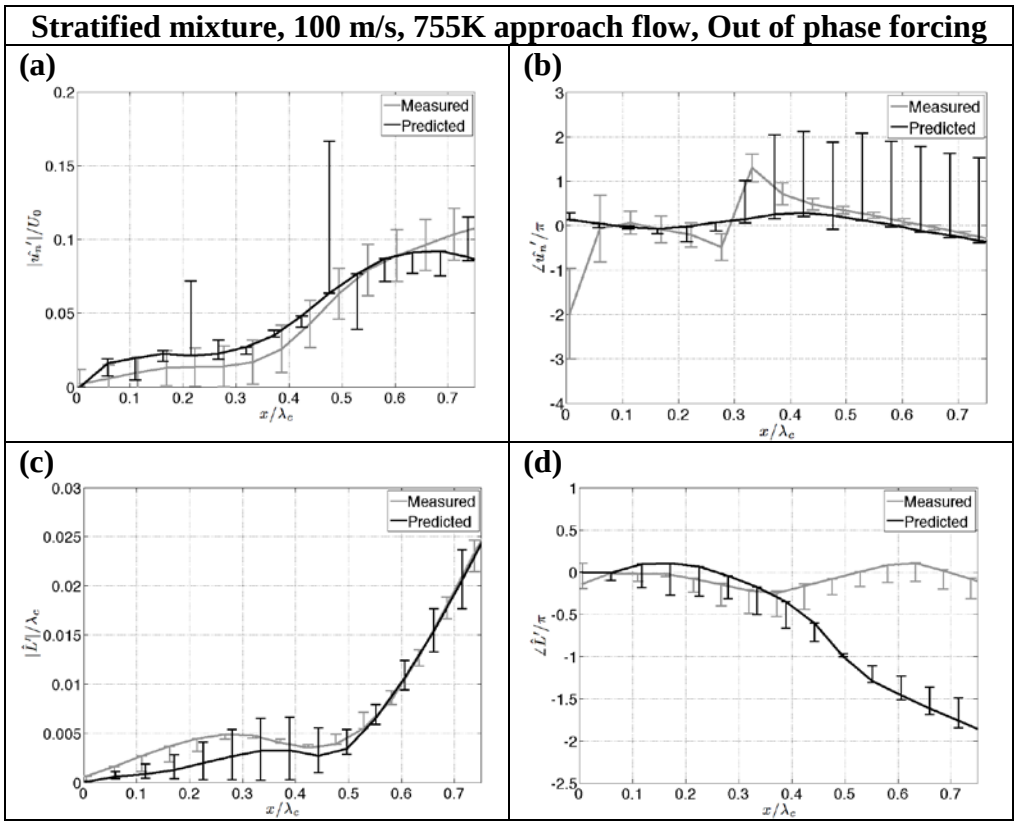

Figure 84. Velocity validation study for Stratified mixture, 100 m/s, 755K approach flow, Out of phase forcing, using Eq.(6.17) with flame edge as input : (a) amplitude comparison, (b) corresponding phase comparison; Flame edge validation study using Eq.(6.18) with velocity as input : (c) amplitude comparison, (d) corresponding phase comparison.

APPENDIX D

NAVIER-STOKES INTERPOLATION PROCEDURE

This section describes the procedure used to interpolate the time averaged and fluctuating disturbance flow fields in between the measurement planes in Chapter 7. Since the symmetric mode is of importance for the axisymmetric model, the data outside of measurement planes can be obtained using a few assumptions:

1. Density is assumed to not change with time.
2. Pressure gradients are neglected. This assumption is appropriate for the linearized disturbance equations, as vortical disturbances do not excite a leading order pressure disturbance [124]. This assumption is most problematic for the mean radial velocity equation, where swirl leads to significant pressure gradients.
3. Linearized analysis: Fluctuations are assumed to be smaller than time-averaged quantities. This allows for the time-averaged behavior to be generated first independently and then used to generate the fluctuations.
4. In case of the asymmetries, the non-linear terms can still lead to a symmetric contribution. For example, in the non-linear term, a negative mode -*m* in one component can interact with the corresponding positive mode +*m* in the other component leading to a symmetric term ($e^{-im\theta}e^{+im\theta}=1$). Hence the governing equations for the symmetric mode can involve the asymmetric modes as well. However, these interactions between non-asymmetries are neglected. Only the symmetric components of the time-averaged quantities are considered. This implies

that we only solve for the symmetric component and hence there is no azimuthal dependence. This reduces the domain to an *r*-*z* plane.

5. The axial velocity as measured in the *r*-*z* data is used in this model without change as $\bar{U}_z(r,z)$ and $\hat{B}_{z,0}(r,z)$.

We shall first consider the time-averaged velocity field generation. The time-averaged radial momentum equation is given by:

$$\bar{U}_r\frac{\partial \bar{U}_r}{\partial r}+\bar{U}_z\frac{\partial \bar{U}_r}{\partial z}-\frac{\bar{U}_\theta^2}{r}=\nu\left[\frac{1}{r}\frac{\partial}{\partial r}\left(r\frac{\partial \bar{U}_r}{\partial r}\right)+\frac{\partial^2 \bar{U}_r}{\partial z^2}-\frac{\bar{U}_r}{r^2}\right] \tag{D.1}$$

The time-averaged azimuthal (swirl) momentum equation is given by:

$$\bar{U}_r\frac{\partial \bar{U}_\theta}{\partial r}+\bar{U}_z\frac{\partial \bar{U}_\theta}{\partial z}+\frac{\bar{U}_r\bar{U}_\theta}{r}=\nu\left[\frac{1}{r}\frac{\partial}{\partial r}\left(r\frac{\partial \bar{U}_\theta}{\partial r}\right)+\frac{\partial^2 \bar{U}_\theta}{\partial z^2}-\frac{\bar{U}_\theta}{r^2}\right] \tag{D.2}$$

The fluctuating part of the radial momentum equation, for the symmetric mode is given by:

$$\begin{aligned} &i\omega\hat{B}_{r,0}+\bar{U}_r\frac{\partial \hat{B}_{r,0}}{\partial r}+\hat{B}_{r,0}\frac{\partial \bar{U}_r}{\partial r}+\bar{U}_z\frac{\partial \hat{B}_{r,0}}{\partial z}+\hat{B}_{z,0}\frac{\partial \bar{U}_r}{\partial z}-\frac{2\bar{U}_\theta}{r}\hat{B}_{\theta,0}\\ &=\nu\left[\frac{1}{r}\frac{\partial}{\partial r}\left(r\frac{\partial \hat{B}_{r,0}}{\partial r}\right)+\frac{\partial^2 \hat{B}_{r,0}}{\partial z^2}-\frac{\hat{B}_{r,0}}{r^2}\right] \end{aligned} \tag{D.3}$$

The fluctuating part of the azimuthal momentum equation, for the symmetric mode is given by:

$$\begin{aligned} &i\omega\hat{B}_{\theta,0}+\bar{U}_r\frac{\partial \hat{B}_{\theta,0}}{\partial r}+\hat{B}_{r,0}\frac{\partial \bar{U}_\theta}{\partial r}+\bar{U}_z\frac{\partial \hat{B}_{\theta,0}}{\partial z}+\hat{B}_{z,0}\frac{\partial \bar{U}_\theta}{\partial z}+\frac{\bar{U}_\theta}{r}\hat{B}_{r,0}+\frac{\bar{U}_r}{r}\hat{B}_{\theta,0}\\ &=\nu\left[\frac{1}{r}\frac{\partial}{\partial r}\left(r\frac{\partial \hat{B}_{\theta,0}}{\partial r}\right)+\frac{\partial^2 \hat{B}_{\theta,0}}{\partial z^2}-\frac{\hat{B}_{\theta,0}}{r^2}\right] \end{aligned} \tag{D.4}$$

The above equations are solved in an *r*-*z* rectangular domain and require boundary conditions. These are obtained from the measured data. Note that each of the unknowns

require two boundary conditions at the outer extents of the rectangular domain, since the governing equations are second order (due to the viscous terms).

The viscosity, v is obtained using the equivalence ratio and preheating temperature for the CH_4/air mixture. The reactant and product values are kept constant at their respective grid points across the flame location. Below is a summary of the measured data and how it shall serve as the boundary conditions, either directly or through some assumptions:

1. The *r*-*z* data provides $\bar{U}_z(r,z)$ and $\hat{B}_{z,0}(r,z)$ everywhere in the domain and this is directly used for the convection terms.
2. On the centerline (*r*=0), the time-average flow boundary conditions are:

   $\bar{U}_\theta(r=0,z)=0$ and $\bar{U}_r(r=0,z)=0$.

   The symmetric mode in the fluctuating flow has the following boundary conditions. The azimuthal component is zero for both the in-phase case and the out-of-phase case: $\hat{B}_{\theta,0}(r=0,z)=0$. The radial component is zero for the in-phase case (due to wave cancellation at the centerline): $\hat{B}_{r,0}(r=0,z)=0$, but for the out-of-phase case this is obtained from the centerline transverse velocity in the *r*-*z* PIV measurement.
3. The *r*-θ data is measured at *z/D*=0.14 and *z/D*=0.5. The symmetric modes of the radial and azimuthal velocity in this plane are the boundary conditions at these two axial locations. i.e., $\bar{U}_r(r,z=0.14D,0.5D)$, $\bar{U}_\theta(r,z=0.14D,0.5D)$ and $\hat{B}_{r,0}(r,z=0.14D,0.5D)$, $\hat{B}_{\theta,0}(r,z=0.14D,0.5D)$.

4. The helical mode amplitudes of the asymmetric modes decay radially, and so at the outer extent of the radial domain the velocity between the two planes (z/D=0.14 and z/D=0.5) is not very different. A linear interpolation between the values is used on this boundary ($r=R_{outer}$).

These PDEs are solved in the r-z domain using simple finite differencing. The time-average equations (Eqs.(D.1) & (D.2)) are solved first and independent of the velocity dynamics. These time-average solutions are then used as inputs to solve for the symmetric mode of the fluctuations (Eqs.(D.3) & (D.4)). An upwind scheme is used for the first derivative and a central difference is used for the second derivatives. A time-marching based method was used to obtain steady-state convergence with an appropriate CFL number based fixed time-step.

REFERENCES

[1] Goy, C., SR, J., and Rea, S., *Monitoring Combustion Instabilities: E.On Uk's Experience*, in *Combustion Instabilities in Gas Turbine Engines: Operational Experience, Fundamental Mechanics and Modeling*, Lieuwen, T. and Yang, V., Editors. 2005. p. 163-175.

[2] Rayleigh, B., *The Theory of Sound*. Vol. 1. 1896: Macmillan.

[3] Zinn, B. and Powell, E., *Nonlinear Combustion Instability in Liquid-Propellant Rocket Engines.* Proceedings of the Combustion Institute, 1970. **13**(1): p. 491-503.

[4] Culick, F., *Combustion Instabilities in Liquid-Fueled Propulsion Systems - an Overview.* AGARD Conference Proceedings, 1977. **450**: p. 1-73.

[5] Culick, F., Burnley, V., and Sweson, G., *Pulsed Instabilities in Solid-Propellant Rocket Engines.* Journal of Propulsion and Power, 1995. **11**(4): p. 657-665.

[6] Wicker, J., Greene, W., Kim, S., and Yang, V., *Trigerring of Longitudinal Combustion Instabilities in Rocket Motors: Nonlinear Combustion Response.* Journal of Propulsion and Power, 1996. **12**(6): p. 1148-1158.

[7] Yang, V. and Anderson, W., eds. *Liquid Rocket Engine Combustion Instability*. Progress in Astronautics and Aeronautics. Vol. 169. 1995, AIAA.

[8] Harrje, D. and Reardon, F., *Liquid Propellant Rocket Combustion Instability*1972.

[9] Lieuwen, T. and Yang, V., eds. *Combustion Instabilities in Gas Turbine Engines: Operational Experience, Fundamental Mechanisms, and Modeling*. Progress in Aeronautics and Astronautics, ed. Lu, F. Vol. 210. 2005, AIAA.

[10] Yang, V. and Culick, F., *Analysis of Low Frequency Combustion Instabilities in a Laboratory Ramjet Combustor.* Combustion Science and Technology, 1986. **45**(1-2): p. 1-25.

[11] Fleifil, M., Annaswamy, A., Ghoneim, Z., and Ghoneim, A., *Response of a Laminar Premixed Flame to Flow Oscillations: A Kinematic Model and Thermoacoustic Instability Results.* Combustion and Flame, 1996. **106**(4): p. 487-510.

[12] Ducruix, S., Durox, D., and Candel, S., *Theoretical and Experimental Determination of the Transfer Function of a Laminar Premixed Flame.* Proceedings of the Combustion Institute, 2000. **28**(1): p. 765-773.

[13] Gutmark, E., Parr, T., Parr, D., Crump, J., and Schadow, K., *On the Role of Large and Small Scale Structures in Combustion Control.* Combustion Science and Technology, 1989. **66**(4): p. 167-186.

[14] Schadow, K. and Gutmark, E., *Combustion Instability Related to Vortex Shedding in Dump Combustors and Their Passive Control.* Progress in Energy and Combustion Science, 1992. **18**(2): p. 117-132.

[15] Altay, H., Speth, R., Hudgins, D., and Ghoneim, A., *Flame-Vortex Interaction Driven Combustion Dynamics in a Backward-Facing Step Combustor.* Combustion and Flame, 2009. **156**(5): p. 1111-1125.

[16] Broda, J., Seo, S., Santoro, R., Shirhattikar, G., and Yang, V., *Experimental Study of Combustion Dynamics of a Premixed Swirl Injector.* Proceedings of the Combustion Institute, 1998. **27**(2): p. 1849-1856.

[17] Menon, S., *Acoustic-Vortex-Flame Interactions in Gas Turbines*, in *Combustion Instabilities in Gas Turbines: Operational Experience, Fundamental Mechanisms, and Modeling*, Lieuwen, T. and Yang, V., Editors. 2005, AIAA. p. 277-310.

[18] Lieuwen, T., Torres, H., Johnson, C., and Zinn, B., *A Mechanism of Combustion Instability in Lean Premixed Gas Tubrine Combustor*. Journal of Engineering for Gas Turbines and Power, 1998. **120**: p. 294-302.

[19] Lieuwen, T. and Zinn, B., *The Role of Equivalence Ratio Oscillations in Driving Combustion Instabilities in Low Nox Gas Turbines.* Proceedings of the Combustion Institute, 1998. **27**(2): p. 1809-1816.

[20] Shreekrishna, Hemchandra, S., and Lieuwen, T., *Premixed Flame Response to Equivalence Ratio Perturbations.* Combustion Theory and Modeling, 2010. **14**(5): p. 681-714.

[21] Kendrick, D., Anderson, T., Sowa, W., and Snyder, T., *Acoustic Sensitivities of Lean-Premixed Fuel Injector in a Single Nozzle Rig.* Journal of Engineering for Gas Turbines and Power, 1999. **121**(3): p. 429-436.

[22] Straub, D. and Richards, G., *Effect of Fuel Nozzle Configuration on Premix Combustion Dynamics*. in *ASME Turbo Expo*. 1998.

[23] Ducruix, S., Schuller, T., Durox, D., and Candel, S., *Combustion Dynamics and Instabilities: Elementary Coupling and Driving Mechanisms.* Journal of Propulsion and Power, 2003. **19**(5): p. 722-734.

[24] Dowling, A. and Ffowcs-Williams, J., *Sound and Sources of Sound*1983: John Wiley & Sons, Inc.

[25] Poinsot, T., Trouve, A., Veynante, D., Candel, S., and Esposito, E., *Vortex-Driven Acoustically Coupled Combustion Instabilities.* Journal of Fluid Mechanics, 1987. **177**(1): p. 265-292.

[26] Preetham, Thumuluru, S., Hemchandra, S., and Lieuwen, T., *Linear Response of Laminar Flames to Flow Oscillations: Unsteady Stretch Effects.* Journal of Propulsion and Power, 2010. **26**(3): p. 524-532.

[27] Wang, H., Law, C., and Lieuwen, T., *Linear Response of Stretch-Affected Premixed Flames to Flow Oscillations.* Combustion and Flame, 2009. **156**: p. 889-895.

[28] Bloxsidge, G., Dowling, A., and Langhorne, P., *Reheat Buzz: An Acoustically Coupled Combustion Instability, Part 2: Theory.* Journal of Fluid Mechanics, 1988. **193**(1): p. 445-473.

[29] Durox, D., Schuller, T., and Candel, S., *Combustion Dynamics of Inverted Concial Flames.* Proceedings of the Combustion Institute, 2005. **30**(2): p. 1717-1724.

[30] Bourehla, A. and Baillot, F., *Appearance and Stability of a Laminar Conical Premixed Flame Subjected to an Acoustic Perturbation.* Combustion and Flame, 1998. **114**(3-4): p. 303-318.

[31] Birbaud, A., Durox, D., and Candel, S., *Upstream Flow Dynamics of a Laminar Premixed Conical Flame Submitted to Acoustic Modulations.* Combustion and Flame, 2006. **146**(3): p. 541-552.

[32] Baillot, F., Bourehla, A., and Durox, D., *The Characteristics Method and Cusped Flame Fronts.* Combustion Science and Technology, 1996. **112**(1): p. 327-350.

[33] Baillot, F., Durox, D., and Prud'Homme, R., *Experimental and Theoretical Study of a Premixed Vibrating Flame.* Combustion and Flame, 1992. **88**(2): p. 149-168.

[34] Markstein, G., *Non-Steady Flame Propagation*1964, New York: Pergamon.

[35] Kerstein, A., Ashurst, W., and Williams, F., *Field Equation for Interface Propagation in an Unsteady Homogeneous Flow Field.* Physical Review, 1988. **A27**: p. 2728-2731.

[36] Williams, F., *Turbulent Combustion*, in *The Mathematics of Combustion*, Buckmaster, J., Editor 1985, SIAM. p. 97-132.

[37] Matalon, M. and Matkowsky, B., *Flames as Gasdynamic Discontinuities.* Journal of Fluid Mechanics, 1982. **124**(1): p. 239-259.

[38] Boyer, L. and Quinard, J., *On the Dynamics of Anchored Flames.* Combustion and Flame, 1990. **82**(1): p. 51-65.

[39] Dowling, A., *Nonlinear Self-Excited Oscillations of a Ducted Flame.* Journal of Fluid Mechanics, 1997. **346**(1): p. 271-290.

[40] Candel, S., *Combustion Dynamics and Control: Progress and Challenges.* Proceedings of the Combustion Institute, 2002. **29**(1): p. 1-28.

[41] Renard, P., Thevenin, D., Rolon, J., and Candel, S., *Dynamics of Flame/Vortex Interactions.* Progress in Energy and Combustion Science, 2000. **26**(3): p. 225-282.

[42] Schuller, T., Ducruix, S., Durox, D., and Candel, S., *Modeling Tools for the Prediction of Premixed Flame Transfer Functions.* Proceedings of the Combustion Institute, 2002. **29**(1): p. 107-113.

[43] Schuller, T., Durox, D., and Candel, S., *A Unified Model for the Prediction of Laminar Flame Transfer Functions: Comparisons between Conical and V-Flame Dynamics.* Combustion and Flame, 2002. **134**(1-2): p. 21-34.

[44] Preetham, *Modeling the Respons of Premixed Flames to Flow Disturbances*, in *School of Aerospace Engineering*2007, Georgia Institute of Technology: Atlanta, GA, USA.

[45] O'Connor, J., *Response of a Swirl-Stabilized Flame to Transverse Acoustic Excitation*, in *School of Aerospace Engineering*2011, Georgia Institute of Technology: Atlanta, GA, USA.

[46] Lacarelle, A., Faustmann, T., Greenblatt, D., Paschereit, C., Lehmann, O., Luchtenburg, D., and Noack, B., *Spatiotemporal Characterization of a Conical Swirler Flow Field under Strong Forcing.* Journal of Engineering for Gas Turbines and Power, 2009. **131**: p. 031504-1-031504-12.

[47] Ho, C. and Huerre, P., *Perturbed Free Shear Layers.* Annual Review of Fluid Mechanics, 1984. **16**(1): p. 365-422.

[48] Oster, D. and Wygnanski, I., *The Forced Mixing Layer between Parallel Streams.* Journal of Fluid Mechanics, 1982. **123**(1): p. 91-130.

[49] Michalke, A., *On the Inviscid Instability of the Hyperbolictangent Velocity Profile.* Journal of Fluid Mechanics, 1964. **19**(4): p. 543-556.

[50] Hirsch, C., Fanaca, D., Reddy, A., Polifke, W., and Sattelmayer, T., *Influence of the Swirler Design on the Flame Transfer Function of Premixed Flames*. in *ASME Turbo Expo*. 2005. Reno, NV, USA: ASME.

[51] Palies, P., Durox, D., Schuller, T., and Candel, S., *The Combined Dynamics of Swirler and Turbulent Premixed Swirling Flames.* Combustion and Flame, 2010. **157**(9): p. 1698-1717.

[52] Liang, H. and Maxworthy, T., *An Experimental Investigation of Swirling Jets.* Journal of Fluid Mechanics, 2005. **525**: p. 115-159.

[53] Wang, S. and Yang, V., *Unsteady Flow Evolution in Swirl Injectors with Radial Entry, Ii: External Excitations.* Physics of Fluids, 2005. **17**: p. 045107.

[54] Ho, C. and Nosseir, N., *Dynamics of an Impinging Jet, Part 1: The Feedback Phenomenon.* Journal of Fluid Mechanics, 1981. **105**: p. 119-142.

[55] Crow, S. and Champagne, F., *Orderly Structure in Jet Turbulence.* Journal of Fluid Mechanics, 2006. **48**(3): p. 547-591.

[56] Cohen, J. and Wygnanski, I., *The Evolution of Instabilities in the Axisymmetric Jet, Part 1: The Linear Growth of Disturbances near the Nozzle.* Journal of Fluid Mechanics, 1987. **176**: p. 191-219.

[57] Chan, W. and Ko, N., *Coherent Structures in the Outer Mixing Region of Annular Jets.* Journal of Fluid Mechanics, 1978. **89**(3): p. 515-533.

[58] Panda, J. and McLaughlin, D., *Experiments on the Instabilities of a Swirling Jet.* Physics of Fluids, 1994. **6**: p. 263.

[59] Gallaire, F., Rott, S., and Chomaz, J., *Experimental Study of a Free and Forced Swirling Jet.* Physics of Fluids, 2004. **16**: p. 2907.

[60] Syred, N., *A Review of Oscillation Mechanisms and the Role of the Precessing Vortex Core (Pvc) in Swirl Combustion Systems.* Progress in Energy and Combustion Science, 2006. **32**(2): p. 93-161.

[61] Thumuluru, S. and Lieuwen, T., *Characterization of Acoustically Forced Swirl Flame Dynamics.* Proceedings of the Combustion Institute, 2009. **32**(2): p. 2893-2900.

[62] Iudiciani, P. and Duwig, C., *Large Eddy Simulation of the Sensitivity of Vortex Breakdown and Flame Stabilisation to Axial Forcing.* Flow, Turbulence and Combustion, 2011. **86**: p. 639-666.

[63] Masselin, M. and Ho, C., *Lock-on and Instability in a Flat Plate Wake*, in *Shear Flow Control Conference*1985, AIAA: Boulder, CO, USA.

[64] Moeck, J., Bourgouin, J.-F., Durox, D., Schuller, T., and Candel, S., *Nonlinear Interaction between a Precessing Vortex Core and Acoustic Oscillations in a Turbulent Swirling Flame.* Combustion and Flame, 2012. **159**(8): p. 2650-2668.

[65] Stohr, M., Boxx, I., Carter, C., and Meier, W., *Experimental Study of Vortex-Flame Interaction in a Gas Turbine Model Combustor.* Combustion and Flame, 2012. **159**(8): p. 2636-2469.

[66] Palies, P., Schuller, T., Durox, D., and Candel, S., *Modeling of Premixed Swirling Flames Transfer Functions.* Proceedings of the Combustion Institute, 2011. **33**(2): p. 2967-2974.

[67] Armitage, C., Balachandran, R., Mastorakos, E., and Cant, R., *Investigation of the Nonlinear Response of Turbulent Premixed Flames to Imposed Inlet Velocity Oscillations.* Combustion and Flame, 2006. **146**(3): p. 419-436.

[68] Balachandran, R., Ayoola, B., Kaminski, C., Dowling, A., and Mastorakos, E., *Experimental Investigation of the Nonlinear Response of Turbulent Premixed*

Flames to Imposed Inlet Velocity Oscillations. Combustion and Flame, 2005. **143**(1-2): p. 37-55.

[69] Dowling, A., *A Kinematic Model of a Ducted Flame.* Journal of Fluid Mechanics, 1999. **394**(1): p. 51-72.

[70] Fanaca, D., Alemela, P., Hirsch, C., and Sattelmayer, T., *Comparison of the Flow Field of a Swirl Stabilized Premixed Burner in an Annular and a Single Burner Combustion Chamber.* Journal of Engineering for Gas Turbines and Power, 2010. **132**(7): p. 071502.1-071502.7.

[71] Komarek, T. and Polifke, W., *Impact of Swirl Fluctuations on the Flame Response of a Perfectly Premixed Swirl Burner.* Journal of Engineering for Gas Turbines and Power, 2010. **132**(6): p. 061503.1-061503.7.

[72] Garcia-Villalba, M., Frohlich, J., and Rodi, W., *Large Eddy Simulation of an Annular Swirling Jet with Pulsating Inflow*, in *Turbulence and Shear Flow Phenomena*2005: Williamsburg, VA, USA.

[73] Straub, D. and Richards, G., *Effect of Axial Swirl Vane Location on Combustion Dynamics*. in *ASME TurboExpo*. 1999. Indianapolis, IN, USA.

[74] Thumuluru, S., Bobba, M., and Lieuwen, T., *Mechanism of the Nonlinear Response of a Swirl Flame to Harmonic Excitation*. in *ASME TurboExpo 2007: Power for Land, Sea and Air*. 2007. Montreal, Canada.

[75] Hield, P., Brear, M., and Jin, S., *Thermoacoustic Limit Cycles in a Premixed Laboratory Combustor with Open and Choked Exits.* Combustion and Flame, 2009. **156**(9): p. 1683-1697.

[76] Lawn, C. and Polifke, W., *A Model for the Thermoacoustic Response of a Premixed Swirl Burner, Part 1: Acoustic Aspects.* Combustion Science and Technology, 2004. **176**(8): p. 1359-1390.

[77] Reddy, A., Sujith, R., and Chakravarthy, S., *Swirler Flow Field Characteristics in a Sudden Expansion Combustor Geometry.* Journal of Propulsion and Power, 2006. **22**(4): p. 800-808.

[78] Alemela, P., Fanaca, D., Hirsch, C., Sattelmayer, T., and Schuermans, B., *Determination and Scaling of Thermo-Acoustic Characteristics of Premixed Flames.* International Journal of Spray and Combustion Dynamics, 2010. **2**(2): p. 169-198.

[79] Venkataraman, K., Preston, L., Simons, D., Lee, B., Lee, J., and Santavicca, D., *Mechanism of Combustion Instability in a Lean Premixed Dump Combustor.* Journal of Propulsion and Power, 1999. **15**(6): p. 909-918.

[80] Stow, A. and Dowling, A., *Thermoacoustic Oscillations in an Annular Combustor*. in *ASME Turbo Expo*. 2001. New Orleans, LA, USA: ASME.

[81] Elias, I., *Acoustical Resonances Produced by Combustion of a Fuel-Air Mixture in a Rectangular Duct.* The Journal of the Acoustical Society of America, 1959. **31**(3): p. 296-304.

[82] Kaskan, W. and Noreen, A., *High-Frequency Oscillations of a Flame Held by a Bluff-Body.* ASME Transactions, 1955. **77**(6): p. 855-891.

[83] Rogers, D. and Marble, F., *A Mechanism for High Frequency Oscillations in Ramjet Combustors and Afterburners.* Jet Propulsion, 1956. **26**(1): p. 456-462.

[84] Macquisten, M. and Dowling, A., *Combustion Oscillations in a Twin-Stream Afterburner*. Journal of Sound and Vibration, 1995. **188**(4): p. 545-560.

[85] Karnesky, A. and Colucci, S., *Recent Occurrences of Combustion Instability in Solid Rocket Motors: An Overview*. Journal of Spacecraft and Rockets, 1975. **12**(1): p. 33-38.

[86] Price, E., *Solid Rocket Combustion Instability: An American Historical Account*, in *Nonsteady Burning and Combustion Stability of Solid Propellants*1992, AIAA. p. 1-16.

[87] Berman, K. and Logan, S., *Combustion Studies with a Rocket Motor Having a Full-Length Observation Window*. Journal of the American Rocket Society, 1952. **22**(2): p. 78-85.

[88] Marshall, W., Pal, S., Woodward, R., Santoro, R., Smith, R., Xia, G., Sankaran, V., and Merkle, C., *Experimental and Computational Investigation of Combustor Acoustics and Instabilities, Part Ii: Transverse Modes*, in *44th AIAA Aerospace Sciences Meeting and Exhibit*2006: Reno, NV, USA.

[89] Ellis, M., Xia, G., Sankaran, V., Anderson, W., and Merkle, C., *Acoustic Mode Simulations in Experimental Rocket Combustors*, in *41st Joint Propulsion Conference and Exhibit*2005: Tuscon, AZ, USA.

[90] Richecoeur, F., Scouflaire, P., Ducruix, S., and Candel, S., *High-Frequency Transverse Acoustic Coupling in a Multiple-Injector Cryogenic Combustor*. Journal of Propulsion and Power, 2006. **22**(4): p. 790-799.

[91] Davis, D. and Chehroudi, B., *Shear-Coaxial Jets from a Rocket-Like Injector in a Transverse Acoustic Field at High Pressures*, in *44th Aerospace Sciences Meeting and Exhibit*2006, AIAA: Reno, NV, USA.

[92] Morgans, A. and Stow, A., *Model-Based Contorl of Combustion Instabilities in Annular Combustors.* Combustion and Flame, 2007. **150**(4): p. 380-399.

[93] Staffelbach, G., Gicquel, L., Boudier, G., and Poinsot, T., *Large Eddy Simulation of Self Excited Azimuthal Modes in Annular Combustors.* Proceedings of the Combustion Institute, 2009. **32**(2): p. 2909-2916.

[94] Wolf, P., Staffelbach, G., Roux, A., Gicquel, L., Poinsot, T., and Moureau, V., *Massively Parallel Les of Azimuthal Thermo-Acoustic Instabilities in Annular Gas Turbines.* Comptes Rendus Mécanique, 2009. **337**(6-7): p. 385-394.

[95] Schuermans, B., Paschereit, C., and Monkiewitz, P., *Non-Linear Combustion Instabilities in Annular Gas-Turbine Combustors*, in *44th AIAA Aerospace Sciences Meeeting and Exhibit*2006: Reno, NV, USA.

[96] Hauser, M., Lorenz, M., and Sattelmayer, T., *Influence of Transversal Acoustic Excitation of the Burner Approach Flow on the Flame Structure*. in *ASME Turbo Expo*. 2010. Glasgow, Scotland: ASME.

[97] Krebs, W., Bethke, S., Lepers, J., Flohr, P., and Prade, B., *Thermoacoustic Design Tools and Passive Control: Siemens Power Generation Approaches*, in *Combustion Instabilities in Gas Turbines*, Lieuwen, T. and Yang, V., Editors. 2005, AIAA. p. 89-112.

[98] Sewell, J. and Sobieski, P., *Monitoring of Combustion Instabilities: Calpine's Experience*, in *Combustion Instabilities in Gas Turbine Engines*, Lieuwen, T. and Yang, V., Editors. 2005, AIAA. p. 147-162.

[99] Smith, K. and Blust, J., *Combustion Instabilities in Industrial Gas Turbines: Solar Turbines' Experience*, in *Combustion Instabilities in Gas Turbine Engines*, Lieuwen, T. and Yang, V., Editors. 2005, AIAA. p. 29-42.

[100] Cohen, J. and Proscia, W., *Characterization and Contorl of Aeroengine Combustion Instability: Pratt & Whitney and Nasa Experience*, in *Combustion Instabilities in Gas Turbine Engines*, Lieuwen, T. and Yang, V., Editors. 2005, AIAA. p. 113-146.

[101] Mongia, H., Held, T., Hsiao, G., and Pandalai, R., *Incorporation of Combustion Instability Issues into Design Process: Ge Aeroderivative and Aeroengines Experience*, in *Combustion Instabilities in Gas Turbine Engines*, Lieuwen, T. and Yang, V., Editors. 2005, AIAA.

[102] Schwieger, R., *Combined Cycle Journal*, Las Vegas, NV: PSI Media.

[103] Schuller, T., Durox, D., and Candel, S., *Self-Induced Combustion Oscillations of Laminar Premixed Flames Stabilized on Annular Burners.* Combustion and Flame, 2003. **135**(4): p. 525-537.

[104] Noiray, N., Durox, D., Schuller, T., and Candel, S., *Self-Induced Combustion Instabilities of Premixed Flames in a Multiple Injection Configuration.* Combustion and Flame, 2006. **145**(3): p. 435-446.

[105] Blimbaum, J., Zanchetta, M., Akin, T., Acharya, V., O'Connor, J., Noble, D., and Lieuwen, T., *Transverse to Longitudinal Acoustic Coupling Processes in Annular*

Combustion Chambers. International Journal of Spray and Combustion Dynamics, 2012. **4**(4): p. 275-298.

[106] O'Connor, J. and Acharya, V., *Development of a Flame Transfer Function Framework for Transversely Forced Flames*. in *ASME Turbo Expo, Power for Land, Sea and Air*. 2013. San Antonio, TX, USA: ASME.

[107] Steinberg, A., Boxx, I., Stohr, M., Carter, C., and Meier, W., *Flow-Flame Interactions Causing Acoustically Coupled Heat Release Fluctuations in a Thermo-Acoustically Unstable Gas Turbine Model Combustor*. Combustion and Flame, 2010. **157**(12): p. 2250-2266.

[108] Huang, Y. and Yang, V., *Effect of Swirl on Combustion Dynamics in a Lean-Premixed Swirl-Stabilized Combustor*. Proceedings of the Combustion Institute, 2005. **30**(2): p. 1775-1782.

[109] Michalke, A. and Hermann, G., *On the Inviscid Instability of a Circular Jet with External Flow*. Journal of Fluid Mechanics, 1982. **114**: p. 343-359.

[110] Liepmann, D. and Gharib, M., *The Role of Streamwise Vorticity in the near-Field Entrainment of Round Jets*. Journal of Fluid Mechanics, 1992. **245**: p. 643-668.

[111] Yule, A., *Large-Scale Structure in the Mixing Layer of a Round Jet*. Journal of Fluid Mechanics, 1978. **89**(3): p. 413-432.

[112] Pier, B., *Local and Global Instabilities in the Wake of a Sphere*. Journal of Fluid Mechanics, 2008. **603**: p. 39-61.

[113] Monkewitz, P., *A Note on Vortex Shedding from Axisymmetric Bluff Bodies*. Journal of Fluid Mechanics, 1988. **192**: p. 561-575.

[114] Loiseleux, T., Chomaz, J., and Huerre, P., *The Effect of Swirl on Jets and Wakes: Linear Instability of the Rankine Vortex with Axial Flow.* Physics of Fluids, 1998. **10**(5): p. 1120-1134.

[115] Worth, N. and Dawson, J., *Self-Excited Circumferential Instabilities in a Model Annular Gas Turbine Combustor: Global Flame Dynamics.* Proceedings of the Combustion Institute, 2013. **34**(2): p. 3127-3134.

[116] O'Connor, J. and Lieuwen, T., *Disturbance Field Characteristics of a Transversely Excited Burner.* Combustion Science and Technology, 2011. **183**(5): p. 427-443.

[117] Malanoski, M., Aguilar, M., Acharya, V., and Lieuwen, T., *Dynamics of a Transversely Excited Swirling, Lifted Flame, Part I: Experiments and Data Analysis*. in *ASME Turbo Expo*. 2013. San Antonio, TX, USA: ASME.

[118] Malanoski, M., Aguilar, M., O'Connor, J., Shin, D.-H., Noble, D., and Lieuwen, T., *Flame Leading Edge and Flow Dynamics in a Swirling, Lifted Flame*. in *ASME Turbo Expo*. 2012. Copenhagen, Denmark: ASME.

[119] Bellows, B., Neumeier, Y., and Lieuwen, T., *Forced Response of a Swirling, Premixed Flame to Flow Disturbances.* Journal of Propulsion and Power, 2006. **22**(5): p. 1075-1084.

[120] Lawn, C., Evesque, S., and Polifke, W., *A Model for the Thermoacoustic Response of a Premixed Swirl Burner, Part 2: The Flame Response.* Combustion Science and Technology, 2004. **176**(8): p. 1331-1358.

[121] Kim, K., Lee, J., Lee, H., Quay, B., and Santavicca, D., *Characterization of Forced Flame Response of Swirl-Stabilized Turbulent Lean-Premixed Flames in a*

Gas Turbine Combustor. Journal of Engineering for Gas Turbines and Power, 2010. **132**: p. 041502.1-041502.8.

[122] Schimek, S., Moeck, J., and Paschereit, C., *An Experimental Investigation of the Nonlinear Response of an Atmospheric Swirl-Stabilized Premixed Flame.* Journal of Engineering for Gas Turbines and Power, 2011. **133**(10): p. 101502.1-101502.7.

[123] Kang, D., Culick, F., and Ratner, A., *Combustion Dynamics of a Low-Swirl Combustor*. Combustion and Flame, 2007. **151**(3): p. 412-425.

[124] Lieuwen, T., *Unsteady Combustor Physics*2013: Cambridge University Press.

[125] Shreekrishna, *Response Mechanisms of Attached Premixed Flames Subjected to Harmonic Forcing*, in *School of Aerospace Engineering*2011, Georgia Institute of Technology: Atlanta, GA, USA. p. 280.

[126] Cho, J. and Lieuwen, T., *Laminar Premixed Flame Response to Equivalence Ratio Oscillations.* Combustion and Flame, 2005. **140**(1-2): p. 116-129.

[127] Hemchandra, S., *Dynamics of Turbulent Premixed Flames in Acoustic Fields*, in *School of Aerospace Engineering*2009, Georgia Institute of Technology: Atlanta, GA, USA. p. 182.

[128] Clanet, C., Searby, G., and Clavin, P., *Primary Acoustic Instability of Flames Propagating in Tubes: Cases of Spray and Premixed Combustion.* Journal of Fluid Mechanics, 1999. **385**: p. 157-197.

[129] Oberlack, M., Wenzel, H., and Peters, N., *On Symmetries and Averaging of the G-Equation for Premixed Combustion.* Combustion Theory and Modeling, 2001. **5**(3): p. 363-383.

[130] Holmes, M., *Introduction to Perturbation Methods*. Texts in Applied Mathematics1995: Springer-Verlag.

[131] Courant, R. and Hilbert, D., *Methods of Mathematical Physics, Volume Ii*1962: Wiley-Interscience.

[132] Delgado, M., *The Lagrange-Charpit Method.* SIAM Review, 1997. **39**(2): p. 298-304.

[133] Whitham, G., *Linear and Nonlinear Waves*. Pure and Applied Mathematics1974: Wiley-Interscience.

[134] Lee, D. and Lieuwen, T., *Premixed Flame Kinematics in a Longitudinal Acoustic Field.* Journal of Propulsion and Power, 2003. **19**(5): p. 837-846.

[135] Kuramoto, Y. and Tsuzuki, T., *Persistent Propagation of Concentration Waves in Dissipative Media Far from Thermal Equilibrium.* Progress in Theoretical Physics, 1976. **55**(2): p. 356-369.

[136] Sivashinsky, G., *Nonlinear Analysis of Hydrodynamics Instability in Laminar Flames-I: Derivation of Basic Equations.* Acta Astronautica, 1977. **4**(11-12): p. 1177-1206.

[137] Creta, F., Fogla, N., and Matalon, M., *Turbulent Propagation of Premixed Flames in the Presence of Darrius-Landau Instability.* Combustion Theory and Modeling, 2011. **15**(2): p. 267-298.

[138] Searby, G. and Rochwerger, D., *A Parametric Acoustic Instability in Premixed Flames.* Journal of Fluid Mechanics, 1991. **231**: p. 529-543.

[139] Strahle, W., *On Combustion Generated Noise.* Journal of Fluid Mechanics, 1971. **49**(2): p. 399-414.

[140] Lieuwen, T., Mohan, S., Rajaram, R., and Preetham, *Acoustic Radiation from Weakly Wrinkled Premixed Flames.* Combustion and Flame, 2006. **144**: p. 360-369.

[141] Crighton, D., Dowling, A., Ffowcs-Williams, J., Heckl, M., Leppington, F., and Bartram, J., *Modern Methods in Analytical Acoustics Lecture Notes.* Journal of the Acoustical Society of America, 1992. **92**(5): p. 3023.

[142] Truffaut, J., Searby, G., and Boyer, L., *Sound Emission by Non-Isomolar Combustion at Low Mach Numbers.* Combustion Theory and Modeling, 1998. **2**(4): p. 423-428.

[143] Lieuwen, T. and Zinn, B., *Application of Multipole Expansions to Sound Generation from Ducted Unsteady Combustion Processes.* Journal of Sound and Vibration, 2000. **235**(3): p. 405-414.

[144] Pierce, A., *Acoustics: An Introduction to Its Physical Principles and Applications*1989: Acoustical Society of America.

[145] Samarasinghe, J., Peluso, S., Szedlmayer, M., DeRosa, A., Quay, B., and Santavicca, D., *3-D Chemiluminescence Imaging of Unforced and Forced Swirl-Stabilized Flames in a Lean Premixed Multi-Nozzle Can Combustor*. in *ASME Turbo Expo*. 2013. San Antonio, TX, USA: ASME.

[146] Jiang, G. and Peng, D., *Weighted Eno Schemes for Hamilton-Jacobi Equations.* SIAM Journal on Scientific Computing, 2000. **21**(6): p. 2126-2143.

[147] Gottlieb, S. and Shu, C., *Total Variation Diminishing Runge-Kutta Schemes.* Mathematics of Computation, 1998. **67**(221): p. 73-85.

[148] Chu, B. and Kovasznay, L., *Non-Linear Interactions in a Viscous Heat-Conducting Compressible Gas.* Journal of Fluid Mechanics, 1958. **3**(5): p. 494-514.

[149] Wen-Huei, J. and Menon, S., *Modes of Oscillation in a Non-Reacting Ramjet Combustor Flow.* Journal of Propulsion and Power, 1990. **6**(5): p. 535-543.

[150] Emerson, B., Mondragon, U., Acharya, V., Shin, D.-H., Brown, C., McDonell, V., and Lieuwen, T., *Velocity and Flame Wrinkling Characteristics of a Transversely Forced Bluff-Body Stabilized Flame, Part I: Experiments and Data Analysis.* Combustion Science and Technology, 2013. **In Press**.

[151] Hegde, U., Reuter, D., Daniel, B., and Zinn, B., *Flame Driving of Longitudinal Instabilities in Dump Type Ramjet Combustors.* Combustion Science and Technology, 1987. **55**: p. 125-138.

[152] Yu, K.-H., Trouve, A., and Daily, J., *Low-Frequency Pressure Oscillations in a Model Ramjet Combustor.* Journal of Fluid Mechanics, 1991. **232**(1): p. 47-72.

[153] Williamson, C., *Vortex Dynamics in the Cylinder Wake.* Annual Review of Fluid Mechanics, 1996. **28**: p. 477-539.

[154] Maxworthy, T., *On the Mechanism of Bluff-Body Flame Stabilization at Low Velocities.* Combustion and Flame, 1962. **6**: p. 233-244.

[155] Shin, D.-H. and Lieuwen, T., *Flame Wrinkle Destruction Processes in Harmonically Forced Turbulent Premixed Flames.* Journal of Fluid Mechanics, 2013. **721**(4): p. 484-513.

[156] Lipatnikov, A. and Sathiah, P., *Effects of Turbulent Flame Development on Thermoacoustic Oscillations.* Combustion and Flame, 2005. **142**: p. 130-139.

[157] Hemchandra, S., Peters, N., and Lieuwen, T., *Heat Release Response of Acoustically Forced Turbulent Premixed Flames: Role of Kinematic Restoration.* Proceedings of the Combustion Institute, 2011. **33**: p. 1609-1617.

[158] Shanbhogue, S., Shin, D.-H., Hemchandra, S., Plaks, D., and Lieuwen, T., *Flame Sheet Dynamics of Bluff-Body Stabilixed Flames During Longitudinal Acoustic Forcing.* Proceedings of the Combustion Institute, 2009. **32**: p. 1787-1794.

[159] Peters, N., *Turbulent Combustion*2000: Cambridge University Press.

[160] Shin, D.-H., Plaks, D., Lieuwen, T., Mondragon, U., Brown, C., and McDonell, V., *Dynamics of Longitudinally Forced, Bluff-Body Stabilized Flame.* Journal of Propulsion and Power, 2011. **27**: p. 105-116.

[161] Pier, B., *Open-Loop Control of Absolutely Unstable Domains.* Proceedings of the Royal Society of London, Series A: Mathematical, Physical and Engineering Sciences, 2003. **459**(2033): p. 1105-1115.

[162] Kim, D., Lee, J., Quay, B., and Santavicca, D., *Effect of Flame Structure on the Flame Transfer Function in a Premixed Gas Turbine Combustor*. in *ASME Turbo Expo: Power for Land, Sea and Air*. 2008. Berlin, Germany: ASME.

VITA

The author of this thesis, Vishal Srinivas Acharya, was born in Bangalore, India in 1984 to Srinivas Acharya and Revathi Srinivas. He completed his middle school (K-8) from the St. John's English School and Junior College in 1998 and High school (K-12) from P. S. Senior Secondary School, both in Chennai, India. During this period, he has been selected to several Indian National Mathematics Olympiad training camps, whose sole purpose is to select the Indian team for the International Mathematics Olympiad.

He earned both his Bachelor of Technology and Master of Technology degrees in July 2007 from the Indian Institute of Technology, Madras campus. At this juncture, he joined the Graduate program at the School of Aerospace Engineering in the Georgia Institute of Technology, Atlanta campus.

Starting in Fall 2007, he began his doctoral research as a Graduate Research Assistant at the Ben Zinn Combustion Lab, under advisor Dr. Timothy Lieuwen. During this course, he earned his Master of Science degree (non-thesis) from the School of Aerospace Engineering in May 2011. During the course of the Ph.D. he has also worked at the General Electric Global Research Center in Niskayuna, NY from May 2012 to August 2012 as part of the Combustion Dynamics and Diagnostics team in the Aero Thermal and Mechanical Systems Lab.

His research focusses specifically on developing reduced order and analytical models for predicting combustion instability markers in premixed land-based and aero-based Gas Turbines. Apart from this, his expertise also includes the user of numerical

methods for analytically intractable solutions and the use of Computational Fluid Dynamics methods for detailed fluid flow and combustion studies.

Outside of these professional interests within the combustion dynamics field, he is also professionally involved in developing open-source modules for digital art and computer generated animation. He has used this expertise in many mainstream visual effects intensive movies for various studios in Hollywood. He also has an interest in sports, specifically in tennis and shuttle badminton, having represented IIT Madras in his undergrad days.